

Electronic Thesis and Dissertation Repository

4-19-2024 11:00 AM

Scale-up and Measurement Enhancements of a BioGenerator Bioreactor

Jason J. Glas, *Western University*

Supervisor: Karamanev, Dimitre, *The University of Western Ontario*

A thesis submitted in partial fulfillment of the requirements for the Doctor of Philosophy degree in Chemical and Biochemical Engineering

© Jason J. Glas 2024

Follow this and additional works at: <https://ir.lib.uwo.ca/etd>

 Part of the [Other Chemical Engineering Commons](#)

Recommended Citation

Glas, Jason J., "Scale-up and Measurement Enhancements of a BioGenerator Bioreactor" (2024).
Electronic Thesis and Dissertation Repository. 10048.
<https://ir.lib.uwo.ca/etd/10048>

This Dissertation/Thesis is brought to you for free and open access by Scholarship@Western. It has been accepted for inclusion in Electronic Thesis and Dissertation Repository by an authorized administrator of Scholarship@Western. For more information, please contact wlsadmin@uwo.ca.

Abstract

Renewable energies in the form of wind and solar have seen steadfast growth across the world, however the abundance of these technologies that demonstrate short-term variability in power output threatens power grid stability and necessitates the use of fossil fuels for rapid throttling capability. A requirement for large scale energy storage systems becomes necessary and a system based on hydrogen generation, storage, and consumption for electrical grid supply-demand stabilization using a ferric sulfate oxidant is herein explored, named the BioGenerator. As the name implies, the system functions as an indirect microbial fuel cell using a biologically active broth dominated by the iron oxidizing microbe *Leptospirillum ferriphilum* obtained from Iron Mountain, California.

Research into the scale-up of a pilot scale system was needed to confirm the validity of laboratory research and assess the energy consumption of the system. A conceptual energy management system is proposed based on the use of a trompe such as that of the Ragged Chute compressed air plant near New Liskeard, Ontario to provide the aeration and heating requirements of the system. Novel methods of accurately measuring dissolved oxygen and volumetric mass transfer coefficient in ferric sulfate broth using microbial biooxidation stoichiometry and electrochemical amplification processes were achieved. Investigation into the direct in-situ measurement of solution pH and iron ion concentration by spectrophotometric techniques on aqueous ferric ions to reduce costs in the wear and tear of pH and redox probes was met with some success. As a result, a strategy for modelling the ferric ion absorbance characteristics has been proposed and a custom built spectrophotometer prototype was produced. Testing of a pilot scale BioGenerator yielded insights into the operating conditions that provide the best performance regarding microbial biooxidation dynamics as well as dissolved oxygen uptake and distribution within the bioreactor. Study into the search for hyperacidophiles thriving in ultra-low pH conditions revealed an interesting finding from the red algae *Cyanidium caldarium* that was demonstrated to show observable growth to pH -0.85 (19.5% w/w H₂SO₄), surpassing the current record holders of *Picrophilus oshimae* and *Picrophilus torridus*. The observation may have relevance in space exploration or genetic engineering applications.

Keywords

BioGenerator, *Leptospirillum ferriphilum*, *Cyanidium caldarium*, acidophile, negative pH, microbial fuel cell, hydrogen energy storage, airlift bioreactor, volumetric mass transfer coefficient

Summary for Lay Audience

Renewable energy technology using wind and solar power is rapidly growing globally but there are issues when wind and sunlight aren't available which can cause power brownouts which limits the amount of renewable power that can be added to the grid. A method of storing energy and releasing it to the grid as a buffer is needed to allow further expansion of renewable energy without compromising the stability of the national electrical grid. A novel energy storage system named the BioGenerator seeks to fill this role using hydrogen gas as a fuel source used in a fuel cell along with a liquid oxidant of ferric sulfate that is regenerated in a bioreactor with iron oxidizing bacteria commonly found in the flood water of abandoned mines. This technology requires research in scaling up the process from the laboratory benchtop to a pilot scale system to assess the operation more realistically and learn of any other unforeseen problems in the process of doing so. This work focuses on improving the monitoring and measurement of the liquid broth in the bioreactor to fine tune large scale construction of the bioreactor for the best energy efficiency. An energy input of low pressure compressed air is required to aerate the bioreactor and allow the bacteria inside to consume reduced ferrous iron ions in the broth, therefore reducing heat losses through exhausted air while maximizing the amount of oxygen dissolving into the broth is crucial for success of the technology and is a major focus of the study. An assessment of the overall system performance was taken to give a realistic expectation of the system in operation where previous studies had been theoretical only. Study of the limits of operation of the bacterial culture in the bioreactor was performed which led to the accidental discovery of higher than expected acid tolerance observed in an alga coexisting in the broth which was greater than the currently held record holding microbes for acid tolerance.

Co-Authorship Statement

Chapter 4. Improvements to the Measurement and Monitoring of the Broth

J. Glas was the principal author of this chapter. Findings in this chapter require further studies and is not yet prepared for publishing.

Chapter 5. Determination of the Broth Oxygen Content

J. Glas was the principal author of this chapter. Revisions and recommendations were made by the supervisor Dr. D. Karamanev. A version of Chapter 6 has been prepared for publishing in an appropriate journal.

Chapter 6. Determination and Measurement Improvements of the Bioreactor k_{LA}

J. Glas was the principal author of this chapter. Revisions and recommendations were made by the supervisor Dr. D. Karamanev. A portion of Chapter 7 has been prepared for publishing in an appropriate journal. This chapter incorporates sections contributed by J. Glas of the following published paper concerning volumetric mass transfer coefficients measured in a benchtop airlift bioreactor:

Glas J, Drandev S, Pupkevich V, Karamanev D. 2019. Energy balance of an airlift bioreactor used for electrical power generation in energy storage. Chemical Engineering Science, 210: 115208.

Chapter 7. Kinetic Study of the BioGenerator

J. Glas was the principal author of this chapter. Revisions and recommendations were made by the supervisor Dr. D. Karamanev. This chapter incorporates sections contributed by J. Glas of the following published paper concerning bioreactor dynamics and hysteresis effects of substrate feed stoppage in a trickling bed bioreactor:

Glas J, Jarboua TA, Nikolov B, Karamanev D. 2021. Process dynamics in a hydrogen-based energy storage system. *Journal of Energy Storage*, 44: 103416.

Chapter 8. Efficiency Analysis of the BioGenerator

J. Glas was the principal author of this chapter. Revisions and recommendations were made by the supervisor Dr. D. Karamanev.

Chapter 9. The Limits of Life – Hyperacidophiles

J. Glas was the principal author of this chapter. Revisions and recommendations were made by the supervisor Dr. D. Karamanev. A version of Chapter 9 has been prepared for publishing in an appropriate journal.

Acknowledgements

I would like to give my sincere gratitude to my supervisor Dr. Dimitre Karamanev for giving me the opportunity to work on this very interesting field of research and all the things learned along the way. I would also like to give special thanks to Dr. Kalin Penev, Dr. Victor Pupkevich, and Dr. Vassili Glibin who helped greatly in the early stages of the research.

Thank you to ICFAR for permitting construction and operation of the final pilot scale version of the BioGenerator on their premises.

Table of Contents

Abstract.....	ii
Summary for Lay Audience.....	iv
Co-Authorship Statement.....	v
Acknowledgements.....	vii
Table of Contents.....	viii
List of Tables	xiv
List of Figures.....	xv
List of Equations.....	xxi
List of Appendices	xxvi
Nomenclature.....	xxvii
Chapter 1	1
1 Introduction.....	1
1.1 Outlook of the Thesis.....	20
1.2 Purpose of this Research.....	21
Chapter 2.....	22
2 Literature Review.....	22
2.1 Energy Storage.....	22
2.1.1 Pumped Hydro	23
2.1.2 Lithium-Ion Batteries.....	25
2.1.3 Emerging Technologies	27
2.1.3.1 Compressed Air Energy Storage (CAES)	28
2.1.3.2 Thermal Energy Storage (TES).....	28
2.1.3.3 Flywheel Energy Storage (FES).....	29
2.1.3.4 Superconducting Magnetic Energy Storage (SMES).....	29

2.1.3.5	Flow Battery Energy Storage (FBES)	29
2.1.3.6	Fuel Cell Hydrogen Energy Storage (FC-HES)	30
2.2	Hydrogen Power	30
2.2.1	Hydrogen Production	31
2.2.1.1	Grey Hydrogen	32
2.2.1.1.1	<i>Production by Steam Methane Reforming</i>	33
2.2.1.1.2	<i>Production by Oil/Naphtha Reforming</i>	34
2.2.1.1.3	<i>Production by Coal Gasification</i>	35
2.2.1.2	Blue Hydrogen	36
2.2.1.2.1	<i>Carbon Capture Technologies</i>	36
2.2.1.2.2	<i>Carbon Utilization Technologies</i>	37
2.2.1.2.3	<i>Carbon Storage Technologies</i>	38
2.2.1.3	Green Hydrogen	39
2.2.1.3.1	<i>Production by Electrolysis</i>	39
2.2.1.3.2	<i>Production by Thermochemical Water Splitting</i>	40
2.2.1.3.3	<i>Production by Photochemical Water Splitting</i>	41
2.2.1.3.4	<i>Production by Biological Microbial Action</i>	43
2.2.1.3.5	<i>Production as Byproducts</i>	44
2.2.1.3.6	<i>Production by Natural Reservoir</i>	44
2.2.2	Hydrogen Transport and Storage	45
2.2.3	Hydrogen Consumption	48
2.3	The BioGenerator	48
2.3.1	Air Supply	57

2.3.1.1	Mechanical Compressor	58
2.3.1.2	Trompe	59
2.3.2	Energy Management	61
2.4	Iron Oxidizing Microbes and Extremophiles of Interest	64
2.4.1	Acidithiobacillaceae.....	67
2.4.2	Leptospirillaceae	70
2.4.3	Ferroplasmaceae and Picrophilaceae	71
2.4.4	Cyanidiophyceae.....	72
Chapter 3	74
3	Materials and Methods.....	74
3.1	Chemicals.....	74
3.1.1	Growth Medium and Microbial Culture	74
3.1.2	Ferrous Sulfate Solution	75
3.1.3	Hydrogen Gas	76
3.1.4	Zero Oxygen Solution.....	77
3.1.5	Cleaning	77
3.2	Analytical Procedures	77
3.2.1	Data Recording	77
3.2.2	Wet Chemistry Determination of Iron Concentration	77
3.2.3	Colourimetric Determination of Iron Concentration	78
3.2.4	Potentiometric Determination of Iron Ratio	79
3.2.5	Absorbance Scanning of Iron Sulfate Solutions	83
3.2.6	Polarographic Determination of DO Concentration	83
3.2.7	Optical Determination of DO Concentration.....	83
3.2.8	k_La Determination by Dynamic Air Stop-Start Method	85
3.2.9	Electrochemical Determination of pH	86

3.2.10 UV Fluorescence Detection of Algae	89
3.3 Experimental Design.....	92
3.3.1 Benchtop Scale BioGenerator.....	92
3.3.2 Semi-Pilot Scale BioGenerator.....	95
3.3.3 Pilot Scale BioGenerator.....	97
3.3.4 Fuel Cell Stack.....	99
3.3.5 Oxygen Solubility Vessel	101
3.3.6 Algae Culture Dishes	102
3.3.7 Jarosite Production Vials	104
Chapter 4.....	105
4 Improvements to the Measurement and Monitoring of the Broth	105
4.1 Model Development.....	106
4.1.1 Extinction Index Model Development.....	109
4.1.2 Molar Extinction Coefficient Model Development	113
4.1.3 Solution Algorithm of the Model.....	115
4.1.4 Discussion of the Model Development.....	117
4.2 Spectrophotometer Prototype Design	118
4.3 Summary of Chapter 4.....	122
Chapter 5.....	123
5 Determination of the Broth Oxygen Content.....	123
5.1 Background.....	123
5.1.1 The Meaning of Saturation	123
5.1.2 The DO Meter	126
5.1.3 Current State of DO Measurement in Iron Sulfate Broths.....	128
5.2 Measurement of Saturated DO with Biooxidation.....	128
5.2.1 Theory of a Novel DO Measurement Technique.....	128

5.2.2	Development of a Novel DO Measurement Technique.....	130
5.2.3	Measurement Process.....	133
5.3	Measurement of Biooxidation Rate with DO	134
5.4	Summary of Chapter 5	135
Chapter 6.....		136
6	Determination and Measurement Improvements of the Bioreactor k_{LA}	136
6.1	Background.....	136
6.1.1	The Meaning of k_{LA}	136
6.1.2	Methods of k_{LA} Measurement.....	138
6.1.2.1	Chemical Sulfite Oxidation Technique	138
6.1.2.2	Physical Outgassing Technique.....	139
6.1.2.3	Biological In-Situ Technique	139
6.1.2.4	Yield-Coefficient Technique	139
6.2	k_{LA} Measurement by Dynamic Air Stop-Start	140
6.2.1	k_{LA} Measurement in a Benchtop Scale Airlift Bioreactor.....	140
6.2.2	k_{LA} Measurement in a Semi-Pilot Scale Airlift Bioreactor.....	141
6.2.3	Shortcomings of Dynamic Methods	143
6.3	k_{LA} Measurement by Static Ferrous Step-Change	144
6.3.1	Development of a Novel k_{LA} Measurement Technique	144
6.3.2	k_{LA} Measurement in a Pilot Scale Airlift Bioreactor	147
6.4	Summary of Chapter 6.....	150
Chapter 7.....		151
7	Kinetic Study of the BioGenerator.....	151
7.1	Biological Aspects	151
7.2	Chemical Aspects.....	154
7.3	Restart Dynamics	157

7.3.1	Dynamics of a Benchtop Scale BioGenerator	157
7.3.2	Dynamics of a Pilot Scale BioGenerator	164
7.4	Summary of Chapter 7	167
Chapter 8	168
8	Efficiency Analysis of the BioGenerator	168
8.1	Bioreactor Thermal Retention and Stability	168
8.2	Packed Bed Aeration.....	169
8.3	Power Output Potential.....	171
8.3.1	Polarization Curves.....	171
8.3.2	Parasitic Losses.....	173
8.3.3	Maximum Power Point	176
8.4	Summary of Chapter 8	178
Chapter 9	179
9	The Limits of Life - Hyperacidophiles	179
9.1	Growth Rate Optimization.....	180
9.1.1	Light Level Optimization.....	181
9.1.2	Effect of Iron.....	183
9.2	Acid Tolerance Examination	184
9.3	Morphology and Identification	187
9.4	Summary of Chapter 9	188
Chapter 10	189
10	Summary of the Results	189
Bibliography	192
Appendices	212

List of Tables

Table 2.1 Lithium-ion battery operating characteristics (adapted from Buchmann 2017).....	25
Table 2.2 Lithium-ion battery type comparative advantage rank (adapted from Buchmann 2017).	26
Table 2.3 List of carbon capture adsorbents and their applications.....	37
Table 3.1 Nutrient media composition of iron sulfate broth.....	74
Table 3.2 pH calibration solution temperature corrections based on PHREEQC 3.7.0.	87
Table 3.3 pH calibration solution density table.	88
Table 3.4 Component list of optical fluorescence sensor.	90
Table 4.1 Extinction index model coefficients for Equations 4.6 – 4.9.....	111
Table 4.2 pH temperature correction model coefficients for Equations 4.11 – 4.13.....	112
Table 4.3 Molar extinction coefficient model coefficients for Equations 4.16 – 4.18.	114
Table 5.1 Salinity model coefficients for seawater (Benson and Krause 1984).....	127
Table 5.2 Parameters of Equation 5.7 at 25.3°C using BioGenerator broth.....	132
Table 5.3 Parameters of Equation 5.7 at 39.3°C using BioGenerator broth.....	132
Table 5.4 Preliminary results of the saturated DO measurement technique.....	134
Table 7.1 Optimal temperature and pH of select <i>L. ferriphilum</i> strains.	152
Table 9.1 Commonly cited extreme acidophiles.....	185

List of Figures

Figure 1.1 Regional energy source production and consumption for the 2021 year (adapted from EIA 2021).....	6
Figure 1.2 US consumer preference by vehicle type (adapted from DoT 2024).....	7
Figure 1.3 US inflation adjusted average gasoline price (adapted from EIA 2024b).....	7
Figure 1.4 Radiation transmission windows of the atmosphere of Earth. (“Atmospheric Transmission - Global Warming Art project” by Robert A. Rohde is licensed under CC BY-SA 3.0 DEED)	12
Figure 1.5 Solar reflectance of the surface of Earth (adapted from Surase et al. 2018).	13
Figure 1.6 Solar energy budget of the Earth (annual mean) (Trenberth and Fasullo 2012)..	13
Figure 1.7 Crop yield per hectare in the OECD nations (adapted from OECD 2021).	18
Figure 2.1 Consumption and production profiles of hydrogen (adapted from IEA 2022b). ..	32
Figure 2.2 Thermochemical water splitting cycles. Left: Cerium oxide two step cycle (Gokon et al. 2013). Right: Copper chloride hybrid cycle (Darmawan et al. 2023).....	41
Figure 2.3 Hydrogen volumetric and gravimetric densities (reprinted from EERE 2024).....	46
Figure 2.4 Simplified design of the BioGenerator.....	49
Figure 2.5 Proton exchange membrane polymer composition.	50
Figure 2.6 Representation of the oxygen reduction reaction (ORR) intermediate steps.	51
Figure 2.7 Biological residue occurring on cathode felt after extended use.....	54
Figure 2.8 Proton exchange membrane demonstrating heavy ferric ion intrusion.	55
Figure 2.9 Platinized felt demonstrating staining from cross-over contamination.	56

Figure 2.10 Regenerative blower with internal workings (Elmo Rietschle – Gardner Denver, Inc.).....	59
Figure 2.11 Diagram of Ragged Chute trompe. (adapted from “Taylor trompe sketch” licensed under CC BY-SA 4.0).....	61
Figure 2.12 Conceptual energy management system for the BioGenerator.	62
Figure 2.13 Diversity of consumption pathways by acidophilic microbes. “Data of the associated studies of Hedrich et al. 2011, Hedrich and Johnson 2013b, and Dopsin 2016” by Malik and Hedrich 2022 is licensed under CC BY.....	65
Figure 2.14 Components of the iron oxidation pathway of <i>Acidithiobacillus</i> spp. “A modified scheme as given by Ilbert and Bonnefoy 2013” by Malik and Hedrich 2022 is licensed under CC BY.....	66
Figure 2.15 Phylogenetic tree of <i>Acidithiobacillaceae</i>	69
Figure 2.16 Phylogenetic tree of <i>Leptospirillaceae</i>	70
Figure 2.17 Phylogenetic tree of <i>Ferroplasmaceae</i> and <i>Picrophilaceae</i>	72
Figure 2.18 Phylogenetic tree of <i>Cyanidiophyceae</i>	73
Figure 3.1 Ferrous iron regeneration apparatus.	75
Figure 3.2 Electrochemical cell representation of redox probe.	79
Figure 3.3 Redox probe assembly with voltage divider and temperature regulation.	81
Figure 3.4 High impedance voltage divider circuit schematic for redox electrode probe.	82
Figure 3.5 True redox output and voltage divider output calibration curves.....	82
Figure 3.6 DO probe assembly with rotary tapping hammer.....	85
Figure 3.7 Typical output response of pH meter (electrometer) using pH calibration standards.	88

Figure 3.8 Design and construction of optical fluorescence sensor.....	91
Figure 3.9 Alga fluorescence decay curve.....	92
Figure 3.10 Benchtop airlift style BioGenerator.....	94
Figure 3.11 Benchtop trickle bed style BioGenerator.	94
Figure 3.12 Semi-pilot scale BioGenerator.	96
Figure 3.13 Semi-pilot scale hydrogen gas circulation loop.....	97
Figure 3.14 Pilot scale BioGenerator.....	98
Figure 3.15 Pilot scale fuel cell bank and gas/liquid circulation loops.	99
Figure 3.16 Fuel cell stack-up of electrode felts, membrane, and gaskets.	100
Figure 3.17 Fuel cell graphite conduction plate and underlying components.	101
Figure 3.18 Oxygen solubility determination vessel.	102
Figure 3.19 Neutral white (4100 K) LED array.....	103
Figure 3.20 Growth caddy lighting circuit (note: right side LM317 circuit repeated x10)..	104
Figure 4.1 Samples of ferric sulfate (~10 g _{Fe3+} /L) at varied acidity from pH 2.20 to 0.00 at 25 °C.	107
Figure 4.2 Absorbance windows in mixed and separate aqueous solutions of ferrous and ferric sulfate.	108
Figure 4.3 Preliminary extinction index model based on measured data.	110
Figure 4.4 Extinction index model coefficient trend lines.....	110
Figure 4.5 pH correction model profiles.....	112
Figure 4.6 Extinction index deviation at low ferric ion concentration.	113

Figure 4.7 Preliminary molar extinction coefficient model based on measured data.....	114
Figure 4.8 Calculation algorithm of preliminary pH and iron concentration model.	116
Figure 4.9 Revised strategy for the redevelopment of the model.	117
Figure 4.10 Simplified operation of spectrophotometer.	119
Figure 4.11 LED and laser diode (LD) operating characteristics.	120
Figure 4.12 Example of uneven quantization error from logarithmic input relationship.	120
Figure 4.13 Prototype spectrophotometer for monitoring of the BioGenerator broth.....	121
Figure 5.1 Theoretical molecular transport across a gas-liquid interface.	124
Figure 5.2 Rate of change of output voltage relative to Fe ²⁺ and Fe ³⁺ ratio.....	129
Figure 5.3 Observed deviation from Nernstian relationship at low concentration ratio.....	130
Figure 5.4 Nernst relationship deviation curve taken at 39.3 °C.....	131
Figure 5.5 Microbial respiration over time.	135
Figure 6.1 Mass transport chain of oxygen in bioreactor from air to microbes.....	138
Figure 6.2 Comparative k _{LA} values in pure water and biological medium as a function of superficial air velocity and bioreactor size (benchtop and semi-pilot scale).....	141
Figure 6.3 k _{LA} and U _G correlation using the dynamic air stop-start method in a semi-pilot scale airlift bioreactor.	142
Figure 6.4 Depiction of DO probe response time error observed in an airlift bioreactor using the dynamic air stop-start method.....	143
Figure 6.5 Step-change addition of ferrous iron into an airlift bioreactor and observed dynamics by a DO probe and redox probe.....	145

Figure 6.6 k_{LA} and U_G correlation using the static ferrous step-change method in a semi-pilot scale airlift bioreactor.	147
Figure 6.7 Relationship of k_{LA} to U_G of a pilot scale BioGenerator.	148
Figure 6.8 Relationship of k_{LA} to VVM of a pilot scale BioGenerator	149
Figure 7.1 Biooxidation rate of <i>L. ferriphilum</i> in the BioGenerator with respect to pH.	152
Figure 7.2 Biooxidation rate of <i>L. ferriphilum</i> in the BioGenerator with respect to temperature.	154
Figure 7.3 Severe mineral depositing of jarosite.	155
Figure 7.4 Acidity effects on jarosite accumulation in the BioGenerator.	156
Figure 7.5 Predicted change in substrate concentration as a result of feed flow interruption and restart.	159
Figure 7.6 Dynamics of a benchtop scale 6 hour feed stoppage.	160
Figure 7.7 Dynamics of a benchtop scale 18 hour feed stoppage.	161
Figure 7.8 Dynamics of a benchtop scale 24 hour feed stoppage.	161
Figure 7.9 Dynamics of a benchtop scale 3 hour feed stoppage.	163
Figure 7.10 Reduction in biooxidation rate as an effect of microbial death in broth stored without substrate.	164
Figure 7.11 Redox probe readings of pilot scale at time of initial substrate stoppage.	165
Figure 7.12 Redox probe readings of pilot scale after 24 hour substrate stoppage.	165
Figure 7.13 DO probe readings of pilot scale at time of initial substrate stoppage.	166
Figure 7.14 DO probe readings of pilot scale after 24 hour substrate stoppage.	166
Figure 8.1 Temperature stabilization of a pilot scale BioGenerator.	169

Figure 8.2 Downcomer packed bed DO profile in semi-pilot scale bioreactor.	170
Figure 8.3 Downcomer packed bed DO profile in pilot scale bioreactor.	171
Figure 8.4 Pilot scale BioGenerator fuel cell bank polarization curves.	172
Figure 8.5 Fuel cell parasitic losses as a measure of excess ferrous ion generation.....	173
Figure 8.6 Voltage-current relationship of ferric sulfate electrolytic cell with carbon felt electrodes (Sigratherm graphite felt 120 cm ²).	175
Figure 8.7 Power output maxima of fuel cell bank.....	177
Figure 8.8 Maximum power point operating curve.	177
Figure 9.1 Light intensity growth optimization (first series).	182
Figure 9.2 Light intensity growth optimization (second series).	182
Figure 9.3 Growth optimization (first series) with iron.	183
Figure 9.4 Acid tolerance of <i>L. ferriphilum</i> with respect to biooxidation capability.	184
Figure 9.5 Lower limit pH study of <i>C. caldarium</i> from Iron Mountain.	186
Figure 9.6 Submerged algal colony growth at pH -0.85 visible to the naked eye.	186
Figure 9.7 Microscope view of <i>C. caldarium</i> (100x mag.). Left: Algal cluster immobilized on glass fiber. Center: Probable reproduction through endospores. Right: Alga cell dispersion on slide surface.	187

List of Equations

2.1 – Polysulfide Bromide Flow Battery Rxn.....	30
2.2 – Steam Methane Reforming Rxn.....	33
2.3 – Water-Gas Shift Rxn.....	34
2.4 – Methane Partial Oxidation Rxn	34
2.5 – CO ₂ Pressure Swing Absorption Rxn	37
2.6 – CO ₂ to Methane Valorization Rxn.....	38
2.7 – CO ₂ to Urea Valorization Rxn	38
2.8 – CO ₂ to Dimethyl Ether Valorization Rxn	38
2.9 – CO ₂ to Formic Acid Valorization Rxn.....	38
2.10 – CO ₂ to Ethanol Valorization Rxn	38
2.11 – H ₂ Production by Chlor-alkali Rxn.....	44
2.12 – Serpentinization Rxn.....	45
2.13 – Iron Hydroxide Oxidation Rxn	45
2.14 – BioGenerator Fuel Cell Rxn	49
2.15 – 4-Electron Pathway Direct Oxygen Reduction Rxn (ORR)	50
2.16 – 2-Electron Pathway Peroxide Formation Oxygen Reduction Rxn (ORR)	50
2.17 – 2-Electron Pathway Peroxide Degradation Oxygen Reduction Rxn (ORR)	50
2.18 – Ferric Ion Reduction Rxn (Fe ^{III} RR).....	52

2.19 – Resistivity Equation	57
3.1 – Oxygen Scavenging Rxn.....	77
3.2 – Dichromate Titration Formula	78
3.3 – Nernst Equation	80
3.4 – Redox Probe Temperature Calibration Equation.....	80
3.5 – Dynamic k_{La} Determination Equation.....	86
3.6 – Linearized Dynamic k_{La} Determination Equation.....	86
3.7 – pH Equation	87
4.1 – Ferric Hexaaqua Ion Equilibrium I.....	107
4.2 – Ferric Hexaaqua Ion Equilibrium II.....	107
4.3 – Ferric Hexaaqua Ion Equilibrium III	107
4.4 – Extinction Index Equation	109
4.5 – Extinction Index pH Correction Equation	111
4.6 – Extinction Index Temperature Correction Coefficient Equation I	111
4.7 – Extinction Index Temperature Correction Coefficient Equation II	111
4.8 – Extinction Index Temperature Correction Coefficient Equation III.....	111
4.9 – Extinction Index Temperature Correction Coefficient Equation IV.....	111
4.10 – pH Temperature Correction Model.....	111
4.11 – pH Temperature Correction Coefficient Equation I	111
4.12 – pH Temperature Correction Coefficient Equation II.....	111

4.13 – pH Temperature Correction Coefficient Equation III.....	111
4.14 – Corrected pH Equation	111
4.15 – Molar Extinction Coefficient Model.....	114
4.16 – Molar Extinction Coefficient Temperature Correction Coefficient Equation I.....	114
4.17 – Molar Extinction Coefficient Temperature Correction Coefficient Equation II	114
4.18 – Molar Extinction Coefficient Temperature Correction Coefficient Equation III	114
4.19 – Beer-Lambert Law	115
4.20 – 487nm Absorbance Correction Equation.....	115
4.21 – Corrected 487nm Absorbance.....	115
4.22 – 520nm Absorbance Correction Equation.....	115
4.23 – Corrected 520nm Absorbance.....	115
4.24 – Corrected Extinction Index	115
4.25 – 980nm Ferrous Ion Concentration Correction Model.....	115
4.26 – 980nm Ferrous Ion Concentration Temperature Correction Coefficient Equation ...	115
4.27 – Corrected Ferrous Ion Concentration.....	115
5.1 – Mortimer (1956) DO Calculation I.....	127
5.2 – Mortimer (1956) DO Calculation II.....	127
5.3 – Mortimer (1956) DO Calculation III	127
5.4 – Mortimer (1956) DO Calculation IV	127
5.5 – Benson and Krause (1984) DO Salinity Correction	127

5.6 – <i>At. ferrooxidans</i> Stoichiometric Biooxidation Equation.....	130
5.7 – Modified Nernst Equation.....	131
6.1 – Oxygen Transfer Rate Equation.....	137
6.2 – Oxygen Uptake Rate Equation.....	137
6.3 – Benchtop Scale k_{LA} - U_G Correlation I	141
6.4 – Benchtop Scale k_{LA} - U_G Correlation II	141
6.5 – Static k_{LA} Determination Equation	146
6.6 – Static k_{LA} Determination Equation (Rearranged)	146
6.7 – Semi-Pilot Scale k_{LA} - U_G Correlation I.....	147
6.8 – Semi-Pilot Scale k_{LA} - U_G Correlation II	147
6.9 – Pilot Scale k_{LA} - U_G Correlation.....	149
6.10 – Pilot Scale k_{LA} - VVM Correlation.....	149
7.1 – Jarosite General Chemical Formula.....	155
7.2 – Process Dynamics Equation I	158
7.3 – Process Dynamics Equation II.....	158
7.4 – Process Dynamics Equation III.....	158
7.5 – Process Dynamics Equation IV	158
7.6 – Process Dynamics Equation V.....	158
7.7 – Process Dynamics Equation VI	159
7.8 – Process Dynamics Equation VII	162

7.9 – Process Dynamics Equation VIII.....	162
8.1 – Ferrate Ion Production Half-Cell Equation.....	176
8.2 – Ferric Ion Reduction Half-Cell Equation.....	176
8.3 – Ferrate Degradation Equation	176

List of Appendices

Appendix A: Apparatus Photographs	212
Appendix B: Electrochemical Stack Design.....	220
Appendix C: Calibrations	226
Appendix D: Chapter 4 Data.....	235
Appendix E: Chapter 5 Data.....	245
Appendix F: Chapter 6 Data	252
Appendix G: Chapter 7 Data.....	261
Appendix H: Chapter 8 Data.....	283
Appendix I: Chapter 9 Data	288
Appendix J: Spectrophotometer Design Notes.....	292

Nomenclature

- A – cross-sectional area (cm^2, m^2)
- \bar{A} – absorbance value (-)
- B – pH model coefficient 1 (-)
- C – pH model coefficient 2 (-)
- D – pH model coefficient 3 (-)
- E – electromotive force (V)
- F – Faraday's constant (96485 C/mol)
- \dot{F} – flow rate (L s^{-1})
- G – DO model correlation coefficient ($\text{mg K}^x \text{L}^{-1}$)
- H – DO model correlation coefficient ($\text{mg K}^x \text{L}^{-1}$)
- I – extinction index model coefficient 1 (-)
- J – extinction index model coefficient 2 (-)
- K – extinction index model coefficient 3 (-)
- K_S – Michaelis constant ($\text{g}_{\text{Fe}^{2+}} \text{L}^{-1}$)
- L – extinction index model coefficient 4 (-)
- M – molar concentration (mol L^{-1})
- N – ferrous ion molar extinction coefficient model coefficient 1 (-)
- P – atmospheric pressure (atm)
- Q – concentration ratio (-)
- R – universal gas constant ($8.314 \text{ J mol}^{-1} \text{ K}^{-1}$)
- R_T – total resistance (Ω)
- S – substrate concentration (g L^{-1})
- T – temperature (K, $^{\circ}\text{C}$)
- U_G – superficial gas velocity (m s^{-1})
- V – volume (mL, L, m^3)
- W – electrochemical production rate ($\text{g}_{\text{Fe}^{2+}} \text{ s}^{-1}$)
- X – ferric ion molar extinction coefficient model coefficient 1 (-)
- Y – ferric ion molar extinction coefficient model coefficient 2 (-)
- Z – ferric ion molar extinction coefficient model coefficient 3 (-)
- a – volumetric interfacial surface area ($\text{m}^2 \text{ m}^{-3}$)

\bar{a} – ion activity (-)
 c – concentration (g L^{-1})
 d – division ratio (-)
 e – ADC error correction (-)
 h – sigmoidal half point (-)
 i – iteration count (-)
 j – sigmoidal minimum horizontal asymptote voltage (mV)
 k – sigmoidal maximum horizontal asymptote voltage (mV)
 k_L – average mass transfer coefficient (m s^{-1})
 l – pathlength (cm)
 m – sigmoidal slope (-)
 \dot{m} – molar mass (g mol^{-1})
 pH – pH value (-)
 q – microbial respiration rate ($\text{mgO}_2 \text{ L}^{-1} \text{ s}^{-1}$)
 r_s – microbial biooxidation rate ($\text{gFe}^{2+} \text{ L}^{-1} \text{ s}^{-1}$)
 s – salinity ($\text{g}_{\text{salt}} \text{ kg}_{\text{brine}}^{-1}$)
 t – time (s, min, hour)
 v – stoichiometric constant (-)
 x – microbial concentration (L^{-1})
 y – substrate/biomass yield coefficient ($\text{gFe}^{2+} \text{ g}_{\text{biomass}}^{-1}$)
 z – ion charge (-)
 Φ – absorbance correction (-)
 Ψ – pH correction (-)
 α – extinction index (-)
 γ – activity coefficient (-)
 ε – molar extinction coefficient ($\text{L mol}^{-1} \text{ cm}^{-1}$)
 ζ – Nernst constant (J C^{-1})
 η – effectiveness factor (-)
 θ – DO model correlation variable (-)
 ι – electric current (A)
 μ – specific growth rate (s^{-1})
 ρ – resistivity ($\Omega \text{ m}$)

Chapter 1

1 Introduction

Energy, it is the most important commodity in our daily lives responsible for our ability to comfortably transport in personal vehicles, keep warm over winter, and produce complex affordable manufactured goods in abundance amongst many other things; yet its importance is often overlooked by the average person until such an event as a power outage occurs. The effective use of a seemingly inexhaustible natural resource of flammable gas, oil, and coal has allowed the rapid transition from agrarian lifestyles to technologically advanced societies in a span of some 250 years through the Industrial Revolution. This transition has not come without consequences however, the processes to generate nitrogen fertilizers and high-productivity cultivation machinery spurred by this revolution has ballooned the world population from one billion to over eight billion, of whom those living in the most developed countries consume energy for personal use to an extent more than 100 times that of undeveloped regions of the world (EIA 2023a). Not only is the overall global population of concern but the rate of global development driving energy use, with an estimated increase of 1 – 2% per year observed at a combined consumption of 180000 TWh in 2022 (Energy Institute 2023). At such consumption rates the supply of non-renewable carbon-based fuels becomes a question of how many years until the supply is exhausted. Secondly is the question of the cumulative effects of modern human activity and the potential ramifications to the surface climate of the Earth.

Perhaps the more important question is not in the future consequences of our present activities but anticipating how we will realistically behave based on the geographical constraints, personal behaviours, and international competition between major energy consuming regions of the world moving into the future. As a general observation in the present day, the world can be split into two significant energy consuming regions separated by cooperative and competitive forces. The first of these regions can be grouped along historical geopolitical lines of similar democratic values often referred to as “the West”, an amalgamation of the Anglosphere and Western European NATO allies during the time of the Soviet Union along with the remainder of the European Union

nations after the collapse of the Soviet Union. The second of these regions can be defined as China, a nation accounting for 17.7% of the global population, where political reforms have generated very rapid technological development resulting in economic output rivaling the United States and still growing. Other nations not specified can still be expected to collectively have an impact where all regions of the Earth have demonstrated long-term growth at some level. The reason for defining these specific groupings is based on the distribution of hydrocarbon fuels between them and their significant production and consumption rates depicted graphically in Figure 1.1. In the Western world, specifically the United States and Canada, abundant quantities of petroleum oil and natural gas deposits supplemented with external imports aided in the development of the continent providing a means of cheap transportation to cover and develop an expansive area. This is in complete contrast to the European Union that demonstrates extremely poor energy security through domestic production where oil and gas are largely imported from regional neighbours such as Norway, the United Kingdom, and until recently, Russia. China finds itself in a similar situation as the European Union where easily extracted oil and gas reserves are scarce and its more abundant coal reserves have been relied on for its rapid development. The nature of this distribution of hydrocarbon resources and the need to maintain energy security allows some room for predictions on how these regions will approach the issue of dealing with dwindling resources along with the pollution and emissions at a regional and global level.

In the case of the United States and Canada, a transition to total renewable energies will likely be the most difficult to implement regionally for multiple reasons. Firstly, the political landscape especially in the United States is a democratic system that has developed a rather polarized nature and makes long term policy difficult to implement without an opposing political party undoing the direction of the previous party. This can create a rather turbulent environment for the marketing and sale of green energy technologies such as photovoltaic systems and electric cars to individual consumers where subsidies and other government led initiatives can suddenly vanish. Alternative energy powered vehicles, especially electric, will play a significant role in this energy transition in particular to reduce petroleum oil consumption where currently transportation purposes are responsible for 29.5% of total energy consumption and 68.3%

of petroleum oil usage in the United States as of 2022 (EIA 2024a). The laissez-faire approach taken towards business transactions that consumers are accustomed to will represent a major obstacle in transitioning, consumers need to be sold on the idea of electric vehicle ownership. Attempts to impose mandates and restrictions to force consumer spending habits tends to be viewed quite negatively as antithetical to Western values and can foster the opposite market response as was intended. Observations of consumer trends better illustrates the underlying problem at hand, particularly in the changing preferences for vehicle type as seen in Figure 1.2. Specifically, a trend for larger and heavier vans, pickup trucks, and SUV style vehicles over more traditional smaller passenger cars indicates the important point that consumers often do not hold fuel milage as the primary factor in their purchasing decisions. Lower transportation costs are often the major selling point used in the promotion of fully electric or hybrid gas-electric vehicle sales, but this appears to fall flat in the face of the many other perceived disadvantages associated with them. The exception to this being electric vehicles produced by the Tesla automotive company. Using successful marketing and branding, Tesla sells their products as luxury or premium goods to take advantage of consumers greater interest in projecting social status and have therefore dominated the market until recently.

The consumer indifference to vehicle fuel milage cost is probably due in large part to the fact that gasoline prices, despite often being a point of contention for many people, have remained rather stable when adjusted for inflation for decades as seen in Figure 1.3. This trend in gas price stability appears to hold true in fact all the way from the beginning of the 20th century. This is somewhat paradoxical as it might be expected that the cost would significantly increase as supply is depleted and extraction of new more challenging reserves would add to overall cost. Though this price stability may be attributed to various factors such as technological improvements keeping extraction costs down, as well as petroleum being a globally strategic material subjected to market manipulating forces. In addition to the general stability of gasoline prices the efficiency of light-duty gas-powered vehicles has increased nearly linearly from an average of 17.4 L/100km in 1970 to 9.3 L/100km in 2020, meaning it is technically about half as expensive in the present day to fill the gas tank than in the past when prices were perceived as “lower”

(EIA 2024a). This point alone severely undermines efforts to push electric vehicles where gasoline remains a highly affordable commodity.

In efforts to compel the transition to non-CO₂ emitting technologies many governments opt to impose additional taxes on gasoline or blanket taxes on all hydrocarbon use as a “carbon tax” to discourage consumption and compel consumers to seek alternatives. Gasoline and generally all hydrocarbon commodities display high demand inelasticity however, which is to say that it has been demonstrated that a short-term doubling in the price of gasoline for example has a barely noticeable change on the overall quantity the average person consumes even in the long term (Eitches and Crain 2016). This is easy to interpret at the consumer level where transportation is a necessity to go to work or a grocery store and the cost of replacing a gas vehicle for an electric vehicle to save a few dollars in fuel isn’t worthwhile. Meaning there are no practical substitute energy commodities that can be chosen without incurring a significant financial/time penalty in the trade/purchase of high value sunk cost assets like a vehicle while consumers are also obliged to hold their travel needs unchanged. It may be argued that these taxes might encourage greater use of public transit to help lower carbon emissions, however it can be observed that the combination of lost opportunity cost of time, inability to transport significant quantities of cargo, and the effects of social stratification congregating low social status individuals to its use doesn’t project attractive qualities to these alternate modes of transport other than in heavily traffic congested cities. The negative qualities of public transportation often act as the incentive to spend more money to purchase and maintain a personal vehicle in the first place. Similar logic in demand inelasticity where the capital cost of an item using energy which is significantly greater than the value of the energy commodity itself such as furnaces, hot water heaters, and other household appliances holds true as well. Where carbon taxes are applied to domestic industry the added costs will be distributed as some combination of profit losses and passing additional expense to consumers in the final product price. This only serves to make domestic products less competitive while foreign imports from nations like China which are heavy CO₂ emitters can sell products easier while skirting imposed emission penalties and regulations. In general, carbon taxes of any kind can not be expected to reduce hydrocarbon consumption and the resultant CO₂ emissions to a significant degree. The

taxes are likely to have the opposite effect where people need to spend more time working to cover the burden of higher prices on finished goods and in doing so emit a greater level of CO₂ emissions in the process. They will likely be inclined to purchase more foreign made goods with higher CO₂ emissions generated in their manufacture as well.

While electric cars have made their entrance to the consumer market over a decade ago, their overall share of US vehicles on the road only accounts for only 1.2% as of 2022 (DoE 2023a). This may be attributed to a slow entry where electric vehicles entering the market are new or were recently manufactured and therefore come with a high price tag as opposed to a more affordable used vehicle powered by gas which limits the market of prospective buyers especially in periods of economic turmoil. Additionally, since the entry of electric vehicles is still recent there can be expected to be a short-term initial surge in sales by consumers particularly interested by the novelty of owning an electric vehicle, though these consumers will be limited in number and will run out in time where sales may then flatline. These initial sales numbers are likely to be used for extrapolation purposes especially by vehicle manufacturers to paint a rosy picture of market projections and should be taken with a grain of salt where there is always a financial incentive to give positive outlooks – bad news doesn't sell cars.

Even though widespread adoption of green energy technologies at the consumer level to any substantial level is likely to be difficult, investments in renewable energy technologies through government spending in whole or in part for grid scale power generation continues to proceed well. In the year 2022, total solar power output capability in the United States and Canada came to 73.5 GW and 4.6 GW respectively while wind power capacity came to 141.3 GW and 17.0 GW (CREA 2023, EIA 2023b). Investments in these technologies continue to demonstrate strong growth with projected combined capacity outputs potentially doubling year-over-year (EIA 2023b).

The European Union in some similarity to the United States and Canada represents a region of densely clustered high per capita energy consuming nations of differing cultures and languages united in common mutual interest and holding similar values of

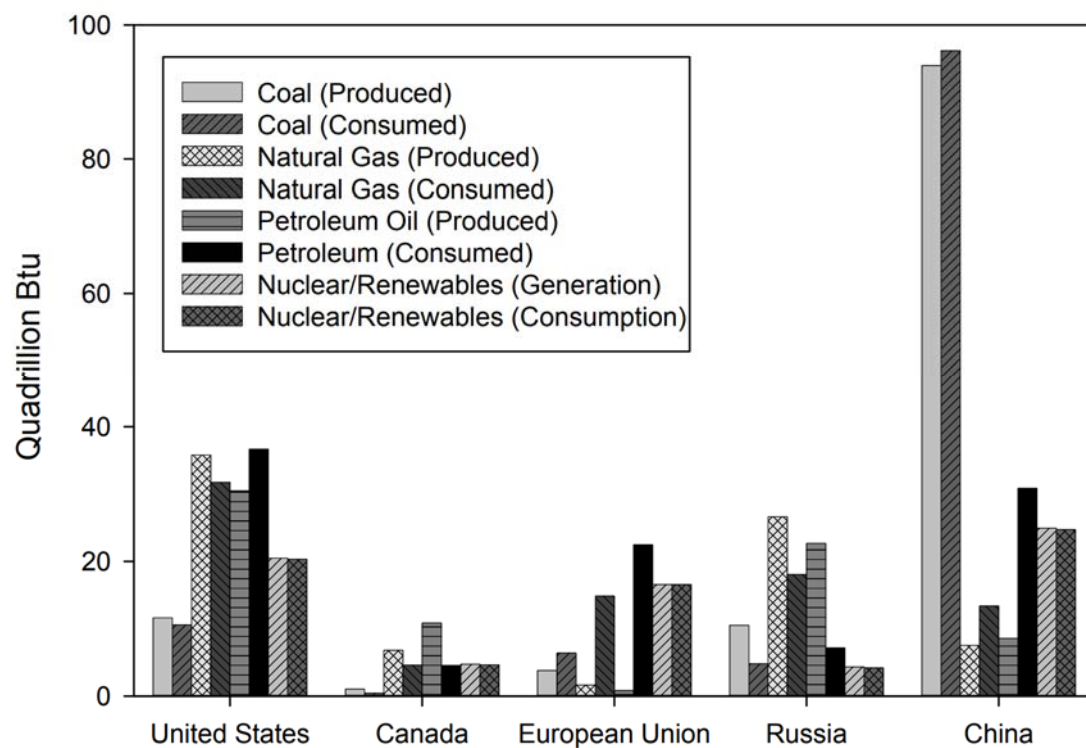


Figure 1.1 Regional energy source production and consumption for the 2021 year (adapted from EIA 2021).

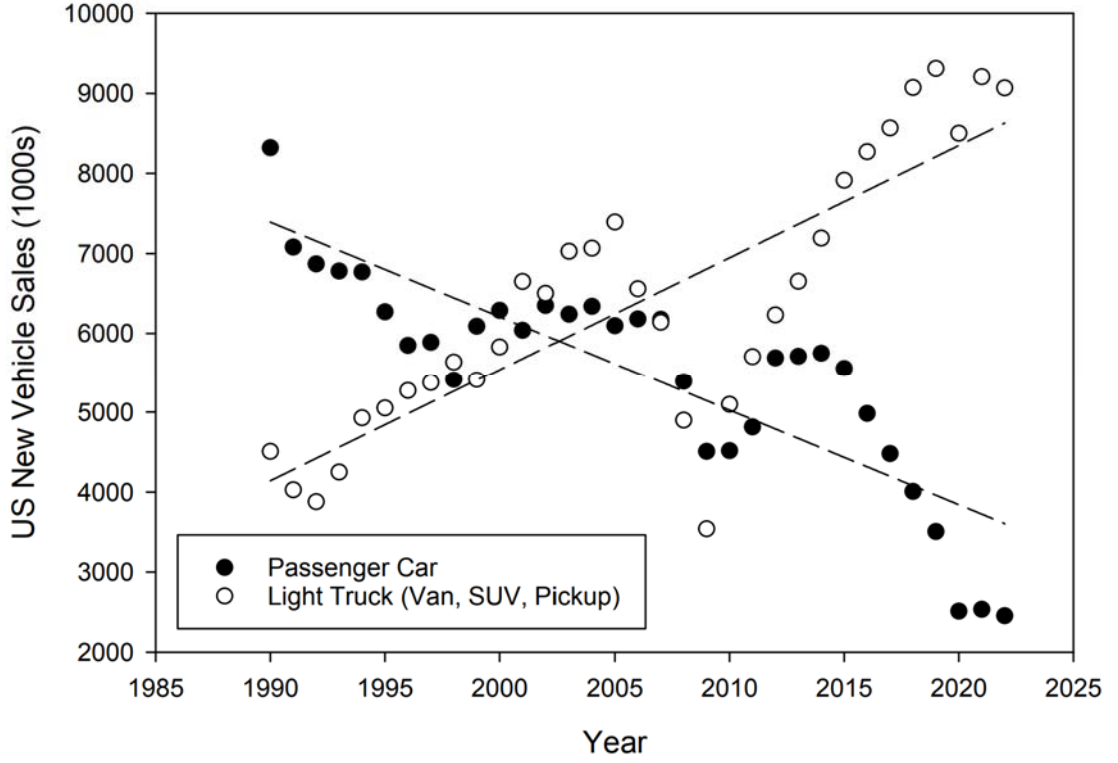


Figure 1.2 US consumer preference by vehicle type (adapted from DoT 2024).

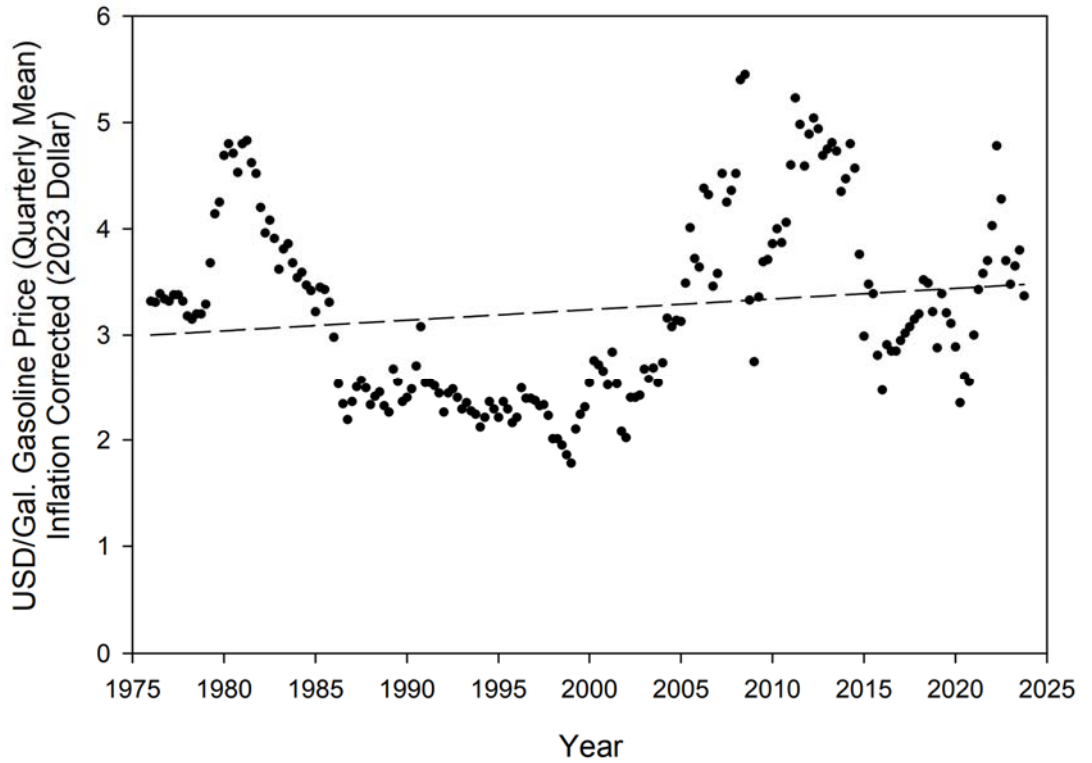


Figure 1.3 US inflation adjusted average gasoline price (adapted from EIA 2024b).

democratic governance. Unlike Canada and the United States however, energy security is quite poor with the specific nations in the union being bereft of large domestic supplies of coal, petroleum oil, and natural gas. Hydrocarbon energy commodities are largely imported with little domestic production (Figure 1.1) and buffered through strategic storage reserves. This lack of resources leaves the European Union highly vulnerable to sudden external events and market upsets, particularly underscored by the 2022 Russian invasion of Ukraine that caused the Western world to split from Russia and left European leaders scrambling to source alternative suppliers to make up the shortfall in the loss of Russian supply. The need to rely on external partnerships to acquire energy sources is generally undesirable for any nation where the relationship is open to exploitation by the supplier in various forms or may be impacted by outside parties. An example being the mysterious bombings of the underwater Nord Stream 1 & 2 gas pipelines by some unknown third party during the same period that physically disconnected supply between Russia and Europe, preventing the possibility of fostering future diplomatic trade negotiations between the two parties. Fortunately, the United States was available to provide an alternative source to Europe to make up the difference in supply through liquified natural gas deliveries at increased price, exporting an average of 232 million m³ per day in 2023 representing 67% of US exports as compared with 93 million m³ two years prior (DoE 2023b).

The precarious nature of an energy dependence relationship with the rest of the world is not beneficial for national interests or security. Therefore, distributed renewable energy sources delivering power domestically in the European Union are not just a tool to be used to meet emission targets but a strategically important asset beneficial to regional and global stability. This is reflected in the drive to move goals towards even greater amounts of grid scale renewable energy projects planned and underway in the European Union. An agreed target of 42.5% renewable power generation in the region by 2030 is being sought after being revised from a previous 32% target in response to the recent events (EU Council 2023). At the consumer level adoption of green technologies is likely to face similar hardships as the United States, though the bureaucratic nature of the European Union to regulate and standardize market goods and conditions may apply a more forceful approach in market affairs of the average consumer.

The issue of energy security is one also echoed by China, another significant region of interest. The political system of China is very different than that of the Western world where the government structure can be described as authoritarian in nature with a relaxed free-market economy. Such governments tend to be hit-or-miss largely depending on leadership quality and direction, which may result in very good or very bad results for those living under it. The nature of this style of government offers advantages particularly in long-term planning where objectives are stable, coherent, and currently structured into 5-year action plans as compared to the direction in democratic systems which by their nature tend to be only short-term oriented. Leadership in modern China has been demonstrated to be quite good, as such, extremely rapid economic development has been achieved with significant increases in standard of living and quality of life. This prosperity achieved in such short time has not come without significant hardship and sacrifice for the citizens of China. The nature of Chinese energy supply is disproportionately centered around coal consumption (Figure 1.1) and the consequences of its use at such staggering scales has made China infamous for its high particulate air pollution amongst other major pollution concerns. Another pressing matter of concern as a result of this economic growth is the explosion of personal vehicle ownership and specifically the associated demands for petroleum oil for liquid fuels to power them. Deposits of easily recoverable natural gas and crude oil are relatively scarce in China and liquid fuel demand has outpaced the domestic production capacity since 1993 growing to an excess demand in 2021 of 524.4 million tons imported over a relatively static domestic production rate of 189.9 million tons in the same year (BP 2022). The continuously growing discrepancy in oil supply continues to be tapered through ever increasing imports from major oil producing nations such as Russia and Saudi Arabia, but the current path is unsustainable and leaves China in a vulnerable position similar to the EU. Other efforts to quell supply deficiencies internally have come in the form of indirect coal liquefaction plants able to generate synthetic liquid fuels from coal. Current coal liquefaction operations in China provide 8 million metric tons of synthetic fuel per year to augment liquid fuel supplies but the process is known to produce very high emissions in the process, greater than 60 million metric tons of CO₂ per year with a process efficiency of just 44% (Li et al. 2021). Not only is petroleum oil an issue but coal supply

as well, where in 2021 a supply-demand mismatch produced price surges resulting in power shortages across the country as a result of combined factors. These factors include a fast economic recovery by China after the Covid-19 pandemic that resulted in a strong demand for energy while demand for coal from foreign nations that had not fully recovered ballooned Chinese exports (Di et al. 2022). These high demand issues were compounded by supply-side re-structural reforms by the Chinese government to curtail coal production implemented in the prior years which narrowed supply (Di et al. 2022).

The problem of oil production imbalance in China can be curtailed at least in part through transition to electric vehicles through its strong manufacturing capabilities and still burgeoning automotive market. This is backed by generous subsidies provided through the Chinese government to stimulate production and ownership of electric vehicles, which make up 4.9% of total cars on the road in China as of 2022 (IEA 2022a, IEA 2023). With this, China has taken the global lead in electric vehicle manufacture in 2022 representing 60% of new sales globally while holding half the world's electric vehicles in operation domestically (IEA 2023). Increasing exports of affordable electric vehicles as a byproduct of Chinese policy direction should be expected to further promote green energy transitions worldwide. This trend of market domination is also reflected in other green energy technologies as well such as wind and solar power making up 400 GW and 520 GW of national capacity respectively (CEC 2023). Investments in grid scale renewable energy investments have been extremely aggressive and as of the start of 2024, the combined power capacity of China's renewables sector (1460 GW) has surpassed that of non-renewables (1370 GW), a stark contrast from even just two years ago (Figure 1.1) (CEC 2023).

Given the recent events that have particularly affected energy security in both the European Union and China, target goals and investments in grid scale renewables have seen accelerated growth. In the case of China renewable energy technology also offers an avenue to escape from its reliance on heavily polluting coal and these factors combined are the likely explanation behind the drive to install renewables so rapidly. The other contributing factor is of course taking action to mitigate the effects of climate change, though the urgency of this factor is mostly manufactured and not critical to short term

national wellbeing. As it stands the United States and Canada have no such short-term urgent factors spurring renewable energy investments and so will likely lag behind China and the European Union. This still offers the advantage of benefitting from any external developments in the technology without needing to make any risky investments as part of the process. Benefits can also be expected in the form of price reductions as a result of the economies of scale from high output manufacturing in China. In any case the current outlook is positive with all parties maintaining a commitment to climate change mitigation intentionally or unintentionally.

A discussion of renewable energy of course would not be complete without an overview of CO₂ emissions and their contribution to climate change. Climate change driven by the greenhouse effect can be described in a basic sense as a balance of electromagnetic black-body radiation entering and leaving the Earth through processes of absorption, reflection, and emission from sunlight exposure. The interaction of these radiation effects with the atmosphere traps thermal energy and keeps surface temperatures 32 °C hotter than if no atmosphere existed, maintaining an average surface temperature of 14 °C (Zhong and Haigh 2013). The greenhouse effect is a natural phenomenon and critically important to maintaining life on Earth. Even though it is not fundamentally difficult to describe the greenhouse effect, the phenomenon is often misunderstood by the average person and easier to explain graphically (Figure 1.4, Figure 1.5, Figure 1.6). The process begins with sunlight emitted as black-body radiation illuminating the surface of the Earth where the atmosphere is transparent to the majority of the light (70 - 75 %) which may enter and exit freely as radiation at wavelengths within 300 – 1200 nm (Figure 1.4 - top-left). The sunlight that is not absorbed into the atmosphere on entry interacts with the surface of Earth (land and water) and depending on the specific spectral reflectivity characteristics some proportion of the light will be reflected back out to space while the remainder is absorbed (Figure 1.6). All absorbed light regardless of wavelength is converted to sensible or latent heat as molecular vibrations. The Earth itself is a black-body emitter just like the sun and also emits a spectrum of light, however since the temperatures are much cooler than that of the sun, the spectrum is shifted into the longwave infrared and composed of light with wavelengths between 4 – 70 μm (Figure 1.4 – top-right).

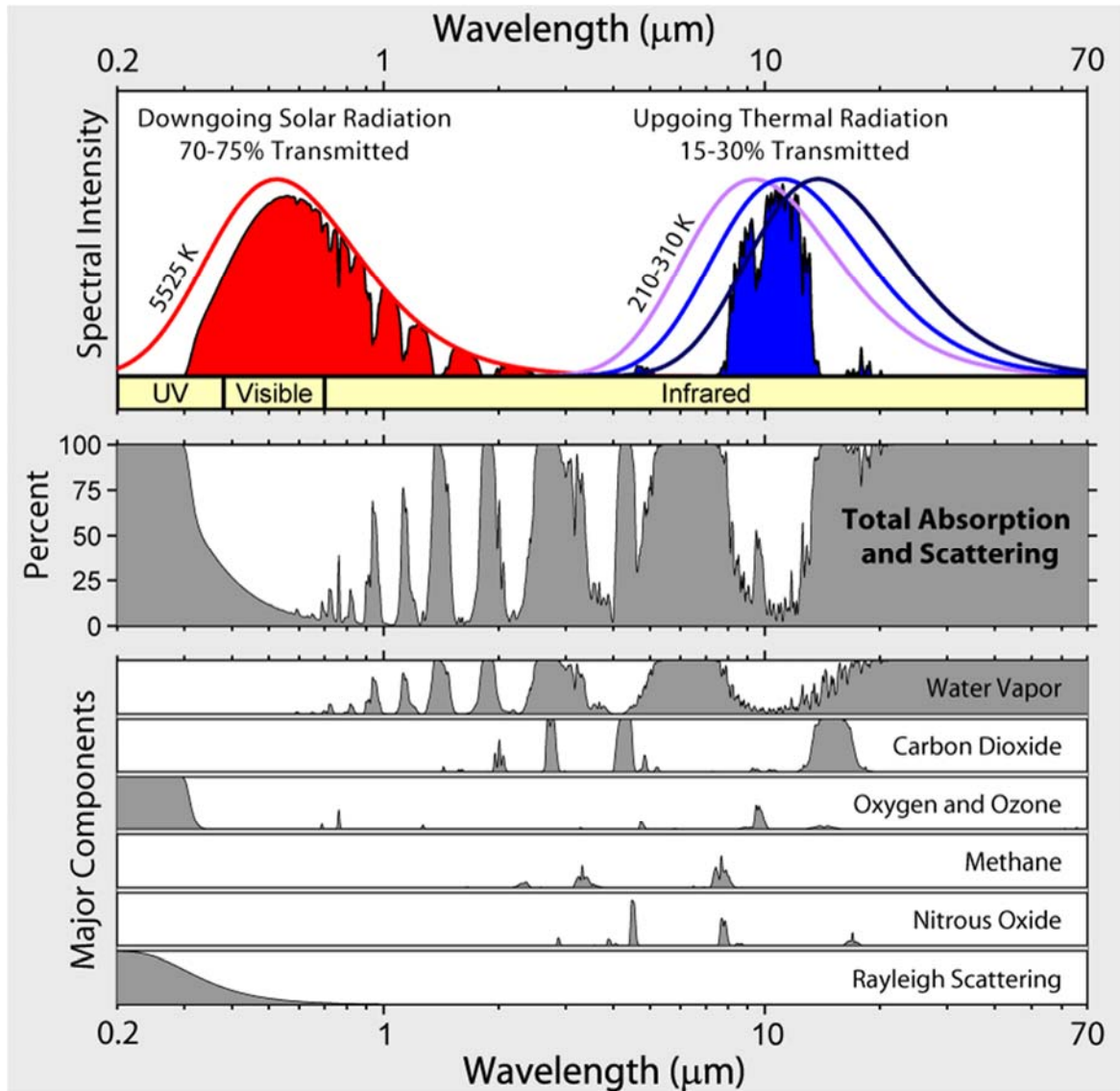


Figure 1.4 Radiation transmission windows of the atmosphere of Earth. (“Atmospheric Transmission - Global Warming Art project” by Robert A. Rohde is licensed under CC BY-SA 3.0 DEED)

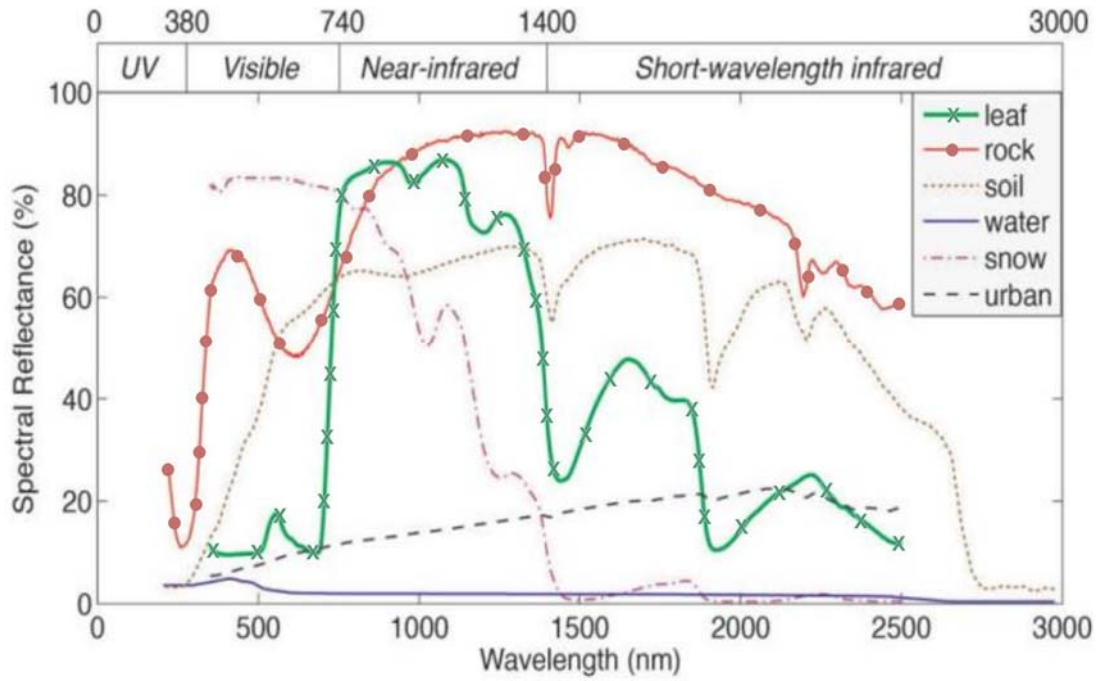


Figure 1.5 Solar reflectance of the surface of Earth (adapted from Surase et al. 2018).

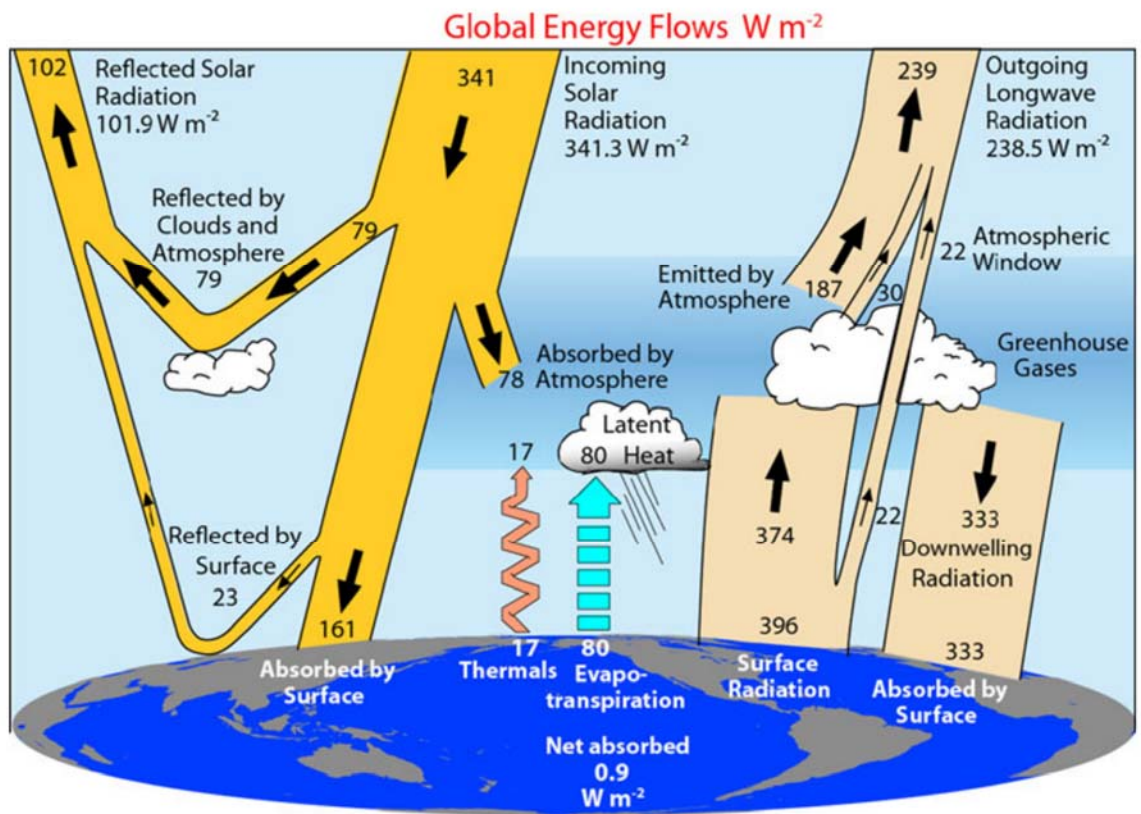


Figure 1.6 Solar energy budget of the Earth (annual mean) (Trenberth and Fasullo 2012).

The atmosphere in this region has high opacity to longwave infrared light except for a transparent window ranging from 8 – 14 μm that allows some (15 – 30%) thermal energy to escape through the atmosphere to space. The infrared light outside this transparent window remains bound between atmospheric gas molecules interconverting between molecular vibration and short-lived infrared photons emitted and absorbed between gas molecules. The cause of atmospheric opacity to some wavelength ranges below 700 nm is the result of the vibrational resonance of the gases present, with water vapor being most significant along with minor contributions by gases such as carbon dioxide and methane (Figure 1.4 – bottom).

It can be seen in Figure 1.4 that water vapor dominates the absorption broadly across the spectrum due to its abundance as air humidity while gases such as carbon dioxide only contribute any effect in discrete bands. Carbon dioxide exhibits four distinct bands, of which the two located at 2.0 and 2.7 μm are strongly overlapped by water absorption and are not relevant, the band at 4.3 μm exists in a region of minimal infrared intensity and so contributes only weakly, while the band at 15 μm represents the bulk of effects having strong absorbance against weak water vapor absorbance and is positioned near the peak of longwave infrared light intensity. The high absorptivity of carbon dioxide in this band (13 – 18 μm) has been demonstrated to be sensitive to its atmospheric concentration and is therefore postulated to result in increasing global temperatures (Zhong and Haigh 2013). The overall effect of energy absorption over this short frequency band is small in relation to all other absorption, nevertheless some additional contribution will still occur. An increase in temperature through this mechanism by some amount must occur in accordance with the laws of thermodynamics.

The knowledge of the greenhouse effect and the contributions to it by CO_2 have been known for more than a century but it wasn't until the 1960s that monitoring of CO_2 levels revealed the extent to which levels were rising (Marisa Dispensa and Brulle 2003). The revelation has since then sparked a flurry of research into predicting future trends and potential consequences of human activity as a result of rising atmospheric CO_2 levels over the decades. Research into climate effects is often made difficult by multiple factors that complicate analyses especially where modeling of atmospheric and oceanic

behaviours is concerned due to the extremely dynamic nature of long-term weather patterns. Effects such as El Niño/La Niña-Southern Oscillation have been known for several hundred years due to their influence on sail ships and represents irregular unpredictable periodic variations in air and sea surface temperatures every few years (Chang et al. 2006). The phenomenon is the result of sun warmed surface waters being driven towards the Asiatic side of the Pacific Ocean through trade winds forming a thermal build-up, reduced wind currents in some years cause the thermal build-up to move back towards South America (Chang et al. 2006, Trenberth and Fasullo 2012). The effect results in oscillations occurring over multi-year long periods with a component of high randomness in overall duration and intensity. This produces significant anomalies in regional temperatures and weather behaviours across the globe whose effects are often erroneously attributed to climate change. These oscillations occur at a frequency high enough that there is never a condition where weather patterns are sustained at stable levels for more than a few years (Chang et al. 2006, Trenberth and Fasullo 2012). While El Niño is the most well-known of long-term weather influencing effects, others exist as well such as Pacific Decadal Variability, Atlantic Multidecadal Variability, the North Atlantic Oscillation, the Southern Annular Mode and the Indian Ocean Dipole (Hernández et al. 2020).

This touches on a major problem plaguing legitimate scientific studies in climate behaviour where various phenomena are misrepresented as primary effects of climate change unintentionally through a lack of better explanations or intentionally in various ways as to accentuate an agenda or for example to act as a convenient excuse for government mismanagement. The extreme complexity and dynamics of the climate and ecosystem mean that many other factors may be at work. In North America for instance, there is evidence to suggest that ongoing desertification effects in observed regions can be attributed to the large and rapid destruction of herbivore megafauna populations, specifically herd animals like bison, during the European colonization of the continent that has led to a slow collapse of plant growth equilibrium (Franke and Kotzé 2022, Gosnell et al. 2020). This may be suggested to be a result of climate change but in actuality has nothing to do with impact by the global climate. The flagrant misuse of climate change as the go-to answer for any perceived negative occurrence should be

discouraged as it only serves to foster distrust in the scientific community which is difficult to re-establish once lost. This is especially so where climate change is used by activists as a basis to claim outrageous near-future consequences if action isn't taken immediately in attempts to spur action, only to reach this point in time where no such disaster ever materializes. In reality, climate change is a process too minor to be observed casually in the short-term but might be expected to contribute minor effects to intensity changes in prominently observed natural weather phenomenon.

Healthy skepticism around CO₂ contributions to sustained global temperature increases deserve merit as well. Despite best efforts to collect representative average temperature data of the Earth's surface faithfully, limitations due to time scaling factors make conclusive determinations difficult. This is to say that the temperature reading data does not contain a long enough baseline to establish a comparative reference to the natural normal and the expected naturally occurring long-term variance in global average temperatures. To formulate a longer baseline it is necessary to reconstruct the probable global average temperature of the past and is achieved through inference of various climate proxies such as ice core drillings, sedimentation patterns, borehole thermal profiles, and decay resistant biological materials (Hernández et al. 2020). Inferred data can never be as faithful as directly measured temperature data with homogenous surface coverage but the summation of many inferred data sets is still able to give an approximation with a margin of error low enough to be relevant for comparisons. The quality of this data and its effective coverage of regional temperature is of course open to scrutiny but currently appears to suggest that the sustained rate of measured average temperature rise exceeds long-term natural variances far outside the margins of data error (Neukom et al. 2019). Acknowledging this trend as unnatural, there remains the question of what percentage of contribution to temperature increases that CO₂ plays a part of as large-scale human activity influences the environment in more than one way and multiple contributing factors can be demonstrated. As an example, the natural land surface of Earth has been modified by human activity through the buildup of large urban centers covering significant area that demonstrate reduced sunlight reflectance over that of natural land (Figure 1.5). Urbanized areas consist of large amounts of asphalt and concrete amongst other materials that absorb sunlight very well over the entire emission

spectrum that will consequently result in sunlight induced thermal energy exhausted into the atmosphere at a greater rate (Lee et al. 2012, Wang et al. 2013). Another example can be demonstrated due to thermal pollution as a byproduct of the cumulative modern human consumption of non-renewable energy, also known as anthropogenic heat emission. Regardless of whether energy is produced through nuclear reactions or the burning of hydrocarbons for any use such as electrical generation or locomotion the result of the final energy use will be the production of thermal energy exhausted by some proportion to water bodies and to the atmosphere, except for an extremely minute fraction escaping through the atmosphere to space as human generated visible light. This released waste heat is subject to the greenhouse effect no different than energy absorbed from the sun and must also contribute to warming effects by some amount.

The most pertinent questions on the matter of climate change are the final consequences of human activity and the extent to which the environment will be affected. These are among the most difficult questions to answer given the extreme complexity and seemingly inexhaustible number of dynamic variables at play within the environment. Some speculated issues include more severe weather, reduced ocean alkalinity, and rising sea levels though evidence suggests that sea levels have always been rising and any human contribution only accounts for a fraction of present increases (Harrison et al. 2019). The effects of a changing environment by human activity are often projected through a human ethical lens imposing a bias that human induced change has negative connotations. The world does not function on mysterious forces of karmic justice however, and just as no good deed goes unpunished the opposite may occur as well where perceived negative action by human activities may end up producing a reward. Consequences of CO₂ emissions may just as well be improved crop yields with more lush forests (Mekonnen and Riley 2023, Yang et al. 2023) and potentially averting the catastrophe of some very long distant future ice age (Ganopolski et al. 2016, Tzedakis et al. 2012). The effect on crops is often a target in climate change discussions as negative effects on them would be immediately dangerous to humanity making it a centerpiece to certain doomsday claims. Examination of arable land productivity in the OECD nations over the last three decades (Figure 1.7) shows no alarming trend however, with production rates demonstrating a consistent linear increase over time trending with CO₂

and global temperature increase with no indications of stopping or slowing. Of course, there are some questions that science can't provide a definitive answer for and taking proactive steps in mitigating changes to the climate in the face of the unknown is the most reasonable and logical course of action to take.

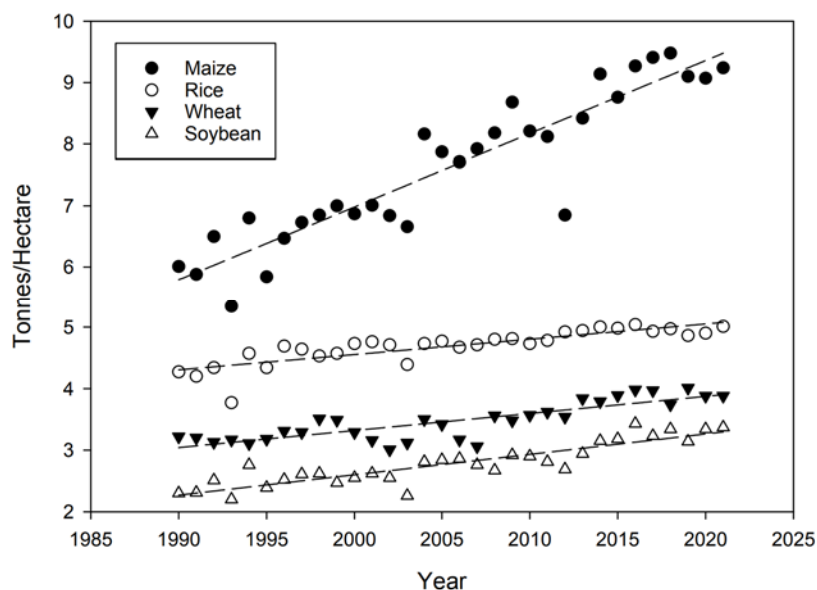


Figure 1.7 Crop yield per hectare in the OECD nations (adapted from OECD 2021).

Question still exists on how to approach the issue of human generated CO₂ that has built up in the air. The distribution of human generated CO₂ is extremely dilute and spread throughout 5.1 trillion trillion kilograms of other gases while its collective mass as of 2022 is 1.7 trillion tons (Friedlingstein et al. 2023), equivalent to the weight of the Great Pyramid of Giza multiplied 300000 times. A realistic solution that can remove these gases is likely reserved to the realm of science fiction. If removal of the gases is not possible, then controlling energy flow becomes the other possibility either through reflecting an increased level of sunlight back to space, actively emitting energy to space through an atmospheric window, or temporarily sequestering thermal energy from the atmosphere deep into the earth or ocean. The sheer scale of the problem makes plausible solutions difficult and will likely have to be funded through international cooperation which further complicates the matter. A solution first and foremost must be of a low cost as the potential for any project to fail always exists and can therefore be viewed as a gamble, if the cost is low then the potential of financial loss is low and therefore more

likely to proceed from the conceptual stage. This constraint alone severely limits possibilities.

Perhaps plant crops could be genetically engineered with better reflective properties in the 1300 – 2000 nm range (Figure 1.5) to better reflect the infrared tail of the sunlight spectrum back to space. Farmland takes up large amounts of the Earth's land surface area and crops can already be grown in massive volumes allowing a plausible solution to meet the scales involved. Also, in the event that it is later learned that this plan has created other problems the plants can be culled from the ecosystem during harvest and replaced with previous non-modified versions without too much trouble. As another possibility in the event that mass production allows solar panels to be so cheap that they result in an energy production over-supply, perhaps they might be engineered in such a way as to accentuate both their ability to convert light into electricity, and through reverse electrification, their ability to emit light. All semiconductor devices exude this photoelectric property though for devices specifically designed for the purposes of absorbing light (i.e. solar cells) or emitting light (i.e. light emitting diodes) the devices are optimized for best use in either-or case. For semiconductors the absorption of light and conversion to electricity is not very efficient (~25% max. through Si PERL cell) but the conversion of electricity to light is of high efficiency (40 - 50% through IR LED) and is also emitted monochromatically (Sze and Lee 2012). It may be a possibility then that the solar panels used for the absorption of sunlight during the day can be operated in reverse to beam infrared light of a wavelength able to pass through an atmospheric window band into space and exhaust energy at night. Such a concept would also require substantial energy storage capacity. Hypothetical solutions such as these if implemented would still unlikely be able to make a significant enough contribution to solve the problem and in the end the current climate effects of CO₂ gas will simply have to be tolerated as a new normal.

The major takeaway from these discussions on energy policy and security as well as climate change are that the world is shifting towards renewable energies as the dominate form of energy source moving into the 22nd century, if not by the intentions to do right but by force of geopolitical factors and the eventual depletion of limited terrestrial energy

resources. The inherent supply fluctuations associated with renewable energy must be accompanied by the construction of energy storage systems proportional to the construction of renewable energy sources. The storage of this energy may take many forms such as hydrostatic potential, electric charge, gas pressure, momentum, magnetism, heat, or chemical bonds. The rapid move into renewables requires equally rapid solutions in feasible energy storage systems. Research on an energy storage solution is herein presented using chemical potential energy bound as hydrogen gas and used for re-electrification into grid level energy through use of fuel cell technology. The system is differentiated from other designs through augmentation with biological oxidation of an aqueous iron sulfate catholyte and is aptly named, the BioGenerator.

1.1 Outlook of the Thesis

The main body of this thesis can be interpreted as three separate sections plus an extra section of a research byproduct. The first section represents the first three chapters; an introduction into the overarching relevance of the research project regarding energy, a literature review of the relevant technologies in the field of energy storage with an emphasis on hydrogen along with an overview of the BioGenerator technology and its practical implementation in a real-world scenario, and finally the methods and materials used in the completion of this study. The second section comprising Chapters 4 to 6 focuses on improvements in monitoring and measurement precision of bioreactor attributes for scale-up purposes with an emphasis on reducing operating costs and fine-tuning of bioreactor design. The third section is represented by Chapters 7 and 8 as performance studies on the scale-up of the BioGenerator from a benchtop unit to a semi-pilot scale version and finally to a true pilot scale system. An additional bonus section covers an accidental discovery as a result of the Covid-19 shutdown of a peculiar algae specimen discovered demonstrating exceptionally high acidic resistance, surpassing that of the current record holding microbes *Picrophilus oshimae* and *Picrophilus torridus*. These sections are followed with an outro of Chapter 10 which concludes the research findings and provides recommendations for future study as well as a bibliography and appendices including photographs of equipment used, raw data, and technical design details of a prototype spectrophotometer for pH and iron concentration measurement.

1.2 Purpose of this Research

Research into the BioGenerator is currently at an advanced stage of progress with the technology prepared to move from the laboratory to pilot scale. Much work has been previously conducted on the system at a physical level as well as in the study of the biological aspects. Studies by Penev (2010) identified the microbial culture of the system, dominated by *Leptospirillum ferriphilum*, and identified the optimum temperature for biological activity at ~ 40 °C. Optimum pH for the microbes was ascertained to exist in the range of pH 1.00 to 1.80 and the kinetics of microbial biooxidation of iron were established. Studies into microbial activity near pH 0 were conducted and determined the culture will shift towards domination by iron oxidizing *Ferroplasma* species with lower limits of activity found at pH -0.15. Later studies by Pupkevich (2014) focused extensively on proton exchange membrane fuel cell design and its operation and stability within the context of the BioGenerator. Synthesis of Nafion-based membranes was explored giving rise to formulations with significantly reduced ferric ion diffusion. Significant improvements were made in fuel cell performance demonstrating ~ 675 mA/cm² through improvements in the membrane, cathode, and flow distribution of the catholyte. Preliminary studies in the cost analysis of a theoretical scale-up of the system to a 1 MW output were conducted by Abou Jarboua et al. 2019.

Continuation of the established research seeks to fill gaps specifically in regard to the move towards pilot scale operations. A focus on improving and developing superior measurement techniques both as a means of achieving cost reduction in sensing equipment and in the optimization of large scale construction to minimize energy losses was identified as a major point. The overall testing of a true pilot scale system was also necessary, as up to this point studies toward focusing on scale-up were theoretical in nature. Lastly, continuation into the study of microbial behaviour at ultra-low pH was considered as a point of interest as the functionality of the BioGenerator system is directly related to the aspects of the microbial culture within it.

Chapter 2

2 Literature Review

A review of current energy storage technologies is presented in this literature review broken down into the current dominant market players (pumped hydro and lithium-ion batteries) followed by a brief overview of emerging energy storage technologies. Specific emphasis is placed on hydrogen as an energy storage medium for which the BioGenerator is based off and an in-depth coverage of the hydrogen economy is covered. Finally, the BioGenerator is introduced in detail based on the current state of the work and the microbial culture that drives its operation.

2.1 Energy Storage

The ability to effectively store and release electrical energy from and to the power grid at large scale is of paramount importance to the ability to implement the transition to renewable energy sources. The requirement for a reliable energy storage strategy is simple, electrical demand must always meet electrical supply in the immediate present to maintain stable synchronous operation of the electrical grid. The issue of course lies in the fact that renewable energy, particularly that of wind and solar, are extremely variable on a day-to-day and even hourly basis while energy demand is correlated to human activity and therefore moderately predictable by time of day but fluctuates highly from an average value. Energy storage provides the means of always meeting the immediate supply and demand through a process often referred to as “clipping the peaks” and “filling the valleys”, which is to say storing energy when it is in excess and releasing it back when in scant supply. The dominant energy storage solution for many decades has been through the use of pumped hydro, though recent advances in electric vehicle production and the consequent mass production availability of lithium-ion batteries has provided a secondary avenue to realistically expand storage capacity. Many other additional energy storage solutions are also under research at the present time. In the absence of sufficient energy storage capability an alternative approach to regulation is often employed through power plant throttling but tends to be suitable only to

combustion-based processes. Throttling is not a very practical solution in the sense that the goal of renewable energies is to limit CO₂ emissions while stability is only provided through CO₂ emissions. Another strategy that may be employed is to build an overcapacity of renewable supply and use it at partial capacity when energy is available to load match, this of course is an ineffective use of finances. An unfortunate reality of renewable energy implementation is the often lack of an effective regulation strategy that results in a trap of having to use infrastructure ineffectively or return to CO₂ emitting energy sources to maintain grid regulation. A failure to effectively regulate the grid may lead to severe consequences similar in nature to widespread grid failures such as occurred in the Northeast blackout of 2003 where the threat of cascading failure and resultant mass disconnection of power producers is an ever-present problem that requires many hours to re-establish full connectivity when the worst-case scenario occurs.

2.1.1 Pumped Hydro

Pumped hydro represents the oldest and most mature form of large-scale energy storage due to the technological simplicity of harvesting energy from hydrostatic potentials and vast storage capacities available through natural terrain features that may be exploited using dams in some cases. The operation closely resembles that of a hydroelectric power plant where a turbine is spun through the power of flowing water from a higher gravitational potential to a lower one which drives an electric generator and yields energy to the electrical grid. Under a pumped hydro scheme, the water reservoir used to provide power is often not continuously replenished by natural means and in fact the turbine is operated in reverse to refill the reservoir during periods of excess electrical energy on the grid. The immense size that reservoirs can be made allow such pumped hydro operations to be able to provide large quantities of sustained power (>1 GW) for comparatively long periods of time, on the order of days, and has the highest rated overall power of available technologies (Georgiou et al. 2018, Ibrahim et al. 2008, Smdani et al. 2023). The round-trip efficiency of charging the reservoir and conversion back to electricity is demonstrated to be quite good at 70 - 80% (Rehman et al. 2015).

While pumped hydro remains extremely effective in energy regulation, geographical constraints limit the development of new constructions to keep up with energy demand.

Currently China represents the dominant share of pumped hydro globally at 57.8% representing 41 GW with another 70 GW planned or under construction spurred through the rapid economic growth of the nation and widespread adoption of renewable energy sources necessitating energy storage (Nikolaos et al. 2023). The significant contribution by China is followed by Japan at 9.5% (15 GW), the United States at 7.2%, followed by small contributions by other nations collectively representing the remaining 25.5% (Nikolaos et al. 2023). Apart from China, very little additional capacity is under construction where nations such as Japan and the US appear to have effectively exhausted potential usable terrain and their capacity has remained stagnant since the 1990s while in other cases other nations may not have significant investments in renewables to necessitate construction (Nikolaos et al. 2023). An exception exists in the case of Canada however where a recent pumped hydro assessment report by Stantec 2023 determined that the vast hydroelectric generation capacity that Quebec and British Columbia are well known for represents terrain of low value particularly well suited for pumped hydro applications with a realistic potential within Canada of 8200 GW and a theoretical potential of 222800 GW. Despite this seemingly inexhaustible potential for energy storage, current pumped hydro use within Canada is surprisingly poor on the order of only 1 GW even with the substantial investments into renewables that have been made. Given this knowledge in the context of renewable energies it would be much more advantageous to develop energy storage potential and curtail additional renewable energy ventures in Canada, especially solar, which the latitude is not particularly effective for use. The close symbiotic relationship between Canada and the United States might be used for mutual gain where the Southern US in particular holds a competitive advantage in energy production through solar while Canada holds an absolute advantage in practical unrealized energy storage potential, an amount more than enough to satisfy all of North America. Such a strategy would be very beneficial to Canada in the long term where pumped hydro installations do not suffer from technological obsolescence and the investments can have functional service life well over a century (Smdani et al. 2023).

2.1.2 Lithium-Ion Batteries

The concept of using rechargeable batteries for large scale grid energy storage has been proposed as a possibility amongst other emerging technologies for many years; in particular, batteries with lithium-ion based chemistries. Lithium batteries exude many favourable qualities compared to other battery formations such as high power density (1500 – 10000 W/L), high energy density (200 – 500 Wh/L), and a high energy efficiency of 85 – 90 % (Smdani et al. 2023). The term “lithium-ion” in fact refers to a family of batteries that use lithium ions as a mobile phase moving between stationary mediums, the six most common chemistries in use are listed in Table 2.1 and Table 2.2 giving operating characteristics and a comparative ranking of their features respectively (Buchmann 2017). Generally, lithium-ion batteries function similarly in operation where under a discharged state lithium ions are bound to the lithium-based cathode and when charged lithium ions are deposited within the graphite sheets of the anode (intercalation) through transport across a polymer ion-permeable separator using an electrolyte of lithium salt (LiPF_6 or LiBF_4) dissolved in an organic carbonate solvent (Buchmann 2017, Passerini and Scrosati 2016). Research into lithium-ion battery technology is still intensive and many other electrode and electrolyte formations are under development. Given the high energy content of the batteries and their propensity to catch fire or explode due to the materials in use, additional electronics are often added to cells to protect against faults such as short-circuit, over-current, thermal overload, over-charge, and over-discharge.

Table 2.1 Lithium-ion battery operating characteristics (adapted from Buchmann 2017).

Type	Anode	Cathode	Specific Energy (Wh/kg)	Cycle Life	Operating Voltage
LCO	Graphite	LiCoO_2	150 - 200	500 -1000	3.0 - 4.2
LMO	Graphite	LiMn_2O_4	100 - 150	300 - 700	3.0 - 4.2
NMC	Graphite	LiNiMnCoO_2	150 - 220	1000 - 2000	3.0 - 4.2
LFP	Graphite	LiFePO_4	90 - 120	>2000	2.5 - 3.7
NCA	Graphite	LiNiCoAlO_2	200 -260	500	3.0 - 4.2
LTO	Li_2TiO_3	LMO or NMC	50 -80	3000 - 7000	1.8 - 2.9

The rise in grid scale energy storage through lithium-ion batteries can be attributed largely to the rise in electric vehicles, specifically through improvements in battery production capacity as well as the abundance of used batteries that are no longer suitable for vehicle use when the storage capacity falls below 80% (Ahmadi et al. 2014). Since 2019 the contributions to grid scale power capacity in the US market by lithium-ion batteries has grown exponentially from 170 MW to 8.8 GW in 2022 with more than half that capacity installed in the same year representing a share of 28.7% of large-scale grid storage with the rest contributed by pumped hydro (EIA 2022). The situation is similar in China where the re-use of electric vehicle batteries contributed 20.6% of total power capacity for the 2022 year and the remainder of storage came primarily from pumped hydro (CNESA 2023). Secondary use of lithium-ion batteries in grid scale storage systems can realistically extract an additional 15% of the storage capacity of the battery before requiring disposal (Ahmadi et al. 2014).

Table 2.2 Lithium-ion battery type comparative advantage rank (adapted from Buchmann 2017).

Type	Specific Energy	Specific Power	Safety	Temperature Performance	Life Span	Cost
LCO	4	2	2	3	2	3
LMO	3	3	3	2	2	3
NMC	4	3	3	3	3	3
LFP	2	4	4	3	4	3
NCA	4	3	2	3	3	2
LTO	2	3	4	4	4	1
1 = Very Undesirable / 4 = Very Desirable						

Disposal of lithium-ion batteries has been a topic of discussion due to the intricacies of dismantling the cells and dealing with the associated waste streams. Increases in the number of batteries requiring disposal has spurred improved practices with more efficient economies of scale but to date remains a problem especially with energy efficient methods in dealing with nickel and cobalt contamination as well as the high amount of fluorine containing chemical components involved (Marchese et al. 2024).

While lithium-ion batteries have demonstrated real-world feasibility especially in the automotive sector, their production does have some drawbacks that are less often talked about, namely the energy investment required in their construction. Production of lithium-ion batteries is an energy intensive process, not including energy consumption for mining the materials or recycling end-of-life units, a surprisingly high energy input in the range of 83 – 700 kWh is required to produce 1 kWh of energy storage capacity (Peters and Weil 2018). Significant energy expenditure in both electrical and natural gas consumption are required for forming operations (48%) and drying operations (52%) in the formation of new cells from raw materials (Degen and Schütte 2022). Such high energy penalties for short term energy storage solutions might be acceptable for vehicles where design constraints oblige their use, however the construction of lithium-ion batteries for primary use as a grid storage solution is inadvisable and grid scale use should be reserved to the reuse of electric vehicle byproducts.

In another line of thinking it may be advantageous to build up lithium-ion battery consumption for grid scale use in the short term as a means of securing a geopolitically important resource, and in fact lithium along with other materials like cobalt have been added to the list of strategic raw materials in many nations (Marchese et al. 2024). While current minable lithium deposits remain numerous, the available supply globally might be expected to produce a maximum of 1.42 billion cars if the resource is fully devoted to car manufacture, an amount insufficient to fully replace the current number of cars on the road globally (Glas 2022). Competing for access to and maintaining security of the national stock of lithium in circulation may be a more pressing concern to national interest than high production energy costs.

2.1.3 Emerging Technologies

In addition to the current primary energy storage methods using pumped hydro and lithium-ion batteries, many other emerging technologies are in the process of development offering certain potential advantages. Many of these technologies have been provably demonstrated to function adequately but are reserved for small-scale applications. Such technologies include compressed air energy storage, thermal energy

storage, flywheel energy storage, superconducting magnetic energy storage, flow battery energy storage, and fuel cell hydrogen energy storage amongst others in development.

2.1.3.1 Compressed Air Energy Storage (CAES)

Of all the emerging technologies CAES looks to be the most promising to achieve a significant entry to large scale energy storage. In this system electrical energy is used to spin a large air compressor to generate pressurized air that may be stored in deep underground caverns, ancient salt mines, re-purposed natural gas storage caves, or even distributed amongst a large network of high-pressure piping where the pressurized air can be released through an expander turbine to recover the energy at a later time (Ibrahim et al. 2008). The efficiency of such systems are largely affected by the thermodynamics of the process where simple diabatic processes give up heat from compression to the atmosphere resulting in unrecoverable energy loss (Bakhtiari and Karamanev 2022). More advanced cycles consist of adiabatic compression systems where heat is either retained in the air during storage or a thermal medium is used to retain heat during compression and later the heat is returned to the air for expansion or alternatively an isothermal process can be used using the high heat capacity of water to absorb heat and allow compression to occur with less work and therefore higher efficiency (Bakhtiari and Karamanev 2022). The efficiency of CAES has proven to be fairly high at 80 – 89% and current power ratings exist up to 300 MW, the highest amongst the emerging technologies (Smdani et al. 2023).

2.1.3.2 Thermal Energy Storage (TES)

TES systems make use of molten salts such as sodium hydroxide, typically heated through solar concentrators but could make use of excess grid power through resistive heating, to accumulate latent and sensible heat which can be converted to electric power on demand through the use of a steam cycle (Ibrahim et al. 2008). The investment costs of these systems are amongst the lowest, and therefore attractive for multi-megawatt installations while not requiring specialized geological features (Ibrahim et al. 2008). TES may be particularly useful for small-scale residential applications using lower temperature heated water where the average US household devotes about two-thirds of

annual energy consumption towards water and air heating and the integration of a liquid water TES system in a home is within the budget of homeowners (Glas 2022). TES systems generating electricity suffer from poor efficiency demonstrated to be in the range of 30 – 60% simply due to Carnot cycle losses, though where sensible thermal energy is used explicitly for heating, efficiencies of 50 – 90% are achievable (Smdani et al. 2023).

2.1.3.3 Flywheel Energy Storage (FES)

FES systems are rather simple mechanical devices that use energy stored as momentum in a spinning mass under a vacuum coupled to a motor/generator to charge and discharge the rotational energy as electrical energy (Ibrahim et al. 2008). Energy storage capacity and supply duration of such technology is generally low and frictional losses in bearings prohibits long term storage, the technology is therefore mostly reserved for small scale back-up power operations (Ibrahim et al. 2008). Despite the limitations of the technology, FES systems can still obtain high energy efficiency at 90 – 95% (Smdani et al. 2023).

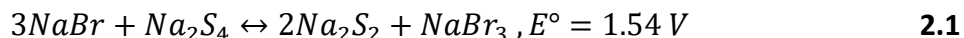
2.1.3.4 Superconducting Magnetic Energy Storage (SMES)

SMES systems achieve energy storage through the induction of electric current into a coil of niobium-titanium alloy filaments, a type-II superconductor, cooled to a temperature of -270 °C (Ibrahim et al. 2008). While maintaining the low temperatures can be done efficiently through insulation design, the high cost of the supporting equipment generally limits SMES to small scale energy storage applications (Ibrahim et al. 2008). Efficiency of SMES systems has been proven to be the highest of the emerging technologies at 95 – 98% and maintains the added feature that all energy potential within the system can be recovered as opposed to other technologies such as lithium-ion batteries which must be restricted to partial discharge to avoid damage (Smdani et al. 2023).

2.1.3.5 Flow Battery Energy Storage (FBES)

FBES operates as a fuel cell system using rechargeable reductive and oxidative electrolyte solutions passed through the cathode and anode compartments separated by an ion-selective membrane (Ibrahim et al. 2008). A FBES system differs from an ordinary battery in that the electrolytes can be stored in large external tanks and continuously fed

to and extracted from the electrochemical cell on demand unlike normal batteries that involve the production of solid compounds (Ibrahim et al. 2008). Such systems may use expensive and exotic electrolyte solutions based on vanadium limiting their size due to expense however newer chemistries such as polysulfide bromide using sodium ions (Equation 5.7) alleviates the issue (Morrissey 2023). Energy efficiency of FBES systems is moderate at roughly 75% (Ibrahim et al. 2008).



2.1.3.6 Fuel Cell Hydrogen Energy Storage (FC-HES)

FC-HES systems are similar to flow batteries in the use of a fuel cell where the electrolyte mixtures are replaced with hydrogen gas and oxygen/air at the anode and cathode respectively. Generally, such systems take the form of low temperature (<100 °C) proton exchange membrane style constructions. Though other designs such as the phosphoric acid fuel cell may be encountered where hydrogen and oxygen gas are separated by a barrier of hot concentrated phosphoric acid (150 - 220 °C) contained between porous catalytically coated electrodes (EG&G 2004). FC-HES suffers from some significant drawback compared to the other technologies, namely that the electrodes used in the fuel cells require expensive precious metals for the catalytic breakdown of hydrogen and oxygen gas and the production and use of hydrogen gas is not very efficient when considering the combined losses between production, storage, and conversion back to electrical power (Bovo et al. 2023).

2.2 Hydrogen Power

The concept of a hydrogen economy centered around the production, transport, and consumption of hydrogen gas has existed since at least the 1970s, a theorized replacement to the current hydrocarbon driven economy the modern world was founded on (Bockris 1972). From a simplistic point of view, hydrogen gas as an energy source is attractive in terms of eliminating pollution and carbon dioxide emissions at the point of use as would occur in the case of hydrocarbon-based fuels. Hydrogen can also be manufactured the easiest of the potential synthetic fuels in terms of chemical reaction pathway thanks to its simple chemical composition which does not result in any side

reaction byproducts to be dealt with. The potential for use as an alternative fuel is not without its drawbacks however, which are many, and in some cases, technologically difficult to overcome.

2.2.1 Hydrogen Production

The efficient production of hydrogen gas is one of the most critical aspects of the development of a hydrogen economy and acts as the foundation of implementation; an inability to efficiently generate hydrogen gas will leave the concept as a perpetual uncompetitive scientific curiosity only and effectively bottlenecks any practical technologies based on its consumption from long-term successful commercialization. This alone of course is not enough to dissuade governments from blindly pushing forwards with such endeavors which are doomed to failure at great expense to taxpayers and of course the associated carbon emissions as a byproduct of the resources which will be wasted. The transition to such a paradigm shift in energy strategy through any new conceptualization requires a cautious approach to be successful, this may include simply doing nothing in the face of calls to action where a scientific breakthrough of significant relevance must be waited on.

The current production of hydrogen gas is often referred to by its mode of generation, that being production from hydrocarbon transformations known as “grey hydrogen” or “blue hydrogen” where an attempt to sequester CO₂ emissions is made known as carbon capture, utilization, and storage (CCUS) (Ajanovic et al. 2022). The production of hydrogen gas with minimal CO₂ production as a waste byproduct is deemed “green hydrogen” (Ajanovic et al. 2022). Currently grey hydrogen dominates as the standard mode of production (>99%) to fulfill the needs of chemical feedstocks in the production of other chemicals while <1% of hydrogen production deploys CCUS technologies or non-CO₂ generating pathways due to the high cost that is 50 – 400% more expensive than that of grey hydrogen (Ajanovic et al. 2022). The current production volumes and uses of hydrogen gas are seen in Figure 2.1.

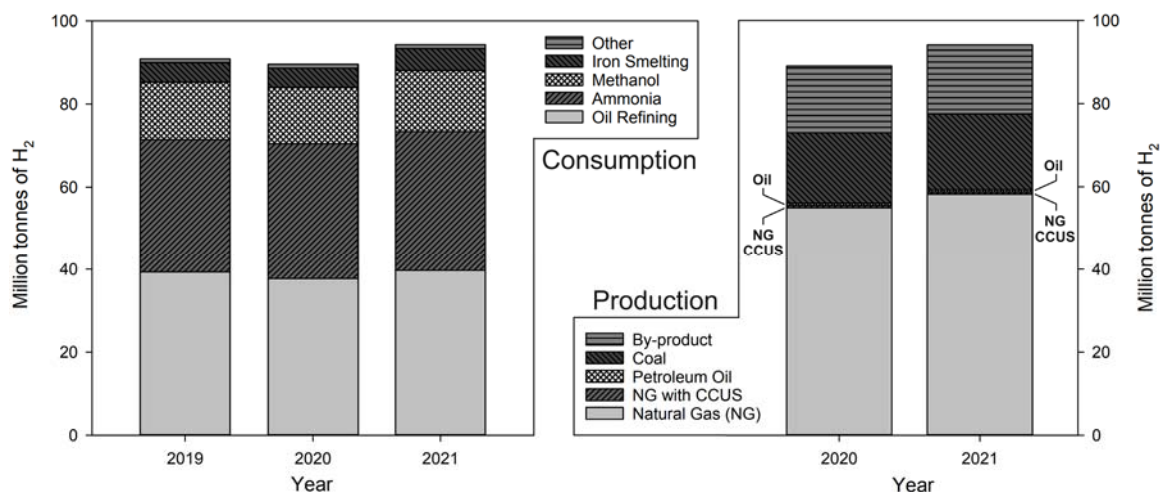


Figure 2.1 Consumption and production profiles of hydrogen (adapted from IEA 2022b).

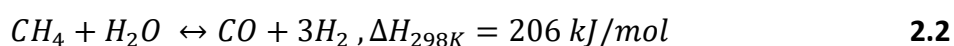
Currently, the most critical issue holding back the blossoming of a true green energy backed hydrogen economy from the present day scheme centered around localized industrial feedstock production has to do with the low round trip efficiency of producing hydrogen gas, storing the gas, and re-converting the hydrogen to useful energy. Hypothetically for round trip electrical energy production the creation of hydrogen gas can be achieved with an efficiency of 93% (Hodges et al. 2022), compression storage can be expected to operate at 94% efficiency (Ni 2006), while re-electrification in fuel cells might be expected to perform with an efficiency of 54% (Wipke et al. 2012), for a final return energy yield of 47% of the input. This efficiency remains rather low in comparison to other competing energy storage and recovery strategies for the time being.

2.2.1.1 Grey Hydrogen

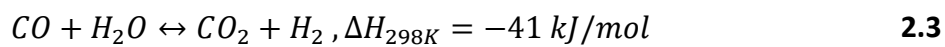
As mentioned, grey hydrogen, or hydrogen produced from hydrocarbon sources with the emission of CO₂ represents the bulk of hydrogen gas production. Three major methods of production exist centered around the use of natural gas, oil, and coal representing 96% of current commercial hydrogen production globally. The processes involved are considered technologically mature, though research in performance improvements remains ongoing.

2.2.1.1.1 *Production by Steam Methane Reforming*

The primary production pathway is known as steam methane reforming (SMR), involving a two-step reaction responsible for 48% of global production (Ewan and Allen 2005). In the first reaction, a mixture of natural gas (primarily methane) and steam is reacted at high temperatures (700 – 1000 °C) in what is known as the steam reforming reaction (Equation 2.2) to reduce water molecules to hydrogen through an intermediate oxidation of methane into carbon monoxide, stripping additional hydrogen from the methane molecules in the process (Mokheimer et al. 2024).

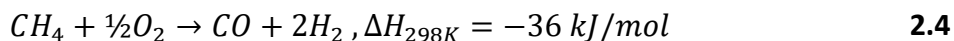


The reaction typically occurs within a series of vertical tubes contained in an oven and heated around their outsides with flame burners offering a simple construction and homogenous thermal distribution (Mokheimer et al. 2024). Alternatively heat for the reaction can be provided by solar concentrators focusing solar energy onto a reactor bed through a quartz window helping to reduce emissions associated with the process (Jin et al. 2018, Möller et al. 2007, Piatkowski et al. 2011). The reaction requires a catalytic material to proceed, generally nickel on an alumina support substrate (Ni/Al₂O₃), however the choice of ceramic has been found to play an important role in maintaining activity of the catalytic metals on their surface which may be severely deactivated in some cases (Mokheimer et al. 2024). Experimentation with various ceramic formulations supporting nickel catalyst have yielded improvements over regular alumina where nickel coated cerium doped zirconia (Ni/Ce-ZrO₂) demonstrates superior catalytic activity believed to occur because of the materials ability to store, release, and exchange oxygen within the ceramic lattice structures while maintaining resistance to carbon depositing (Dewoolkar et al. 2017, Roh et al. 2002, Zhao et al. 2020). Catalysts used in the process are sensitive to sulfur contamination and an upstream desulfurization operation is typically required (Mokheimer et al. 2024). Upon exiting the steam reforming reactor, the gases are sent to a final reactor to complete the second transformation known as the water-gas shift reaction (Equation 2.3) yielding additional hydrogen gas from the production of carbon dioxide.



In the final reaction step, the gases are reacted at a much lower temperature (330 – 530 °C) due to the exothermic nature of the reaction where lower temperatures are thermodynamically favoured for conversion (Tonkovich et al. 1999). Likewise to the steam reforming reaction, reactions occur over a fixed bed of catalytic material (chrome and zinc promoted iron and copper oxide) in the presence of steam (Tonkovich et al. 1999). Reacted gases are separated through pressure-swing absorption that takes advantage of the high solubility of carbon dioxide under high pressure in specific absorptive materials compared to that of hydrogen. Hydrogen under high pressure exits as a near pure stream from the absorption system and carbon dioxide is evacuated from the system through routine depressurization and purge cycles.

The typical final efficiency of the conversion process is the highest amongst the current hydrogen production options at 76% (Ewan and Allen 2005) and combined with cheap natural gas as the only major feedstock requirement, the process maintains the position as the most economically attractive, hence its market domination. Additional research exploring alternative reactions to the highly endothermic steam reforming reaction have been considered such as the partial oxidation reaction (Equation 2.4) which offers benefits in the form of faster reaction kinetics, smaller reactor sizes, and simplified separation of hydrogen gas through a catalytic-permeable-membrane tube made of nickel (Fukada and Ono 2007, Osman 2019). The partial oxidation process does not require a catalyst to proceed making the process sulfur tolerant and more cost effective, whereas the similar autothermal reforming process makes use of a catalyst to achieve lower process temperatures but runs the risk of sulfur inhibition (Mokheimer et al. 2024).



2.2.1.1.2 *Production by Oil/Naphtha Reforming*

Production of hydrogen through the reforming of oil occurs primarily as a consequence of the large material demand for liquid hydrocarbon fuels, hydrogen gas byproducts from these refinery unit operations encompass 30% of global hydrogen production (Ewan and

Allen 2005). Specifically, hydrogen gas is produced in large volumes from upgrading processes such as catalytic reforming units and isomerization units that generate hydrocarbon products with superior anti-knocking properties. Both units perform a similar task of rearranging straight alkanes into branched forms releasing hydrogen in the process of enriching the molecular ratio of carbon to hydrogen bonds, differing primarily only in the feedstocks and operating parameters. Catalytic reforming focuses on the conversion of heavy (C_{7+}) low-octane paraffins and naphthenes into high-octane aromatics while isomerization focuses on the conversion of low-octane light n-paraffins (C_5/C_6) into high-octane isoparaffins (Valavarasu and Sairam 2013). While the production of hydrogen gas is considerable from these processes, the demand for hydrogen gas in other refinery operations tends to negate the potential of hydrogen gas as a salable refinery fuel product for consumer use and instead, its use is internalized.

2.2.1.1.3 *Production by Coal Gasification*

Production of hydrogen gas from coal as a mixture together with carbon monoxide (syngas) represents the last major pathway to hydrogen production currently employed commercially accounting for 18% of production globally (Ewan and Allen 2005). The use of coal to produce syngas has received renewed attention in recent years as a cleaner alternative to direct coal combustion helping to reduce airborne particulate matter spurred by economic development especially in China and India. Global coal consumption currently accounts for 26.9% of total energy consumption with China making up 50.5% of the total coal consumption (Dai et al. 2023). Coal represents a critical energy source for China, having significant domestic deposits while lacking in oil and gas, its consumption is especially necessary to maintain electrical power generation where consumption in 2021 totaled 8.31 trillion kWh, just over double that of the United States at 4.07 trillion kWh in 2022 (EIA 2024a, Wang et al. 2022). It should be noted however in terms of CO_2 emissions that coal gasification still contributes significantly (132.6 kg_{CO_2}/GJ primary energy), producing almost double that of hydrogen production with natural gas using steam methane reforming (68.2 kg_{CO_2}/GJ primary energy) as a natural consequence of the proportion of carbon to hydrogen (Ewan and Allen 2005).

Consumption of coal for the production of syngas is typically performed in a high temperature (800 – 1700 °C) vertical reactor designed for gas-particulate interactions and may take the form of a fixed bed, circulating fluidized bed, or entrained bed using a combination of steam, air, and nitrogen as the gasifying agent (Dai et al. 2023). Syngas containing carbon monoxide extracted from the reactor may be subjected to an additional water-shift gas reaction to enhance hydrogen production as is used in steam methane reforming. The final conversion efficiency of hydrogen production from coal gasification stands at a modest 59% but may increase as research spurred by the necessary consumption of coal as a geopolitically strategic resource continues despite desires to reduce consumption to curb CO₂ emissions (Ewan and Allen 2005, Wang et al. 2022).

2.2.1.2 Blue Hydrogen

The production of blue hydrogen is generally done so as a process of augmenting grey hydrogen processes with CCUS technology. Widespread use of this technology has not been adopted to date due to its negative returns on investment and is only spurred in growth primarily through government initiatives. CCUS technology is not exclusively investigated for use with hydrogen production however, which is beneficial in broadening the breadth of research potential and research breakthroughs in unrelated chemical processes that may overlap in use with strictly hydrogen producing processes.

2.2.1.2.1 *Carbon Capture Technologies*

In the simplest collection scheme, purely combustive processes can be reworked as oxy-fuel systems; the combustion of carbonous fuel with pure oxygen gas produces an exhaust stream of concentrated CO₂ for collection, particularly suited for coal-fired operations (Guo et al. 2024). Oxy-fuel operations are limited in applicability and in general post-combustion carbon capture technologies most often take advantage of CO₂ selective adsorption/absorption materials to concentrate CO₂ and release it from the process in controlled purges, able to recover on average 90% of CO₂ process emissions (Mullen et al. 2023). In fact, the pressure swing absorption operation used in the purification of hydrogen from grey hydrogen production processes unintentionally performs this task producing a waste stream of highly concentrated CO₂. Various

adsorbents have been studied for use at differing process temperatures relying on molecular surface adhesion or liquid chemical absorption where surface reaction of MgO and derivatives (Equation 2.5) are the most relevant for water-gas shift reactions and hydrogen production, a list of common adsorbents/absorbents and operating temperatures is seen in Table 2.3 (Liu et al. 2024, Zhao et al. 2024). Once released from the adsorbents, the gaseous CO₂ can be liquified for short term storage and distribution for the purposes of valorization into useful chemical products as a feedstock or alternatively for terrestrial storage.



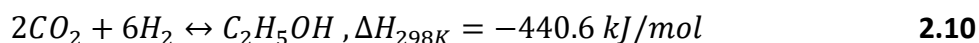
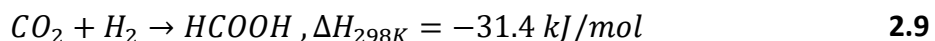
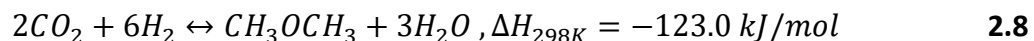
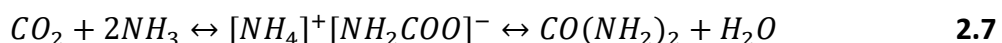
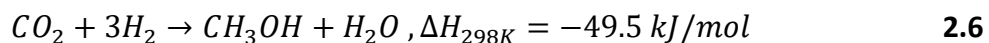
Table 2.3 List of carbon capture adsorbents and their applications.

Material	Type	Operating Temperature	Application
Activated Carbon	Solid	0 - 50 °C	Room Temperature Direct Air Capture
Metal Organic Frameworks	Solid		
Amine-based Solvent	Liquid		
Ionic Liquid-based Solvent	Liquid		
Alkaline-based Solvent	Liquid		
Amino Acids-based Solvent	Liquid		
Solid Amine	Solid	120 °C	Plant Smoke
Li ₈ SiO ₆ (high pressure)	Solid	210 °C	Plant Smoke/Water-Gas Shift
Dawsonite	Solid	220 °C	Water-Gas Shift
Layered Double Hydroxides	Solid	240 °C	
MgO	Solid	320 °C	
Li ₂ ZrO ₃	Solid	500 - 800 °C	Steam Reforming/Gasification
Li ₂ BO ₃	Solid		
Li ₄ SiO ₄	Solid		
CaO	Solid		
KNaTiO ₃	Solid		

2.2.1.2.2 Carbon Utilization Technologies

Carbon dioxide is a necessary feedstock in some chemical processes and used most significantly in the food and beverage industry, however its overall production massively dwarfs its practical usefulness in the production of final goods. In the production of chemicals, CO₂ is used most often in the generation of simple feedstocks such as

methanol and urea (Equations 2.6 and 2.7) but comes at the expense of hydrogen consumption and in some niche applications such as mineral carbonation (Bui et al. 2018). Ongoing research into the conversion of CO₂ into other useful products such as dimethyl ether (Equation 2.8) using bifunctional catalysts, useful as a replacement to diesel, have shown conversion yields of 21% (Ge et al. 1999). Additionally, it is reported that conversion to formic acid (Equation 2.9) using ruthenium-based catalysts gives considerable yields while conversion to ethanol (Equation 2.10) using iron or rhodium-based catalysts can be achieved at relatively low yields of 16% (Panzone et al. 2020). Overall carbon utilization can provide minor pathways to diminishing CO₂ emissions, though the demand for products incorporating CO₂ will never realistically meet the generation rate of CO₂ and storage technologies must be relied on as the primary sink of CO₂.



2.2.1.2.3 Carbon Storage Technologies

Large-scale storage of carbon dioxide is generally achieved through reservoir injection below 800 m to achieve geological sequestration of CO₂ in a supercritical fluid state and can be divided into four mechanisms; structural space storage, bound space storage, dissolution storage, and mineralization storage (Wang et al. 2023). Structural space storage (structural trapping) represents the mechanism responsible for greatest storage where CO₂ is injected into a permeable rock layer in a supercritical state where it migrates upwards until collecting under an impermeable rock dome remaining trapped. The geological formations required for structural trapping are the same as those responsible for collecting oil and gas deposits and therefore are readily available from

depleted oil and gas fields. The second mechanism known as bound space storage (residual trapping) refers to CO₂ trapped in rock pores where the bulk flow of CO₂ displaces the existing liquids in the rock (primarily brine water) leaving behind immobilized CO₂ pockets. The third mechanism, dissolution storage (solubility trapping), involves the process of CO₂ dissolving into brine water in the porous rock and converting to carbonic acid. The fourth and final mechanism of the storage involves mineralization storage (mineral trapping), where carbonic acid interconverts to bicarbonate ions and reacts with magnesium in the porous rock to form solidified MgCO₃ over time, permanently trapping the CO₂ and preventing the possibility of migration back to the surface (Liu et al. 2024, Zapata et al. 2020). A more straightforward approach to carbon dioxide sequestration is the production of biochar which due to its ability to resist abiotic and biotic degradation (recalcitrance) makes it a plausible option. Mixing of biochar into soil has been investigated as a potential CO₂ sequestration option where it can be produced easily even in highly impoverished regions of the world and offers added benefits to soils through the prevention of nutrient run-off losses and improved water-holding capacity (Woolf et al. 2010).

2.2.1.3 Green Hydrogen

Green hydrogen generally entails processes that directly or indirectly produce hydrogen gas through the use of renewable energies that contribute minimal CO₂ emissions. Production technologies under this classification may be considered as semi-mature or still emerging with significant research potential. Recorded efficiencies are often low and production outputs encompass only a very small fraction of total global hydrogen production.

2.2.1.3.1 *Production by Electrolysis*

Production of green hydrogen through electrolysis of water represents the most straightforward mode of generation when electrical energy is provided by renewables, and is currently the only significant production route outside grey hydrogen representing 3.9% of global production (Ewan and Allen 2005). Electrolysis represents a useful process where low volumes of on-site hydrogen gas are required as the process is

generally simple and requires only purified water as a chemical input. The most important aspect of design comes down to the electrolytic cell configuration where catalytic reduction of water on platinized electrodes and transfer of H^+ ions through proton exchange membranes have been the dominant design for many years thanks in part to their decreased resistance and improved performance over older simpler configurations involving submergence of both anode and cathode into water. The major issue in liquid submergence being bubble formation on electrode surfaces that reduces liquid contact area with the catalysts and decreases efficiency, where modern asymmetric PEM electrolysis cells partially rectify the issue by removing water submergence from the cathode entirely (Shiva Kumar and Himabindu 2019). Recently, further improvements to cell design have been made that removes the issue of bubble formation at both the anode and cathode entirely by using a porous interelectrode separator acting as a capillary wick that keeps both electrodes wetted without intrusion of water into the electrodes which allows gases to escape freely and improves operational efficiency (Hodges et al. 2022). The new design boasts noticeable reductions in both capital expenditures and operating expenses compared to conventional water electrolyzers, able to produce hydrogen gas at a more cost-competitive level compared with fossil fuels (Hodges et al. 2022).

2.2.1.3.2 Production by Thermochemical Water Splitting

Thermochemical water splitting exposes water to high temperatures in the presence of reactive materials to generate a chemical cycle that produces hydrogen gas and regenerates the necessary chemical reactants. Studies into hydrogen production from thermal reduction of water are mature with many process cycles developed (>300) in the last six decades such as the more prominent Halide Processes, Reverse Deacon Reaction Processes, Iron/Carbon Oxide Processes, and Metal/Metal-Alkali Processes (Chao 1974, Lee et al. 2022). The energy sources proposed for reaching the necessary temperatures without the use of hydrocarbons are generally restricted to solar concentrators and nuclear reactors. Factors that have stymied commercialization of these technologies include the high costs associated with solar concentrator construction and nuclear reactor redesign along with improvements in the efficiency and durability of the reactant-cycle

materials (Perret et al. 2011). Chemical cycles may consist of a less complex single stage cycle or hybrid cycles that are more complex but may be driven with lower temperatures making them thermally favourable. Examples of such hybrid processes include the cerium oxide-two step cycle (Gokon et al. 2013) and the copper chloride hybrid cycle (Darmawan et al. 2023). Thermochemical processes are notable for their efficiency of conversion standing at 50%, significantly higher than is found with many other green hydrogen producing processes (Ewan and Allen 2005).

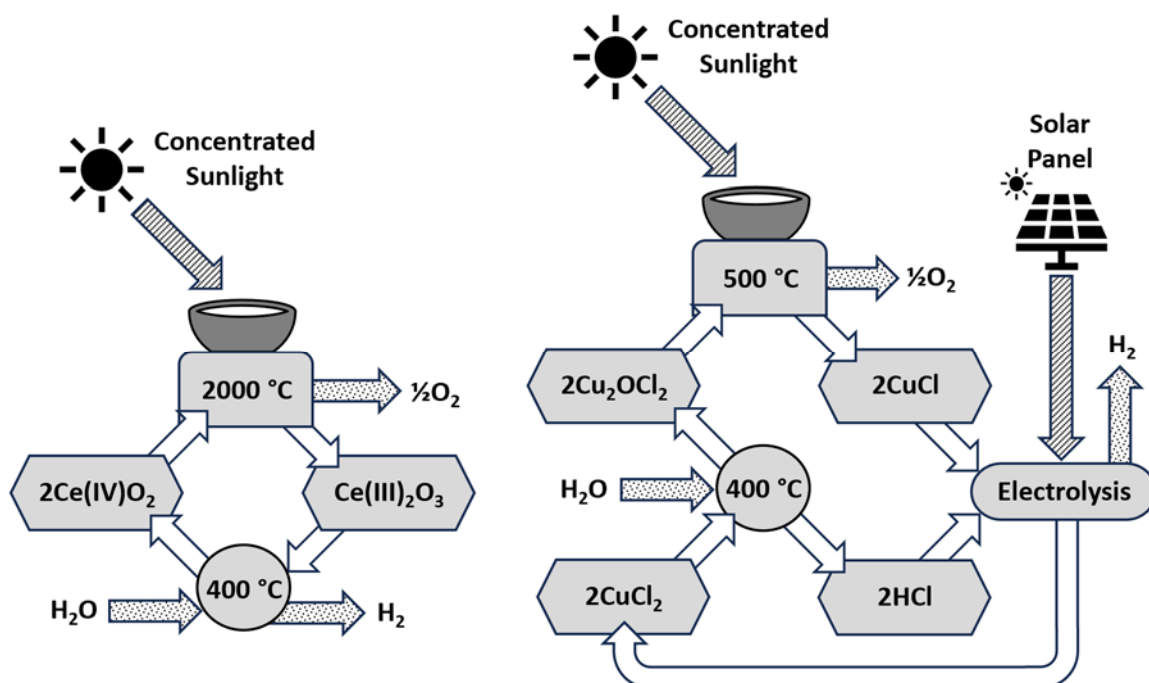


Figure 2.2 Thermochemical water splitting cycles. Left: Cerium oxide two step cycle (Gokon et al. 2013). Right: Copper chloride hybrid cycle (Darmawan et al. 2023).

2.2.1.3.3 Production by Photochemical Water Splitting

The light-initiated breakdown of water into its gaseous components of hydrogen and oxygen using semiconductor materials is another method of green hydrogen production using direct sunlight as an energy source. A distinction is made between photoelectrochemical systems and photochemical systems, where the former incorporates a construction similar to electrolysis using wired electrodes covered in photoactive semiconductors and catalytic noble metals, while the latter induces conversion of water to

hydrogen and oxygen directly at a semiconductor surface. Semiconductor material differs from conductive material where its atomic valence electron shells are full and the electrons are paired and bound to the atom strongly which prevents the transfer of electrons between the orbitals of adjacent atoms. As described by Sze and Lee (2012), during stimulation by an external photon (or an internal thermal vibration phonon) with sufficient energy, a tightly bound electron can be ejected into a higher orbital (the conduction band) which is weakly bound, and the electron becomes mobile through the higher orbitals of adjacent atoms and prevented from collapse back to a lower stable orbital through the existing total electron occupancy of the lower orbitals of surrounding atoms. Likewise, through the loss of an electron from the lower orbital shell of an atom a positively charged “hole” appears that can abstract an electron from a neighbouring atoms lower orbital shell allowing the hole to also be mobile across atoms. The generation of an electron-hole pair, which is better described as a strong positive and negative point charge on the surface acts to give up or accept electrons from molecules in contact with the semiconductor surface, able to reduce water into oxygen gas and H^+ ions through absorption of an electron into a hole as well as the conversion of H^+ to hydrogen gas through emission of a surface electron from a mobile electron (Acar et al. 2014).

The photoelectrochemical effect of breaking down water has been known for some time, specifically reactions observed to occur through illumination of a semiconductive TiO_2 electrode with wavelengths greater than 415 nm and electrically connected to a second platinum black electrode submersed in water (Fujishima and Honda 1972). Alternatively, strict photochemical systems have been explored with designs based on exposure of the semiconductor materials as either panelized systems containing immobilized photocatalysts or through mixed particulate slurries of photocatalytic material. In the case of particle-based systems the production of hydrogen and oxygen may proceed as a one-step excitation or through a more complex two-step excitation using two different photocatalytic media with an electron mediator where the excitation level of the catalysts can be tuned to produce only hydrogen gas and oxygen gas in separated compartments (Ma et al. 2023). Research on improved excitation pathways and the development of better performing photocatalytic agents often constructed with a co-catalyst (usually platinum) have been underway for some time and are numerous, though they all currently

suffer the same issue of requiring UV/near-UV light to overcome the 1.23 eV bandgap necessary for the splitting of water (Acar et al. 2018). As a result of the spectral limitations of the light that can be effectively used to produce hydrogen gas, efficiency remains low at roughly 4% and production remains at the experimental stage, though this efficiency is somewhat comparable to photovoltaic cells with efficiency of 11% indicating photocatalysis is still a viable avenue for hydrogen production research (Acar et al. 2018, Ewan and Allen 2005).

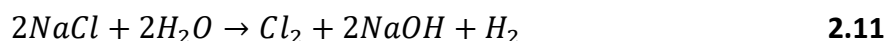
2.2.1.3.4 *Production by Biological Microbial Action*

Production of hydrogen gas through microbial action may proceed as either a direct process of generation from fermentation or may take an indirect route using microbial fuel cells containing electricigens. Electricigens are used to break down organic matter into CO₂ at the anode under an applied voltage to generate hydrogen gas at the cathode from H⁺ released into solution by microbial metabolic processes. Of the two processes, direct generation from anaerobic fermentation as a mixture of hydrogen and methane (biogas) is the most promising where significant quantities can be created at relatively low capital expenditure. Substrate materials for fermentation are diverse and include lignocellulosic wastes, sewage sludge, sugars or sugar containing wastes, polyethylene glycol, dairy wastes, fermentation metabolites, and algal biomass (Kumar et al. 2016, Xia et al. 2015). The choice of microbial culture (containing hydrogenase enzymes) and substrate pre-treatment to physically breakdown the materials is an important aspect in the production of high hydrogen gas yields (Muthudineshkumar and Anand 2019). Typical anaerobic biogas is composed largely of methane and carbon dioxide with minor amounts of hydrogen and so operating conditions need to be modified to favour hydrogen generation. Suppression of methanogenic activity is accomplished primarily through pH where more acidic conditions (pH 4.3 – 6.5), optimized depending on the exact microbes used, shift fermentation towards hydrogenic activity (Ayodele et al. 2023). The inclusion of methanogenic inhibiting agents may be included to improve yield in addition to pH control such as sodium 2-bromoethanesulfonate in a 1 M concentration (Wongthanate et al. 2014). The most cited bacterial genera associated with bio-hydrogen production are *Clostridium* though many others are of interest including *Enterobacter*, *Lactobacillus*,

Bacillus, *Klebsiella*, *Citrobacter*, *Anaerobiospirillum*, *Thermoanaerobacterium*, *Thermotoga*, and *Caldicellulosiruptor* (Ayodele et al. 2023, Boodhun et al. 2017, Kayano et al. 1981, Nagarajan et al. 2019, Xia et al. 2015) Operating temperatures are dependent largely on the selection of microbial culture which may fall under mesophilic (35 °C), thermophilic (55 °C), or hyperthermophilic (70 °C) conditions, where best yields were recorded under thermophilic conditions in a study using a sewage sludge microflora using a substrate of food and beverage wastes mixed with raw starch waste producing 0.28 L_{H₂}/L_{substrate} (Wongthanate et al. 2014).

2.2.1.3.5 *Production as Byproducts*

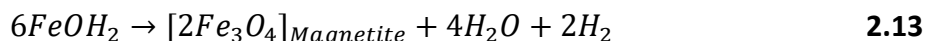
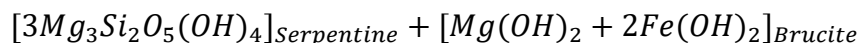
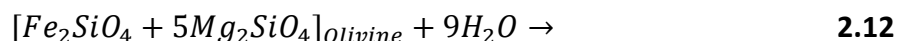
Generation of hydrogen gas as unneeded byproducts from other chemical processes represents a minor supply globally, most notably in chlor-alkali electrolysis. The chlor-alkali process generates chlorine gas and sodium hydroxide as necessary commodity chemicals from sodium chloride brine while generating hydrogen gas in the process (Equation 5.7). While the production of hydrogen is constrained by the intended output products, total production of hydrogen nonetheless currently represents 3.5% of European production and 3.9% of US production (Lee et al. 2018, Paulu et al. 2024). Production of products in the chlor-alkali process occurs with electrical energy that can be sourced from green sources and so can be considered a producer of green hydrogen.



2.2.1.3.6 *Production by Natural Reservoir*

Recent discoveries of naturally occurring sources of hydrogen gas similar to methane based natural gas deposits have been discovered that may play a key role in the development of large scale environmentally friendly hydrogen production. These deposits are typically found as mixtures along with nitrogen and methane, but their discovery has often gone unnoticed simply because portable gas analyzers used in gas field detection lack a hydrogen sensor and gas chromatograph systems often use hydrogen as the carrier gas which masks its presence (Zgonnik 2020). The formation of this hydrogen gas is believed to mainly occur underground under anoxic conditions at temperatures between 200 – 300 °C and pressures of 500 – 20000 bar through a process known as

serpentinization involving a hydration reaction (Equation 2.12) followed by an oxidation reaction (Equation 2.13) that liberates hydrogen gas (Blay-Roger et al. 2024). While serpentinization is believed to be the bulk contributor to the generation of hydrogen deposits, other minor processes such as pyritization, siderite hydration, and radiolysis may play a role as well (Blay-Roger et al. 2024). Many of these deposits have been located globally with the bulk of currently identified locations residing in the United States, Europe, and Russia, it should be noted however that the current identifications are only due to a higher prevalence of searching in these areas and not because these regions are richer in hydrogen (Blay-Roger et al. 2024, Zgonnik 2020). Given that the discovery of these natural hydrogen resources are quite recent, it is likely that many more will be discovered worldwide in due time.



2.2.2 Hydrogen Transport and Storage

Hydrogen gas, despite its rather high gravimetric energy content being more than double that of various hydrocarbon fuels, is not a very consumer friendly commodity having a rather low volumetric density whether in a cryogenically liquefied state (<-253 °C) or as a gas under high compression (350 – 700 bar) (Figure 2.3). Low volumetric density is an undesirable quality generally for use in vehicles where larger tanks are required, occupying more space or resulting in reduced mileage between tank fills. Strictly from a safety point of view, fuel under high pressure or as easily volatized cryogenic liquid will always carry serious risks especially in the form of fuel-air explosions and is especially so in the case of hydrogen. Hydrogen gas displays large ranges of flammable mixtures (4 – 75%) and explosive mixtures (18 – 59%) with air compared with hydrocarbons and the minimum ignition energy of hydrogen is amongst the lowest of all combustible fuels at 0.018 mJ, compared to 0.220 – 0.280 mJ for straight chain alkanes (C₁ – C₇) (Crowl and Louvar 2002).

A second complication surrounding consumer hydrogen use comes in the form of room temperature hydrogen embrittlement of metals, particularly that of carbon steel where diatomic hydrogen adsorbed on the surface may be dissociated into its atomic components which can enter the metal grain and recombine internally trapped along grain boundaries or within crystal lattice vacancies as diatomic hydrogen (Lyu et al. 2023). The overall effect results in a substantial reduction in ductility from the expected and in the worst case the initiation of crack formation. Hydrogen embrittlement is most prominent in high strength steels containing high portions of martensite where the reduction in metallic grain size results in significantly greater grain boundary areas to accumulate hydrogen (Li et al. 2022, Lyu et al. 2023). Hydrogen embrittlement can be mitigated with appropriate strategies however such as grain boundary size control and the inclusion of agents to limit hydrogen diffusivity or with the removal of impurities to eliminate crystal matrix vacancies, alternatively certain surface treatments may be used to limit hydrogen diffusivity such as dense surface coatings of Cd, Zn, or Ni along with some gases present with hydrogen able to form passivation layers such as carbon monoxide (Li et al. 2022). Hydrogen embrittlement does not explicitly prohibit the use of low-cost steel and in fact pure hydrogen gas under high pressure is commonly found transported in steel cylinders without incident where proper metallurgical specifications have been observed.

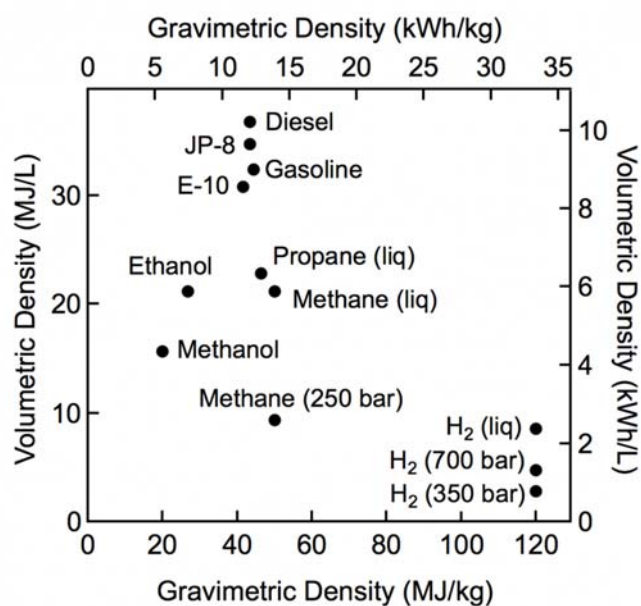


Figure 2.3 Hydrogen volumetric and gravimetric densities (reprinted from EERE 2024).

Large scale bulk storage of hydrogen is often accomplished through physical-based methods such as cryogenic dewar tanks, high pressure compressed gas tanks, or at lower pressures in large sealed geological cavities (Elmanakhly et al. 2021). In addition to physical-based methods, considerable research has been undertaken in material-based hydrogen storage adsorbed on or absorbed in suitable medium in efforts to provide alternatives to the use of very low temperatures or high pressures. The need for adsorbents or absorbents, especially where used in light vehicles, adds dead weight and reduces overall fill capacity and falls under the same problem as batteries used in electric cars. Examples of such adsorbent medium include metal organic frameworks (ex. MOF-5), organic liquids (ex. BN-methyl cyclopentane), interstitial hydrides (ex. LaNi_5H_6), complex hydrides (LiAlH_4), and chemically bound hydrogen (NH_3BH_3) but are typically expensive and difficult to apply at large scales where more traditional physical-based storage prevails (Panda et al. 2023, Sun et al. 2013). Larger freight vehicles such as trains and cargo ships may be more applicable to early hydrogen fuel transition where volumetric and weight constraints are less limited and hydrogen may be practically stored cryogenically or under pressure. Present research has demonstrated the possibility of straightforward retrofits that may be applied with the added benefit of improved efficiency using hydrogen through combustion or electrochemically in fuel cells (Boretti 2023, Knibbe et al. 2023, Seyam et al. 2022, Ye et al. 2022).

While hydrogen may be transported in bulk such as in liquified tanker cars or high-pressure tubes, a more realistic transport scheme comes in the form of pipelines to distribute gas to many consumers. The obvious drawback in the development of such infrastructure is the cost, which is quantified not only in material cost but the cost of placement and disruptions as a result of such construction. Such large expense items also come with political hurdles where it may be seen as a risky gamble to devote large tax expenditure on public projects that may only show returns on investment long after the current political body has been disbanded for a new one or the infrastructure may fail to be useful at all. The distribution of hydrogen in this way is more likely to proceed through piggybacking off existing infrastructure, specifically through blending into natural gas for distribution. Current research indicates that mixtures of approximately 5-10% hydrogen into natural gas streams can be used with no modifications to burner

equipment necessary and offers an avenue to easy integration of hydrogen gas into the hands of consumers (Elmanakhly et al. 2021, IEA 2022b). Where pure hydrogen gas is required, technologies such as polysulfone or polyimide membrane filters might be used to separate hydrogen from natural gas mixtures due to the high difference in molecular weight between the gases.

2.2.3 Hydrogen Consumption

The consumption of hydrogen at the present time is largely reserved in use as process feedstocks in the production of other chemicals and goods. A significant use of hydrogen gas occurs in oil refineries for upgrading feedstocks. One such main use is hydrotreating on molybdenum catalyst designed to convert sulfur and nitrogen into removable hydrogen sulfide and ammonia gases while simultaneously causing saturation reactions to aromatics and olefins (Valavarasu and Sairam 2013). The second main use is in hydrocracking processes meant for the breakdown of hydrocarbons residues into more valuable light distillates such as diesel, kerosene, and naphtha (Valavarasu and Sairam 2013). Hydrogen used in refineries is often sourced from other operations within the same refinery so it may be viewed as an internalized production and consumption. Outside of refinery operations the most significant use of hydrogen globally is in the production of ammonia, primarily for fertilizers, at 62% of hydrogen demand followed by methanol production consuming 27%, direct reduced iron smelting processes at 9%, and 2% for other uses (Figure 2.1) (IEA 2022b). Hydrogen may find additional use industrially in high temperature operations such as cement, steel, and glass production which are more difficult to bring to operational temperatures through electricity as production and distribution of hydrogen matures (Paulu et al. 2024).

2.3 The BioGenerator

In brief, the BioGenerator can be described as a regenerative indirect microbial fuel cell system using hydrogen gas (Karamanev 2009) designed with the intention of grid scale power regulation to aid in the transition to emerging renewable energy sources, particularly those of wind and solar. The system is broken down into two major subsystems; a bioreactor used to generate a ferric ion oxidant, and a fuel cell array that

combines oxidant and stored hydrogen gas to output electrical energy (Figure 2.4). The system may be described functionally as a hybrid hydrogen fuel cell flow battery energy storage system meant to overcome shortcomings in standard hydrogen-air fuel cell energy storage systems using the electrochemical reaction in Equation 2.14.

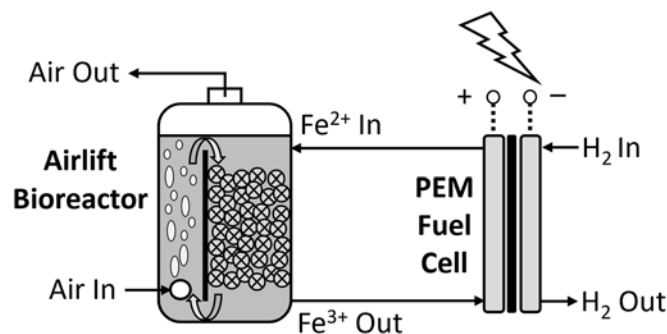
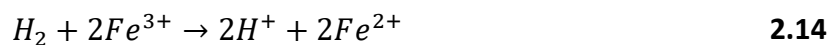


Figure 2.4 Simplified design of the BioGenerator.

Stored hydrogen gas acts as the energy source for the system and is fed to the anode side of a proton exchange membrane (PEM) fuel cell where it adheres to the surface of a noble metal catalyst, a platinum particle dispersion on carbon felt in this case. The catalyst serves to break the bond between H₂ through surface adhesion to generate freed H⁺ ions that can move through the membrane polymers held in intimate contact which are a special formulation of branched chain fluorocarbons containing ionizable sulfonic acid groups (-SO₃H) at the tips (Figure 2.5). The nature of the hydrophilic sulphonated groups and hydrophobic fluorocarbon backbones causes the natural formation of spherical reverse micelles of congregated sulfonic acid groups interconnected by short narrow channels during formation of the membrane (Hsu and Gierke 1982). Hydration of the polymer causes the bound sulfonic acid channels to absorb water and form dissociated ion pairs (-SO₃⁻ / H₃O⁺) along their track allowing the transport of H⁺ ions between the anionic charge centers while retaining the properties of a strongly chemically resistant physical barrier preventing bulk liquid and gas exchange. In practice some small amount of water will be seen to cross the membrane since water hydrates the hydrophilic channels of the polymer, and this must be continuously carried away through the

circulation of hydrogen gas to maintain functionality. The exact design and chemical make-up of PEM may be varied by producers and some specific membrane formulations may give better results than others in practice.

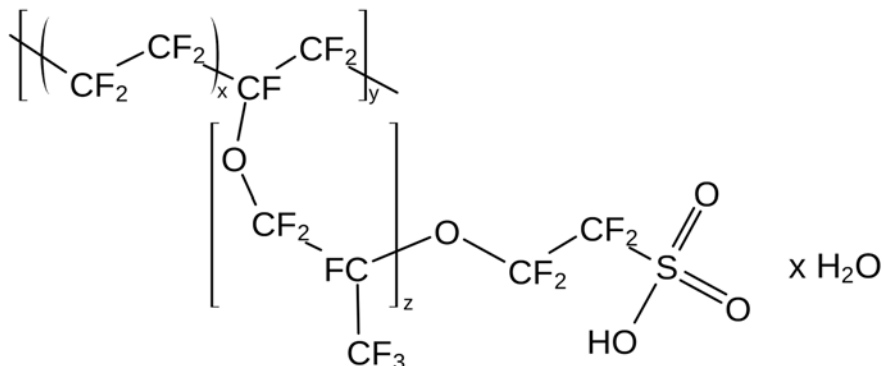
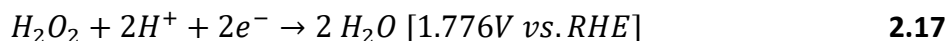
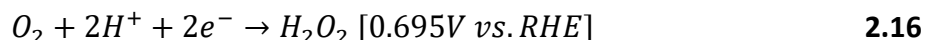


Figure 2.5 Proton exchange membrane polymer composition.

Electrochemical reactions occurring at the fuel cell cathode are of greater relevance to efficiency and overall performance. PEM fuel cells are often depicted using oxygen in air or pure oxygen swept through the cathode to act as the chemical oxidant, absorbing electrons and H^+ ions to produce water and generating a useful electromotive force in the process. This oxidation process is termed the oxygen reduction reaction (ORR) and is believed to occur via two separate possible multi-step pathways under acidic conditions on a catalytic noble metal surface; the first reaction is the direct four-electron pathway Equation 2.15 and the second is the two-electron pathway (the peroxide pathway) Equations 2.16 and 2.17 (Aysla Costa de Oliveira et al. 2020).



The intermediate surface reaction steps of the ORR that occur on the platinum catalyst are more complex than described by the above equations and are more easily understood as a physical representation of the chemical interactions between the cathode catalyst and the PEM illustrated in Figure 2.6 (Sui et al. 2016). Fuel cell reactions proceeding with the

ORR tend to be undesirable commercially for the main reason that the strong double bond of oxygen gas requires a high activation energy to break (498 kJ/mol), necessitating the use of a precious metal catalyst to proceed and acts as a bottleneck in the process where the reaction kinetics of the dioxygen splitting step are comparatively slow (Rismani-Yazdi et al. 2008, Rozendal et al. 2008). Due to the need for precious metals in the cathode the cost of the cell becomes quite high, where the cathode material can account for about 50% of the total cost of the cell (Aysla Costa de Oliveira et al. 2020). Additionally, the presence of the two-electron ORR pathway generates hydrogen peroxide which has been demonstrated to decrease operating efficiency and leads to fuel cell component degradation over time (Choi et al. 2014, Li et al. 2019). There is therefore a commercial incentive to seek new fuel cell designs and indeed much scientific research has been invested in the search for alternative more cost-effective solutions to H_2/O_2 PEM fuel cell constructions and operations.

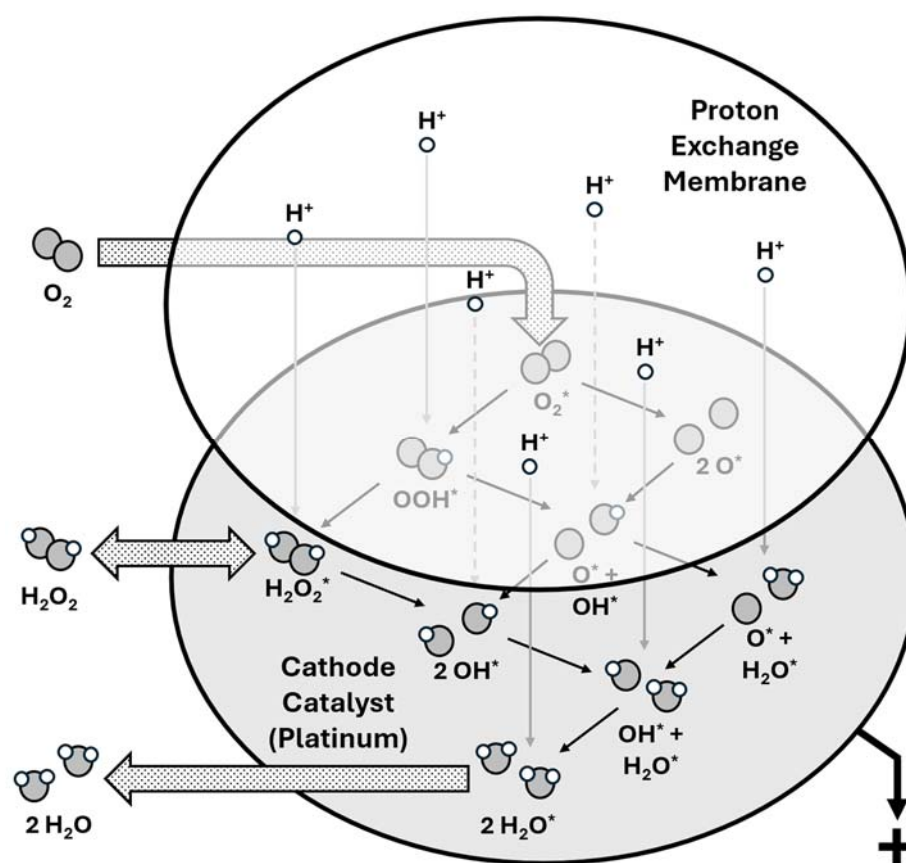
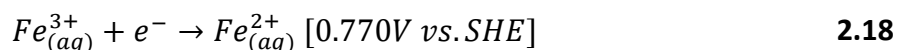


Figure 2.6 Representation of the oxygen reduction reaction (ORR) intermediate steps.

From a technical perspective the BioGenerator system serves to accomplish one specific objective, to remove oxygen gas as the oxidant at the cathode and replace it with the kinetically and chemically more favourable ferric ion reduction reaction (Fe^{III}RR). More specifically, ferric ions act as an intermediary oxidant produced and regenerated from oxygen gas as a byproduct of microbial respiration. The Fe^{III}RR is much more straightforward in comparison to the ORR and can be represented as Equations 2.18.



The Fe^{III}RR displays a lower electrode potential at standard conditions than the ORR which is not as desirable as less energy is yielded per coulomb of electrons and the associated ferric ions converted in the reaction. The electrode potential can be improved somewhat however with the adjustment of ferric and ferrous ion activities or factors such as temperature in accordance with the Nernstian properties of fuel cell operation. Theoretical thermodynamic efficiency of the BioGenerator with faster kinetics at the cathode can approach that of the theoretical maximum efficiency (83%) of an H₂/O₂ fuel cell under certain conditions (Penev 2010). Additionally, the Fe^{III}RR does not require expensive noble metal catalysts to proceed, an inexpensive high surface area carbon felt is sufficient to act as the cathode which significantly lowers the construction cost of the cell.

Of course, the consumption of the oxidant ferric ions in a fuel cell means the ions must be regenerated in some manner to maintain the functionality of the system. The regeneration process takes advantage of the aerobic chemotrophic properties of iron oxidizing microbes commonly associated with acid mine drainage and will be discussed in greater detail in the next section. In order to oxidize ferrous ions a continuous air supply is required necessitating the need for a separate bioreactor component. Options for bioreactor construction are numerous and may take the form of fixed-bed airlift reactors or sprayed trickle bed reactors as were both used in this work. Other more complex bioreactors include mobile particle beds such as circulating bed reactors (Penev and Karamanev 2010), spouted bed reactors (Karamanev et al. 1992), and inverse fluidized-bed biofilm reactors (Nikolov and Karamanev 1987).

As previously stated, the BioGenerator is an indirect microbial fuel cell (MFC) system, which is to say, the microbes used are not directly coupled to the electrodes but instead feed on the ferrous ion waste generated from the fuel cell to regenerate ferric ions. This contrasts with the more intensively researched direct MFCs which use specialized microbes deemed electricigens contained in biofilms in direct electrical contact with the fuel cell electrode. Essentially a direct MFC couples the internal electron transport chain of electricigens directly to a conductive substrate through cellular features such as membrane-bound multiheme c-type cytochrome, conductive pili, or redox-active mediators to achieve goals such as desalination, wastewater treatment, or biosensors (Luo et al. 2023, Rozendal et al. 2008). Applications using direct MFCs tend to differ in objective to purely electrical generation intentions however, as the issue of ORR kinetics is not normally addressed and the adhered electricigens are not geared to sustain intermittent periods of continuous high current production. Power output of direct MFCs compared to electrode size tends to be low, on the order of 1 W/m², and not practical for the purposes of large-scale energy production (Prashanthi 2023). To date, few systems similar to the BioGenerator are reported operating as indirect MFCs, one MFC system based on an acetate/Fe³⁺ chemistry consists of a similar layout of a separate fuel cell and bioreactor (Ter Heijne et al. 2007). Some recent renewed interest has been demonstrated in the use of AMD microorganisms in MFCs but are of the direct MFC construction (Rojas et al. 2017, Stom et al. 2021, Zhang et al. 2021).

One of the distinctive features of direct MFCs is the presence of naturally occurring biofilms which are unwanted in the case of indirect MFCs as they act to foul the fuel cell cathode. Compounding issues of fouling is the slow production of insoluble mineral deposits crystallizing from the combination of iron and nutrient salts dissolved in solution. Prevention of biofilm growth and mineral fouling in the BioGenerator is controlled using low pH levels (pH <1) which ensures surfaces are kept clean internally. Such low pH levels are difficult conditions for survival for many known acidophiles and in fact the BioGenerator microflora consists exclusively of hyperacidophiles and is dominated by the iron oxidizing microbe *L. ferriphilum* (Penev 2010). The term “hyperacidophile” is not widely used amongst academic sources, though its definition is loosely agreed to be representative of lifeforms that grow optimally below pH 1 (Johnson

and Aguilera 2019). Operation at the high ionic strengths needed for efficient electrical power generation and low pH necessary to prevent fouling result in a rather chemically harsh environment for sensing equipment as well as the PEM fuel cell. While long term operation of the PEM fuel cell has been successively demonstrated it has been observed that the PEM fuel cell suffers from a rapid drop in the observed maximum output power in the first few weeks of operation and eventually tapers off to an intermediate output level. While the issue is not a complete roadblock in feasibility it still acts as a hinderance to commercialization of the technology through added financial costs of requiring greater amounts of expensive platinized anode felt and PEM material.

The issue of reduced PEM fuel cell output remains an unresolved issue at the current time of this work. Some general conclusions are apparent through observation of the fuel cell components after extended periods of exposure to the chemical broth and operation at high power output. Firstly, despite the low pH and lack of apparent biofilms anywhere inside the bioreactor, organic deposits are still often found to develop within the cathode carbon felt (Figure 2.7) likely due to favourable surface properties from a microbial perspective, though this is generally less of a concern as the carbon felt is inexpensive and can be cleaned but results in greater maintenance and downtime. The biological deposits act to hinder mass transport of ions in solution to the cathode.

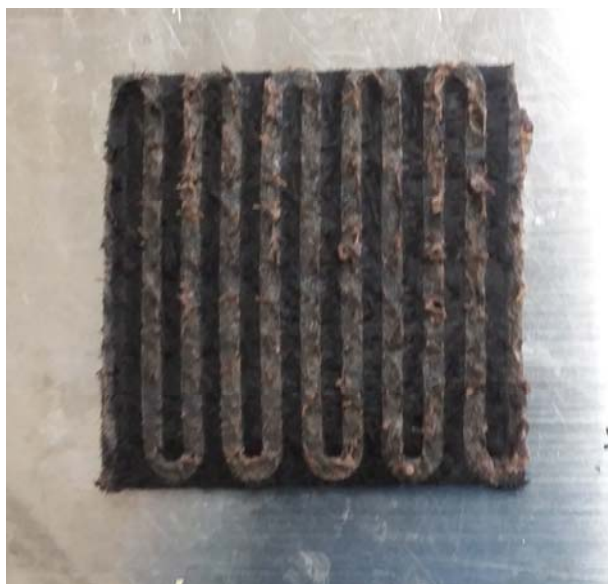


Figure 2.7 Biological residue occurring on cathode felt after extended use.

Secondly, the PEM material shows discolouration consistent with that of ferric ion intrusion throughout the thickness of the material and its binding to the sulfonic acid groups within the membrane polymers leading to a reduction in H^+ transport (Figure 2.8). Despite the common marketing of these polymers as being “impermeable” to the components of the chemical broth, there is sufficient evidence from practical operation to suggest otherwise. For example, the fluorocarbon-based membranes used in Clarke style dissolved oxygen sensors exposed to the chemical broth develop a similar observed discolouration and have been found to pass detectable levels of iron ions into the electrode space causing interference (Penev 2010). Likewise, iron ions can be detected in low concentration in the water expelled from the anode of the PEM fuel cells in operation with a measured acidity in the range of pH 2. The issue of ferric ion contamination is in fact a documented phenomenon where the effects of electro-osmosis of H^+ ions aren't strong enough to counter the high ionic gradient of ferric ions which then penetrate the membrane (Pupkevich et al. 2007a). The problem is not easily mitigated and is something that must simply be tolerated in operation, careful selection of the membrane type offers some relief where the double-layer construction Selemion HSF membrane was shown to have the lowest sensitivity to ferric ion contamination and was selected for use with the BioGenerator (Pupkevich et al. 2007a).



Figure 2.8 Proton exchange membrane demonstrating heavy ferric ion intrusion.

Lastly, the expensive platinum coated anode felts show signs of chemical staining consistent with that of iron compounds (Figure 2.9). Despite the low measured pH of pass-through water in the anode compartment which might be expected to keep iron ions in a soluble state, large patches of staining can occasionally be encountered. It should be noted however that often the staining is not homogeneously distributed, and this may be indicative of a microscopic penetration of the membrane. Because the construction of the anode felts is more complex and involves the addition of hydrophobic treatments to improve hydrogen gas entry and liquid water removal, fouling of the hydrophobic fibers will interfere with mass transport and will lead to reduced power from the fuel cell. It may be beneficial to circulate dissolved chelating agents in the water passing across the anode compartment to mitigate surface fouling, though this has not yet been performed experimentally.

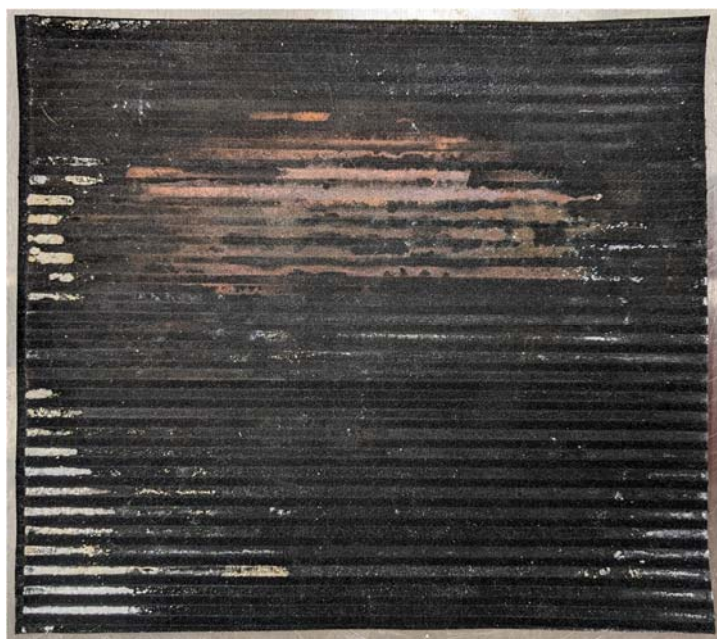


Figure 2.9 Platinized felt demonstrating staining from cross-over contamination.

A final point on fuel cell operation and performance issues comes from a purely electronic perspective which has to do with the external construction, more specifically electrical contact and conductivity between graphite conduction plates and copper collector plates. In the case of fuel cells, the voltages involved tend to be quite low and rely on high currents to generate practical power, therefore power output performance

can be severely affected by milliohm levels of resistance in accordance with Ohm's law. Even though the electrical resistance of graphite is regarded as high compared to that of metals, it is important to note that the total resistance (R_T) is measured as a function of cross-sectional area (A) in relation to the material resistivity (ρ) and the thickness (length) of the plate (l) (Equation 2.19) and therefore the overall resistance can be made very small with respect to the quality of the contact patch between copper and graphite.

$$R_T = \rho \frac{l}{A} \quad \mathbf{2.19}$$

When compressed together the actual summated contact point area may be substantially smaller than expected depending on the flatness and surface finish of the copper and graphite. Additionally, the chemical broth is highly corrosive to copper and can easily seep from gaskets finding its way in between the contact region between graphite and copper leading to widespread surface corrosion and breakdown of electrical contact. Even long-term exposure to air can produce light surface tarnish of the copper leading to reduced contact area. It is therefore recommended to clean the copper surface of all tarnish and apply a very thin layer of conductive carbon paste between these two components to seal them and ensure homogenous electrical contact across the full surface of the plates when pressed together for best performance.

2.3.1 Air Supply

One apparent drawback to the BioGenerator as an energy storage system is the need for a near continuous energy input in the form of compressed air to maintain and operate the system. Large volumes of air must be compressed and released through the bioreactor broth for aeration of microbes with a low overall uptake of the oxygen available in the gas before escaping the liquid. The air additionally acts as the energy source for circulation pumping of the bioreactor contents and must therefore be of a sufficiently high flow rate. Indeed, energy consumption by air compression represents the bulk of energy input where total energy input is anticipated to be more than ten times greater than that of the next most significant energy consumer, which is the fuel cell circulation pumps (Abou Jarboua et al. 2019). An energy consumption requirement for an energy

storage system at face value appears counter to the objective and excessive operating costs will undoubtedly call into question the economic viability of such a system by public and private interests. Therefore, a brief review of the methodology and delivery requirements associated with air supply for the BioGenerator is warranted.

2.3.1.1 Mechanical Compressor

The air input for the BioGenerator will require a high flow rate at a low pressure of 140 – 690 millibar (2 – 10 psi) minimum for use with low pressure loss spargers, which is necessary to overcome both the hydrostatic liquid pressure and restrictions in piping and sparging (Abou Jarboua et al. 2019). Naturally the first go-to choice for the production of compressed air tends to be electrically powered reciprocating or rotary machinery. In this case, reciprocating machinery is not very ideal to meet the flow rate requirements while in addition such designs require rather complex internal component mating and tribology which is less suited to long term continuous use. Rotary machinery is therefore the more ideal choice where much higher flow rates at lower pressures can be achieved and moving parts can be reduced to a single spindle driven directly from the output of an electric motor with only replaceable ball bearings taking the brunt of wear. Such rotary designs take many forms but come with various limitations in output capability and construction costs. The centrifugal blower is probably the most ubiquitous of such designs, simple and cheap to construct, it can produce the high air flow rates necessary for the BioGenerator but unfortunately won't meet the pressure differential necessary for aeration. Turbo-compressors, while capable of meeting the flow rates and pressures required, involve highly complex component geometries which become expensive at scale-up. The most ideal equipment for the task has been found to be the regenerative blower which can closely match both the pressure and flow rate requirements needed while also maintaining a relatively simple internal construction that can be manufactured at a reasonable cost (Jarboe 2008). A regenerative blower was used for aeration of a pilot scale BioGenerator and found to perform adequately. The internal operating principles of the blower can be seen in Figure 2.10 where the physical appearance is similar to that of a centrifugal blower however the operation is not the same. In the regenerative blower an intake of air is progressively compressed along an outer ring where each vane generates

an individual air vortex that acts as a multi-stage compression until release at the outtake (Badami and Mura 2012).

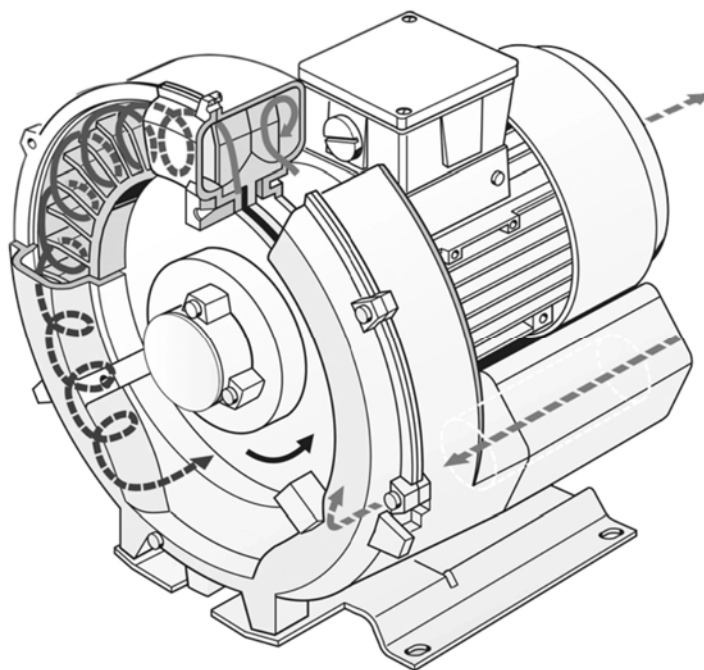


Figure 2.10 Regenerative blower with internal workings (Elmo Rietschle – Gardner Denver, Inc.).

A preliminary study of a 1 MW 2500 m³ volume BioGenerator scale-up suggests a conservative estimate of 120 kW for aeration purposes (Abou Jarboua et al. 2019) while a pilot scale system (this work) was found to require 1.3 kW to supply aeration of 100 kg/h to a single 2 m³ airlift bioreactor segment at a pressure of 155 millibar. Clearly even with economies of scale under consideration the energy input will be quite high requiring the output of a small power plant to maintain operations for a grid scale project and alternative strategies need to be considered for the concept to be competitive with other energy storage technologies.

2.3.1.2 Trompe

Ideally the compressed air energy input to the BioGenerator might be obtained at low cost from renewable energy sources, such an aspiration is realistically possible with the use of a more obscure type of hydropneumatic power generation system known as a

trompe. A trompe is powered by water much like a hydroelectric dam, however instead of using water to produce rotary motion as is normally the case, the water is instead used to directly produce large quantities of compressed air. The first recorded use of the trompe dates back more than 400 years in Europe as a source of air for iron bloomeries in place of manually operated bellows (Tomàs 1999). Since then, the trompe has found practical use in large scale compressed air generation for mining activities in the 20th century (M.P. 1908), most notably the Ragged Chute facility located in New Liskeard, Ontario that provided compressed air to silver mining operations around Cobalt, Ontario (Miller 2014). An illustration of the Ragged Chute trompe can be seen in Figure 2.11 where the design is quite simple, similar to an airlift pump in reverse, requiring no moving parts which results in long service life.

The trompe works through suction of air at the inlet by water falling into the downcomer shaft through the Venturi effect. Hydrostatic pressure then isothermally compresses entrained air bubbles, releasing them at the bottom in the separation gallery. Water returns to the surface through the riser shaft while the compressed air is captured from the separation gallery for use. Efficiency of the Ragged Chute trompe was reportedly quite high at 83%, delivering 61500 kg/h of air compressed at 923 kPa (134 psi), though recent revisions place the efficiency closer to 65% based on losses to air absorption in water (Pavese et al. 2016). The proven high air output a trompe can provide is well within the magnitude required for the BioGenerator to function at grid scale and can be depended on as a reliable source of renewable power due to the short-term predictability of hydro power compared to wind and solar. Use of a trompe in place of complex electrically powered compressors is therefore highly recommended for the feasibility and commercialization of the BioGenerator.

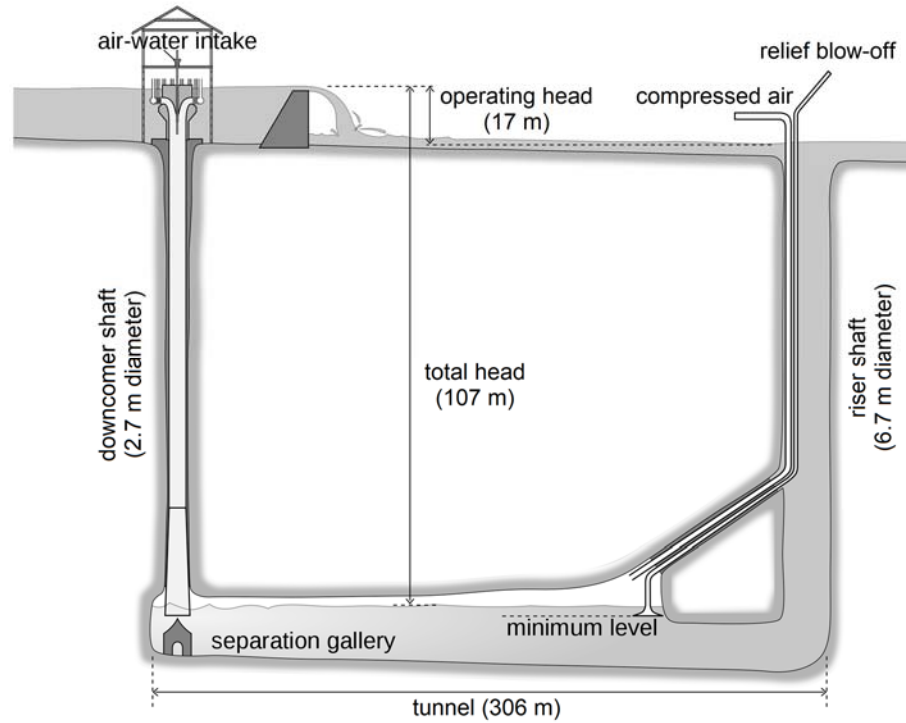


Figure 2.11 Diagram of Ragged Chute trompe. (adapted from “Taylor trompe sketch” licensed under CC BY-SA 4.0)

2.3.2 Energy Management

The inevitable question of the BioGenerator system must be answered, if the goal is to store energy and the system requires multiple energy inputs to sustain itself (aeration, pumping, heating, cooling), how can this be realistically implemented? An energy management system (Figure 2.12) based on hydropneumatic power generation provided by a trompe is presented as a means of answering this question.

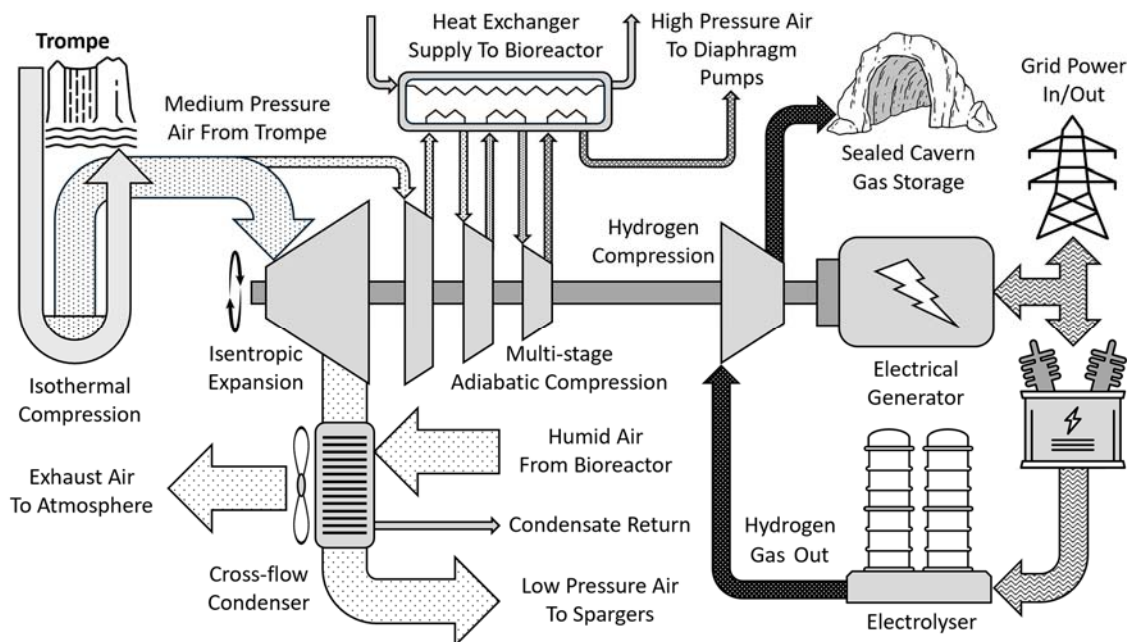


Figure 2.12 Conceptual energy management system for the BioGenerator.

The BioGenerator might ideally be located in Northern Ontario, British Columbia or Quebec to take advantage of the vast hydrostatic potentials of fresh water available to create a trompe of suitable size (Stantec 2023). The system may work best as both a combined power generation and energy storage system to make the best use of resources. The bulk of compressed air from the trompe is passed through a large isentropic expansion turbine to generate rotational mechanical energy as the primary power source for all operations. The nature of air compression in the trompe naturally produces dry air due to the cold temperature of the water (Chen and Bice 1982), ideal for use in turbomachinery. Air leaving the turboexpander will be cold in temperature due to the isentropic process and therefore useful as a means of condensing water vapor and iron sulfate containing aerosols leaving in exhaust air and returning them back to the bioreactor. The expansion process and overall flow rate of air will provide a sufficient amount to cover sparging operations where the final pressure needed is rather low, 155 mbar (2.2 psi or 62" H₂O) for a tested pilot scale bioreactor in this work that had a liquid depth of 1.52 m. Given that a pilot scale unit consumed 100 kg/h of air through a volume of 2 m³, a theoretical 1 MW BioGenerator with a bioreactor volume of 2500 m³ at 50% duty cycle (air on to air off time within 24 hours) might therefore be expected to consume

62500 kg/h or 48100 m³/h of air at peak operation, which is within the supply capability of a large trompe. Locating the BioGenerator in a northern climate will require greater attention to thermal control of the bioreactor, ideally operation near 45 °C produces the best bio-oxidative rates however operation at reduced temperature of 20 °C is a more technically feasible goal to limit heat loss while still maintaining a reasonably high rate of biological activity.

While thermal losses across the bioreactor walls can be easily mitigated with sufficient insulation, the operation of air passing through the broth will naturally strip heat from the system and therefore the losses must be dealt with in some manner. Heating at full scale could be provided thermodynamically through the adiabatic compression of a stream of compressed air provided by the trompe in a multi-stage turbine powered from the turboexpander. Heat from compression can be delivered to a heating medium in a heat exchanger and circulated through the bioreactor unit as needed. The high pressure air from the multi-stage compression is then useful for operating the many liquid pumps needed for circulation of broth through fuel cells and heating medium for thermal regulation with the use of pneumatically powered diaphragm pumps.

A second consideration that needs to be addressed is the production, and more importantly, the storage of hydrogen gas fuel needed for the BioGenerator system. Mechanical energy provided from the turboexpander might be used in a second compression turbine to pressurize the gas for storage. The location of the construction could be chosen in proximity to an abandoned mine in the same northern region which could be repurposed as a gas storage cavern (Matos et al. 2019), making use of a pre-existing feature. An electric generator attached to the system would create electric power to be used in electrolysis or sent to the grid depending on supply and demand requirements. Energy for electrolysis would largely be extracted from the grid during periods of electrical oversupply with the generator acting only in a supplementary role. Sizing of the trompe would need to ensure a sufficient air flow to maintain the BioGenerator system during seasonal periods of lowest water flow availability and coldest outdoor temperatures. The electric generator would be used to bleed unneeded excess energy during seasonal periods where the trompe overproduces compressed air

and the turboexpander is used in a secondary role for direct electrical power generation. In this way rotational mechanical energy transferred across a single shaft can be used to provide bioreactor make-up heating and regulation, water vapor condensation and return from the exhaust air, broth pumping through fuel cells, hydrogen gas compression for storage, and output electrical power generation from surplus mechanical energy all within a single rotary unit.

2.4 Iron Oxidizing Microbes and Extremophiles of Interest

Iron oxidizing microbes form the heart of the BioGenerator system acting to perform the necessary biooxidation of ferrous iron to ferric ion through the respiration of dissolved oxygen gas. These microbes are often found living naturally in peculiar habitats toxic to most other organisms, generally in areas of sulfurous hot springs, coal seams, and geological iron deposits (particularly pyrite). Sulfur and iron bearing materials act as a food source for the microbes converting them into sulfuric acid and acid salts under aerobic and anaerobic conditions defining them as chemolithotrophs. In addition, these unique extreme environments may harbor other microbes of scientific interest including autotrophic algae and various organic substrate consuming heterotrophs. Human activity also tends to contribute to environments supporting these lifeforms such as mine tailings and the mines themselves. In abandoned mines that become flooded with water these microbes represent the principal agent in the formation of acid mine drainage, an ecologically harmful discharge. When acid mine drainage enters natural waterways, a combined damaging effect occurs by way of reducing pH, contamination by heavy metals (As, Cd, Pb, Zn, and Cu), along with large amounts of yellow-orange iron precipitate that deposits on stream beds and hinders biological action (Jain and Das 2017). The biochemical reactions involved in the formation of acid mine drainage are diverse and the microbial make-up dictated by the pH, temperature, and composition of the drainage at a given time. The consumption pathways demonstrated by the various microbes present as a co-culture also differ from one another, in some cases robust multi-substrate consumption pathways are demonstrated under aerobic and anaerobic conditions (*Acidithiobacillus* spp.), in other cases only specific modes of substrate consumption

exist (*Leptospirillum* spp.). Examples of these substrate consumption pathways are demonstrated in Figure 2.13.

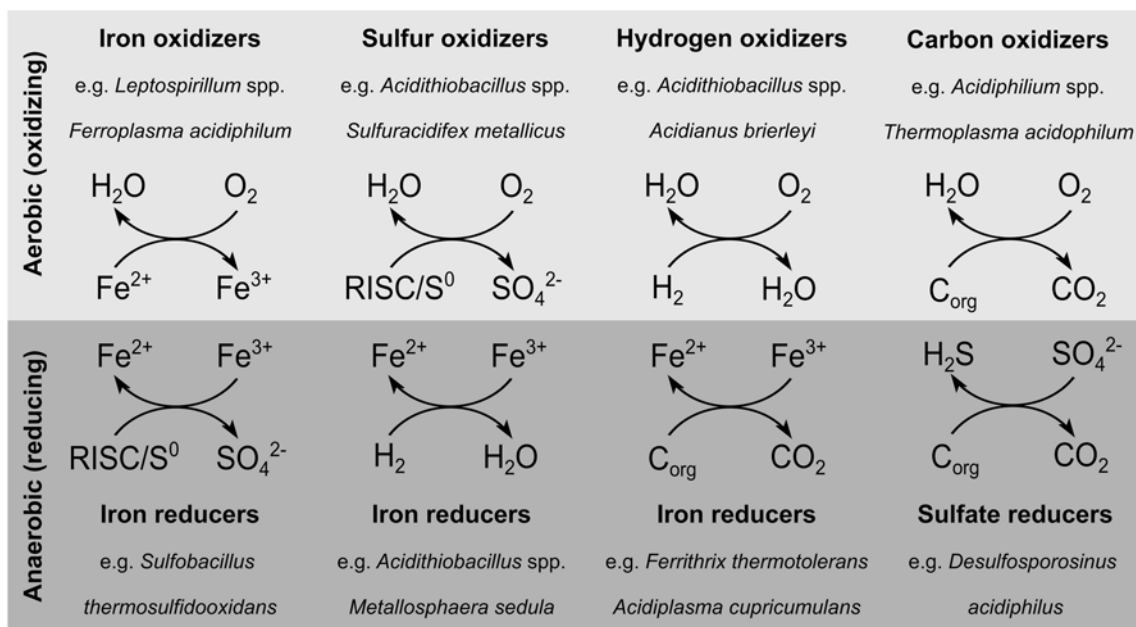


Figure 2.13 Diversity of consumption pathways by acidophilic microbes. “Data of the associated studies of Hedrich et al. 2011, Hedrich and Johnson 2013b, and Dopsin 2016” by Malik and Hedrich 2022 is licensed under CC BY.

Of significant importance with respect to the BioGenerator is the aerobic iron oxidation process. These reactions proceed through a protein super-complex located on the inner and outer membranes of the cell and operate similarly to the electron transport pathways of organelles such as mitochondria and chloroplasts. A simplified diagram of the electron transport pathway is shown in Figure 2.14 representative of that found in *Acidithiobacillus* spp. the model organism for iron biooxidizing microbes. Note that the Cyc2 protein of the electron transport pathway is exposed to the exterior of the cell and is the property that gives rise to the direct excitation by electrical activity demonstrated by electricigens found in microbial fuel cells. In the case of the BioGenerator, the operation acts as an indirect microbial fuel cell and so excitation of the Cyc2 protein occurs through interaction with ferrous iron ions, oxidizing the ion to ferric iron and abstracting an electron in the process. The iron oxidizing super-complex (Figure 2.14) is composed of three complexes secured in the inner membrane (aa₃ cytochrome oxidase complex,

cytochrome bc_1 complex (bc_1), and NADH dehydrogenase complex (NDHI)) followed by four electron transporters; a cytochrome c_2 protein (Cyc2) secured in the outer membrane along with three soluble proteins rusticyanin (Rus), cytochrome c_1 (Cyc1), and cytochrome a_1 (CycA1) free-floating within the periplasm. The electron transporting proteins contain heme molecules using copper (rusticyanin) or iron (cytochrome) ions bound at their center which allows them to be reduced (charged) or oxidized (discharged) according to their relative redox potential with one another, facilitating a controlled transmission of electrons (Zhan et al. 2019).

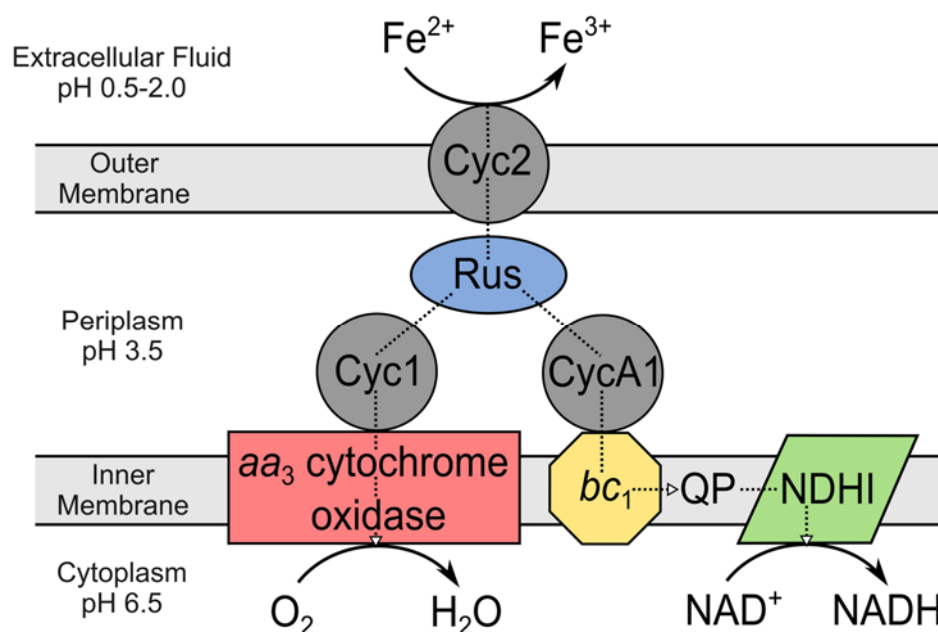


Figure 2.14 Components of the iron oxidation pathway of *Acidithiobacillus* spp. “A modified scheme as given by Ilbert and Bonnefoy 2013” by Malik and Hedrich 2022 is licensed under CC BY.

The stepwise transmission of electrons is demonstrated to take one of two paths after exciting the rusticyanin protein; the downhill pathway to the aa_3 cytochrome oxidase complex that consumes oxygen to act as a proton (H^+) pump and the uphill pathway to the bc_1 complex that drives a Q-cycle to generate NADH from the NDHI complex (Zhan et al. 2019). In the uphill pathway using the Q-cycle, amphipathic molecules of ubiquinone bound within the inner membrane acting as a quinone pool (QP) are reduced to ubiquinol through the bc_1 complex which are in turn used to drive the NDHI complex

to generate energy for the microbe and converted back to ubiquinone in the process (Zhan et al. 2019). Of the two pathways, the downhill pathway is the most important accounting for 95% of the electron consumption from rusticyanin that pumps protons from the cytoplasm into the periplasm (Zhan et al. 2019). The H^+ gradient across the inner membrane provides the energy source used to drive ATP synthase complexes as well as the bc_1 complex and NDHI complex, altogether responsible for ATP production (Zhan et al. 2019).

In the case of Gram-negative acidophilic bacteria, the inner and outer membranes also play the important role of barricading the cytoplasm from the highly acidic extracellular fluid. Acid resistance mechanisms in *Leptospirillum* spp. have been predicted by Vergara et al. (2020) through gene analysis of those related to low pH resistance. A dual strategy line of defense against H^+ intrusion is suggested; the first line of defense lies in reducing permeability of the outer membrane while the second line of defense is achieved through the expulsion and neutralization of H^+ entering the cytoplasm. In the first line of defense the outer membrane is thickened and reduced in permeability through the insertion of various molecular agents such as bacteriohopanepolyols (BHP), starvation lipoproteins, and spermidine. The second line of defense uses primarily the aa_3 cytochrome oxidase complex to neutralize four H^+ for every O_2 molecule consumed while driving four additional H^+ from the cytoplasm into the periplasm. Additional protein complexes in the cytoplasm help to neutralize H^+ as an energy source along with antiporters in the inner membrane that push H^+ into the periplasm at the expense of sodium, potassium, and chloride ions released from the periplasm to the cytoplasm. The acidity of the periplasm itself plays a role as well in acid resistance by helping reduce the H^+ gradient across the outer membrane.

2.4.1 Acidithiobacillaceae

The *Acidithiobacillaceae* family encompasses multiple species of the genus *Acidithiobacillus* bacterium and includes the most well-known and studied species of iron oxidizing acidophiles, *Acidithiobacillus ferrooxidans*. Members of this family are non-spore forming chemolithotrophs capable of fixating atmospheric carbon dioxide and identified by their motile, Gram negative, rod-shaped prokaryotic cells having a length of

1.2 μm and width in the range of 0.5 – 0.6 μm commonly associated with acid mine drainage (AMD) where they were first identified (Jensen and Webb 1995). *At. ferrooxidans* has maintained significant interest with respect to its industrial importance as a bioleaching and biomining agent along with both *At. thiooxidans* and *At. caldus* to a lesser extent (Quatrini et al. 2005). All species in this family display acidophilic properties, existing in the pH range of 0.5 - 6.0, and are generally found to reside in natural locations containing sulfur, coal, or iron deposits. The bacteria typically survive through the oxidation of reduced inorganic sulfur compounds (RISCs) such as pyrite bearing minerals, thiosulfate ($\text{S}_2\text{O}_3^{2-}$) ions, tetrathionate ($\text{S}_4\text{O}_6^{2-}$) ions, and in some cases hydrogen sulfide gas or dissolved hydrosulfuric acid (SH^-) into sulfuric acid (Malik and Hedrich 2022, Nemati et al. 1998, Parker 1945). Alternatively, a divergent branch of the family contains iron oxidizing enzymes embedded in their outer cell membrane capable of oxidizing elemental iron to aqueous ferrous iron acid salt and subsequently the oxidation of ferrous iron ions into ferric ions. Iron oxidation processes within the cells must proceed through the use of molecular oxygen due to the high oxygen-reduction potential (ORP) of the medium making the process strictly aerobic (Johnson 1998). It should be noted however that since iron oxidation is not the only energy production biochemical pathway available, anaerobic processes may still occur such as iron reduction coupled to sulfur oxidation (Kucera et al. 2016, Osoria et al. 2013). Energy producing pathways under both aerobic and anaerobic conditions are a necessity for survival where environmental conditions often consist of stagnant liquid mediums where oxygen penetration into the liquid is low. *At. ferrooxidans* has been particularly important in the determination of the electron transport chain model and protein complexes associated with iron biooxidizing processes, specifically the cytochrome c and rusticyanin chain contained in the periplasmic space along with the various inner membrane complexes such as cytochrome bc_1 and variants (Malik and Hedrich 2022). In recent years the number of species in the family has expanded considerably, a phylogenetic tree including the most recent additions has been prepared in Figure 2.15 (Moya-Beltrán 2021, Norris et al. 2020). Most of the species are taxonomically separated according to anomalies in their DNA profiling, having differences in optimum growth temperature and pH but few other physically relevant features leaving them as mostly

scientific curiosities for the time being. The species *At. albertensis* is physically differentiated from the other species with the presence of a tuft of polar flagella in place of the usual single flagella (Bryant et al. 1983). The species *At. concretivorus* has relevance as a contributor to the corrosion of concrete by sulfuric acid in sewer pipes above the water level through the biooxidation of hydrogen sulfide present as a component of sewer gas (Parker 1945). The species *At. caldus* may have some commercial relevance due to a high tolerance to arsenic dissolved in solution that developed over a number of years from exposure in gold recovery operations (Rawlings 2008).

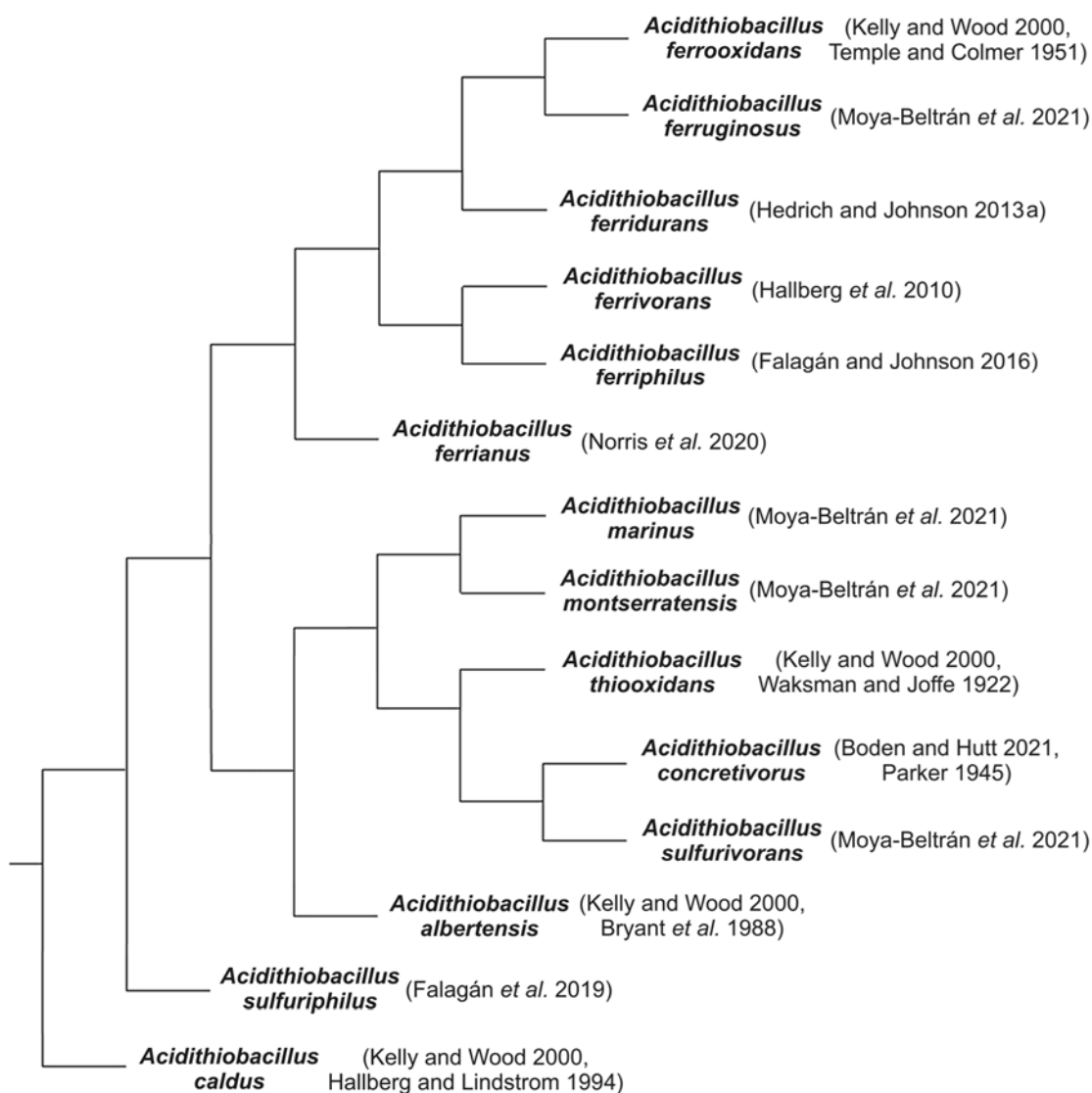


Figure 2.15 Phylogenetic tree of *Acidithiobacillaceae*.

2.4.2 Leptospirillaceae

The *Leptospirillaceae* family is a more recently discovered series of iron oxidizing microorganisms with a less diverse metabolic pathway than the *Acidithiobacillaceae* family, being capable of only aerobic digestion of aqueous ferrous iron (Song et al. 2011). Similarly to *Acidithiobacillaceae*, members of the *Leptospirillaceae* family are Gram negative motile prokaryotic bacterium containing a single polar flagellum and fixate atmospheric CO₂ as a carbon source. The bacteria are notable for their distinctive helical shape having a width of 0.3 – 0.5 µm and a length of 0.9 – 3.0 µm. The family consists of three distinct species listed in the phylogenetic tree of Figure 2.16. The bacteria tend to dominate at lower pH levels than that of *Acidithiobacillaceae* (pH <1.5) and contain a modified metabolic pathway that does not use rusticyanin whose presence isn't found in the periplasm, a novel deep red coloured cytochrome is used in its place (Blake II et al. 1993). In addition to atmospheric CO₂ fixation the species *L. ferrooxidans* and *L. ferrodiazotrophum* also display the ability to fixate atmospheric nitrogen while the species *L. ferriphilum* has lost the ability and sources nitrogen from dissolved nutrients (Tyson et al. 2005). *L. ferriphilum* is important commercially in bioleaching and biomining operations in a similar capacity to *At. ferrooxidans* having a similar function and also high resistance to ordinarily toxic metal ions such as those of copper and arsenic (Martínez-Bussenius et al. 2017, Rawlings 2008). *L. ferriphilum* plays a particularly important role in the BioGenerator being the primary iron biooxidizer and is useful among the many choices of iron oxidizing species where its pH tolerance is the highest among the three *Leptospirillum* species and those of the *Acidithiobacillaceae* family which is beneficial for operations (Coram and Rawlings 2002; Tyson et al. 2005).

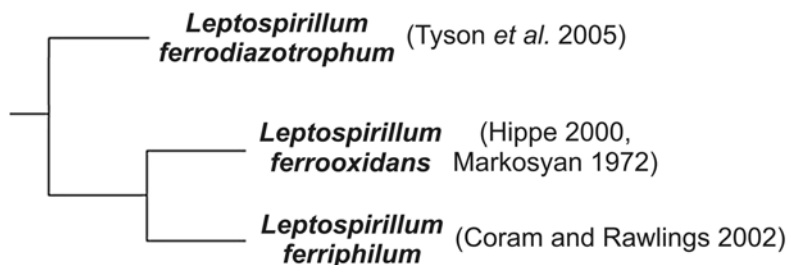


Figure 2.16 Phylogenetic tree of *Leptospirillaceae*.

2.4.3 Ferroplasmaceae and Picrophilaceae

The *Ferroplasmaceae* and *Picrophilaceae* families are a taxonomically related cluster of obligately aerobic archaeal prokaryote acidophiles that display high pH tolerance (pH 0.0 – 2.0) and optimal growth at elevated temperatures of 35 – 55 °C. Species of *Ferroplasma* display pleomorphic morphology consisting of cells 1.0 – 3.0 µm long with width of 0.3 – 1.0 µm that lack a cell wall and any form of flagella (Dopson et al. 2004). All species of *Ferroplasma* display mixotrophic properties, being able to aerobically oxidize ferrous iron and require an organic carbon source for growth as they do not natively possess the ability to fixate atmospheric carbon dioxide. Species of *Picrophilus* display a rounded form of smaller size with a diameter of 0.9 – 1.5 µm and differ from the *Ferroplasmaceae* family by the inclusion of a protective S-layer cell wall (Schleper et al. 1996). *Picrophilus* species similarly consume organic carbon for growth and do not fixate atmospheric carbon dioxide but differ in their lack of ability to oxidize ferrous iron. Both families contain few known species which are listed in the phylogenetic tree of Figure 2.17.

The species *F. acidarmanus* carries relevance to the BioGenerator as it coexists with *L. ferriphilum* as a minor component of the broth flora acting as a scavenger of carbon-based breakdown products in solution. The cell concentration of *F. acidarmanus* remains low in operation due to the need for high concentrations of carbon-based organic matter to grow in significant quantity but is not available. The presence of *F. acidarmanus* amongst the BioGenerator microbial culture was a natural occurrence where the microbe was originally isolated from the same source the *L. ferriphilum* was obtained at Iron Mountain CA from AMD (Dopson et al. 2004).

The species *P. oshimae* carries significant scientific interest as it has maintained the world record of the most pH tolerant organism currently known (Pikuta et al. 2007). Some debate about the delineation of *P. oshimae* and *P. torridus* as separate species currently exists as both species are 99.4% genetically similar (Habib et al. 2023), higher than the recognized threshold of 98.6% for bacterial delineation (Kim et al. 2014). The genome of *Picrophilus* species is also known to be amongst the smallest of non-parasitic free-living organisms due in part to adaption to extreme pH levels with a high average

coding density of 91.7% (Angelov and Liebl 2006), so some leeway in the definition of species delineation based on genetic profiles as an exact percentage may be in order. The speciation therefore may be revised and treated as a single species in some more recent works.

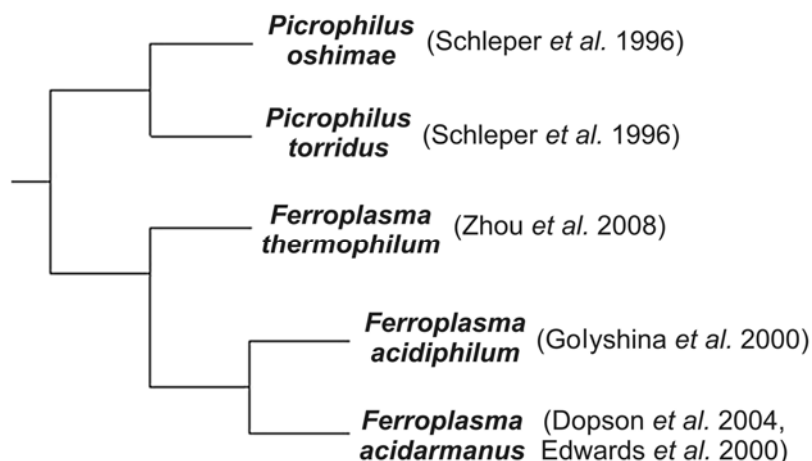


Figure 2.17 Phylogenetic tree of *Ferroplasmaceae* and *Picrophilaceae*.

2.4.4 Cyanidiophyceae

The *Cyanidiophyceae* is a class of extremophilic red algae encompassing four distinct families based on classification revisions developed by Park et al. 2023; *Galdieriaceae*, *Cavernulicolaceae*, *Cyanidiaceae*, and *Cyanidioschyzonaceae*. While recognized genetically as “red algae” it should be noted that their physical appearance is closer to a blue-green colour due to the pigments c-phycoyanin and chlorophyll-a, in some cases more yellow where cell concentrations are low or breakdown of the cells may be occurring (Toplin et al. 2008). While none of the species of this class are known to oxidize iron, they are nonetheless relevant to this work and the BioGenerator, especially that of *Cyanidium caldarium* which has been identified as a component of the microbial community of the BioGenerator (Penev 2010) and its growth observed visually with the naked eye in the presence of a light source. Members of the *Galderiaceae* family display a versatile metabolic system capable of photoautotrophic, heterotrophic, and mixotrophic growth being able to thrive on more than fifty organic carbon sources (Barbier et al.

2005). Members of the *Cyanidioschyzonaceae*, *Cavernulicoaceae*, and *Cyanidiaceae* families in contrast display a more straightforward metabolic pathway restricted to photoautotrophic growth. *C. caldarium* represents the most widely researched of the species in the *Cyanidiophyceae* class and is notable for a similarly high tolerance to low pH levels as *P. oshimae* recorded in literature (Pikuta et al. 2007). The *Cavernulicolaceae* family, informally known as “cave *Cyanidium*” represents a significant departure from the other three families in environmental characteristics being a neutrophile instead of an acidophile, though retaining its title as an extremophile in its ability to live under conditions of very low light availability, nutrient availability, and humidity (Ciniglia et al. 2019). The algal species are seen to be morphologically similar to each other under the microscope and their specific organization is seen in the phylogenetic tree of Figure 2.18.

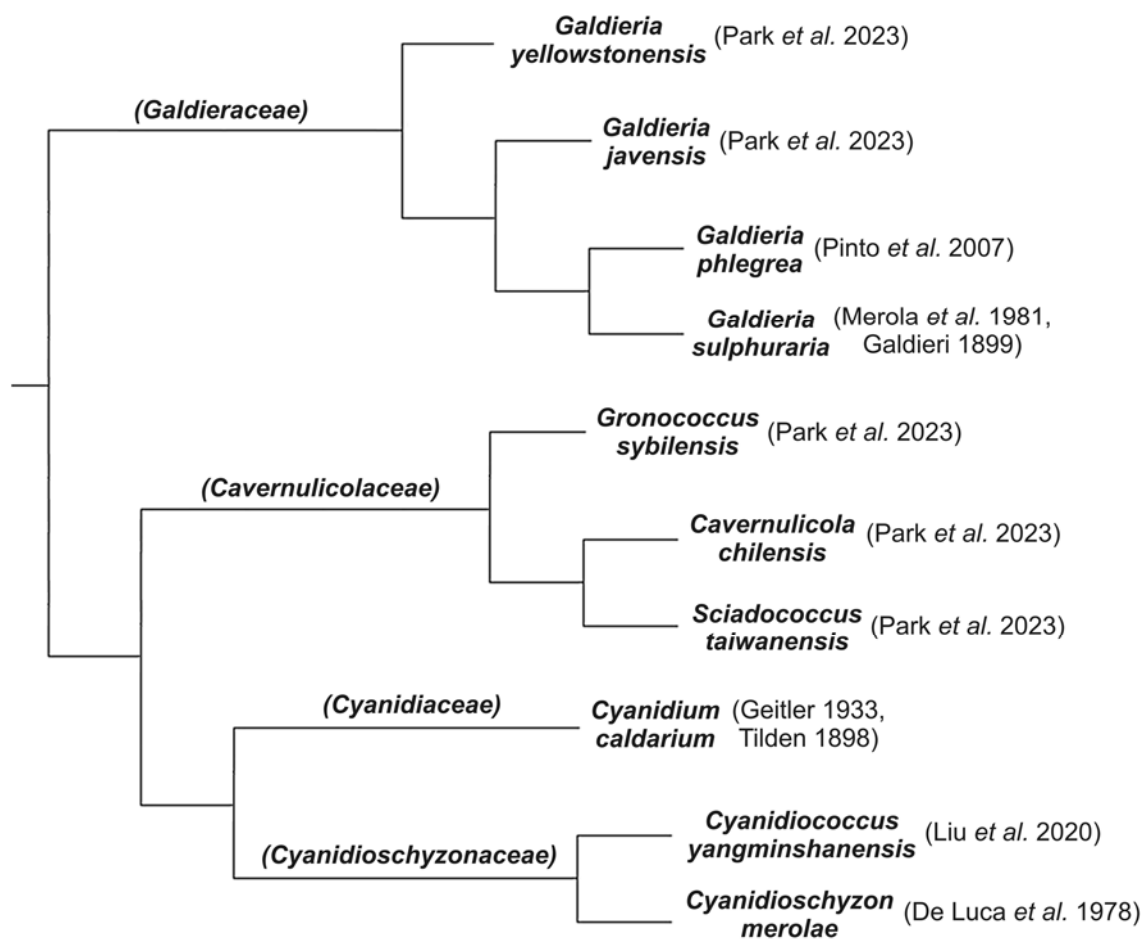


Figure 2.18 Phylogenetic tree of *Cyanidiophyceae*.

Chapter 3

3 Materials and Methods

3.1 Chemicals

3.1.1 Growth Medium and Microbial Culture

Growth medium used in bioreactor broths consisted of a modified 9K nutrient medium (Silverman and Lundgren 1959), the composition of which is specified in Table 3.1.

Table 3.1 Nutrient media composition of iron sulfate broth.

9K Media		
Nutrient	Concentration	Supplier
FeSO ₄ •7H ₂ O	Varied	Caledon Laboratories Ltd., Georgetown ON, Canada
H ₂ SO ₄	Varied	Caledon Laboratories Ltd., Georgetown ON, Canada
(NH ₄) ₂ SO ₄	3.00 g/L	Caledon Laboratories Ltd., Georgetown ON, Canada
MgSO ₄ •7H ₂ O	0.50 g/L	Caledon Laboratories Ltd., Georgetown ON, Canada
K ₂ HPO ₄	0.50 g/L	Caledon Laboratories Ltd., Georgetown ON, Canada
KCl	0.10 g/L	Sigma Aldrich, St. Louis MO, USA
Ca(NO ₃) ₂	0.01 g/L	Sigma Aldrich, St. Louis MO, USA

Ferrous iron concentrations were varied between experiments, typically within the range of 25 – 50 g/L and pH generally set to initial levels of 0.7. Oxidation of ferrous iron causes pH to rise and final pH levels on full consumption of the ferrous ions were adjusted to 0.8 in order to eliminate issues of mineral deposits such as that of jarosite. Sterilization procedures were found to be unnecessary and not conducted on the nutrient media as the high acidity of the broth sterilizes against non-extremophile microbes. Some care was required in the order and method of mixing the nutrient salts, particularly the dipotassium hydrogen phosphate which must be mixed into a small amount of water separately and only then added, where the direct addition of the dry salt causes the formation of insoluble precipitates. Concentrated sulfuric acid was added in minor amount to the solution mixture prior to the addition of ferrous sulfate to avoid the immediate oxidation of the ferrous ions followed by final pH adjustment after all nutrients were mixed and the liquid volume was set to the correct level. All chemicals

used for nutrients were of analytical grade quality. The microbial culture used in the study was obtained from acid mine drainage samples collected from the defunct Iron Mountain Mine near Redding CA, USA and contained *Leptospirillum ferriphilum* as the principal bio-oxidizing agent as a co-culture along with trace presence of *Cyanidium caldarium* and likely *Ferroplasma acidarmanus* with a third undetermined γ -proteobacterium microbe as determined through PCR-DGGE analysis (Penev 2010).

3.1.2 Ferrous Sulfate Solution

Solutions of ferrous sulfate were required in experimentation for enabling biological reactions, examination of physical properties, and calibrations. Where ferrous sulfate was needed for initiating biological reactions, and hence the presence of iron oxidizing microbes and growth media salts in solution was not of concern, ferrous sulfate was regenerated from ferric sulfate straight from bioreactor broth through continuous recirculation through a short-circuited PEM hydrogen fuel cell (Figure 3.1). A lack of aeration ensured that microbes would quickly consume any residual DO, producing an anoxic environment that inhibited further bioreactions of ferrous ions to ferric ions.

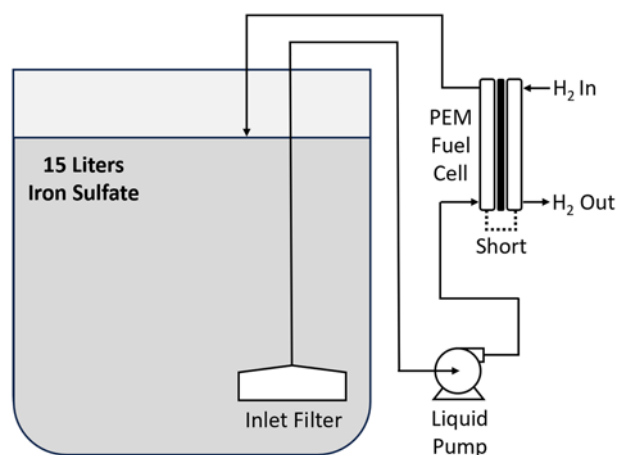


Figure 3.1 Ferrous iron regeneration apparatus.

Where high purity ferrous sulfate was required for examination of physical properties, a technique of filtration and recrystallization was used. Into a large beaker, deionized water was filled half-way and acidified with sulfuric acid to a pH of approximately 0. The acidified water was heated to boiling and technical grade ferrous sulfate heptahydrate

(Caledon Laboratories Ltd., Georgetown ON, Canada) was continuously dissolved in small additions until the solution had reached saturation. (Important: Do not add concentrated sulfuric acid to boiling solutions as the additional heat of dilution will cause an eruption of steam and violently eject liquids from the beaker!) Pieces of fine iron wool were shredded and added to the beaker contents acting to reduce any potential ferric iron generated from heating and was allowed to mix for several minutes. The beaker contents were quickly and carefully vacuum filtered through a ceramic Buchner funnel with fine porosity filter paper and the filtrate was dumped into a heavily insulated vessel and left to cool slowly at room temperature over the course of a day. The vessel was then removed from the insulation and placed in a refrigerator on the second day to finalize the crystal formation. Large crystal growths of high purity ferrous sulfate were formed on the walls of the vessel and the remaining liquid was discarded. The crystals were left in place, rinsed with acidified water at 0 pH, and stored in the refrigerator under the same clean acidified water for use when needed.

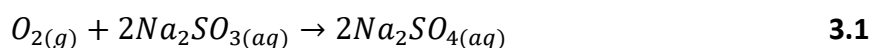
Where ferrous ions were needed for calibration, solutions were produced using crystalline ferrous ammonium sulfate hexahydrate owing to the stability of the salt (while undissolved) from oxidizing to ferric ions in storage and allowing for accurate weighing of amounts of the crystalline salt. Into a 100 mL volumetric flask, 0.7022 g of ferrous ammonium sulfate hexahydrate was placed, and the remainder filled with deionized water. The solution was mixed until all crystals had dissolved producing a calibration solution containing 1.0000 g/L of ferrous ions. Ferrous ions in solution are naturally unstable and will oxidize to ferric ions in the presence of oxygen over time, therefore short term storage of the solution was completed in sealed glass vessels in a refrigerator when necessary but avoided otherwise.

3.1.3 Hydrogen Gas

Hydrogen gas for experiments was supplied by a Hogen S20 electrolyser (ProtonOnsite, Wallingford CT, USA) able to supply up to 530 L/h of high purity hydrogen gas produced from deionized water. In some cases where only a small flow rate of hydrogen was needed a compressed gas cylinder (Linde Canada Inc., London ON, Canada) was used.

3.1.4 Zero Oxygen Solution

A purely anoxic solution was required for the zero point calibration of DO meters. Into a 100 mL volumetric flask, 25.0 g of anhydrous sodium sulfite (Caledon Laboratories Ltd., Georgetown ON, Canada) acting as an oxygen scavenger (Equation 3.1) was placed, and the remainder filled with deionized water. The solution was mixed until all crystals had dissolved, placed in a sealed glass vessel with low air headspace, and left to fully react with any residual DO for a period of 24 hours before use. Solutions were discarded after two weeks or after significant contamination.



3.1.5 Cleaning

General clean-up of iron sulfate spills was completed using acidified (H₂SO₄) water. Removal of insoluble iron stains and decontamination of residual iron was completed through soaking in oxalic acid solutions (~1%) and rinsing in deionized water. Removal of jarosite and other mineral deposits was achieved with some success by soaking in concentrated sulfuric acid for several days, breaking the deposits down into a white slurry.

3.2 Analytical Procedures

3.2.1 Data Recording

General purpose data recording was performed with a GoSafe S810 dashboard camera (Papago! Inc., Walnut CA, USA) used in timelapse mode which allowed for a simple method of monitoring instruments over long periods of time. The UniAmp F4 module (Unisense, Aarhus, Denmark) used for temperature and DO measurements contained an internal data recorder.

3.2.2 Wet Chemistry Determination of Iron Concentration

Ferrous ion concentration for general measurement was performed through potentiometric titration with 0.0167 M potassium dichromate (Ricca Chemicals, Arlington TX, USA) and N-phenylanthranilic acid indicator (Acros Organics, Geel AN,

Belgium) dissolved in 95% ethyl alcohol. To a flask, 50 mL of DI water was added along with 3 mL of concentrated sulfuric acid and two drops of indicator. A 1 mL aliquot containing ferrous ions in unknown concentration was added to the flask and swirled. Potassium dichromate titrant was dripped into the analyte causing the solution in the flask to slowly turn pale green followed by a sudden flash to deep purple indicating the endpoint of the titration. The concentration of ferrous ions was calculated through Equation 3.2. The overall resolution of the method was generally low due to the limitations in measurement from the burette as marked in increments of 0.1 mL and therefore spectrophotometric methods were more preferable for data collection.

$$c_{Fe^{2+}} = 6 M_{Cr_2O_7} \left(\frac{V_{Cr_2O_7}}{V_{Fe^{2+}}} \right) \left(55.85 \frac{g}{mol} \right) \quad 3.2$$

3.2.3 Colourimetric Determination of Iron Concentration

Determination of iron ions in solution as the ferric and total concentration (g/L) was completed using methods adapted from (Karamanev et al. 2002) using 5-sulfosalicylic acid dihydrate (Alfa Aesar, Ward Hill MA, USA) and 30% ammonium hydroxide (VWR International, Radnor PA, USA). The methodology was modified slightly from the original source, where 100 mL of 0.3% w/v 5-sulfosalicylic acid dihydrate solution is normally specified, the sample and reagent volumes used were halved to allow the use of 50 mL conical tubes that could be filled and stored in a dark cool location in large quantity. Absorption measurements were taken using a Genesys 10S UV-Vis spectrophotometer (Thermo Fisher Scientific, Waltham MA, USA) and calibrated using a standard solution (traceable to SRM from NIST) of 1000 mg/L Fe^{3+} as $Fe(NO_3)_3$ in 0.5 mol/L HNO_3 (Sigma Aldrich, St. Louis MO, USA). For aqueous iron sulfate samples containing more than 10 g/L of iron ions, the samples were diluted to an appropriate level. Care was taken in dilution as the nature of concentrated iron sulfate solutions makes them “sticky”, with a tendency to leave behind micro-droplets in pipettor tips that can lead to significant reading variances. Slight discrepancies were noted in the values given for ferric and total iron readings in practice when measuring samples known to be fully oxidized to ferric ions using the generated calibration curves. This was determined to be an interference caused by the high acidity of the calibrant solution. The error was

adequately eliminated by adding a correction factor to the total iron calibration curve of -0.001 Abs per 1 g/L of Fe^{3+} from the calibrant. For high precision measurements of ferrous ion concentration in ferric iron dominated solutions a potentiometric measurement yielding ion ratios was preferred using the value of total iron from the colourimetric method as the basis of concentration.

3.2.4 Potentiometric Determination of Iron Ratio

Determination of the ratio of ferrous to ferric ions in solution was achieved using a redox probe assembly employing an Ag/AgCl reference half-cell and Pt indicator electrode. Since the broth chemical composition in the bioreactors is a controlled environment, the oxidation-reduction potential is dependent primarily on the ferric-ferrous ion equilibrium while the presence of 9K nutrient media salts appear to produce no detectable differences in the probe output redox potential. The redox potential of the cell can be represented as the combination of two electrochemical processes occurring at the same time, one process involving an electromotive force resulting in the Ag/AgCl half-cell giving up electrons to the Pt electrode while the other process involves electrochemical equilibrium reactions along the Pt electrode surface between ferric and ferrous ions resulting in a polarization potential on the Pt electrode (Figure 3.2) (Bagotsky 2006).

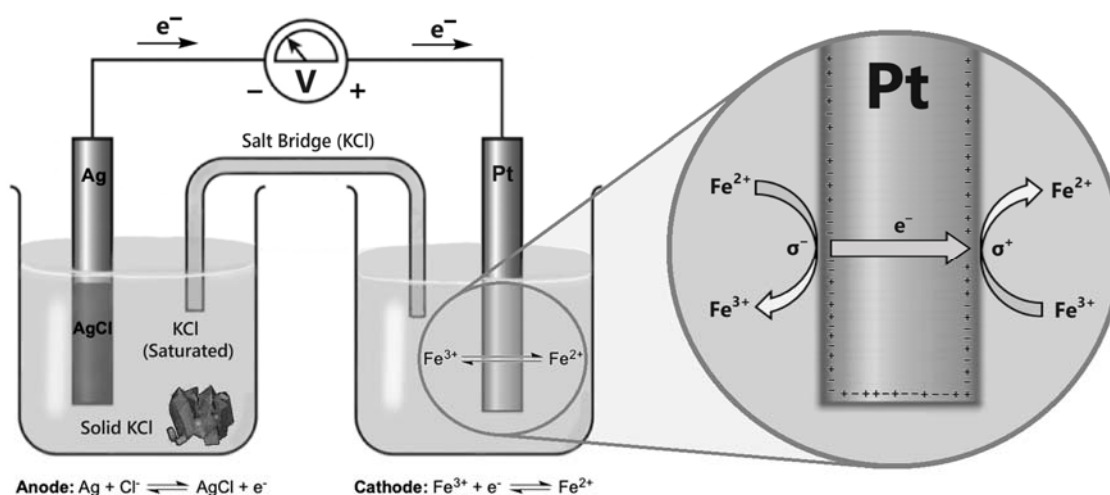


Figure 3.2 Electrochemical cell representation of redox probe.

The redox potential is modelled mathematically using the Nernst equation based on the participating ions present in solution represented as:

$$E_h = E' - \frac{RT}{zF} \ln \left[\prod_i \bar{a}_i^{v_i} \right] = E' - \frac{RT}{zF} \ln \left[\frac{(c_{Fe^{2+}} \gamma_{Fe^{2+}})(c_{Cl^-} \gamma_{Cl^-})}{(c_{Fe^{3+}} \gamma_{Fe^{3+}})} \right] \quad \mathbf{3.3}$$

Where the measured redox potential (E_h) is given as the formal potential (E') subtracted by the observed behavioural effects of the participating ions in solution represented by the ion activity (\bar{a}) or alternatively as the ion concentration (c) multiplied by the activity coefficient (γ) along with the stoichiometric value (v). Since the chloride ion concentration remains constant in the Ag/AgCl reference electrode, the half-cell voltage also remains constant, and the contribution can be merged into the value of E' leaving only ferrous and ferric ion activities present. Temperature (T) represents an important aspect of consideration when using the redox probe as it directly affects the Nernst equation and therefore must be monitored in conjunction with the redox potential. Since the temperature of the electrodes may also be different from one another, a Nernst coefficient (ζ) was sometimes used to simplify calculation represented as:

$$\zeta = RT_{av}/zF \quad \mathbf{3.4}$$

In practice the effects of temperature can also be seen to affect the value of E' , where E' can be represented as the standard-state potential (E°) plus minor contributions such as junction potentials caused by diffusion effects and other phenomena. Redox probe calibrations where large temperature swings during experimentation were expected were therefore more accurately modelled using linear functions for both the values of E' and ζ with respect to temperature. A probe assembly that included a temperature correction bath and liquid inlet thermistor was routinely used for measurements to stabilize temperatures and simplify data collection where necessary as seen in Figure 3.3.

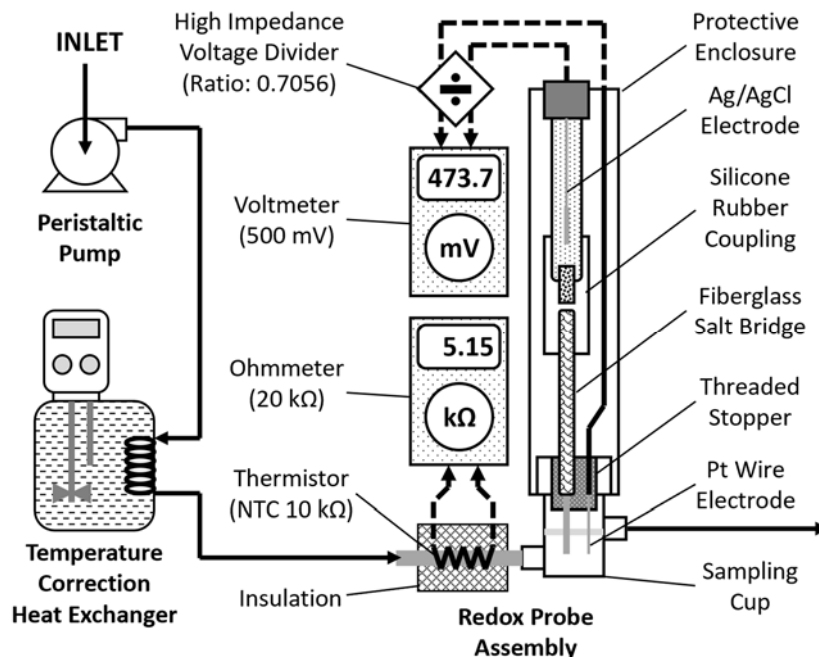


Figure 3.3 Redox probe assembly with voltage divider and temperature regulation.

Typical redox potentials encountered in measurement were found to range from 0.750 V (fully oxidized to Fe^{3+}) to 0.372 V (fully reduced to Fe^{2+}) at 22 °C. An additional enhancement to the redox probe assembly was made by including a high impedance voltage divider (Figure 3.4) between the probe and a Greenlee DM-810 (Emerson Electric Co., Ferguson MO, USA) voltmeter to bring the maximum expected output voltage to approximately 500 mV, allowing the output to fall within the typical millivolt range of digital voltmeters and gaining an extra digit of precision in measurements.

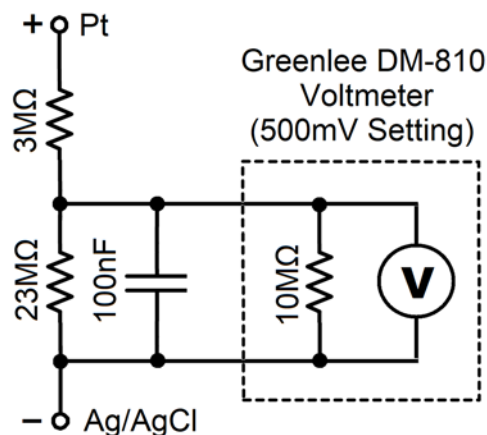


Figure 3.4 High impedance voltage divider circuit schematic for redox electrode probe.

The addition of the voltage divider was tested to ensure that its output maintained a continuous ratio of the input where excessive current draw could lead to deviation, however this was not found as the resistance values used produced a combined resistance equivalent to the commonly encountered 10 M Ω internal reference resistor in most voltmeters. The division ratio (d) was found to be 0.7056 ± 0.0007 based on the calibration curve depicted in Figure 3.5.

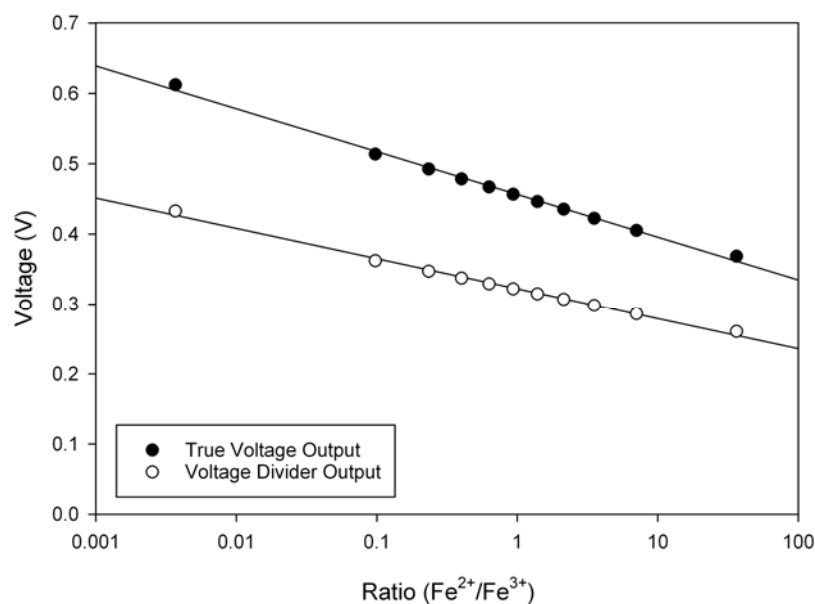


Figure 3.5 True redox output and voltage divider output calibration curves.

3.2.5 Absorbance Scanning of Iron Sulfate Solutions

Direct absorbance scanning of iron sulfate solutions was completed using a Cary 50 UV-Vis spectrophotometer (Varian Inc., Palo Alto CA, USA) with a GL40 glass cuvette with Teflon lid (FireflySci, Northport NY, USA). A custom made cuvette holder was built for the spectrophotometer using 4 by 4 cm aluminum water heating/cooling blocks pressed against both sides of the cuvette with compression springs. Water from a Julabo F12-ED cooling and heating bath (Julabo GmbH, Seelbach, Germany) was pumped to the aluminum blocks to allow temperature control of the cuvette contents. A Teflon lid was used on top of the cuvette to limit evaporation effects and a small hole was drilled in the center to insert an OptoTemp temperature probe (Unisense, Aarhus, Denmark) to monitor the temperature of the cuvette contents. Two small air jets using compressed filtered air were placed at the bottom of both cuvette windows to prevent the formation of condensation at low temperatures.

3.2.6 Polarographic Determination of DO Concentration

Measurement of DO was originally undertaken using an Orion 3 Star Dissolved Oxygen Benchtop meter equipped with a temperature compensated Orion 081010MD oxygen probe (Thermo Fischer Scientific, Waltham MA, USA). Usage of membrane polarographic probes in iron sulfate solutions of high ionic strength and acidity showed poor overall performance, where ion intrusion into the electrode space across the membrane was a prevalent problem after short periods of time and is discussed in greater detail in other works (Penev 2010). Calibration of the sensor was performed using a provided storage sleeve containing a wetted foam plug at the bottom that provided a reference environment equal to a value of 102.3% air saturation. The use of polarographic probes for data collection was quickly abandoned in favour of superior equipment based on optical fluorescence measurements.

3.2.7 Optical Determination of DO Concentration

Measurement of DO was conducted using a Unisense Opto-F4 UniAmp optical dye style DO meter with an Opto-3000 optical dye oxygen probe and a separate OptoTemp temperature sensor (Unisense, Aarhus, Denmark) for the majority of data collection. The

equipment was found to give high performance in the chemically aggressive broths showing no signs of damage or deviation in the DO probe output after more than a year of continuous chemical exposure while the temperature sensor probe required one replacement due to a dissolved solder seal that allowed liquid intrusion. Calibration of the probe was performed using a two-point 0% and 100% reading achieved by first dipping the probe into an aerated fully oxidized ferric sulfate broth with conditions the same as those to be studied and then secondly dipping the probe into a zero-oxygen solution to set the 0% baseline, in both cases a short period of time was required to achieve stabilization. While the DO probe was routinely used in simple form to provide percent air saturation measurements in the broth, measurements near or within aerated broth required an additional strategy to mitigate the effects of air bubble contact with the probe surface that resulted in significant reading error and settling time of probe dynamics. A suction sleeve and probe cluster arrangement was constructed as seen in Figure 3.6 for use in sampling DO concentrations from broth containing bubbles and froth. This design helped to block large bubbles and allowed any micro-bubbles to be blown away from the probe surface by the liquid jet of the incoming broth. A small rotary hammer was also used with great effect to dislodge and prevent the build-up of adhered micro-bubbles by tapping a stainless steel sleeve containing the DO probe approximately twice per second which resulted in very clean noise-free data.

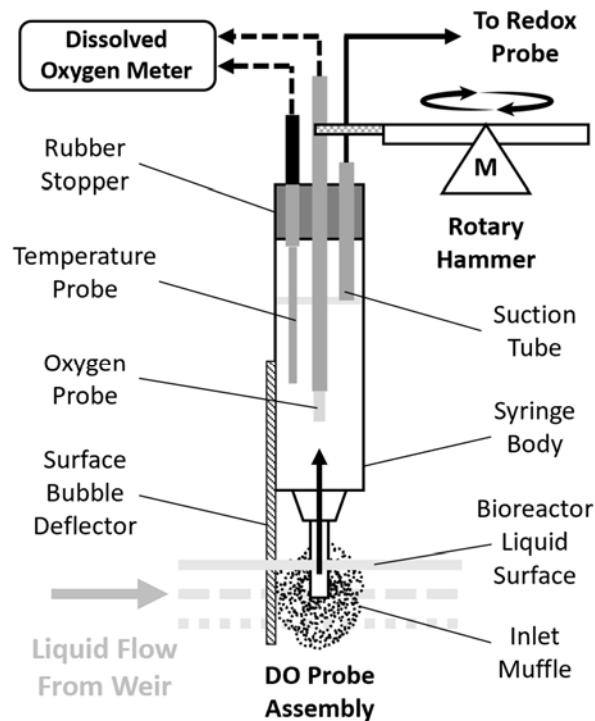


Figure 3.6 DO probe assembly with rotary tapping hammer.

3.2.8 k_{LA} Determination by Dynamic Air Stop-Start Method

Preliminary determination of the volumetric oxygen mass transfer coefficient (k_{LA}) within the bioreactor was performed using the well documented biological dynamic air stop-start procedure (Bandyopadhyay et al. 1967). A biologically active aerated liquid medium is contained within a vessel of known volume, and it is required to evaluate the efficiency of oxygen delivery to the living organisms from the supply of air entering the vessel. This is achieved through examination of the equilibrium of oxygen uptake rate (OUR) by the microbes and the oxygen transfer rate (OTR) of oxygen diffusion into the liquid. Stopping the air flow and monitoring the DO concentration of the liquid over time yields a value for the microbial consumption rate, or OUR. Starting the flow of air through the liquid after a period of microbial oxygen consumption leads to start-up dynamics as the system shifts towards the equilibrium DO concentration which is used to solve the OTR. The curvature of the DO concentration during the dynamic period can be taken as the derivative to yield dc/dt in Equation 3.5 to allow for a solution. The value of k_{LA} is found through simple rearrangement of Equation 3.5 into Equation 5.7 generating a

linearized function where the slope of the function is the negative reciprocal of $k_L a$. This approach carries the advantage that the saturated DO concentration (c^*) does not need to be determined to find the $k_L a$ as its value acts as the y-intercept which is irrelevant to the value of slope.

$$\frac{dc_{DO}}{dt} = k_L a (c_{DO}^* - c_{DO}) - qx \quad 3.5$$

$$c_{DO} = -\frac{1}{k_L a} \left(\frac{dc_{DO}}{dt} + qx \right) + c_{DO}^* \quad 3.6$$

3.2.9 Electrochemical Determination of pH

Routine measurement of solution pH was conducted using a double junction Orion 8102BN ROSS pH probe along with an Orion 3-Star Benchtop pH electrometer (Thermo Fisher Scientific, Waltham MA, USA) due to its ability to accurately measure under a wide temperature range and recover quickly from temperature change effects. Calibration of the probe for measurements greater than pH 0.8 was carried out using a three-point calibration using pH buffers of 1.00, 2.00, and 4.00 (VWR International, Radnor PA, USA). Measurements below pH 0.80 result in non-Nernstian output from electrochemical probes, a deviation known as “acid error”. Such probes have been demonstrated to still be functional to pH -4.00 however using multiple calibration solutions whose true pH is specified through equilibrium calculations using the MacInnes convention for scaling of the Pitzer single-ion activity coefficients (Nordstrom et al. 2000). The application of these activity coefficients (γ_{H^+}) to the H^+ concentration yields the H^+ activity (\bar{a}_{H^+}), which is a representation of how the ions behave physically in solution and is applied to the pH equation as Equation 3.7. Since measurement of pH in-situ is necessary for monitoring of the bioreactor broths, the environmental temperature may realistically be anywhere from 5 – 50 °C instead of the usual 25 °C standard and therefore the pH calibration standards given by Nordstrom et al. (2000) have been expanded on using PHREEQC Version 3.7.0 software to provide additional temperature compensation information as specified in Table 3.2 along with that of the standard pH buffers used. Cleaning of the pH probe prior to returning to the storage solution used a double rinse method due to the ionic composition of the test samples where the probe was rinsed first in acidified water (pH 1)

and then a second time in near-neutral water in the hopes of washing away most of the iron sulfate to avoid build-up of iron hydroxides within the ionic junction exposed directly to the test solution. Junction clogging was found to noticeably reduce response and settling time of the pH probe.

$$pH = -\log_{10}(\bar{a}_{H^+}) = -\log_{10}(\gamma_{H^+}[H^+]) \quad 3.7$$

Table 3.2 pH calibration solution temperature corrections based on PHREEQC 3.7.0.

Temperature (°C)	5	10	15	20	25	30	35	40	45	50
Neutrality Point	7.37	7.27	7.17	7.08	7.00	6.92	6.84	6.77	6.70	6.63
pH 4.00 (Buffered)	4.00	4.00	4.00	4.00	4.00	4.01	4.02	4.03	4.04	4.06
pH 2.00 (Buffered)	1.90	1.93	1.98	1.98	2.00	2.01	2.03	2.03	2.04	2.04
pH 1.00 (Buffered)	0.91	0.95	0.98	1.00	1.00	1.02	1.02	1.02	1.04	1.05
pH 0.86 (H ₂ SO ₄)	0.82	0.83	0.84	0.85	0.86	0.86	0.87	0.88	0.88	0.89
pH 0.09 (H ₂ SO ₄)	0.05	0.06	0.07	0.08	0.09	0.10	0.11	0.12	0.12	0.13
pH -0.38 (H ₂ SO ₄)	-0.44	-0.42	-0.41	-0.40	-0.38	-0.37	-0.36	-0.35	-0.34	-0.33
pH -0.79 (H ₂ SO ₄)	-0.87	-0.85	-0.83	-0.81	-0.79	-0.78	-0.77	-0.76	-0.74	-0.73
pH -1.07 (H ₂ SO ₄)	-1.16	-1.13	-1.11	-1.09	-1.07	-1.06	-1.04	-1.03	-1.01	-1.00
pH -1.41 (H ₂ SO ₄)	-1.50	-1.48	-1.45	-1.43	-1.41	-1.39	-1.37	-1.35	-1.34	-1.32
pH -1.78 (H ₂ SO ₄)	-1.88	-1.85	-1.83	-1.80	-1.78	-1.76	-1.73	-1.72	-1.70	-1.68
pH -2.18 (H ₂ SO ₄)	-2.28	-2.25	-2.23	-2.20	-2.18	-2.16	-2.14	-2.12	-2.10	-2.08
pH -3.11 (H ₂ SO ₄)	-3.20	-3.17	-3.15	-3.13	-3.11	-3.09	-3.07	-3.05	-3.03	-3.01
pH -4.04 (H ₂ SO ₄)	-4.11	-4.09	-4.07	-4.06	-4.04	-4.03	-4.02	-4.00	-3.99	-3.98
Entries of pH shaded in grey have been extrapolated.										

Calibration solutions were produced in the laboratory through the mixing of concentrated sulfuric acid (93 - 98%) into deionized water to meet a specific molal value expected for the solution using a 25 mL pycnometer of known exact volume and a Sartorius TE64-0CE laboratory scale with precision to 0.1 µg (Sartorius AG, Göttingen, Germany) calibrated with a 50 g stainless steel weight with ISO/IEC 17025:2017 certificate of calibration. Exact densities of the calibration solutions interpolated from data tables given from Perry's Chemical Engineering Handbook 8th Ed. (2008) are listed in Table 3.3 along with temperature adjustment for production in a typical room temperature range environment. Temperatures were measured via an OptoTemp temperature probe (Unisense, Aarhus, Denmark) with 0.01 °C accuracy.

Table 3.3 pH calibration solution density table.

pH Calibration Solutions - Density Table							
Molality	% (w/w)	Density at Given Temperature (kg/L)					pH
		20 °C	21 °C	22 °C	23 °C	24 °C	
0.146	1.412	1.00786	1.00759	1.00732	1.00706	1.00679	0.86
0.734	6.716	1.04337	1.04299	1.04262	1.04225	1.04187	0.09
1.497	12.803	1.08598	1.08553	1.08507	1.08461	1.08416	-0.38
2.319	18.530	1.12827	1.12772	1.12715	1.12660	1.12603	-0.79
2.918	22.251	1.15676	1.15613	1.15551	1.15488	1.15426	-1.07
3.657	26.399	1.18939	1.18873	1.18807	1.18741	1.18675	-1.41
4.485	30.550	1.22301	1.22231	1.22161	1.22091	1.22021	-1.78
5.413	34.679	1.25720	1.25648	1.25576	1.25504	1.25432	-2.18
7.622	42.777	1.32742	1.32666	1.32590	1.32514	1.32438	-3.11
9.850	49.137	1.38673	1.38593	1.38513	1.38433	1.38353	-4.04

The typical output response of pH in relation to the pH meter (electrometer) output voltage is shown in Figure 3.7 as measured at 25 °C.

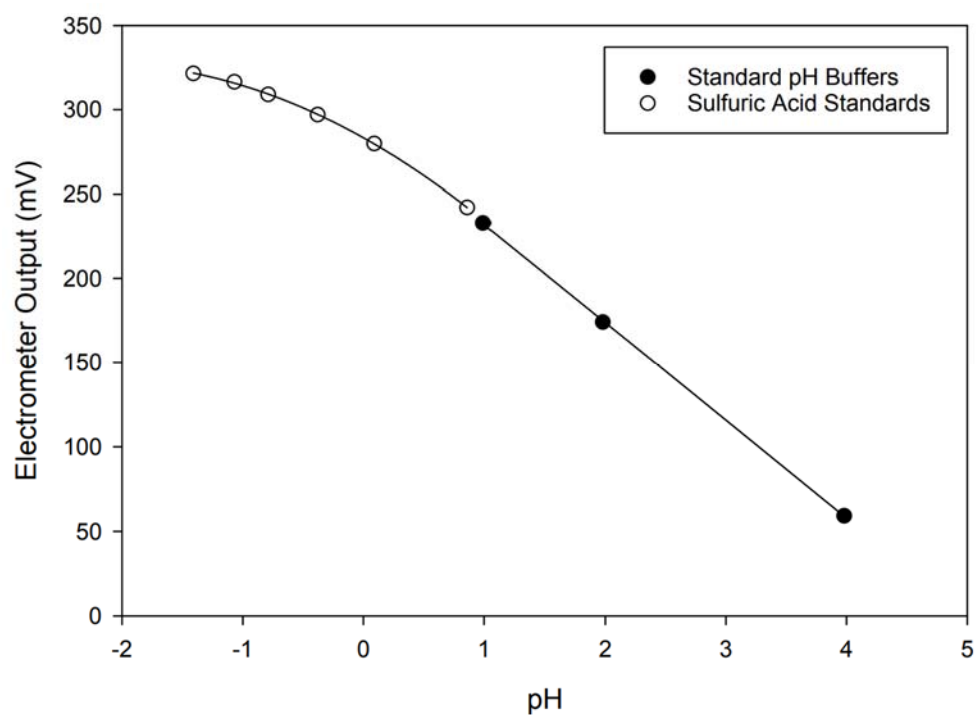


Figure 3.7 Typical output response of pH meter (electrometer) using pH calibration standards.

It has been reported that accurate measurement with the pH probe at elevated temperatures (>40 °C) proves difficult (Penev 2010). A hypothesized reason for this may lie in the electrolyte filling solution, where the exact composition of the electrolyte solutions used within the probe is a trade secret, it is known from the technical manuals that the filling solution is comprised mostly or completely of KCl and is at the saturation point. Similarly to the Ag/AgCl electrode used in the redox probe, keeping the electrolyte solution at saturation is likely important to maintaining electrode stability. Consequently, as temperature elevates, the pH probe filling solution becomes increasingly unsaturated leading to probable instabilities and therefore crystals of KCl were added to the filling solution inside the probe (obtained from evaporating filling solution) to maintain an environment of constant electrolyte saturation within the probe. The pH probe containing crystallized salts was operated up to 50 °C showing no obvious signs of abnormal operation over a span of two hours of measurement and produced a drift of approximately 1 mV from the original calibration.

3.2.10 UV Fluorescence Detection of Algae

Study of algal growth derived from the ferric sulfate broth required some means of comparative measurement of cellular quantity and while cell counting of mobile micro-organisms such as that of *L. ferriphilum* is relatively easy with a microscope and volumetric conversion factor, quantifying biomass concentration for immobilized specimens presents a challenge. For immobilized micro-organisms such as *C. caldarium*, growth occurs in patches or colonies on surfaces and may be trapped within fibrous support structure or microscopic crevices, vibrating the microbes into solution may not give accurate results when counted under the microscope. A technique of UV fluorescence measurement was instead employed taking advantage of the chlorophyll emission peak near 690 nm under the exposure of 365 nm UV-A light to achieve a bulk measurement more suited to surface analysis. UV-A light was generated using a uvBeast V3 ultraviolet flashlight (uvBeast, Portland OR, USA) mounted 20 cm from the sample surface at a 45° angle. Detection of fluorescent intensity was performed using a homemade optical sensor based around the OPT101 self-contained photodiode and transimpedance amplifier IC and telescope optical components were used to manipulate

the light and provide a protective housing. The design and construction of the sensor is illustrated in Figure 3.8 along with the component list in Table 3.4. Incoming light as a beam enters through the front shroud and interacts with a UV/IR rejection dichroic filter that protects the underlying dye filter from unwanted fluorescence, the shroud ensures that the dichroic filter is protected from UV light entering at a high angle of incidence which may bypass the filter due to the nature of dichroic filters to shift the wavelengths of their transmittance profile with respect to incident angle. Visible light then passes through the second dye filter to transmit only red light before entering a convex lens where the light is focused onto the photodiode die of the OPT101 and converted to an output voltage relative to the intensity through the internal transimpedance amplifier circuit. The internal circuitry is electrically simple, requiring only a single 100 M Ω resistor in addition to the IC. The finished circuit board was washed in 4140A Flux Remover (MG Chemicals, Burlington ON, Canada) to remove soldering flux and fingerprint oils which may attract moisture and act as unwanted stray parallel resistance paths leading to offset errors where resistors of very high resistance are used in design.

Table 3.4 Component list of optical fluorescence sensor.

Part #	Component Description	Quantity
1	1.25" \varnothing 23A Red Filter (SVbony)	1
2	1.25" \varnothing UV/IR Cut Filter (SVbony)	1
3	1.25" \varnothing 0.5x Magnification Focal Reducer Lens Type: F9115A (SVbony)	1
4	1.25" \varnothing 20mm Length F-F Extension Tube with 28.5x0.6mm Thread [Obtained from 68° UW 15mm Focal Length Eyepiece (SVbony)]	1
5	1.25" \varnothing 20mm Length M-F Extension Tube with 28.5x0.6mm Thread (Unbranded)	4
6	1.25" \varnothing M End Cap with 28.5x0.6mm Thread (Blue Fireball Technologies)	1
7	OPT101P 8-DIP Monolithic Photodiode Transimpedance Linear Amplifier (Texas Instruments)	1
8	8-Pin DIP Socket (TE Connectivity AMP Connectors)	1
9	100 M Ω 1% Resistor 2.50mm x 6.00mm Axial (Stackpole Electronics Inc.)	1
10	1m Length 26AWG 3.99mm Jacket \varnothing 3-Wire Cable (Tensility International Corp.)	1
11	Double Side Protoboard PCB at least 10x10 Holes (Unbranded)	1
12	26mm \varnothing Painted Washer Plate with Mounting Holes and 8mm \varnothing Central Hole (Custom Made)	1
13	M3 20mm Length Brass Spacer (Unbranded)	2
14	M3 Phillips Panhead Screw 12mm Length Below Head (Unbranded)	4
15	M3 Nut (Unbranded)	2

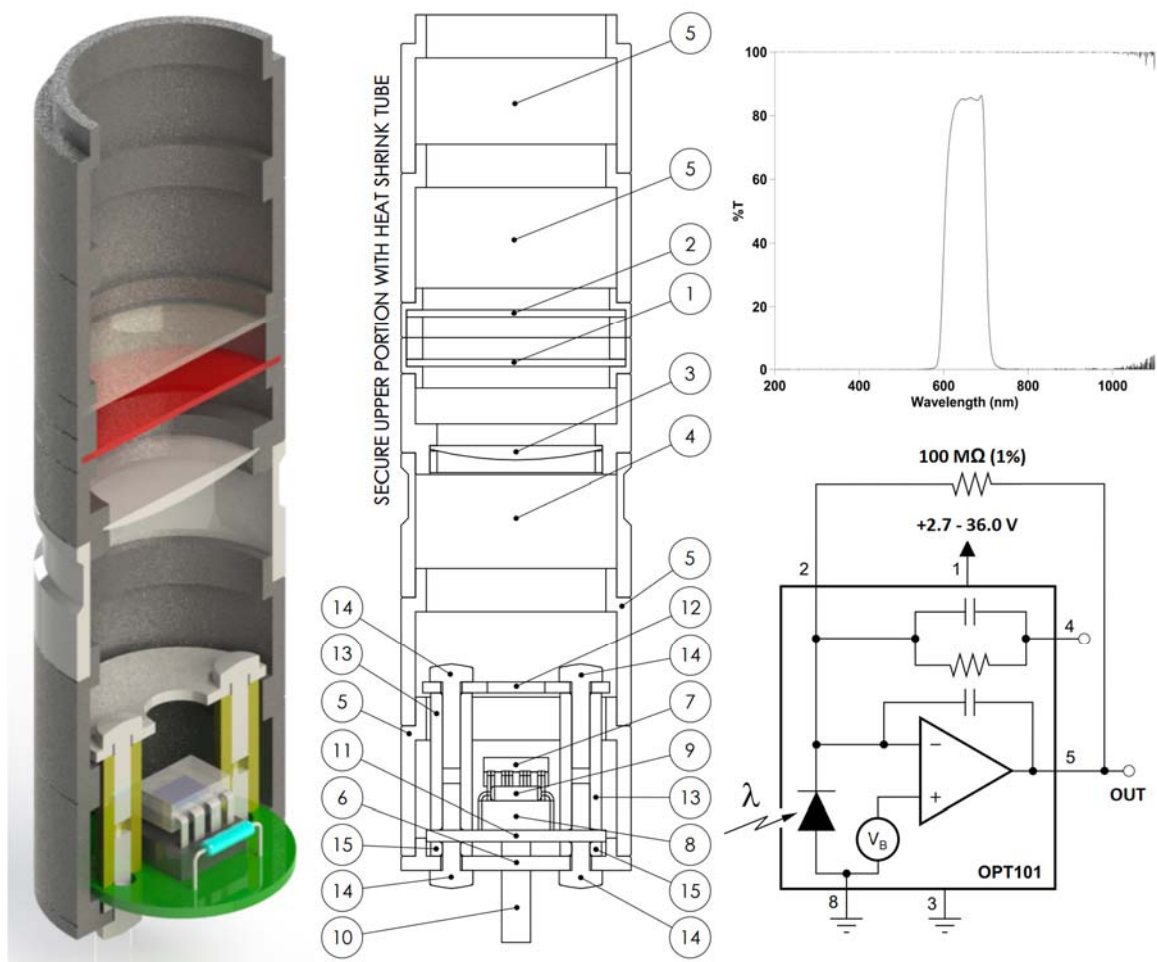


Figure 3.8 Design and construction of optical fluorescence sensor.

Exposure of the algae to high intensity UV-A light will cause a temporary saturation of the electron transport chain within the chloroplasts and the observed fluorescence will quickly diminish, therefore readings must always be taken as soon as the sample is illuminated on the first attempt to acquire data of any relevance. The typically encountered emission intensity profile of a sample over time is seen in Figure 3.9. The characteristic fluorescence decay rate can be used as an additional indicator of the presence of viable chlorophyll containing cells helping to set the result apart from an erroneous reading produced by some other fluorescent foreign material.

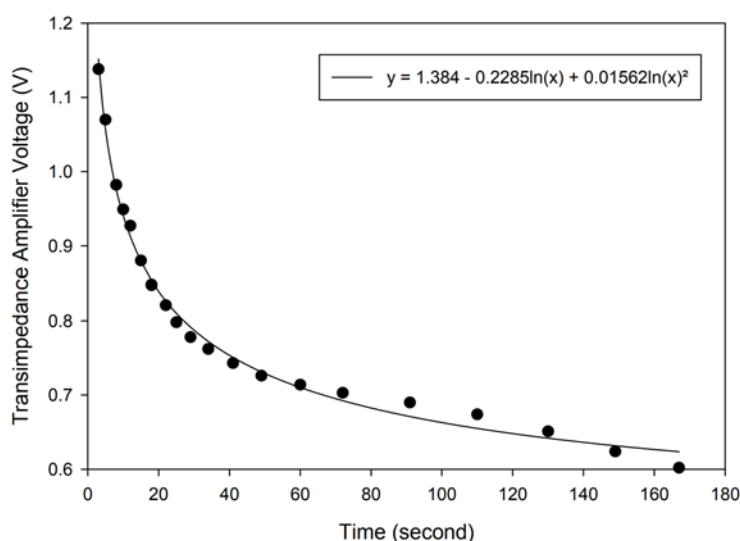


Figure 3.9 Alga fluorescence decay curve.

3.3 Experimental Design

3.3.1 Benchtop Scale BioGenerator

Preliminary studies were conducted in a benchtop scale bioreactor having a square profile with a riser to downcomer cross-sectional area ratio of 1:2 based on previous work suggesting an optimal mass transfer (Drandev et al. 2016). The unit was constructed of transparent acrylic having a total height of 90 cm with internal riser dimensions of 2.2 by 4.4 cm and downcomer dimensions of 4.4 by 4.4 cm with an operating volume of 2.2 L. The unit was fitted with a stainless-steel mesh lid on the top to allow air to escape, air supply was controlled using a Gilmont B9500 rotameter (Thermo Fisher Scientific, Waltham MA, USA). The downcomer was filled with 2-inch polypropylene glass-filled

Jaeger Tri-Packs (Fabco Plastics Wholesale Ltd., Maple ON, Canada) spheres with a geometric surface area of $158 \text{ m}^2/\text{m}^3$, 93.5% void space, and bulk density of $67 \text{ kg}/\text{m}^3$. Packing was placed in an ordered configuration of one whole sphere followed by a sphere cut into quarters and fitted to the inside corners of the downcomer to act as a microbial biofilm support. Iron ratio of the bioreactor broth was monitored by a redox probe assembly (Section 3.2.4), DO concentration was monitored with a polarographic probe (Section 3.2.6), and data was recorded with a camera (Section 3.2.1). Make-up water was provided to the bioreactor through a homemade level controller to counter the effects of evaporation losses over time. The bottom half of the bioreactor assembly was submerged into a heating bath controlled by a DC 10 water heater (Thermo Fisher Scientific, Waltham MA, USA) to maintain an internal temperature of $40 \text{ }^\circ\text{C}$. A fuel cell system comprised of two PEM cells, wired in series electrically and chemically fed in parallel, was operated off a recirculation loop of broth extracted from the bioreactor with a 7521-50 peristaltic pump (Thermo Fisher Scientific, Waltham MA, USA). Hydrogen gas (99.99% purity) was fed to the cells on a separate recirculation loop powered by a DOA-V152-AA vapor diaphragm pump (Gast Manufacturing Inc., Benton Harbor MI, USA) and supplied from a compressed gas cylinder (Linde Canada Inc., London ON, Canada). A glass Allihn condenser fed with chilled water from a Polystat 6-Liter heating and cooling bath (Cole-Parmer, Vernon Hills IL, USA) was used to condense and remove water from the hydrogen stream where the water was fed to an oil covered water trap that allowed the water to sink below the oil and prevent it from evaporating back into the hydrogen gas. Each fuel cell was constructed from two 5 by 5 cm graphite conduction plates containing a serpentine pathway for chemical flow on the front sides with the back sides in contact with a 1 mm thick copper collector plate and held together with $\frac{3}{4}$ inch polycarbonate compression plates with four bolts at the corners. The anodes were cut to 4 by 4 cm and made from ELAT LT 250EWSI platinized woven-web carbon felt (BASF, Iselin NJ, USA) with a platinum loading of $500 \text{ mg}/\text{cm}^2$ while the cathodes were also cut to 4 by 4 cm and made of Sigratherm graphite felt (SGL Carbon, Wiesbaden, Germany) at an uncompressed thickness of about 3 mm. A 5 by 5 cm piece of Selemion HSF proton exchange membrane (AGC Engineering, Asahi, Japan) was placed between the carbon felts and sealed to the graphite conduction plates with silicone gaskets. A Chroma 63106

DC electronic load (Chroma Systems Solution Inc., Lake Forest CA, USA) operated in constant current mode was used to monitor the cell voltage and control the power draw from the cells, subsequently regulating the ferrous iron production to the bioreactor in the process. The apparatus was configured for operation in two schemes, as an airlift bioreactor using a Teflon sparger tube containing ten 2 mm diameter holes mounted downwards (Figure 3.10), as well as a trickling bed bioreactor with unsubmerged height of 55 cm (Figure 3.11).

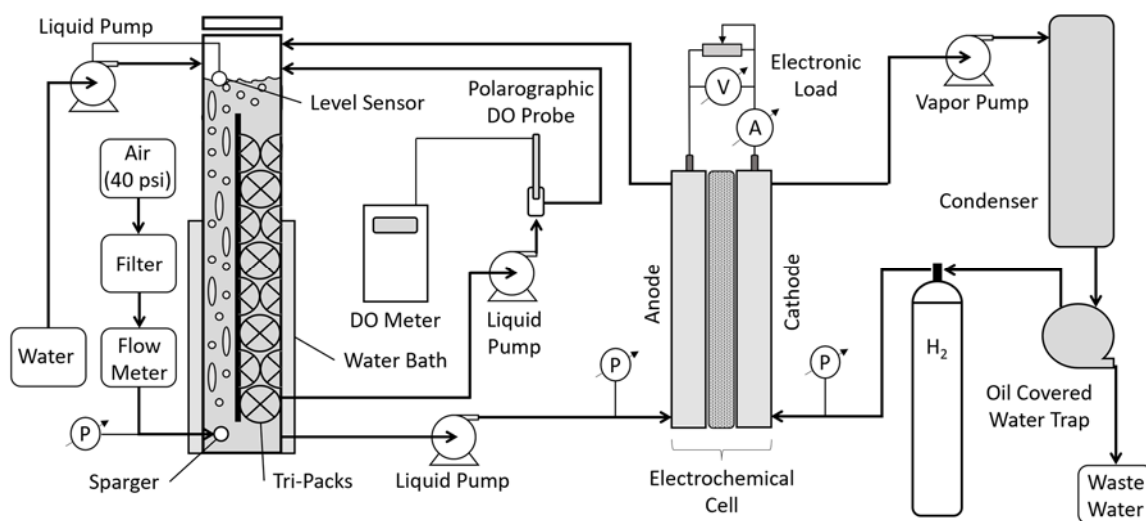


Figure 3.10 Benchtop airlift style BioGenerator.

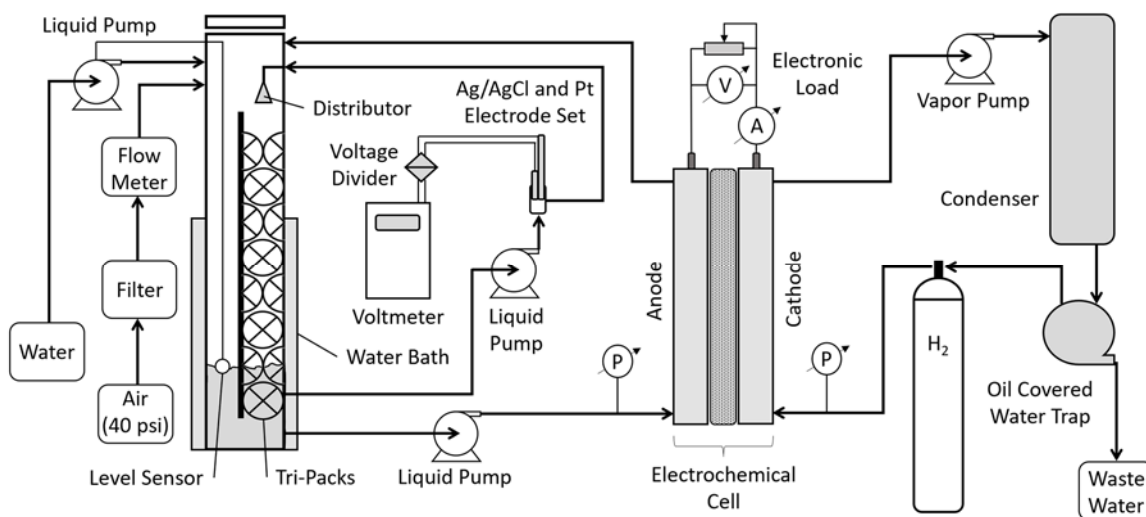


Figure 3.11 Benchtop trickle bed style BioGenerator.

3.3.2 Semi-Pilot Scale BioGenerator

Laboratory scale-up of the BioGenerator from benchtop testing was conducted with a 600 L stainless-steel semi-pilot scale segmented airlift bioreactor. The bioreactor contained five separate airlift segments each holding approximately 120 L with 3 cm weirs to allow drainage from one segment into the next along the tops (Figure 3.12). Riser sections measured 90 cm long and 5.5 cm wide with a liquid depth to the bottom of 70 cm. A random orientation packed bed of 1-inch polypropylene glass-filled Jaeger Tri-Packs (Fabco Plastics Wholesale Ltd., Maple ON, Canada) spheres with a geometric surface area of $280 \text{ m}^2/\text{m}^3$, 90.0% void space, and bulk density of $99 \text{ kg}/\text{m}^3$ was situated in the downcomer having a bed dimension of 90 cm long and 14 cm width with a height of 55 cm. A Teflon tube acting as the sparger was mounted at the bottom of each riser having an external diameter of 1.5 cm and 75 cm length with 300 holes of 1 mm diameter drilled along the axis pointing downward. Air supply to the spargers was taken from a 275 kPa (40 psi) compressed air spigot in the laboratory and flow regulated with a Brooks 1110-08H2G1F rotameter (Emerson Electric Co., Markham ON, Canada) with a pressure gauge mounted at the outlet to correct for changes in pressure. The bioreactor was heated with a Julabo HE-Basis heated water bath (Julabo USA Inc., Allentown PA, USA) with water circulated through a stainless-steel pipe loop mounted in the riser section above the sparger and the exterior walls of the bioreactor were insulated with 5 cm thick Styrofoam sheathing to retain heat. A DO probe assembly (Section 3.2.7) was placed at the top of the tallest airlift segment to draw broth for sampling which was also fed to a redox probe assembly (Section 3.2.4) to monitor iron ion conversion. Liquid recirculation through a PEM fuel cell was achieved with a 75226-12 centrifugal chemical pump (Cole-Parmer, Vernon Hills IL, USA) and flow regulated at the output with a ball valve. The pumped broth was passed through a corrugated $30 \text{ }\mu\text{m}$ sediment filter to protect the upstream fuel cell from clogage in the carbon felt and monitored with a pressure gauge. The fuel cell (Section 3.3.4) was short circuited with a copper wire to act as a ferrous iron generator in order to maintain long-term biological activity within the bioreactor.

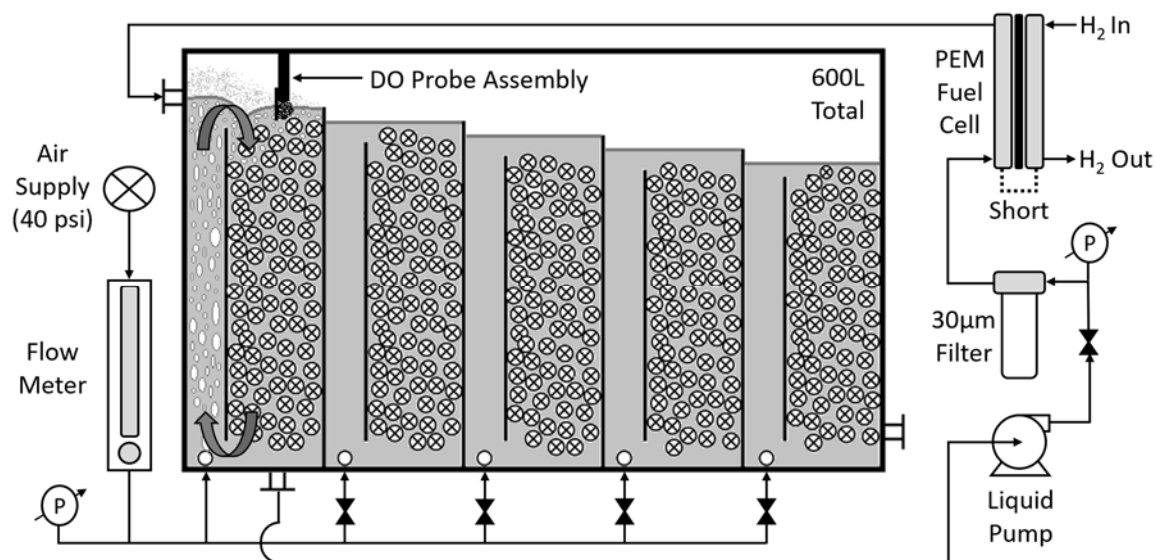


Figure 3.12 Semi-pilot scale BioGenerator.

Hydrogen gas was provided by an electrolyser (Section 3.1.3) and circulated with a PU1823-N838.0-12.05 twin diaphragm pump (KNF, Trenton NJ, USA) through the PEM fuel cell and an AHP-300CP thermoelectric cooling plate condenser (TECA, Chicago IL, USA) to remove water from the stream (Figure 3.13). Condensate collected from the hydrogen gas stream was passed through a small packed bed of copper pellets to chemically reduce the ferric ions and produce a less chemically aggressive discharge to be handled by a Bekomat electronically controlled condensate drain valve (Beko Technologies GmbH, Neuss, Germany) into a waste receiving bottle. The cooling plate, diaphragm pump, and condensate drain valve were all powered by a PMT-24V350W1AK power supply (Delta Electronics, Taipei City, Taiwan). A pressure gauge mounted at the outlet of the gas diaphragm pump was used to adjust the system pressure to approximately 35 kPa (5 psi) and monitored to ensure enough back pressure was applied to the proton exchange membrane inside the fuel cell to counteract the liquid pressure on the opposing side while also ensuring the pressure did not reach above 55 kPa (8 psi) to protect the membrane from failure by ballooning, pin holing, or rupturing.

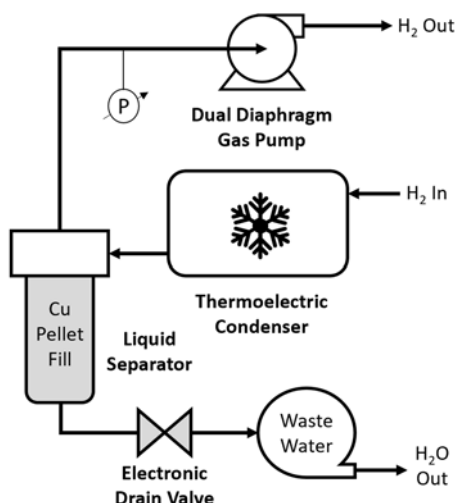


Figure 3.13 Semi-pilot scale hydrogen gas circulation loop.

3.3.3 Pilot Scale BioGenerator

Final scale-up of the BioGenerator from pilot-scale testing was conducted with a 10000 L stainless-steel segmented airlift bioreactor similar in design as the semi-pilot scale version. The bioreactor contained five separate airlift segments each holding approximately 2000 L with 7 cm weirs to allow drainage from one segment into the next along the tops (Figure 3.14). Riser sections measured 200 cm long and 18 cm wide with a liquid depth to the bottom of 155 cm. A random orientation packed bed of 2-inch polypropylene glass-filled Jaeger Tri-Packs (Fabco Plastics Wholesale Ltd., Maple ON, Canada) spheres with a geometric surface area of $158 \text{ m}^2/\text{m}^3$, 93.5% void space, and bulk density of $67 \text{ kg}/\text{m}^3$ was situated in the downcomer having a bed dimension of 200 cm long and 43 cm width with a height of 110 cm. The bioreactor was operated outdoors and clad with two layers of 37 mm thick Styrofoam sheathing with a 13 mm layer of fiberglass batt sandwiched between them. Air was provided to the bioreactor through a sparger tube mounted along the bottom of the riser using a G-BH1 regenerative blower (Elmo Rietschle, Schopfheim BW, Germany) regulated by a ball valve at the outlet side. A Brooks 12-1110 rotameter (Emerson Electric, Markham ON, Canada) was used to monitor air flow to the bioreactor and was calibrated using a DAM100B vane anemometer (Dawson Tools Inc., Diamond Bar CA, USA) mounted to the blower intake along with the known cross-sectional area to determine the flow rate. Air pressure at the

blower outlet was monitored with a Magnahelic 2080 differential pressure gauge (Dwyer Instruments, Michigan City IN, USA). The bioreactor was heated with a Julabo HE-Basis heated water bath (Julabo USA Inc., Allentown PA, USA) with water circulated through a stainless-steel shell and tube heat exchanger on the shell side and bioreactor broth passed through the tubes. A DO probe assembly (Section 3.2.7) was mounted at the top of the lowest airlift segment.

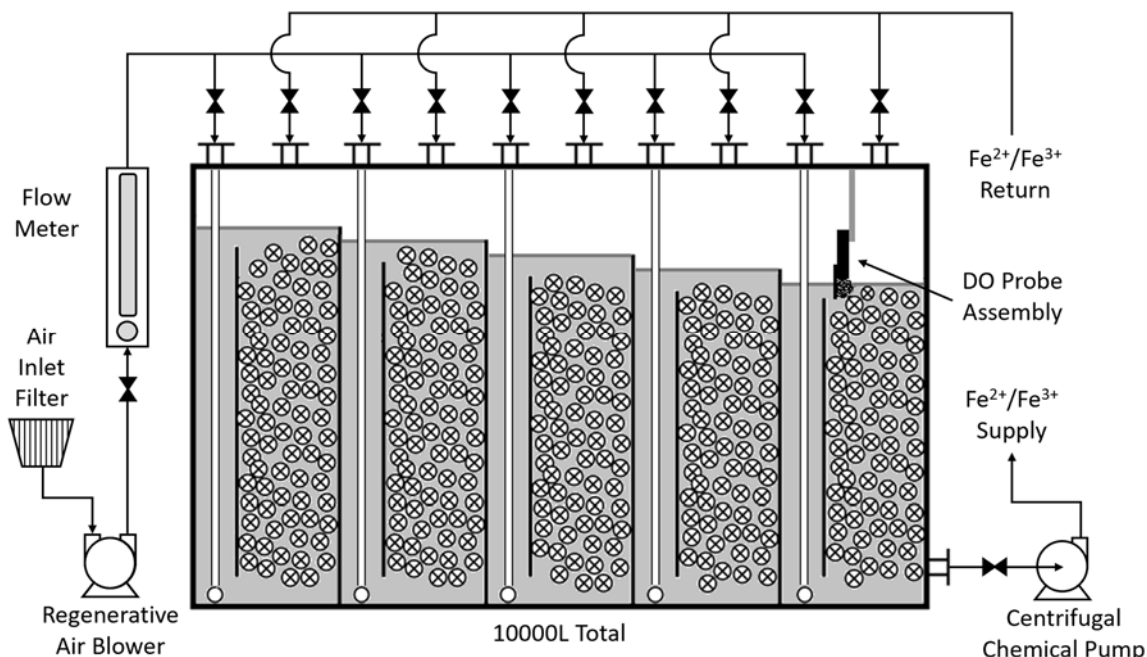


Figure 3.14 Pilot scale BioGenerator.

Liquid recirculation through a PEM fuel cell bank was achieved with a 75226-12 centrifugal chemical pump (Cole-Parmer, Vernon Hills IL, USA) and flow regulated at the liquid inlets of the individual fuel cells with SSB0.50 flow regulators (Calefactio Solutions Inc., Blainville QC, Canada). Liquid broth was passed through a 200 μm sock filter to capture entrained debris and particulate matter to protect the downstream fuel cells from clogage. A redox probe assembly (Section 3.2.4) was placed after the filter to monitor iron ion conversion and was flow regulated with a hosecock clamp. A bank of four PEM fuel cells (Section 3.3.4) was wired in series electrically and fed in parallel with broth from the bioreactor and the electric output was regulated with a Chroma 63106 DC electronic load (Chroma Systems Solution Inc., Lake Forest CA, USA) operated in

constant current mode. Hydrogen gas from an electrolyser (Section 3.1.3) was circulated through the fuel cell bank (Figure 3.15) using four PU2159-N813.0-3.08 diaphragm pumps (KNF, Trenton NJ, USA) with each pump feeding one individual cell to maintain balanced gas flow. A cooling bath provided by a Polystat 6-Liter heating and cooling bath (Cole-Parmer, Vernon Hills IL, USA) was passed through a stainless-steel tube and shell heat exchanger to provide a means of condensing water in the hydrogen stream with the coolant passed through the shell side. Condensed water in the hydrogen stream was removed with a 1-LDC free-floating lever drain trap (Armstrong Steam and Condensate Group, Three Rivers MI, USA) and the system pressure was regulated at 35 kPa (5 psi) with a pressure relief valve venting excess hydrogen to the atmosphere.

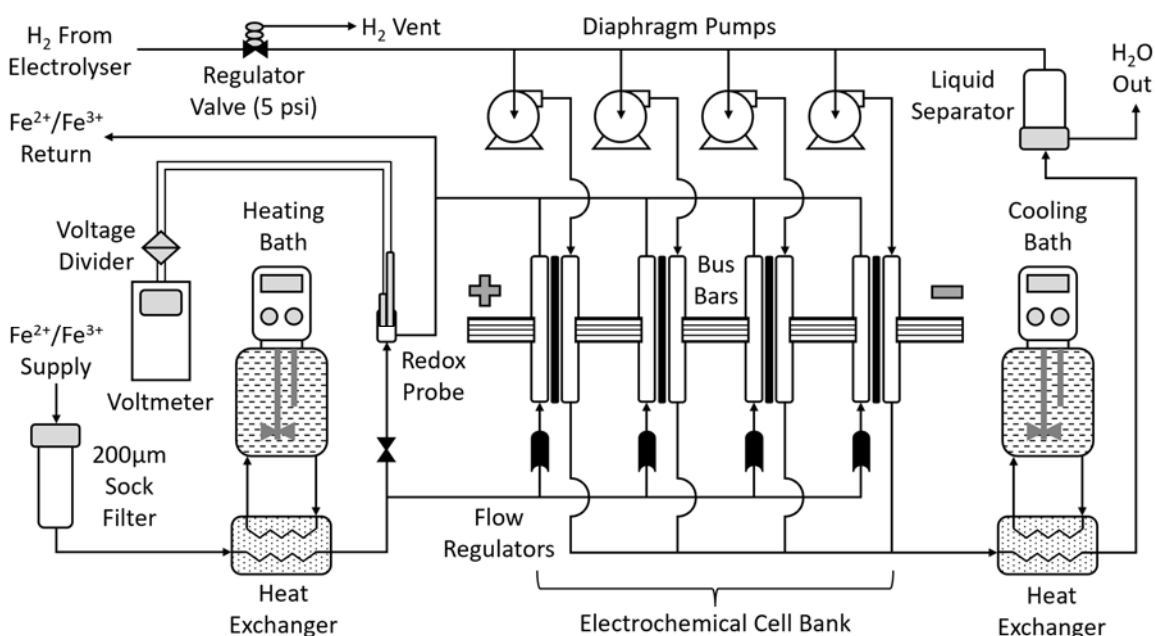


Figure 3.15 Pilot scale fuel cell bank and gas/liquid circulation loops.

3.3.4 Fuel Cell Stack

Hydrogen fuel cells for the semi-pilot and pilot scale BioGenerator were custom built single-cell units using Selemion HSF proton exchange membranes (AGC Engineering, Asahi, Japan) for ion flow. Cathodes were cut from Sigratherm graphite felt (SGL Carbon, Wiesbaden, Germany) at a thickness of approximately 5 mm while the anodes were cut from ELAT LT 250EWSI platinized woven-web carbon felt (BASF, Iselin NJ,

USA) with a platinum loading of 500 mg/cm^2 , both felts were cut to a size of 20.0 by 22.5 cm providing an active area of 450 cm^2 per cell. Carbon felts and proton exchange membrane were assembled using a series of four thin silicone gaskets (0.25 mm thickness) for gas/liquid sealing and two graphite sheet gaskets (0.50 mm thickness) to help provide a frame to attach the proton exchange membrane for easier handling due to its tendency to scroll up in the presence of moisture. The stack up of membrane, electrode felts, and gaskets is depicted in Figure 3.16.

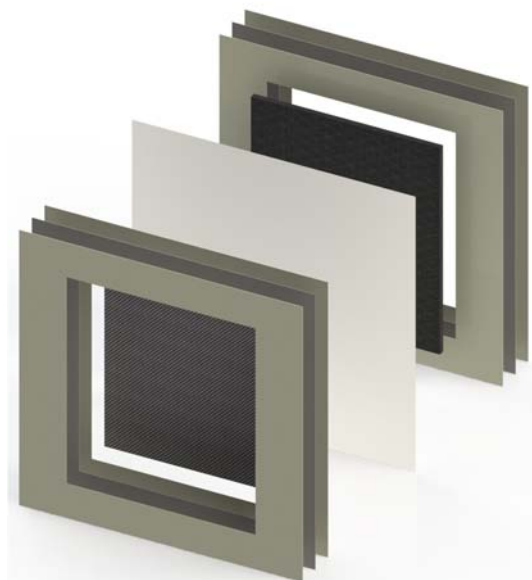


Figure 3.16 Fuel cell stack-up of electrode felts, membrane, and gaskets.

Liquid and gas flow across the electrode felts was achieved using 12" by 12" graphite conduction plates using a parallel groove flow field cut into the front side with three entry and exit points per plate. The back sides of the graphite conduction plates were pressed against a 12" by 12" copper collector plate and a film of conductive carbon paste was applied in between the interface to help improve electrical contact and prevent possible intrusion by electrolytes that result in surface corrosion and lead to a reduction in conductivity. A PVC plastic distributor plate was used to anchor stainless-steel pipe nubs for the gas and liquid entry using a feedthrough gasket on the sides of the copper collector plate to seal against the underside of the graphite conduction plate entry and exit holes. The entire assembly was clamped together with two 14" by 14" painted $\frac{3}{8}$ " thick carbon-steel compression plates held together with twelve $\frac{3}{8}$ "-16 stainless steel bolts with

a copper based anti-galling paste applied to the threads. A partial view of the graphite conduction plate and underlying components is seen in Figure 3.17.

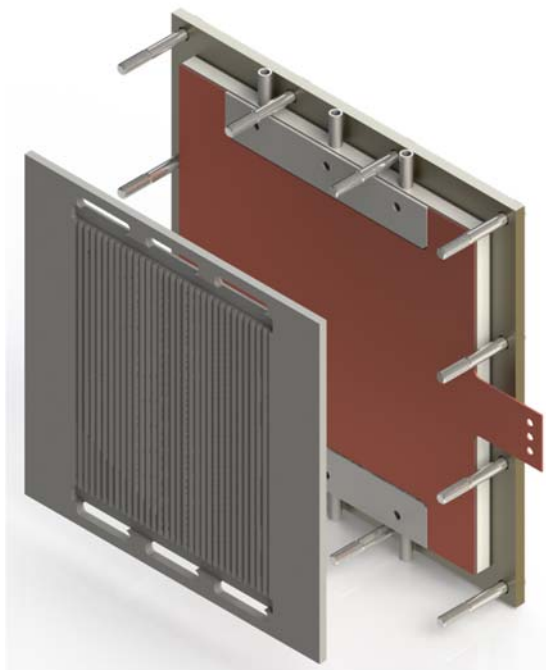


Figure 3.17 Fuel cell graphite conduction plate and underlying components.

3.3.5 Oxygen Solubility Vessel

Dissolved oxygen solubility determination was conducted within an enclosed 500 mL capacity water jacketed vessel (Figure 3.18) filled with ferric sulfate broth and active microbial culture that was temperature controlled using a Polystat 6-Liter heating and cooling bath (Cole-Parmer, Vernon Hills IL, USA). A magnetic stir plate and stir bar spindle contained within the vessel provided homogenous mixing of the internal contents. Percent air saturation measurements were performed using an optical DO probe and thermal probe (Section 3.2.7) inserted through the upper rubber stopper lid, tapping of the DO probe sleeve with a metal rod helped to clear any adhered bubbles caused from sparging and improved reading quality. A sintered powder stainless steel sparge head was used to administer compressed air or nitrogen gas to the liquid contents of the vessel to vary the percent air saturation levels from 0 to 100 percent as needed with a 10A3135N rotameter (Fischer and Porter, Toronto ON, Canada). An additional gas inlet connection

through the upper stir bar rod support in the lid allowed the introduction of nitrogen gas into the headspace area to blanket and protect the liquid surface from oxygen intrusion during operation where needed. The presence of a small rubber stoppered addition cup at the liquid return line of the vessel provided an entry point to introduce ferrous sulfate solution with a pipettor when necessary. Coupling of the vessel to the redox probe assembly (Section 3.2.4) allowed precision monitoring of the iron ion ratio within during operation. In addition to oxygen solubility measurements the apparatus was found to be useful for measuring the biooxidation rate of the microbes under controlled conditions.

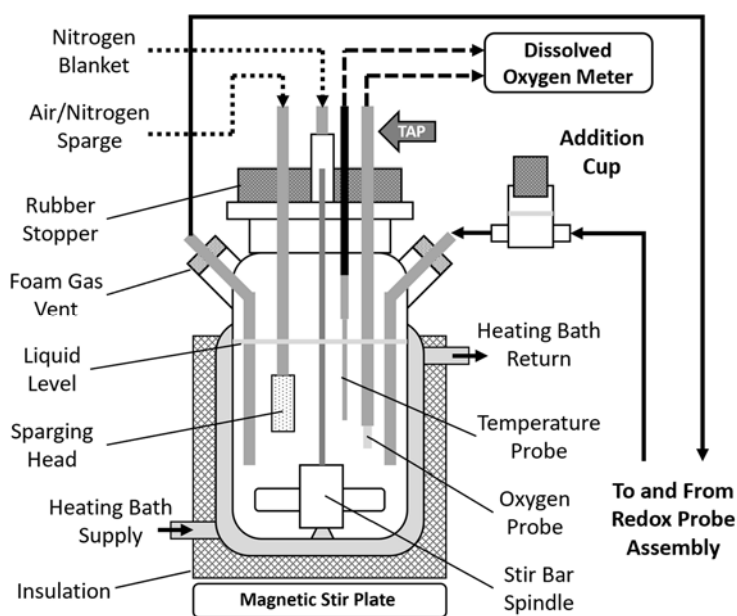


Figure 3.18 Oxygen solubility determination vessel.

3.3.6 Algae Culture Dishes

Growth of algal specimens was completed inside 30 mL Falcon 3013 tissue growth containers (Becton Dickinson Labware, Lincoln Park NJ, USA) containing a 4.0 by 6.5 cm fiberglass ribbon strip to act as a growth surface held to the bottom using stainless-steel compression springs placed in the inside corners. Culture dishes were filled with 15 mL of nutrient solution (Section 3.1.1) acidified with sulfuric acid as needed and inoculated with 50 μ L of inoculant by a pipettor. A rubber plug stamped from a 1/4" thick sheet of Viton rubber was used to seal the culture dishes and a syringe needle was inserted through the tops of the plugs to act as a small pressure relief vent. Culture dishes

were assembled into a 2 by 5 array inside a homemade growth caddy that contained a neutral white (4000 K) 24-volt star style LED array with a phosphor diameter of 18 mm (Figure 3.19) mounted above each dish. Growth caddies were placed inside a MAXQ 4000 incubator (Thermo Fisher Scientific, Waltham MA, USA) set at a temperature of 40 °C with agitation set to 25 rpm.



Figure 3.19 Neutral white (4100 K) LED array.

The walls of the growth caddy were blackened to reject external light and prevent internal reflections of light so that the light intensity could be calibrated and delivered onto the fiberglass ribbon in a controlled amount. Calibration of the light intensity was performed using an SM206 solar power meter (Bestone Industrial Co., Shenzhen GD, China) attached to a cover bracket designed to hold the meter at the same distance (45 mm) from the LED as the fiberglass ribbon inside the culture dish. The LEDs were driven with a constant current circuit based around the LM317 regulator as seen in Figure 3.20. Measurement of the algal content was completed by breaking open the container, placing the fiberglass ribbon onto a sheet of UV absorbing carbon felt, and using a UV fluorescence sensor (Section 3.2.10) mounted 10 cm above the sample to quantify the result as a voltage reading from the transimpedance amplifier. The voltage reading could then be converted to an equivalent cell count value through a conversion factor developed with the use of a hemocytometer and microscope.

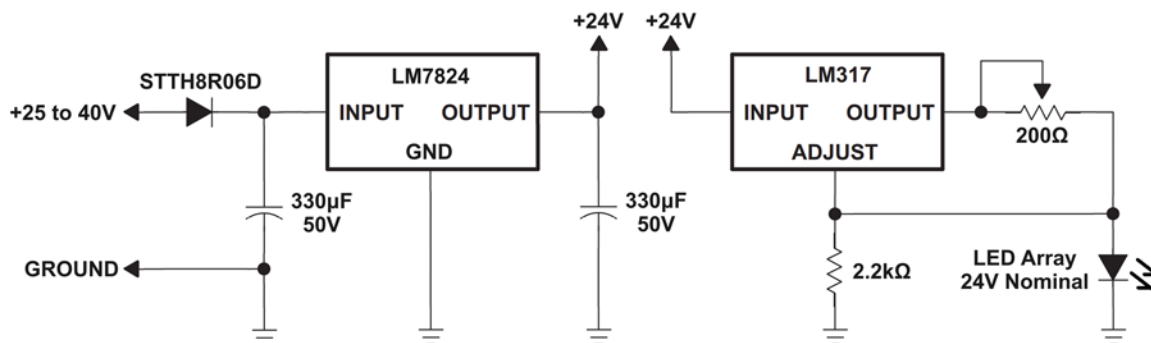


Figure 3.20 Growth caddy lighting circuit (note: right side LM317 circuit repeated x10).

3.3.7 Jarosite Production Vials

Measurement of jarosite growth deposits in BioGenerator broth was completed using glass test tubes containing 10 mL of broth acidified by increments of 0.05 pH units and capped with a rubber stopper. The vials were placed into a MAXQ 4000 incubator (Thermo Fisher Scientific, Waltham MA, USA) set at a temperature of 40 °C with agitation set to 25 rpm and left to develop jarosite scale on the interior walls for a period of six months. Using a laboratory scale, the before and after weight of the glass vials was used to determine the dry weight of jarosite accumulation. Jarosite production was generated by non-biological means as ferrous ions and aeration needed to support iron oxidizing microbes were not present.

Chapter 4

4 Improvements to the Measurement and Monitoring of the Broth

The scale-up of the BioGenerator will need to take into consideration instrumentation and monitoring of the bioreactor broth conditions which at a laboratory scale can be done with commercially available means but ignores the associated costs of the equipment and the rapid wear and tear caused by the chemically aggressive broth. It is of high importance to monitor the pH and the ferric and ferrous ion content of the broth to ensure day to day operations can be maintained. Current methods of measure rely heavily on wet chemistry and electrochemistry methods that are acceptable for periodic laboratory analysis but are less desirable for situations requiring continuous automated measurements such as recording bioreactor dynamics and industrial control systems. The most prominent methods of iron concentration and pH measurement are:

- Colourimetric indicator dyes
- Redox titration
- Redox potential electrodes
- Glass membrane pH electrodes

All four methods listed carry drawbacks with their use, especially in terms of time and cost. Where wet chemistry methods such as colourimetric indicator dyes and potentiometric titrations are concerned, the methods are prone to human error during handling and dilution of samples and therefore require multiple runs to ensure no significant errors are present. Setup times are also required with wet chemistry to correctly measure and mix reagents for testing where most methods can only measure one type of iron ion at a time. In addition, wet chemistry methods require a trained person to correctly perform the measurements, adding to costs. Solution pH can not be determined with wet chemistry acid-base titrations in this case since the solution contains strong acids and weak acids in varying levels of dissociation. Continuous measurement of redox potential and pH with electrodes in such high ionic strength environments is not

advisable due to ionic diffusion and the potential blockage of the ionic junctions by hydroxides or insoluble jarosite deposits caused by the pH differential which will eventually permanently damage the expensive probes.

A new method of measure involving the in-situ determination of both ferrous and ferric ion concentrations as well as pH levels simultaneously using colourimetric methods on the bioreactor broth is explored as a means of providing a simple cost-effective solution for applications in industrial settings. The procedure is based on the absorption measurement (\bar{A}) of non-turbid iron sulfate solution in a standard disposable cuvette at three wavelengths (487 nm, 520 nm, and 980 nm) as well as the accurate measurement of solution temperature followed by mathematical conversion of these inputs to the pH, ferrous ion concentration, and ferric ion concentration. It should be stated that the following work was not successful in fulfilling the goal, it did however provide a better understanding of the absorption properties of the iron sulfate, importantly determining that predictable behaviours are present. The work was useful as a foundation to develop measurement techniques and revise the strategy in the modelling. The absorbance characteristics were found to be quite convoluted and as such the assembled model is in fact derived from several sub-models produced using trial and error methods, therefore some decisions in the production of the overall model may appear illogical as presented.

4.1 Model Development

The basis of the model relies on the fact that the absorption characteristics of the ferric ion changes in response to the pH, temperature, and ferric ion concentration of the solution. The absorption spectrum of the ferrous ion was found not to be affected by pH or temperature, and other ions in solution such as those of growth salts demonstrate no detectable absorption in the visible and near infrared band. The ferric ion may therefore be considered a potential pH indicator if the behaviour can be modelled adequately, while the overall concentration of ferric and ferrous ions might be resolved concurrently through absorption at specific wavelengths. A visual example of the ferric ion absorbance response at differing pH levels is seen in Figure 4.1 and occurs within the range of pH the BioGenerator operates at. The creation of a base model using a 10 g/L ferric ion solution was attempted where correction factors might then be applied to equate values back to it.

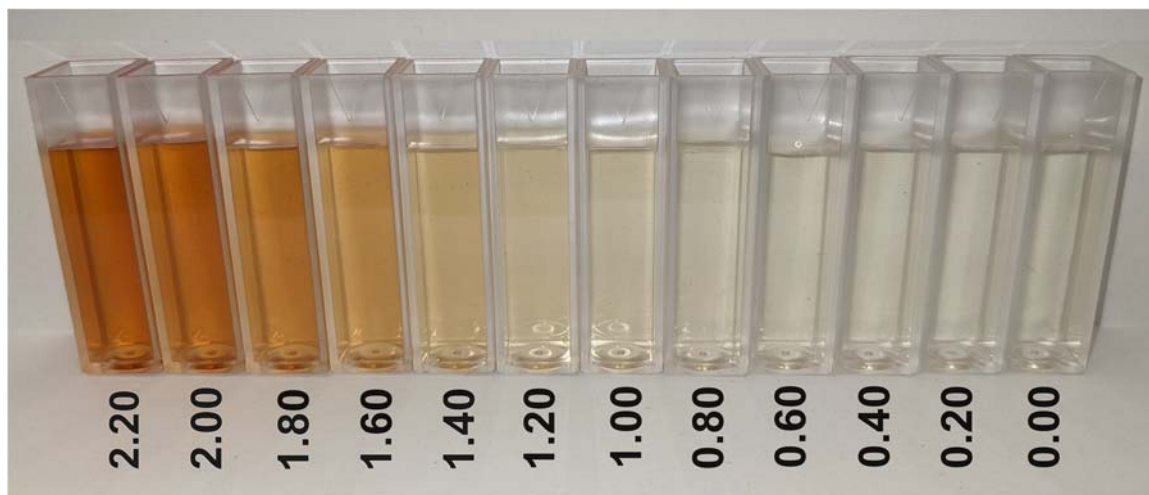
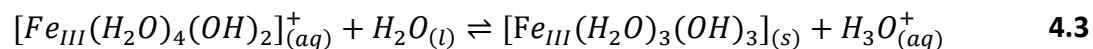
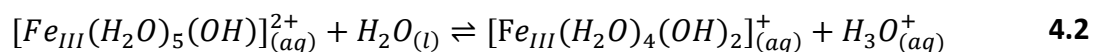
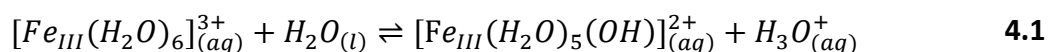


Figure 4.1 Samples of ferric sulfate ($\sim 10 \text{ g}_{\text{Fe}^{3+}}/\text{L}$) at varied acidity from pH 2.20 to 0.00 at 25 °C.

The observed colour changes are likely as a result of shifts in the equilibria reactions between the ionization states of the ferric hexaaqua complexes that act as weak acids given by Equations 4.1, 4.2, and 4.3. The hexaaqua complexes of iron are of importance to the visible colour of the solutions as the ligands surrounding the iron atom influence the band gap of its 3d orbital electrons and the frequency range of photons that may be absorbed. In addition, ferric ions may also dimerize with one another forming larger complexes such as the dihydroxo and μ -oxo forms in addition to others which have their own unique absorption profiles (Zhu et al. 2013). Sulfation of the complexes further complicates the equilibrium chemistry where water molecules may be displaced by sulfate ions as well.



The first major obstacle in development of the model was finding a way to easily distinguish between the ferric and ferrous ions that coexist in solution. Observing the absorbance spectra of the ions separately and mixed it was found that measurement of the

ion absorbance can take place within two distinctive windows that show high selectivity for only one of the two ions as seen in Figure 4.2. Ferrous ions are found to maintain a constant molar extinction coefficient (ϵ) regardless of temperature or pH and can be best measured with infrared light, however this value varies significantly for ferric ions which are best measured with blue-green light. The exact wavelengths of light chosen for absorption measurements were 980 nm, 520 nm, and 487 nm which correspond with the outputs of commercially available laser diodes.

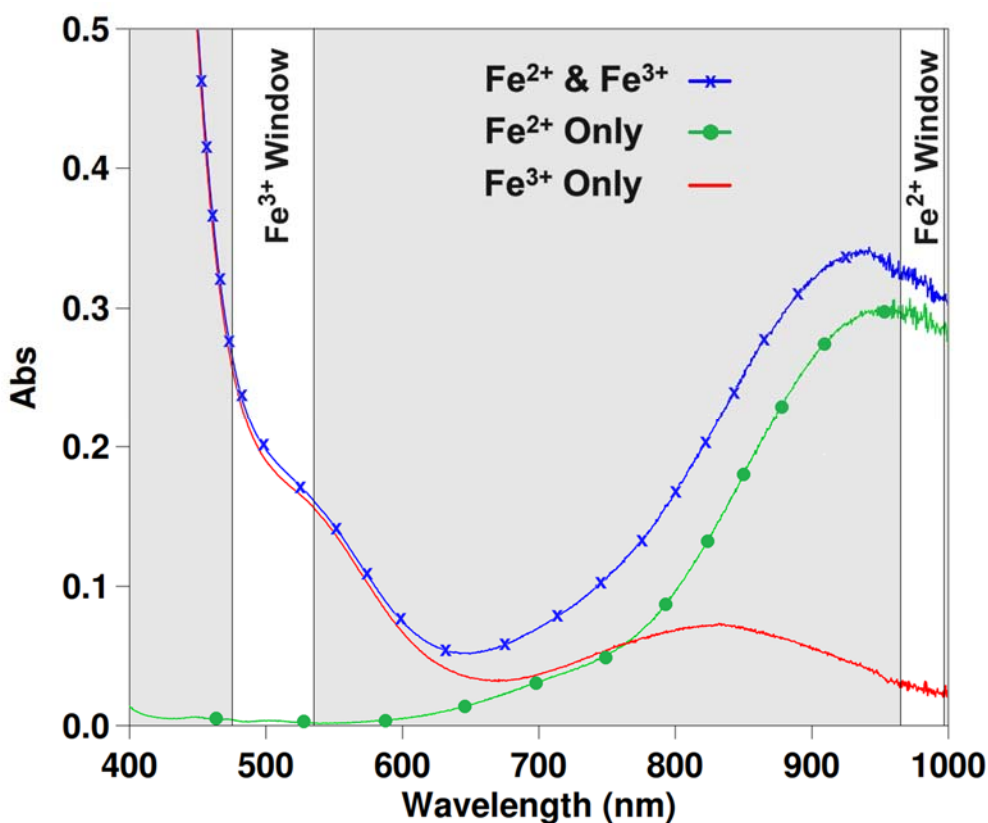


Figure 4.2 Absorbance windows in mixed and separate aqueous solutions of ferrous and ferric sulfate.

Given the niche application of the modelling of iron sulfate solution absorbance, no previous published research was found as a guide to the development of a model. It had been observed that the behaviour of the ferric ions followed a cubic function within the ferric window and that the shape of the curve changes in relation to the ferric ion concentration, temperature, and pH. It was decided to target this as a potential input

parameter in the form of a ratiometric measurement. Some literature was found expressing the use of ratiometric absorbance measurements in practice for instance in quantifying the purity of DNA and RNA samples with UV light (260/280 nm) (Glasel 1995) as well use in some applications in drug purity testing with a Q-absorbance ratio method (Hirt et al. 1954, Singh et al. 2012). The models specified in the literature were not useful in this application and an alternate technique was formulated introducing a new variable termed the extinction index (α).

4.1.1 Extinction Index Model Development

The extinction index formulates a single variable out of the absorption measurements taken at 520 nm and 487 nm by taking the difference between the two values and dividing by the average as given in Equation 4.4. The objective of this being to eliminate the factor of the absolute absorbance measurements to produce a variable that is based on the curve geometry proportionality and not related to absolute absorbance measurement as would normally be the case using the Beer-Lambert Law. This was then used as a means of quantifying the value of pH at 25 °C across a selected temperature range (5 – 50 °C) with a temperature correction model applied to the pH value afterwards.

$$\alpha = (\bar{A}_{487} - \bar{A}_{520}) / \left(\frac{\bar{A}_{487} + \bar{A}_{520}}{2} \right) \quad 4.4$$

A series of solutions measured at differing pH and temperature were used to generate a preliminary model of the extinction index behaviour as seen in Figure 4.3. The data collected showed a fair amount of high-frequency noise, attributed to turbidity effects, but overall could be mapped with a high coefficient of determination (0.993 +0.004/-0.012) as a series of cubic functions. The individual trend lines were then meshed with one another by graphing and curve fitting their coefficients (Figure 4.4) to produce a mathematically contiguous model represented as Equations 4.5 – 4.9 along with the coefficients in Table 4.1.

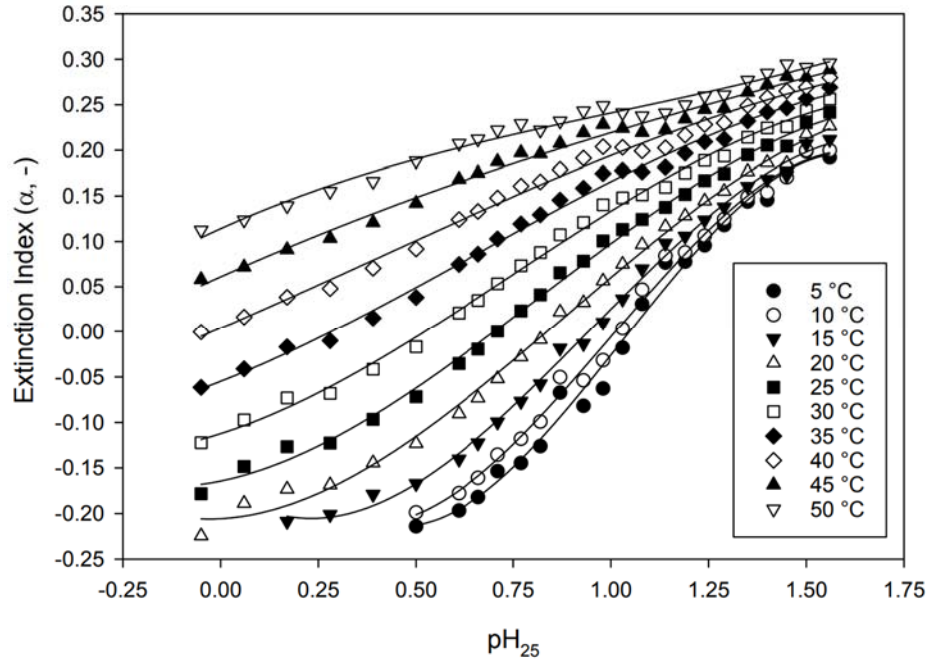


Figure 4.3 Preliminary extinction index model based on measured data.

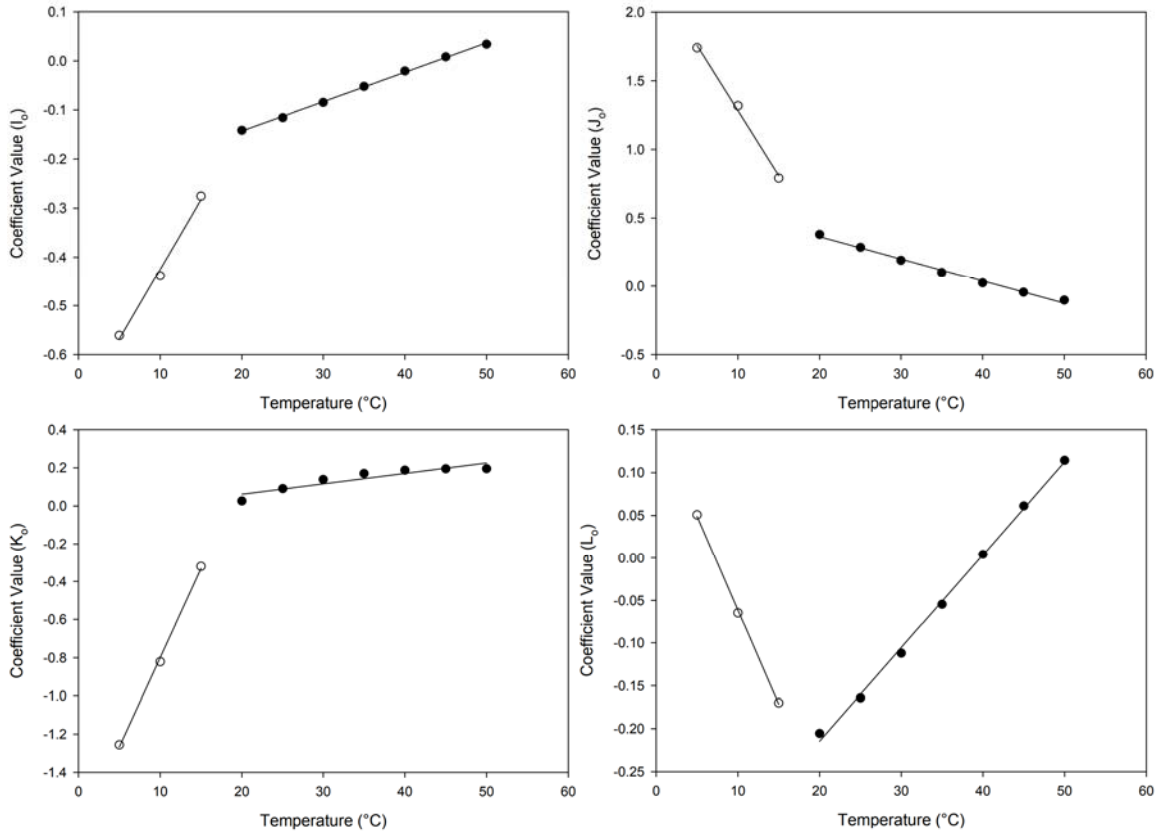


Figure 4.4 Extinction index model coefficient trend lines.

$$\alpha = I_0 pH_{25}^3 + J_0 pH_{25}^2 + K_0 pH_{25} + L_0 \quad 4.5$$

$$I_0 = \left(\frac{I_1 T + I_2}{1 + e^{(T-18.838)}} \right) + \left(\frac{I_3 T + I_4}{1 + e^{-(T-18.838)}} \right) \quad 4.6$$

$$J_0 = \left(\frac{J_1 T + J_2}{1 + e^{(T-18.838)}} \right) + \left(\frac{J_3 T + J_4}{1 + e^{-(T-18.838)}} \right) \quad 4.7$$

$$K_0 = \left(\frac{K_1 T + K_2}{1 + e^{(T-18.838)}} \right) + \left(\frac{K_3 T + K_4}{1 + e^{-(T-18.838)}} \right) \quad 4.8$$

$$L_0 = \left(\frac{L_1 T + L_2}{1 + e^{(T-18.838)}} \right) + \left(\frac{L_3 T + L_4}{1 + e^{-(T-18.838)}} \right) \quad 4.9$$

Table 4.1 Extinction index model coefficients for Equations 4.6 – 4.9.

l ₁	3.2531E-02	J ₁	-1.0540E-01	K ₁	1.0012E-01	L ₁	-2.1061E-02
l ₂	-7.6288E-01	J ₂	2.3681E+00	K ₂	-1.8307E+00	L ₂	1.6953E-01
l ₃	5.9911E-03	J ₃	-1.6300E-02	K ₃	5.4647E-03	L ₃	1.0904E-02
l ₄	-2.6292E-01	J ₄	6.8972E-01	K ₄	-4.7690E-02	L ₄	-4.3262E-01

Since the pH scale changes based on temperature it is necessary to correct for measurements of pH outside the standard pH 7 neutral point scale at 25 °C. Temperature corrections were generated using PHREEQC Ver. 3.7.0 and are described in Section 3.2.9. A pH correction factor (Ψ) can be applied to the extinction index model through Equations 4.10 – 4.13, represented graphically as Figure 4.5, along with coefficients in Table 4.2 once the 25 °C standard pH (pH_{25}) is determined. The final pH of the solution is then given simply as Equation 4.14.

$$\Psi = B_0 T^2 + C_0 T + D_0 \quad 4.10$$

$$B_0 = B_1 pH_{25}^4 + B_2 pH_{25}^3 + B_3 pH_{25}^2 + B_4 pH_{25} + B_5 \quad 4.11$$

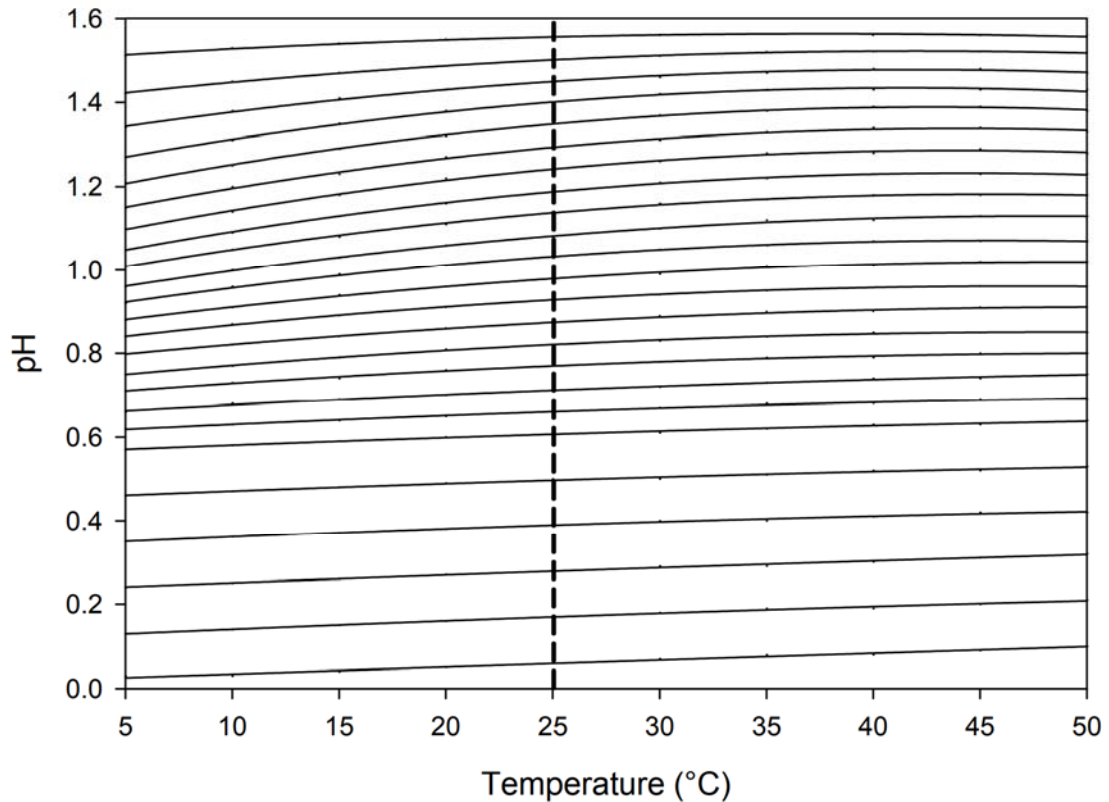
$$C_0 = C_1 pH_{25}^4 + C_2 pH_{25}^3 + C_3 pH_{25}^2 + C_4 pH_{25} + C_5 \quad 4.12$$

$$D_0 = D_1 pH_{25}^4 + D_2 pH_{25}^3 + D_3 pH_{25}^2 + D_4 pH_{25} + D_5 \quad 4.13$$

$$pH = pH_{25} + \Psi \quad 4.14$$

Table 4.2 pH temperature correction model coefficients for Equations 4.11 – 4.13.

B ₁	5.7878E-04	C ₁	-4.8809E-02	D ₁	8.5848E-01
B ₂	-1.5294E-03	C ₂	1.2733E-01	D ₂	-2.2273E+00
B ₃	1.2110E-03	C ₃	-9.8706E-02	D ₃	1.7108E+00
B ₄	-3.7838E-04	C ₄	2.8885E-02	D ₄	-4.8563E-01
B ₅	3.0350E-05	C ₅	-5.1642E-04	D ₅	-6.0580E-03

**Figure 4.5** pH correction model profiles.

The functionality of the model is dependent on the extinction index remaining constant over all ferric ion concentration levels to resolve the pH value; however, the current model breaks down under this assumption. As seen in Figure 4.6 the value of the extinction index, holding temperature and pH constant, deviates significantly at low concentrations and demonstrates a logarithmic relationship. Where the concentration is high, the logarithmic function approaches a horizontal asymptote and behaves closer to the desired constant value. In hindsight, the selection of a base model with a ferric ion concentration of 10 g/L was a poor choice as a representative of the system, this value was originally chosen to achieve the most accuracy in the measurement of ferric ions so

that a dilution step that adds additional uncertainty would not be required. Despite this, the behaviour of the system is still adequately demonstrated, providing valuable insights to approach the problem from a different angle.

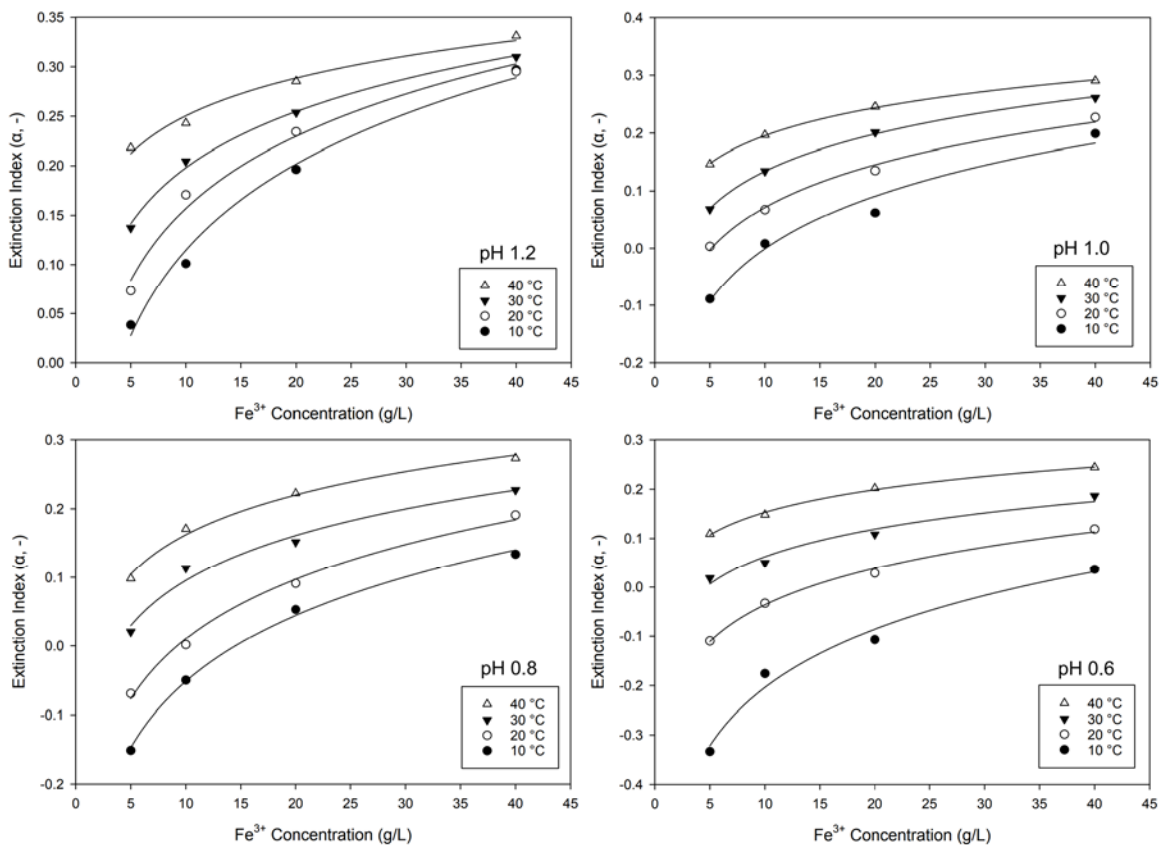


Figure 4.6 Extinction index deviation at low ferric ion concentration.

4.1.2 Molar Extinction Coefficient Model Development

Likewise to the production of the extinction index model, the same series of 10 g/L ferric sulfate solutions were measured at the same pH and temperature values to generate a preliminary model of the molar extinction coefficient behaviour taken at 487 nm as seen in Figure 4.7. Similarly, the data collected showed a fair amount of high-frequency noise but was still mapped with a high coefficient of determination ($0.970 +0.017/-0.039$) as a series of three parameter exponential functions. Individual trend lines were meshed with one another to produce a mathematically contiguous model represented as Equations 4.15 - 4.18 along with the coefficients in Table 4.3.

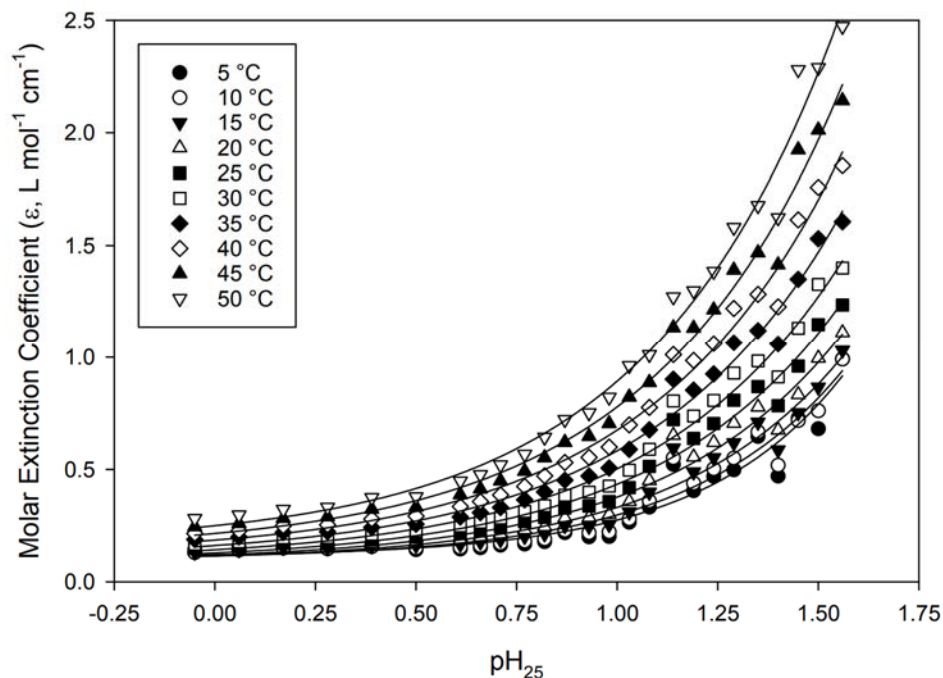


Figure 4.7 Preliminary molar extinction coefficient model based on measured data.

$$\varepsilon_{487} = X_0 + Y_0 e^{Z_0 pH_{25}} \quad 4.15$$

$$X_0 = X_1 T^2 + X_2 T + X_3 \quad 4.16$$

$$Y_0 = Y_1 T^2 + Y_2 T + Y_3 \quad 4.17$$

$$Z_0 = Z_1 T^2 + Z_2 T + Z_3 \quad 4.18$$

Table 4.3 Molar extinction coefficient model coefficients for Equations 4.16 – 4.18.

X_1	9.0976E-05	Y_1	8.6170E-06	Z_1	6.8242E-04
X_2	-3.9504E-03	Y_2	1.3253E-03	Z_2	-5.2144E-02
X_3	1.3041E-01	Y_3	1.1648E-03	Z_3	3.0549E+00

With a known value for the molar extinction coefficient, the concentration of ferric ions in solution is calculated from Equation 4.19 at 487 nm wavelength. Since the ferrous and ferric windows used in absorbance measurements do not allow perfect differentiation between the two ions it is also necessary to add corrections to account for the offset error produced by the non-target ion to be measured. Offset error by ferrous ions in the ferric window can be determined by Equations 4.20 and 4.22 based on the Beer-Lambert law.

The calculated offset error is then subtracted from the original absorbance measurement to yield the corrected absorbance (\bar{A}') by Equations 4.21 and 4.23 along with the corrected extinction index (α') in Equation 4.24 to be used in an iterative solution method. Since the overall absorbance measurements may vary significantly, special attention to the pathlength (l) of the cuvette chosen should be considered to give the best result (avoiding very high or low absorbance readings that produce high noise levels).

$$M_{Fe3+} = \bar{A}'_{487} / (\epsilon_{487} l) \quad 4.19$$

$$\Phi_{487} = (0.0161 \text{ L/mol} \cdot \text{cm}) l M_{Fe2+} \quad 4.20$$

$$\bar{A}'_{487} = \bar{A}_{487} - \Phi_{487} \quad 4.21$$

$$\Phi_{520} = (0.0119 \text{ L/mol} \cdot \text{cm}) l M_{Fe2+} \quad 4.22$$

$$\bar{A}'_{520} = \bar{A}_{520} - \Phi_{520} \quad 4.23$$

$$\alpha' = (\bar{A}'_{487} - \bar{A}'_{520}) / \left(\frac{\bar{A}'_{487} + \bar{A}'_{520}}{2} \right) \quad 4.24$$

Measurement of ferrous ion concentration at a wavelength of 980 nm conversely is straightforward by Equation 4.27 but requires an additional error correction model to account for offset produced by ferric ions using Equations 4.25 and 4.26.

$$\Phi_{980} = (N_0 e^{1.819 pH_{25}} - 0.020) l M_{Fe3+} \quad 4.25$$

$$N_0 = 0.0002573 T + 0.003727 \quad 4.26$$

$$M_{Fe2+} = (A_{980} - \Phi_{980}) / ((0.3861 \text{ L/mol} \cdot \text{cm}) l) \quad 4.27$$

4.1.3 Solution Algorithm of the Model

The solution of the model requires an iterative approach to resolve the output values and a solution algorithm is proposed in Figure 4.8. The equations listed in the calculation algorithm are in reference to those found in this chapter.

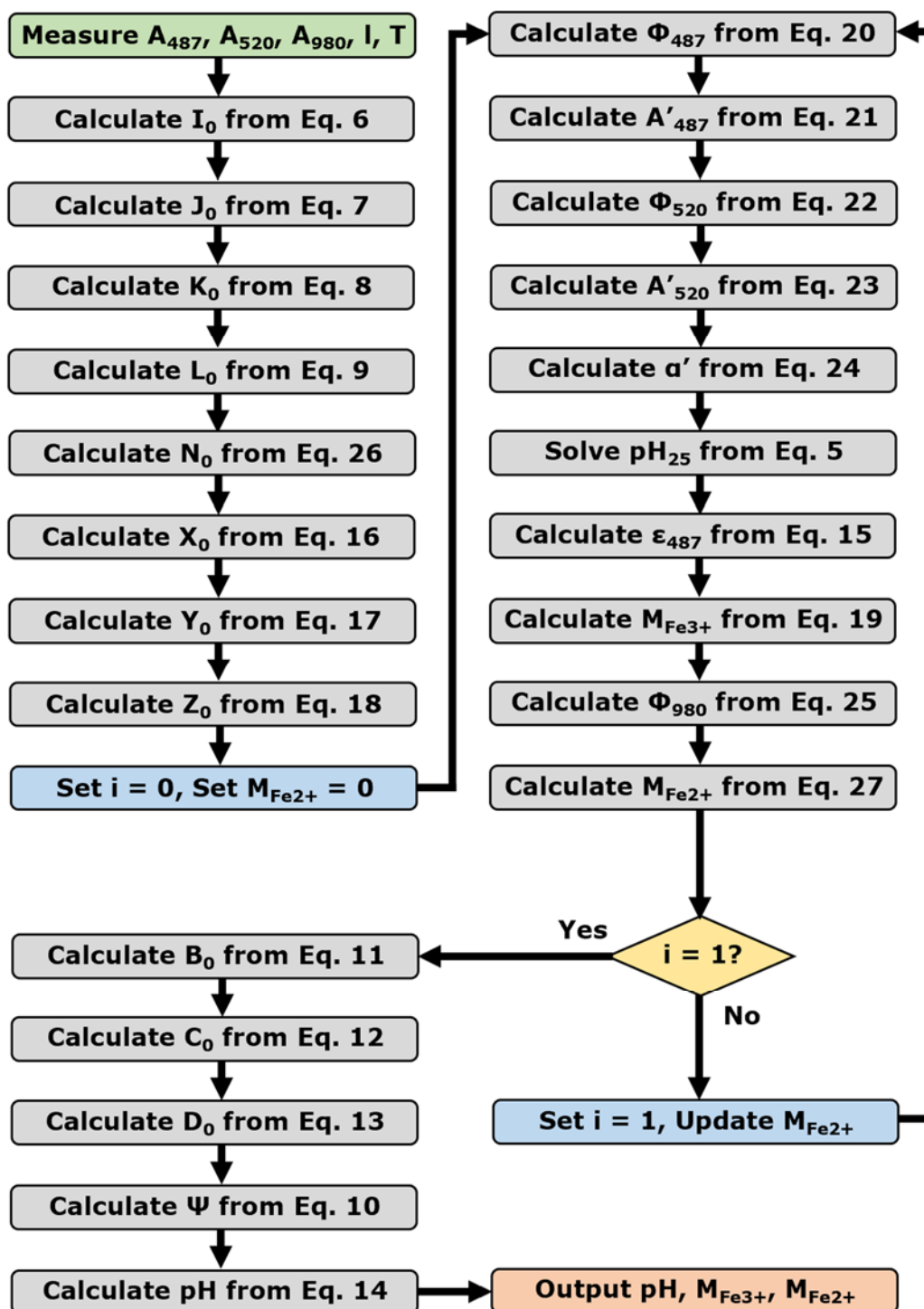


Figure 4.8 Calculation algorithm of preliminary pH and iron concentration model.

4.1.4 Discussion of the Model Development

As previously stated, the model was not successful in fulfilling the final objective since the calculation currently only functions at a ferric ion concentration of ~ 10 g/L and strongly deviates from predicting pH and iron ion concentrations outside this value. The issue primarily lies in the level of complexity displayed by the ferric ion and the development of a single base model with adjustment factors isn't sufficient to adequately model the solution. The findings of this preliminary study suggest a new approach should be taken where the temperature of the solution exists as the only independent model input, a series of models should be developed at incrementing temperature values (0.5 or 1.0 °C per model) and the results interpolated as presented in Figure 4.9. For a temperature span of 5 to 50 °C with a model at every 1 °C a total of 45 separate models would be required. Given the amount of time needed to generate the preliminary model, further development was discontinued for the time being.

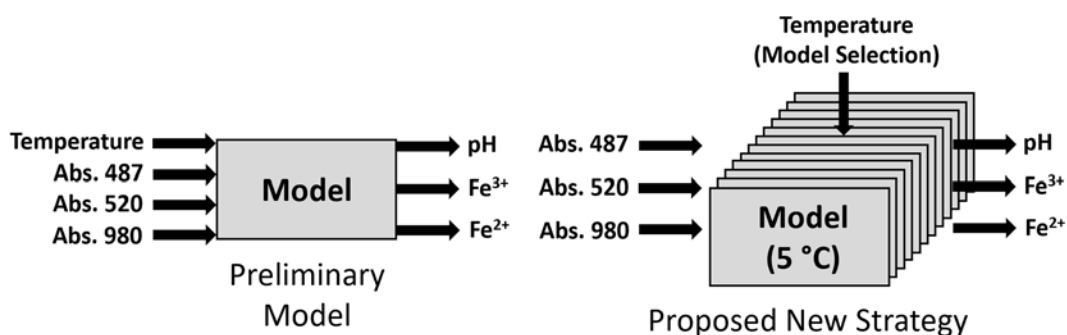


Figure 4.9 Revised strategy for the redevelopment of the model.

Some discussion on the various pitfalls encountered in the development of such models is warranted to improve accuracy. A significant source of error in absorption measurements was encountered through the presence of microcrystalline jarosite suspension in solution that forms spontaneously at $\text{pH} > 0.8$. These suspensions may not be visible to the naked eye and solutions above $\text{pH} 0.8$ should always be filtered prior to measurements with an appropriate filter (Whatman 7141-104, 0.45 μm pore). A second significant source of error identified was in the spectrophotometer operation, specifically in the baseline stability. Measurements of 487 nm and 520 nm were taken together as a short scan in the region and were found to be impacted quite dramatically in some cases where the

baseline shifted over time, not only as a simple constant offset but as a linear deviation which strongly impacts ratiometric calculations. Selection and testing of a suitable spectrophotometer for the task that can maintain stable baselines over time is critical for maintaining model accuracy.

It is probable that the use of absorbance measurements at 487 nm and 520 nm to resolve the pH and ferric ion concentration will not give a unique answer. An additional model input may be required to differentiate between cases where two possible answers exist for a given ratiometric measurement such as a case of high pH and low ferric ion concentration or vice versa. A potential solution to this could be achieved through speed of sound measurements through a fixed length column of the solution in conjunction with the known temperature.

4.2 Spectrophotometer Prototype Design

Application of a mathematical model to assess the bioreactor broth conditions will require an electronic sensing unit and in a large scale operation may require many such units. The use of commercially available spectrophotometers for such an application is likely to be cost prohibitive and therefore a much cheaper electronic prototype for a spectrophotometer for this unique application was developed. The development of custom spectrophotometers has been aided by the ease of modern printed circuit board (PCB) prototyping services and much recent work has been published in low cost designs using LEDs as the light source (Chen et al. 2017, Debarshi and Khan 2019, Nandiyanto et al. 2018, Núñez et al. 2022, Prairie et al. 2020, Rajak et al. 2015, Veras et al. 2009). From a technical point of view some designs presented in the literature are not true spectrophotometers where monochromatic light sources are used, making them simply photometers, however the terminology of “spectrophotometer” will be used for these instances as has been used in previous literature including in this work which makes use of monochromatic light sources.

All the homemade spectrophotometer designs in the literature function on a similar principle using a light source (typically an LED) illuminating a sample, with some cases using a filter or diffraction grating, and then passing the exiting light onto a photodiode

for amplification and digital processing to yield the absorbance reading depicted as Figure 4.10 (without the use of filters or diffraction grating). Light that strikes the photodiode generates an electric current proportional to the number of photons striking its surface multiplied by the quantum yield which is specific to the photodiode and wavelength of light. This tiny current generated by the photodiode is then amplified with an op-amp circuit known as a transimpedance amplifier which converts electric current input into a voltage output. The voltage output from the amplifier may be conditioned through additional amplification or offset to produce a signal compatible with an analog to digital converter (ADC) to be processed by a microcontroller for output to a screen.

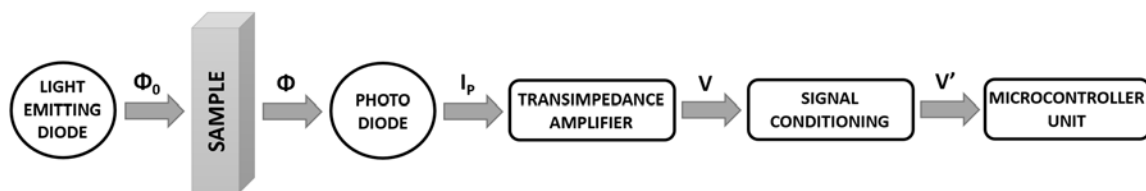


Figure 4.10 Simplified operation of spectrophotometer.

The design in this work makes use of monochromatic light sources and seeks to improve on similar previous designs using LEDs for illumination. In this case three laser diodes (980 nm, 520 nm, 487 nm) are used as illuminating sources in place of LEDs to produce light at precise wavelengths. This contrasts with LEDs which, while monochromatic, generate light output through spontaneous emission with a Gaussian curve covering a range of frequencies (Figure 4.11). Laser diode output properties are strongly correlated with the power level of the device, which is an important consideration. Unlike many other light sources that can be dimmed as needed by regulating electric power, laser diodes must be driven at their rated power to pass into the stimulated emission state and narrow their output to a single frequency (Figure 4.11). The laser light can then be attenuated using neutral density filters to achieve the final desired optical power. An additional consideration of laser diode use is in temperature control where the output wavelength is a function of the semiconductor cavity structure geometries which are subject to thermal expansion/contraction and results in an effect known as mode hopping where the principal output wavelength hops to an adjacent peak (Acsente 2007).

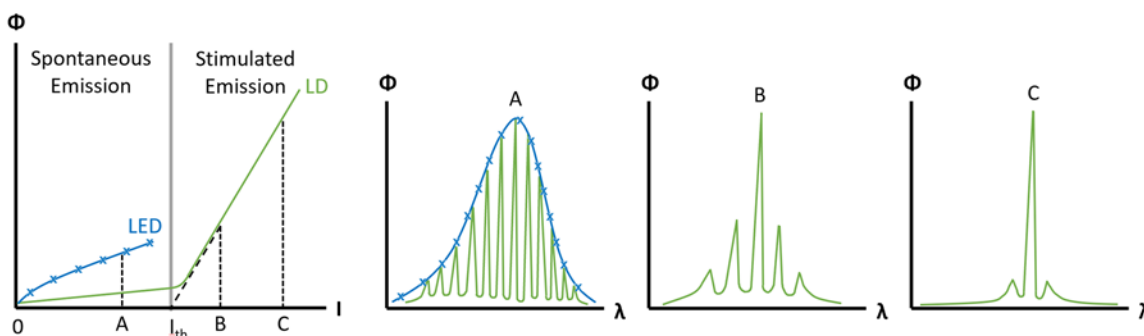


Figure 4.11 LED and laser diode (LD) operating characteristics.

A second improvement over existing designs presented in the literature is made in the analog circuitry of the transimpedance amplifier stage. Current designs use a linear amplification step which is then delivered to an ADC; however, this is undesirable from a mathematical point of view as the Beer-Lambert absorbance law is expressed as the base ten logarithm of the incoming optical power divided by the outgoing optical power. Passing a logarithmic signal to a linear ADC will lead to an uneven distribution of quantization error where the resolution becomes poor at high absorbance readings and unnecessarily high at low absorbance readings where it is not needed. This effect of quantization error is better explained graphically using Figure 4.12 where a 3-bit ADC is demonstrated for illustrative purposes.

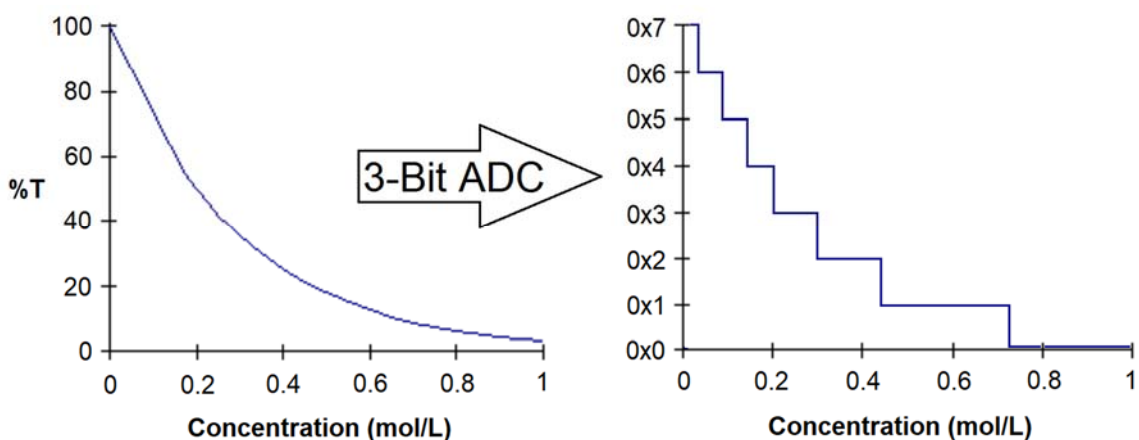


Figure 4.12 Example of uneven quantization error from logarithmic input relationship.

The transimpedance amplifier in this work makes use of a logarithmic op-amp (LOG101) that performs the conversion of the logarithmic Beer-Lambert law in the analog

electronics and outputs a linear relationship to the ADC, thereby equalizing the quantization error over the range of measurement.

A working prototype was assembled and tested as seen in Figure 4.13 and the details of design are provided in Appendix J. The cost of construction is substantially lower than the cost of commercial spectrophotometers while the performance of the prototype was found to meet and exceed that of laboratory instruments. The prototype is found to work especially well in the infrared range where the laser intensities can be separately adjusted, and the 980 nm laser output can be made intentionally high to produce a cleaner signal through aqueous solutions where water absorbs strongly in the infrared. Laboratory spectrophotometers can be seen to demonstrate significant noise in the infrared region (Figure 4.2) where the light source intensity is fixed and much of the infrared light is absorbed by the water, providing a weaker signal with low resolution and high noise levels once the baseline is established.



Figure 4.13 Prototype spectrophotometer for monitoring of the BioGenerator broth.

4.3 Summary of Chapter 4

Exploration of a new method of monitoring pH and iron ion concentrations in the BioGenerator broth using direct spectrophotometry measurements along with a measurement of the temperature was undertaken. A preliminary model based around absorbance readings within two spectral windows with high selectivity for ferric or ferrous ions was proposed. A ratiometric calculation was formulated to solve for the pH, and from this, calculation of the ferric ion concentration. An absorbance measurement in the infrared was used as a means of determining the ferrous ion concentration. An iterative calculation algorithm was devised to solve the system but was found not to be successful as the ferric absorbance system was more convoluted than had been hoped. The findings of the preliminary model suggest that modelling of the broth through in-situ measurements appears feasible but requires the generation of a more complex model set able to isolate for temperature. A low cost prototype spectrophotometer was developed making use of laser diodes and a logarithmic amplifier at its core. The spectrophotometer was found to function quite well, offering a plausible means to replace the use of expensive electrochemical pH and redox probes in favour of an easily replaced sacrificial cuvette. Given the time consuming nature of developing a revised model, the prototype spectrophotometer may also find use as a means of automating the process of data collection.

Chapter 5

5 Determination of the Broth Oxygen Content

Oxygen represents a fundamental chemical reactant in the overall electrochemical conversion of hydrogen to electric power. Its transport, concentration, and delivery for final consumption as the driver of microbial biooxidation processes is of the utmost importance in optimizing the BioGenerator system to achieve high catholyte recharge rate with minimal energy expenditure. Given that the biological reactions involved in the process occur exclusively in the liquid phase it is of considerable importance to know the dissolved oxygen (DO) content of the bioreactor broth in order to sustain a livable environment for the microbes and monitor bioreaction rates. The concentration of oxygen available in solution is generally quite low relative to that found in the air ($\sim 0.260 \text{ gO}_2/\text{L}_{\text{air}}$) and is therefore often measured as milligrams of oxygen per liter of liquid volume. Given this low concentration of oxygen by a physical constraint, oxygen represents the rate limiting reagent in the process. Accurately determining a value for the saturated DO at a given set of conditions (temperature, air pressure, and salinity) is critical where this value acts as the reference for DO meters to be able to output valid information. A poor understanding of the process of obtaining the saturated DO concentration value often results in incorrect use of DO meters applied to systems beyond environments such as fresh water or seawater and therefore needs to be addressed.

5.1 Background

5.1.1 The Meaning of Saturation

Measurement of DO levels in natural waters is a routinely practiced assessment of water body health that provides numerical values for comparison relative to the saturation level of the water (100% air saturation). While many layman sources explain the DO level in water relative to the saturation value in terms of safe limits to aquatic life, the actual physical meaning of saturation is often never presented. Moreover, how does a quantity of liquid “know” what its capacity to hold a certain quantity of dissolved gas is.

It might be thought that the liquid acts as a sort of container to hold gas and when filled can hold no more, therefore being full or saturated. To some extent this is true in that space in-between molecules held in a liquid state physically constrains the practical amount of gas that may occupy the mixture. Though it is a commonly observed occurrence to have readings in excess of 100% saturation, especially where water aerated when cool with low oxygen demand later warms and has a lower saturation value but has not exhausted the excess oxygen. In other cases such as the chemical decomposition of hydrogen peroxide in solution, the DO reading may read multiple times the saturation concentration. In both cases water can be demonstrated to be able to hold more oxygen than the saturation concentration in a meta-stable state and so it is not so simple as a limit set by physical capacity. In actuality, the saturation value is determined as both a limitation set by volumetric storage and also the gas-liquid interface equilibrium of the probability of molecules passing across the interface or remaining in their current phase of matter.

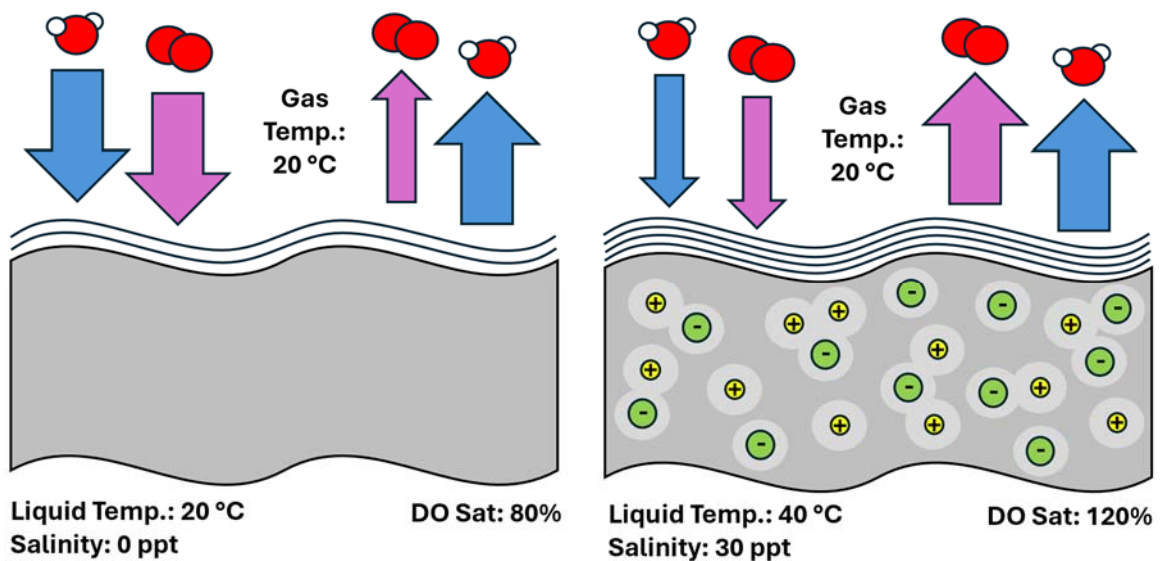


Figure 5.1 Theoretical molecular transport across a gas-liquid interface.

An illustration of the phenomenon is presented in Figure 5.1 as two example scenarios and is related to the process of evaporation or condensation which is similar in nature. In this example, the liquid is water and its molecules are tightly attracted to one another through intermolecular forces of hydrogen bonding while the bulk gas is composed

primarily of oxygen. In the first example (Figure 5.1 – Left) the liquid-gas system is at a low temperature that is equal in both phases and the gas above the liquid is at 100% humidity (containing water vapor at partial pressure equal to its vapor pressure). In this state, water molecules enter and exit the interface at the exact same rate and the system is therefore at an equilibrium, it is not evaporating or condensing water. The oxygen gas molecules behave in a similar fashion, in this case the saturation level is only 80% and not at an equilibrium. This means that the current concentration of oxygen dissolved in the liquid is too low to be ejected as frequently as the incoming gas molecules which enter more frequently. When the frequency of oxygen leaving and entering the interface reaches parity then the solution will be considered saturated.

The effects of heat and dissolved solids in the water greatly effects the equilibrium state of molecular movement across the interface layer, in the second example (Figure 5.1 – Right) the water is heated and salt (as sodium chloride) is added. In the case of higher temperature, the water molecules vibrate more violently and those at the interface are more likely to bounce away an incoming gas molecule while at the same time more likely to eject a molecule into the gas phase. The equilibrium saturation level will suffer a reduction as oxygen gas molecules more readily exit the liquid phase while they are simultaneously inhibited from entry from the gas phase at a greater rate. The addition of salts also acts to reduce the equilibrium saturation level at the volumetric level by crowding out space that oxygen gas can occupy. When ionic compounds are dissociated into water the electric charge of their ions is neutralized through the dipole attraction of surrounding water molecules that cluster against the ion, forming a hydration shell (solvation shell) that collectively behaves as a neutrally charged molecule (Andreev et al. 2018). A consequence of the formation of hydration shells is that the water behaves as if less molecules are present to hold oxygen gas, which places the oxygen under a greater potential to leave the liquid phase. This behaviour is commonly referred to as the “salting out” effect.

The presence of hydration shells is also responsible for the effects of solution non-ideality with increasing solute concentration. Where ionic concentrations become quite high, the rate of interaction and overlap of these shells occurs more frequently and the

behaviour of the solution drifts away from what might be expected based on solutions at lower concentration. This discrepancy gives rise to the use of activity (\bar{a}) and activity coefficients (γ) in place of concentration. While concentration is a quantity of actual material in solution, the activity is representative of observed behaviour which is often of more importance and is analogous to fugacity applied to gases.

5.1.2 The DO Meter

DO meters are commonly encountered equipment found in laboratories useful for measuring the level of oxygen present in solution as either percent air saturation values (0 to >100%) or as oxygen concentration (mg/L). A proper understanding of the inner workings of the instrument are necessary where applied for use outside typical applications for instance in fresh water or seawater. In the case of this work the application is in the measurement of DO in a highly acidic (pH ~0.8) iron sulfate (~40 g_{Fe}/L) broth with the addition of 9K nutrient salts (Silverman and Lundgren 1959). Generally, the probes used with DO meters operate on either electrochemical principles (O₂ reduction at a platinum cathode) or function based on optical fluorescence (O₂ extinguishing the effect of stimulated fluorescence in an optical dye) (YSI 2009). In either case the underlying physical principles of measurement are the same, oxygen levels in the solution are determined through proportionality of the partial pressure in air by Henry's law (YSI 2009).

The fact that DO meters only definitively measure samples based on diffusivity means that in solutions outside anticipated use only the measurement as a reading of percent air saturation is valid. DO concentration is calculated internally using the percent air saturation value entered into mathematical models that give the expected result. This is a common source of error in using the instrument as for example in iron sulfate solutions, apart from a small note buried in the technical manual, the meter itself does not give any indication to the user that its output is incorrect when in operation. An example of this internal model may take the form of Equations 5.1 to 5.4 valid over 273.15 – 310.65 K and 0.5 – 1.1 atm (Mortimer 1956).

$$c = c^* P_A \left[\frac{(1 - \frac{P_{WV}}{P_A})(1 - \theta P_A)}{(1 - P_{WV})(1 - \theta)} \right] \quad 5.1$$

$$\ln c^* = 7.7117 - 1.31403 \ln (T - 227.22) \quad 5.2$$

$$\ln P_{WV} = 11.8571 - \left(\frac{3840.70}{T} \right) - \left(\frac{216961}{T^2} \right) \quad 5.3$$

$$\theta = 0.009671 - (4.942 \cdot 10^{-5} T) + (6.436 \cdot 10^{-8} T^2) \quad 5.4$$

Where salinity needs to be accounted for, an additional conductivity sensor is often used to provide an additional salinity value (s). The model for salinity is based off DO concentration in seawater, primarily as sodium chloride. An alternative model for the standard-pressure saturated oxygen concentration (c^*) value can be used in place of Equation 5.2 using Equation 5.5 with the model coefficients in Table 5.1 valid over 273.15 – 313.15 K and 0 – 40 g_{salt}/kg_{brine} (or ppt) (Benson and Krause 1984).

$$\ln c^* = G_0 + \frac{G_1}{T} + \frac{G_2}{T^2} + \frac{G_3}{T^3} + \frac{G_4}{T^4} - s \left(H_0 + \frac{H_1}{T} + \frac{H_2}{T^2} \right) \quad 5.5$$

Table 5.1 Salinity model coefficients for seawater (Benson and Krause 1984).

G ₀	-139.34411	G ₄	-8.621949·10 ¹¹
G ₁	1.575701·10 ⁵	H ₀	0.017674
G ₂	-6.642308·10 ⁷	H ₁	-10.754
G ₃	1.243800·10 ¹⁰	H ₂	2140.7

The generation of models such as these is generally completed through use of wet chemistry techniques such as the Winkler titration and its variants (Bryan et al. 1976, Theriault et al. 1932) or for seawater a method based on absorbency readings using an alkaline catechol/ferrous ion indicator solution might be used instead (Lang et al. 1979).

5.1.3 Current State of DO Measurement in Iron Sulfate Broths

More recently, interests in bioleaching of copper deposits through the use of ferric sulfate solutions has spurred attempts to produce similar models for use in iron ion and copper ion solutions accounting for pH and temperature. Mazuelos et al. (2017) has proposed a model for the saturated DO concentration through subtractive terms of the contributions of ferric, ferrous, and copper ions and the pH of the system at a temperature of 30 °C. A similar model is presented by Huang et al. (2022) to achieve the same purpose. Inspection of the measurement apparatus and DO meters used in both cases however suggests that measurements have been taken incorrectly and essentially produce a mathematical model built unknowingly from output generated off a seawater DO concentration model.

A valid model for the determination of saturated DO concentration in iron sulfate solutions remains elusive at the present date. Much of the difficulty in production of a model in this case comes from the complexity of the solution in combination with the ionic strengths and chemical aggressiveness of the solution. While the chemical composition of the broths used in this work are generally held similar, such models will need to be applicable to more than just niche uses, meaning they have to take into account additional leachate ions expected to be encountered and also must factor in the effects of growth media salts. These chemical mixtures are not well suited to wet chemistry techniques devised for other cases either due to chemical incompatibility. Additionally, certain effects such as ferric ion dimerization in solution introduce the possibility of other unique oxygen displacement factors further complicating modelling (Zhu et al. 2013).

5.2 Measurement of Saturated DO with Biooxidation

5.2.1 Theory of a Novel DO Measurement Technique

Where a wet chemistry method for determining saturated DO concentration is not present in literature and it is not very simple to develop mathematical models where none exist that are reliable, a new method of determination must be created. In general, a method of measuring DO in a solution relies on some form of amplification process where the concentration of oxygen is only a few milligrams per liter of solution. This can be

achieved for example through chemical stoichiometry such as in the Winkler titration (one O_2 yields two $MnO(OH)_2$ and two $MnO(OH)_2$ react with four $S_2O_3^{2-}$ in the titrant) or with methods such as sensitive colourimetric indicating dyes. A potential amplifying mechanism for the case of iron sulfate solutions was observed through the properties of the potentiometric redox probe (Section 3.2.4) operated in conditions where the ratio of ferric iron to ferrous iron is extremely high. Under these conditions the change in output voltage becomes very sensitive to changes in concentration ratio (Q) (Figure 5.2).

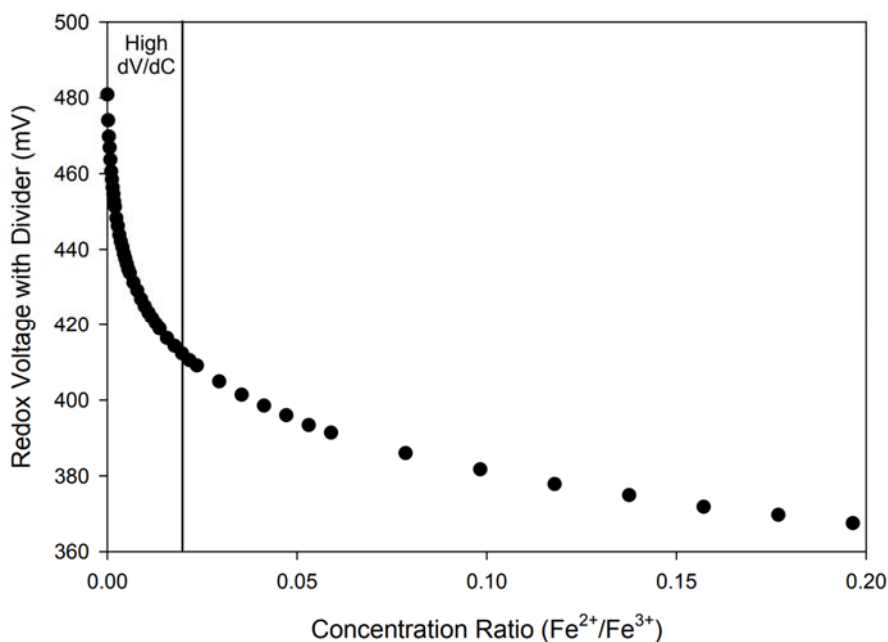
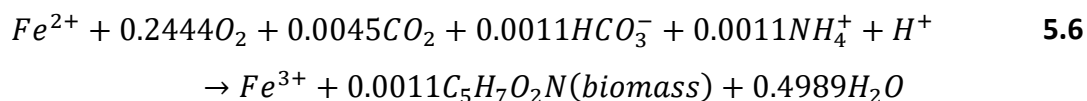


Figure 5.2 Rate of change of output voltage relative to Fe^{2+} and Fe^{3+} ratio.

This property was found to be useful when applied through the biooxidation of a small quantity of ferrous iron solution in the presence of iron oxidizing microbes. The consumption of ferrous ions through biooxidation is stoichiometrically proportional to the amount of oxygen consumed and offers a simple method to determine the saturated DO concentration using easily measured ferrous iron consumption as a proxy. The stoichiometric equation linking ferrous iron and oxygen consumption can be obtained from the well-studied *At. ferrooxidans* and given as Equation 5.6 (Nemati et al., 1998) (Note: a misprint in the original source has been corrected with regard to the dioxygen balance). Though this work used *L. ferriphilum* as the principal iron oxidizing microbe,

all iron oxidizing microbes are expected to share a similar stoichiometry where O_2 use for energy production is substantially greater than that of incorporation in biomass and therefore the substitution is valid. It is also observed that an additional amplification process is provided through stoichiometry where the consumption of every dioxygen molecule equates to the conversion of approximately four ferrous ions to ferric ions.



5.2.2 Development of a Novel DO Measurement Technique

The use of the redox probe in the manner described must be approached with caution as the output will deviate from the predictable Nernstian relationship where the probe output reaches a maximum or minimum output voltage at 100% ferric or ferrous ion concentration respectively (Figure 5.3).

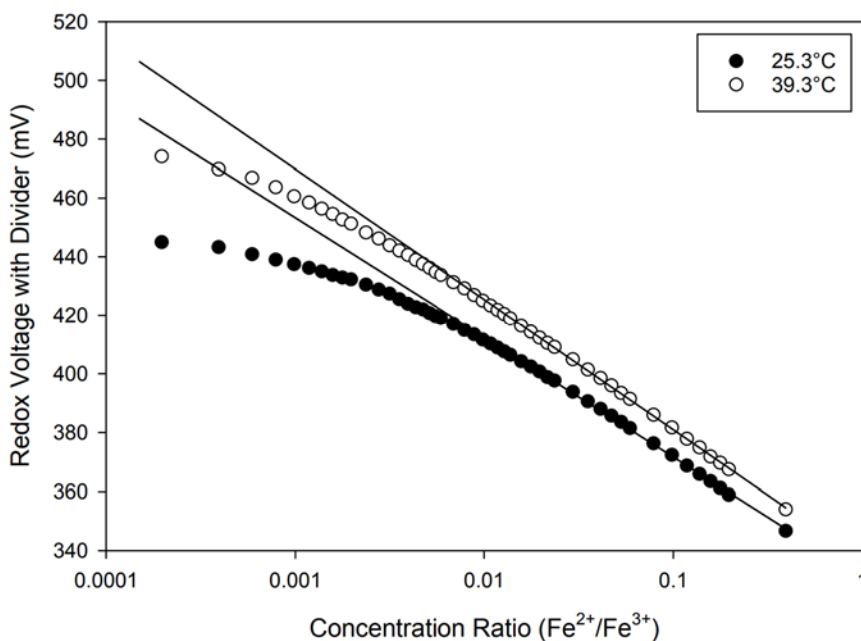


Figure 5.3 Observed deviation from Nernstian relationship at low concentration ratio.

Pronounced deviation is observed to occur at values of concentration ratio less than 0.02 which is directly in the region of interest for the DO measurement technique. The

deviation is simple to model however and can be internalized into a modified Nernst equation to correctly model the output behaviour. The deviation from the expected relationship is plotted and a curve of best fit is applied (Figure 5.4) to produce a deviation correction curve.

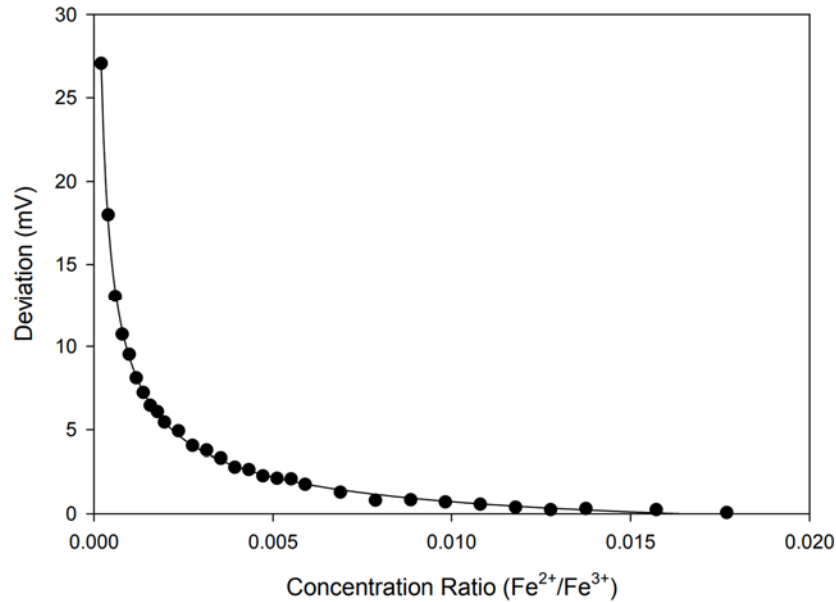


Figure 5.4 Nernst relationship deviation curve taken at 39.3 °C.

The curve is found to fit best to a sigmoidal four parameter logistic curve with the minimum horizontal asymptote (j) set to -2.0 mV. With an equation representing the deviation curve established it can be used in a subtractive manner from the Nernst equation to yield a final modified Nernst equation represented as Equation 5.7. The model was applied to a bioreactor broth with an iron content of $33.3 \pm 0.4 \text{ g}_{\text{Fe}^{3+}}/\text{L}$ and pH 0.87 with the inclusion of 9K media in an unknown proportion at two operating temperatures yielding example model parameters specified in Tables 5.2 and 5.3.

$$E_d = d \left[E^o - \frac{RT^*}{zF} \ln Q \right] - \left[j + \frac{k}{1 + \left(\frac{Q}{h} \right)^m} \right] \quad 5.7$$

Table 5.2 Parameters of Equation 5.7 at 25.3°C using BioGenerator broth.

E°	468.9 mV	d	0.7056
R	8315 mJ/mol·K	j	-2.0 mV
T^*	291.5 K	k	65.14 mV
z	1	h	$3.125 \cdot 10^{-4}$
F	96485 C/mol	m	0.8523

Table 5.3 Parameters of Equation 5.7 at 39.3°C using BioGenerator broth.

E°	476.9 mV	d	0.7056
R	8315 mJ/mol·K	j	-2.0 mV
T^*	317.2 K	k	406.2 mV
z	1	h	$3.246 \cdot 10^{-6}$
F	96485 C/mol	m	0.6214

Because the process involves operation in such a sensitive region of the redox probe, additional tests were performed to examine potential deviations caused by other factors. Firstly, the dissolved oxygen in solution might affect the redox probe output where it could be broken down on the exposed platinum electrode and alter the output voltage. A minute quantity of ferrous sulfate was added to a fully oxidized solution of ferric sulfate that had been stored for a month to allow the culture to die. The redox probe was exposed to the solution and the DO concentration was varied between 0 and 100% through sparging with compressed air and nitrogen. No effect on the output voltage was observed for any differences in oxygenation level. Next, the possibility of the redox probe behaving as a microbial fuel cell was considered where microbes immobilized on the exposed platinum electrode could act as electricigens and generate unwanted voltage variations. The redox probe was calibrated with a modified Nernst model in the presence of active microbial culture. The probe electrodes were then immersed in acidified water (H_2SO_4) for a period of 50 days to allow microbes on the surface to die in the absence of food substrate. The probe was then used again in a sterile ferric iron solution with additions of ferrous iron to record the output response. No deviation was observed in the output response of the probe in the presence or absence of microbes. Deviations in Nernstian behaviour of Pt-Ag/AgCl redox couples have been demonstrated to occur in the presence of phosphate ions when the ratio of ferrous ions is very high to that of ferric

ions (Avdeev et al. 2022). Since phosphate ions are present in solution as a component of 9K media, an examination of the reverse effect where the ferric ion ratio is very high to that of ferrous ions was examined. Phosphate deviation was not found to occur under the normal operating conditions of high ferric ion ratio and was only found to have effect under high ferrous ion ratio. Fouling of the platinum electrode surface was found to produce deviation, though the process occurs very slowly. Cleaning of the platinum electrode after extended use (several months) with a scouring pad caused the normally observed deviation to reduce in magnitude.

5.2.3 Measurement Process

With a redox probe calibration curve model established for a given solution temperature, the determination of the saturated DO content of the solution was then found in a straightforward manner using the following steps:

1. Fill the oxygen solubility determination apparatus (Section 3.3.5) with 500 mL of ferric sulfate solution with active culture and add an amount of ferrous sulfate to give a 0.004 concentration ratio of ferrous to ferric ions under nitrogen de-aeration to set the zero point baseline voltage reading.
2. Clean and refill the apparatus with 500 mL of ferric sulfate solution with active culture and aerate until a 100% air saturation reading is given on the DO meter, then stop aeration.
3. Apply a nitrogen blanket to the headspace of the mixing vessel and add the same amount of ferrous sulfate as used to generate the zero baseline until the microbes have depleted all available DO in solution as given by a 0% air saturation reading on the DO meter and record the final voltage.
4. Using the developed redox probe calibration curve, convert the recorded voltages into ferrous iron concentrations and determine the amount of ferrous iron consumed in the volume of liquid as $\text{mg}_{\text{Fe}^{2+}}/\text{L}$.
5. Convert the iron concentration from mg/L to mol/L and multiply the result by the stoichiometric conversion constant (0.2444 from Equation 5.6) to obtain the mol/L of DO consumed.

6. Convert the mol/L of DO to mg/L to arrive at the solution for the saturated DO concentration.

The technique was tested on fully oxidized BioGenerator broth with a ferric ion content of 33.3 g_{Fe3+}/L and containing an active culture with nutrient salts. Ferrous sulfate solution necessary for the procedure was produced from recrystallized ferrous sulfate with a ferrous ion content of 32.7 g_{Fe2+}/L. Measurements were taken as the average of ten readings over four days from an operational bioreactor. The precision of the final result was found to be largely influenced by the skill of the operator and the first results obtained with the procedure are recorded in Table 5.4 as a benchmark. With practice, the uncertainty in final measurement was reduced from ±6.9% to ±2.0%.

Table 5.4 Preliminary results of the saturated DO measurement technique.

mg Fe ²⁺	19.65	±1.35
mol Fe ²⁺	3.519·10 ⁻⁴	±2.417·10 ⁻⁵
mol O ₂	8.600·10 ⁻⁵	±5.907·10 ⁻⁶
mg O ₂	2.75	±0.19
mg O ₂ /L	5.50	±0.38

5.3 Measurement of Biooxidation Rate with DO

A byproduct of the process of measuring the percent air saturation for the determination of the saturated DO concentration with this method provides an alternative to yield the biooxidation rate of the microbes in solution. The linear decrease in percent air saturation (Figure 5.5) can be converted to mgO₂/L consumed over time using the value of saturated DO concentration. In this case respiration rates of 26.9 µgO₂/Ls (25.3 °C) and 55.2 µgO₂/Ls (39.3 °C) were measured and through stoichiometry converted to the biooxidation rate of ferrous iron as 192.1 µg_{Fe2+}/Ls (25.3 °C) and 394.2 µg_{Fe2+}/Ls (39.3 °C).

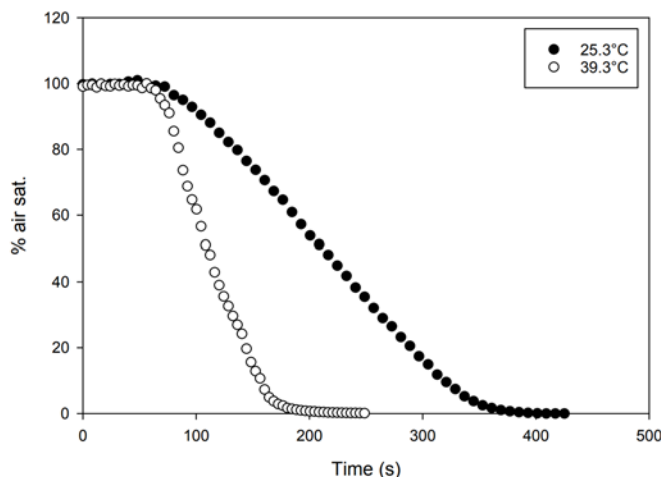


Figure 5.5 Microbial respiration over time.

5.4 Summary of Chapter 5

A simple method of determining the saturated DO concentration in iron sulfate broths was needed for a general understanding of the limitations presented to the process of iron biooxidation where the DO availability in solutions represents a limit to both the ability of biooxidation to proceed as well as the maximum cell concentration which dictates the maximum biooxidation potential. The determination of the saturated DO concentration was also required for later work for application in the determination of average mass transfer coefficients. Current work into developing mathematical models for use with iron sulfate containing solutions appear to be flawed through a misunderstanding of the internal workings of DO meters and are further complicated by the presence of nutrient growth salts which are at concentrations high enough that they can not be considered negligible. A novel method of determining the saturated DO concentration was developed using the measurable biochemical reaction of ferrous iron consumption as a proxy for oxygen consumption in solution yielding the oxygen concentration. A redox probe was used to amplify the reading by modelling its output behaviour under very high ferric to ferrous ion concentration ratio where the output voltage deviates mathematically from the Nernst relationship. A final reading was obtained with an error level low enough that it could be used for a practical purpose. The apparatus was also found to be useful for determination of the biooxidation rate of the microbes through monitoring of the DO concentration.

Chapter 6

6 Determination and Measurement Improvements of the Bioreactor k_{La}

The efficient transfer of oxygen from air into the bioreactor broth for microbial consumption in the BioGenerator system represents a critically important parameter for commercialization of the technology. The value of this parameter is defined as the volumetric oxygen mass transfer coefficient which is often alternatively referred to by name as its combined mathematical variables, termed k_{La} . In the case of the BioGenerator, aeration represents energy loss in the form of excessive circulation pumping in the airlift bioreactor as well as thermal losses as the air absorbs heat from the liquid broth and carries it away as exhaust. Ideally then the mass flow rate of air must be kept as low as possible to mitigate energy losses which would defeat the purpose of the system as an energy storage technology. Reducing the flow rate of air through the broth will negatively affect the rate of ferrous iron biooxidation and will also ultimately limit the density of the microbial culture in solution though. Therefore, efficient transfer of oxygen into the liquid media is paramount to satisfying high overall energy conversion efficiency. The value of k_{La} must be as high as possible to achieve high catholyte recharge rates at minimum energy loss and be determined with high accuracy to allow fine-tuned optimization of the bioreactor design to reach the highest k_{La} possible.

6.1 Background

6.1.1 The Meaning of k_{La}

In Chapter 5 it was demonstrated that oxygen gas diffusion into a liquid was influenced through molecular interactions at the interface layer between the two phases and that an equilibrium concentration would be developed based on the resulting rates of molecular emission and absorption across this layer. The specific rate of oxygen entering a liquid (or leaving) is termed the oxygen transfer rate (OTR), defined as a term specifying the conductance of molecules across the interface layer of a given volume (k_{La}) multiplied by the gradient potential (Equation 6.1). The gradient potential is simply the difference

between the equilibrium saturated DO concentration of a liquid (c_{DO}^*) and its measured DO concentration value (c_{DO}) which acts as the driving force of diffusion. The $k_L a$ term is itself a grouping of two separate terms, the average mass transfer coefficient (k_L) and the volumetric interfacial area (a). The k_L value represents the moles per second of oxygen crossed per area of gas-liquid interface (m^2) per relative concentration difference in the liquid (mol/m^3). The value of a represents the interface transfer area (m^2) available per unit of gas and liquid mixture volume (m^3). On their own, k_L and a can be difficult to assess individually (especially a) but as a combined value may be quantified relatively easy and so for convenience are simply left as a grouped coefficient.

$$OTR = k_L a (c_{DO}^* - c_{DO}) \quad \mathbf{6.1}$$

In a simple system of, for example pure water, a value of c_{DO} not equal to c_{DO}^* will produce a non-zero OTR and oxygen will either be expelled or absorbed until the saturated 100% DO level is reached where the OTR equals zero. In many cases though the liquid system is complex and involves chemical or biological agents in solution that consume oxygen (e.g. microbial respiration or sodium sulfite oxidation (Section 3.1.4)) or evolve oxygen (e.g. hydrogen peroxide decomposition). In the BioGenerator microbial respiration is always present in operation and therefore a second rate term of oxygen consumption in the liquid volume is present as the oxygen uptake rate (OUR). For microbial respiration, the OUR is defined as the mass of oxygen consumed per mass of biomass per second (q) multiplied by the mass of biomass per volume (x) (Equation 6.2).

$$OUR = qx \quad \mathbf{6.2}$$

In such complex gas-liquid systems where a non-zero OUR exists, a gradient potential in the liquid will always exist and therefore a non-zero OTR will also always exist. Where the OTR equals the OUR, the system will exist in a static or steady state form where c_{DO} will remain constant at some value below 100%. Where the OTR does not equal the OUR, the system will exist in a dynamic state where c_{DO} will change over time until leveling off to a value where OTR equals OUR and the system returns to steady state. This transfer and consumption of oxygen in the airlift bioreactor is represented graphically in Figure 6.1 where a molecule of oxygen from a bubble in the riser enters the

DO unsaturated broth (1) where it is carried in solution into the downcomer region (2) and eventually consumed in the cytoplasm of a microbe (3). A gradual decrease in DO concentration through the depth of the downcomer region will be observed proportional to its residence time in solution as it is consumed.

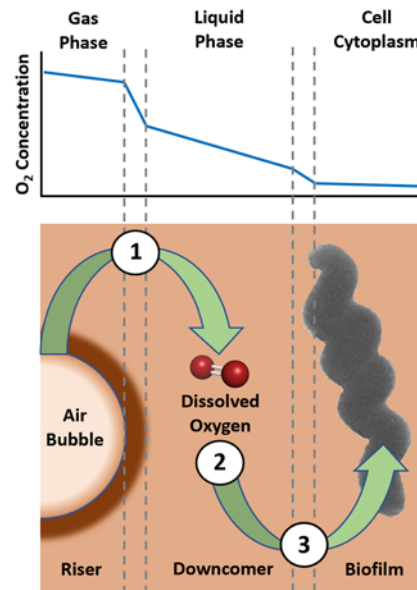


Figure 6.1 Mass transport chain of oxygen in bioreactor from air to microbes.

6.1.2 Methods of k_{LA} Measurement

The measurement of k_{LA} may be performed by one of several general methods depending on the system complexity. For use in the BioGenerator, only the biological in-situ technique can be used.

6.1.2.1 Chemical Sulfite Oxidation Technique

Measurement of k_{LA} through the chemical consumption of sodium sulfite represents one of the simplest methods available and is outlined by Yoshida and Akita (1965). Sodium sulfite is mixed into solution along with a cobalt or copper catalyst to consume all available DO and the remaining sulfite concentration is then set as the starting reference point. Air is then bubbled through the solution to induce oxygen transfer. In this state the c_{DO} value is essentially held at zero and the oxidation rate of the sulfite over time is equal to the OTR where any oxygen entering the solution is immediately consumed by sulfite.

Samples of the liquid are taken periodically and titrated to reveal the sulfite concentration, and from this the OTR and through Equation 6.1 the k_{La} . The process does not require a DO meter to perform. Though a major drawback to the technique is the nature of the chemical make-up of the solution which is not representative of what the intended broth will be, the k_{La} is likely to be over-estimated (Shuler and Kargi 2002).

6.1.2.2 Physical Outgassing Technique

The physical outgassing technique also known as the dynamic unsteady-state method involves the use of a DO probe to monitor DO concentration dynamics in the absence of a microbial culture and is outlined by Wernau and Wilke (1973). The technique relies on the outgassing of oxygen from the solution through sparging with an inert gas (typically nitrogen) followed by monitoring of the increase in DO concentration upon re-aeration and agitation to solve for k_{La} . The accuracy of the method is hindered by the DO probe response time which produces error under dynamic conditions where DO concentration is non-constant.

6.1.2.3 Biological In-Situ Technique

The biological in-situ technique also known as the dynamic air stop-start method involves the use of a DO probe to monitor DO concentration dynamics in the presence of a microbial culture and is outlined by (Bandyopadhyay et al. 1967). The technique involves halting air flow to the bioreactor to determine the OUR as the linear microbial respiration rate followed by restarting aeration and using the dynamic response of the system returning to steady state (OTR equal to OUR) to calculate the k_{La} . Likewise to the physical outgassing technique, the DO probe response time contributes to error under dynamic conditions.

6.1.2.4 Yield-Coefficient Technique

Measurement of k_{La} through the yield-coefficient is outlined by Wang et al. (1979) and involves mathematical determination through stoichiometric balances and oxygen growth yields within an active microbial culture. The bioreactor is treated as a respirometer where oxygen mass balance in the outgoing streams and contained in the liquid broth as

DO can be used to determine the k_{LA} (Shuler and Kargi 2002). While the yield-coefficient technique demonstrates the highest accuracy amongst the general methods, expensive equipment is required to accurately monitor oxygen content, mass flow, system pressure, and system temperatures to achieve good results. This equipment is not necessarily compatible with the acidic high ionic strength broth used in the BioGenerator.

6.2 k_{LA} Measurement by Dynamic Air Stop-Start

6.2.1 k_{LA} Measurement in a Benchtop Scale Airlift Bioreactor

Initial measurement of k_{LA} was performed in a benchtop airlift bioreactor (Section 3.3.1) using pure water and a physical outgassing technique along with iron sulfate broth containing active culture of *L. ferriphilum* using a biological in-situ technique (Section 3.2.8). Problems were encountered and documented relating to the DO probe as well as benchtop bioreactor design. A polarographic DO probe (Section 3.2.6) was used for these experiments but was found to have wide variation in the output readings ($\pm 4\%$ air saturation) as well as a tendency to deviate from its proper calibration point after 5 to 10 minutes of continuous submergence in the broth, requiring cleaning of the internal electrodes. The benchtop airlift bioreactor itself was designed to act in some manner as a segment of a semi-pilot scale version, however because of the small size internally, bubble flow and formation was observably disrupted. Air and broth moving up the riser tended to move as a slug flow pattern instead of a dispersion of small bubbles, crashing at the top and leading to froth and small bubble formation that were sucked downwards into the downcomer. The issue was found to be exasperated when increasing airflow. One notable observation from this unwanted operating mode was the fact that bubbles that had been sucked into the downcomer demonstrated rather long residence times in some cases where the upward buoyant forces were counteracted by the liquid current. This phenomenon could potentially be exploited for improved aeration within the downcomer packed bed where pure oxygen gas from electrolysis operations might be released as controlled bubble sizes remaining suspended by counteracting forces. Despite the observed issues the final preliminary data sets showed reasonably good consistency between one another and to that of a few k_{LA} readings from a semi-pilot scale reactor using biological medium (Figure 6.2). The mathematical relationship of k_{LA} to the

superficial gas velocity (U_G) in the benchtop scale is given as Equation 6.3 for pure water and Equation 6.4 for use with biological media. Given the apparent issues with the apparatus, only a limited number of measurements were taken in this case, though were enough to demonstrate the anticipated power relationship (Liu and Hermanowicz 2008).

$$k_L a = 4.81 U_G^{1.35} \quad \mathbf{6.3}$$

$$k_L a = 4.13 U_G^{1.28} \quad \mathbf{6.4}$$

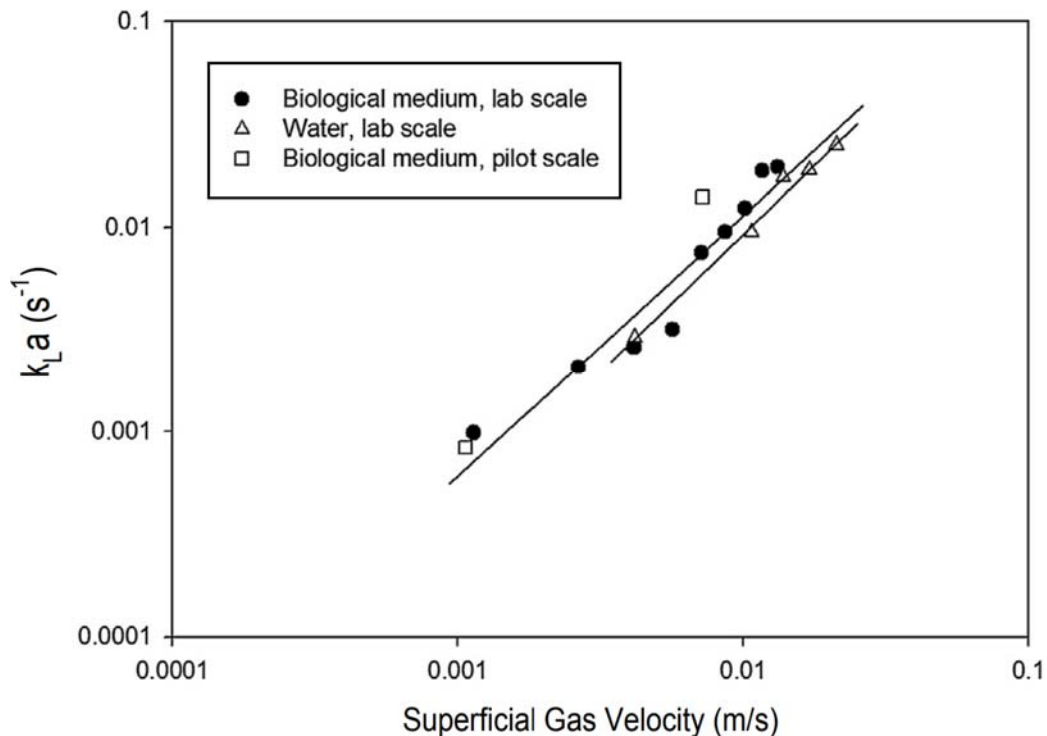


Figure 6.2 Comparative $k_L a$ values in pure water and biological medium as a function of superficial air velocity and bioreactor size (benchtop and semi-pilot scale).

6.2.2 $k_L a$ Measurement in a Semi-Pilot Scale Airlift Bioreactor

With the shortcomings of the benchtop scale airlift bioreactor identified a more thorough and accurate analysis of the $k_L a$ to U_G relationship could be attempted. Firstly, the DO probe and meter were replaced with a much more stable and accurate optical dye style (Section 3.2.7). Secondly, the semi-pilot scale airlift bioreactor (Section 3.3.2) was reconfigured for use in determining $k_L a$ using one segment of the five with a volume of

about 120 L. The dimensioning of the riser and downcomer were observed to be sufficiently large to demonstrate the proper bubble formation. Measurements were taken over two expected operating temperatures, one near room temperature (25.7 ± 0.1 °C) and at an elevated temperature (37.5 ± 0.1 °C) for improved bioactivity (Figure 6.3).

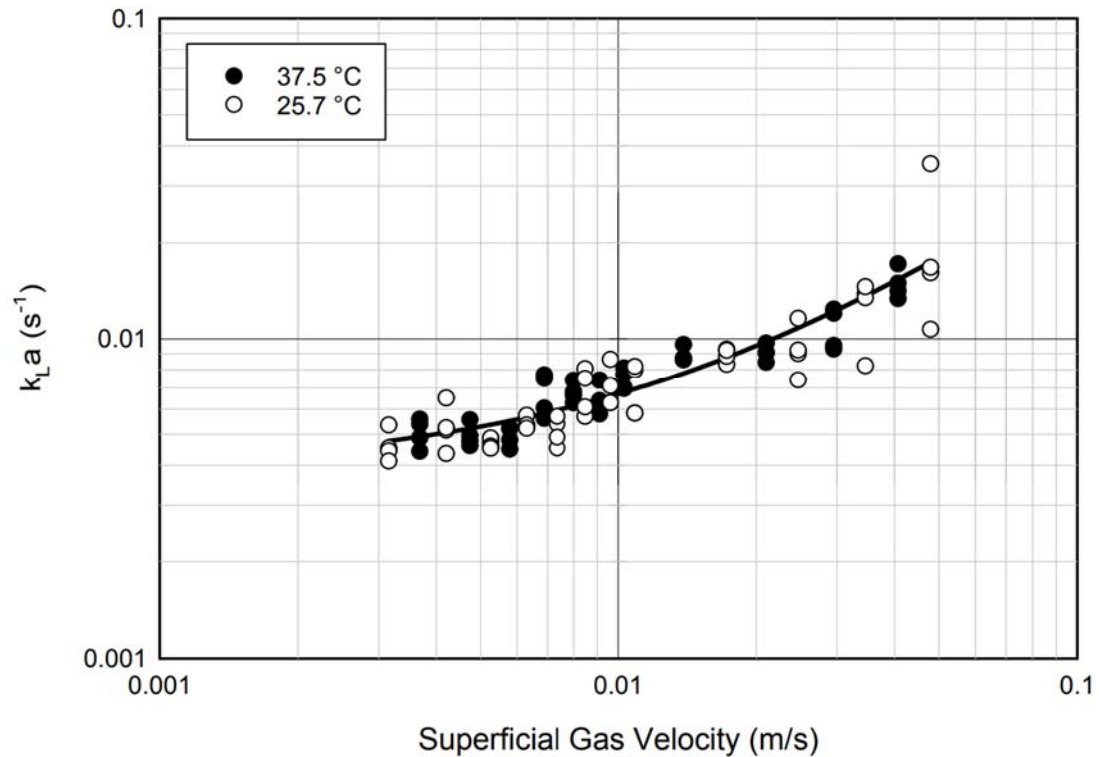


Figure 6.3 k_{LA} and U_G correlation using the dynamic air stop-start method in a semi-pilot scale airlift bioreactor.

As seen in Figure 6.3, despite best efforts to perform experiments accurately, large variations in k_{LA} values were obtained at all tested airflow levels. A general correlation could be fit to the data as a linear function, however given the logarithmic scaling in both axes the level of error in k_{LA} rises very high as U_G increases. From a practical standpoint the data is not useful for the intended purposes of optimizing the bioreactor to minimize energy losses with maximized catholyte regeneration.

Several factors were identified as contributing to the low accuracy and precision of the method in this case. These factors were primarily found to be a result of the style of the bioreactor itself in that homogenous mixing of the contents is directly related to the

aeration. During the air stoppage phase of the technique, all mixing stops and ferrous iron from the fuel cell that is necessary to induce the dynamic effects during air restart pools in one corner of the bioreactor. When aeration is restarted a brief period (1-2 minutes) of heterogenous reactor contents exists where the bioreactivity will be inconsistent throughout the broth through uneven distribution of ferrous iron and DO. Also, because the measurements of k_{LA} are inherently long to perform the entire data set was the culmination of several weeks of testing. In this time changes in the fuel cell output and biomass density of the reactor were expected to occur.

6.2.3 Shortcomings of Dynamic Methods

The most significant shortcoming in any of the dynamic methods of k_{LA} measurement is a known issue of DO probe response time resulting in serious error and discrepancies demonstrated to be up to 100% percent error in practice (Tribe et al. 1995). In fact, the observed patterns of DO probe response time error were observed in the raw data sets to strongly match those reported in the literature (Tribe et al. 1995) and a diagram of these accounts is illustrated in Figure 6.4.

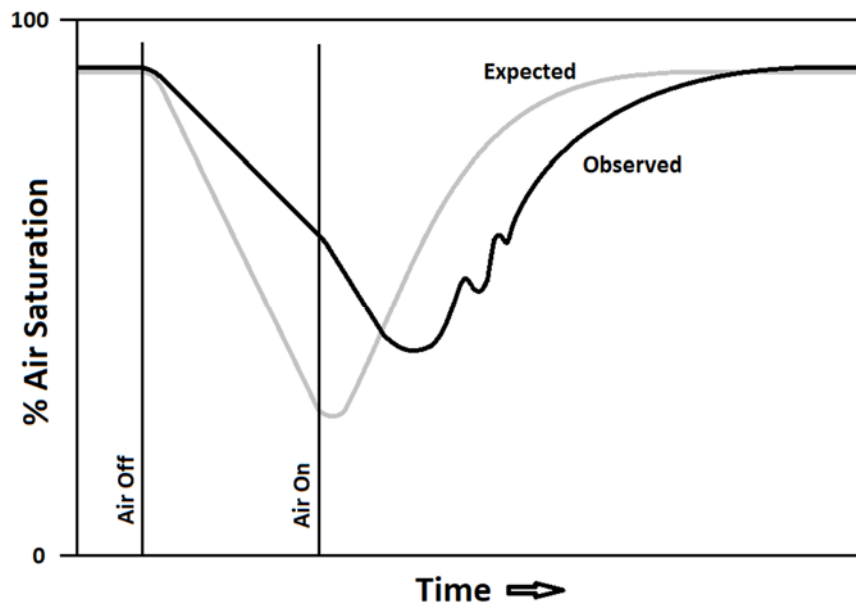


Figure 6.4 Depiction of DO probe response time error observed in an airlift bioreactor using the dynamic air stop-start method.

Major deviations occur in the observed output as a combination of both the lag induced by the responsivity of the probe and the liquid composition mixing inside the bioreactor. When airflow is stopped, liquid movement around the probe ceases which induces a lower than expected OUR where oxygen diffusion out of the probe dye is impeded by the lack of mixing in the liquid directly in contact with the probe face. It can be seen in Figure 6.4 that when airflow is restored, and hence mixing returns, a more pronounced drop in the percent air saturation reading occurs as the stored oxygen in the probe tip is emitted at a higher rate followed by an inversion as DO levels begin to rise from the aeration. The dynamic return curve as the system approaches steady state also displays characteristics of DO probe response time lag but is more difficult to see having been shifted far from the expected response by air stoppage phase. One curious phenomenon not reported in literature was small amounts of oscillatory behaviour sometimes observed in the raw data during the upswing in percent air saturation. This effect was observed to occur both in the semi-pilot scale bioreactor using the optical dye DO sensor as well as the benchtop scale bioreactor with the polarographic probe. In the case of the polarographic probe, the data resolution is too low to observe a smooth sinusoidal function and instead the DO meter appears to bounce wildly between values for a short period of time. The likely explanation for this oscillation is in the heterogenous nature of the bioreactor contents where pockets of high ferrous iron content will cause temporary oxygen depleted zones amongst highly oxygenated regions that cycle around the riser and downcomer. It has also been demonstrated that oxygen deprivation during the air stoppage phase can shock microbes which may also introduce process upset during the restart of aeration (Bandyopadhyay et al. 1967). This has not been demonstrated to be an issue with *L. ferriphilum* however and the microbes can be rapidly transitioned from an oxygen saturated state to near anoxic conditions and back again without any noticeable changes in performance.

6.3 k_{La} Measurement by Static Ferrous Step-Change

6.3.1 Development of a Novel k_{La} Measurement Technique

It is clear from the results obtained through dynamic methods that accurate measurement of k_{La} can't be achieved through these techniques and alternative methods need to be

explored. The obvious conclusion is that a new technique is needed that can measure the OTR and OUR values at the same time under steady state conditions where the response time of the DO probe is no longer a source of error. The airflow of the system in general must not be disturbed so as not to interfere with mixing and so some other parameter must be targeted. Much like the saturated DO concentration determination method developed in Chapter 5 (Section 5.2.2), the consumption of ferrous iron acting as a proxy for oxygen consumption through stoichiometry can be applied to produce a novel technique for this niche application. By combining both a DO probe and redox probe it is possible to determine k_{LA} under steady state conditions. The DO probe is used to determine the steady state c_{DO} value of the system while the redox probe having a very fast response time can be used to determine the OUR of the system through ferrous iron consumption stoichiometry. The process is achieved with a simple step change in the ferrous iron concentration by adding an excess amount to trigger a hypoxic transition and a steady state period long enough in duration to produce a visible trend. The output of the DO probe and redox probe are demonstrated in Figure 6.5 producing a distinct steady state region.

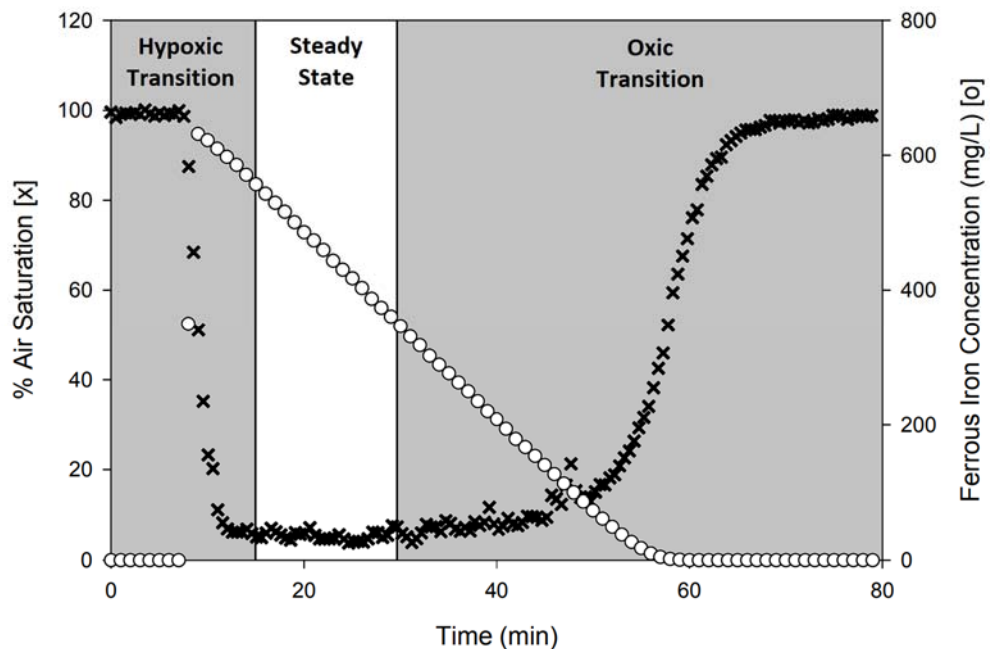


Figure 6.5 Step-change addition of ferrous iron into an airlift bioreactor and observed dynamics by a DO probe and redox probe.

In Figure 6.5 it can be seen that a steady state period is indeed formed where the DO probe levels off to a constant value and the consumption of ferrous iron by microbes is demonstrated to be linear over time. Mathematically, the process of finding k_La becomes quite simple as compared to dynamic methods of measurement as seen in Equations 6.5 and 6.6. The value of qx is found as a combined constant as the milligrams per second per liter of oxygen consumed which is equated to the milligrams per second per liter of ferrous ions consumed through stoichiometry (Equation 5.6). The technique requires knowledge of the saturated DO concentration to perform calculations which can be solved through the technique developed in Chapter 5 (Section 5.2.2).

$$\frac{dc_{DO}}{dt} = 0 = k_La(c_{DO}^* - c_{DO}) - qx \quad 6.5$$

$$k_La = qx / (c_{DO}^* - c_{DO}) \quad 6.6$$

The adequate amount of ferrous iron needed for a step-change was best found through trial and error. Too small an amount and the steady state window will not materialize and too large an amount will produce a steady state window of unnecessarily long time. As superficial gas velocities are increased the amount of ferrous sulfate added needs to be increased to accommodate the faster reaction rates. Monitoring the location of theoxic transition is also important, the dynamic behaviour in this region is slow compared to that of the hypoxic transition and the slow rise at the start may be mistaken as the steady state region if an insufficient amount of ferrous sulfate is used in the step change. The technique was applied to the semi-pilot scale airlift bioreactor at the temperatures used with the dynamic air stop-start method yielding the results found in Figure 6.6. The increased accuracy and precision produced as a result of the technique are immediately clear. Formation of a trend can be produced from just single trials at differing superficial gas velocities which greatly reduces the experimental time from weeks to days to acquire a reliable trend. The accuracy is high enough to differentiate temperature effects on the k_La value, holding all other variables constant, and demonstrates the correct pattern observed in literature where higher temperatures produce greater values of k_La (Chern and Yu 1997, Vogelaar et al. 2000). The trend was found to be best fit to a linear relationship however with increasing superficial gas velocity the trend may better fit a

power trend. Distortion of the trend line in Figure 6.6 is caused by the disproportionate logarithmic scaling on both axes.

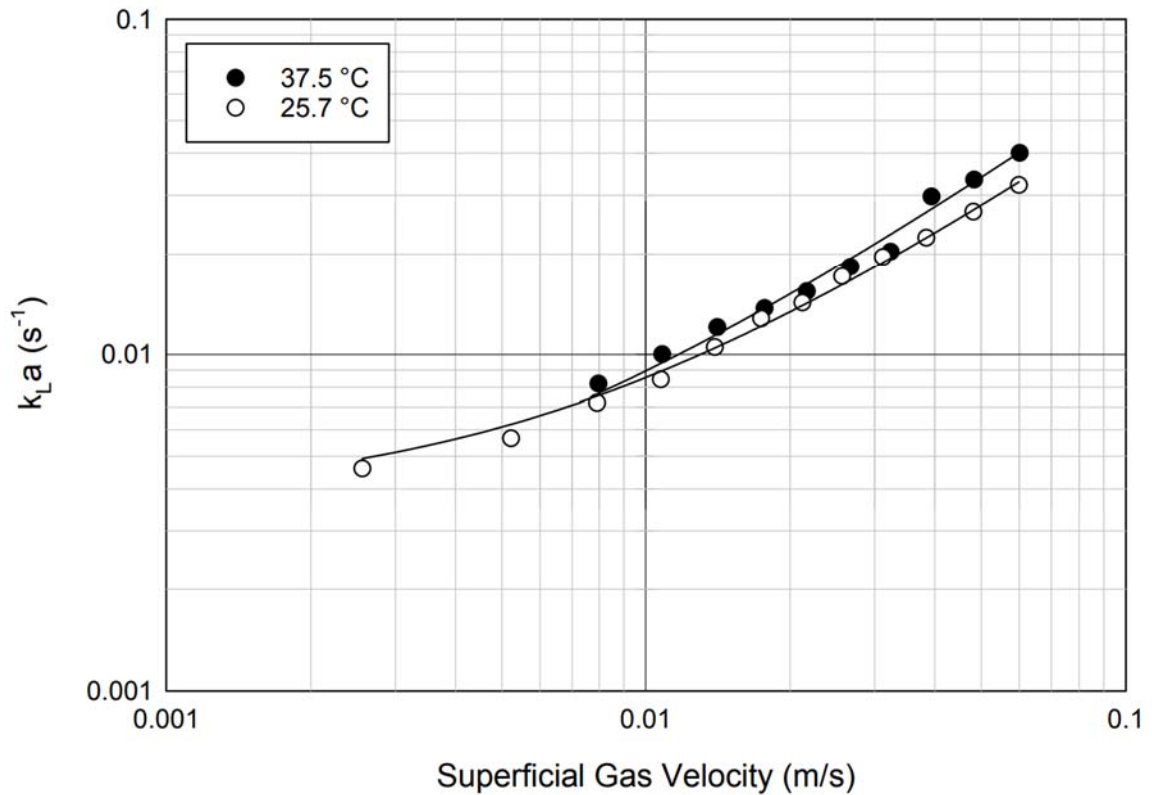


Figure 6.6 k_{La} and U_G correlation using the static ferrous step-change method in a semi-pilot scale airlift bioreactor.

The k_{La} with respect to U_G in the semi-pilot scale is represented by Equation 6.7 (at 25.7 °C) and Equation 6.8 (at 37.5 °C).

$$k_La = 0.6244U_G + 0.0027 \quad 6.7$$

$$k_La = 0.4865U_G + 0.0037 \quad 6.8$$

6.3.2 k_{La} Measurement in a Pilot Scale Airlift Bioreactor

The static ferrous step-change method was applied for practical use on a pilot scale airlift bioreactor operating at 20.2 ± 0.1 °C with an iron ion concentration in the broth of 47.5 g/L. The findings of the k_{La} measurement are in accordance with the power relationship

expected from a square airlift bioreactor (Liu and Hermanowicz 2008) and are plotted logarithmically against superficial gas velocity (Figure 6.7) along with a plot against the vessel volumes per minute of airflow (Figure 6.8). The results maintain a high level of precision in a real-world application and will allow optimization of the bioreactor internals to achieve the best k_{LA} performance possible. The performance overall was not as good as was demonstrated with the semi-pilot scale version. Though this was more than likely due to a design flaw in the pilot scale regarding the sparger. During construction the sparger was mounted with the holes facing upwards and could not be accessed to rotate them to point downward. With the holes positioned upwards the incoming air is unable to fully clear the sparger tube of liquid and an uneven distribution of bubbles is produced in the riser.

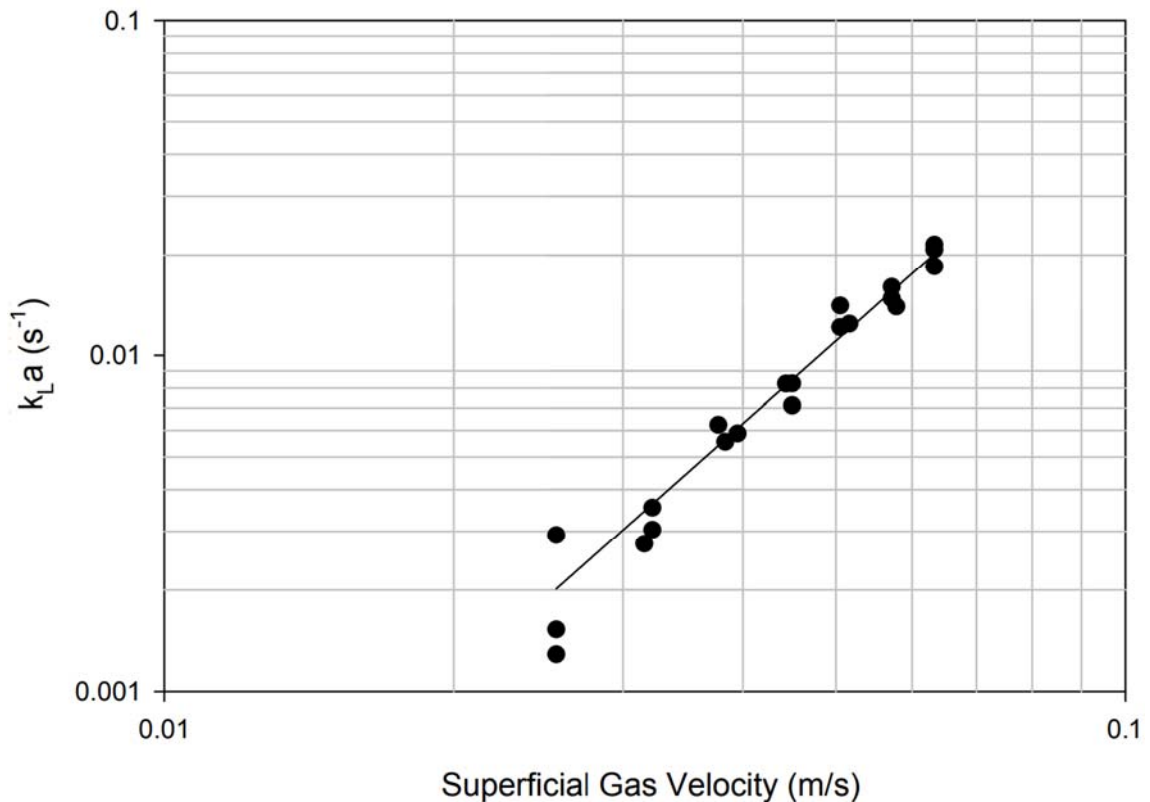


Figure 6.7 Relationship of k_{LA} to U_G of a pilot scale BioGenerator.

The data obtained demonstrates a high level of correlation and corresponds to the curve fit in Equation 6.9. A notable source of error along the k_{LA} axis was observed with

respect to changes in the bioreactor liquid level height. Small variances between the amount of liquid removed from the bioreactor prior to addition during the ferrous iron step-change procedure likely interferes with bubble interactions at the top of the liquid. Small height changes at the top of the reactor likely affect the undertow behaviour as liquid from the riser crests over the divider wall into the downcomer, which has been observed in the benchtop scale bioreactor to draw air bubbles into the packed bed and retain them.

$$k_L a = 35.283 U_G^{2.696} \quad \mathbf{6.9}$$

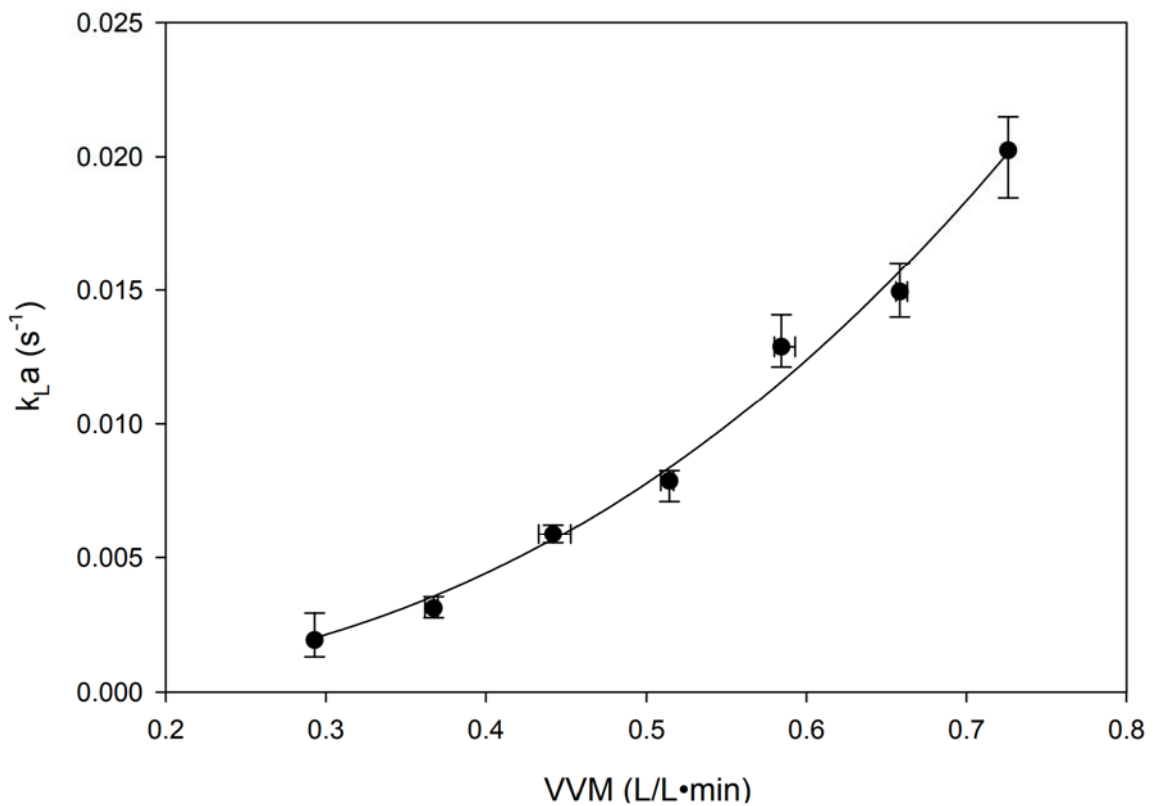


Figure 6.8 Relationship of $k_L a$ to VVM of a pilot scale BioGenerator

The curve fit of the relationship of $k_L a$ to VVM in Figure 6.8 is given as Equation 6.10.

$$k_L a = 0.490 VVM^{2.696} \quad \mathbf{6.10}$$

6.4 Summary of Chapter 6

The average mass transfer coefficient (k_{LA}) was analyzed between a benchtop scale, semi-pilot scale, and pilot scale BioGenerator system. Initial study of the k_{LA} proceeded using a benchtop airlift bioreactor but was found to suffer from wall effects that interfered with the possibility of any realistic comparisons. A semi-pilot system was chosen as its replacement using a commonly performed dynamic air stop-start method to yield k_{LA} but was found to give excessive variance in this application. A unique method of k_{LA} determination for application with iron oxidizing microbes was formulated based on a step-change of ferrous iron in the system while leaving air flow untouched and taking readings at static (steady state) condition. The new method proved to be much more precise, allowing the capability to fine tune bioreactor parameters needed for optimizing operational energy efficiency. The findings from both the semi-pilot scale and pilot scale system were similar and agreed with the literature on similar rectangular airlift bioreactors in terms of the magnitude of k_{LA} to the superficial gas velocity. The results suggest that the sparging action is currently underperforming compared to literature and is likely due to poor bubble break-up at the air outlets of the sparge tube.

Chapter 7

7 Kinetic Study of the BioGenerator

The bioreactor broth of the BioGenerator is a corrosive mixture of aqueous iron sulfate dominated by ferric ions (~40 g/L) with the inclusion of nutrient salts and acidified with sulfuric acid to a pH below 1. The chemical composition and operating conditions of the broth are constrained by multiple factors such as electrochemical compatibility with fuel cells, biological compatibility with biooxidizing microbes, process stability, and the long term effects of surface fouling. With the goal of commercialization of the technology in mind these aspects need to be balanced to achieve the best economic return on investment. While the BioGenerator contains many other components to its operation, the broth characteristics represent the factor with the most room for adjustment and tuning of overall performance. An analysis of the major operating parameters of the BioGenerator at pilot scale is necessary as to the date of this work it has not yet been completed outside a laboratory setting. Specifically, the dynamic behaviour of the bioreactor under the given application is in question where periods of sudden high ferrous iron production will be encountered followed with its absence in accordance with the needs of energy production on the grid. These dynamics represent process start-up instability where ferrous ions are suddenly introduced into the broth and a period of microbial adjustment is likely to be encountered.

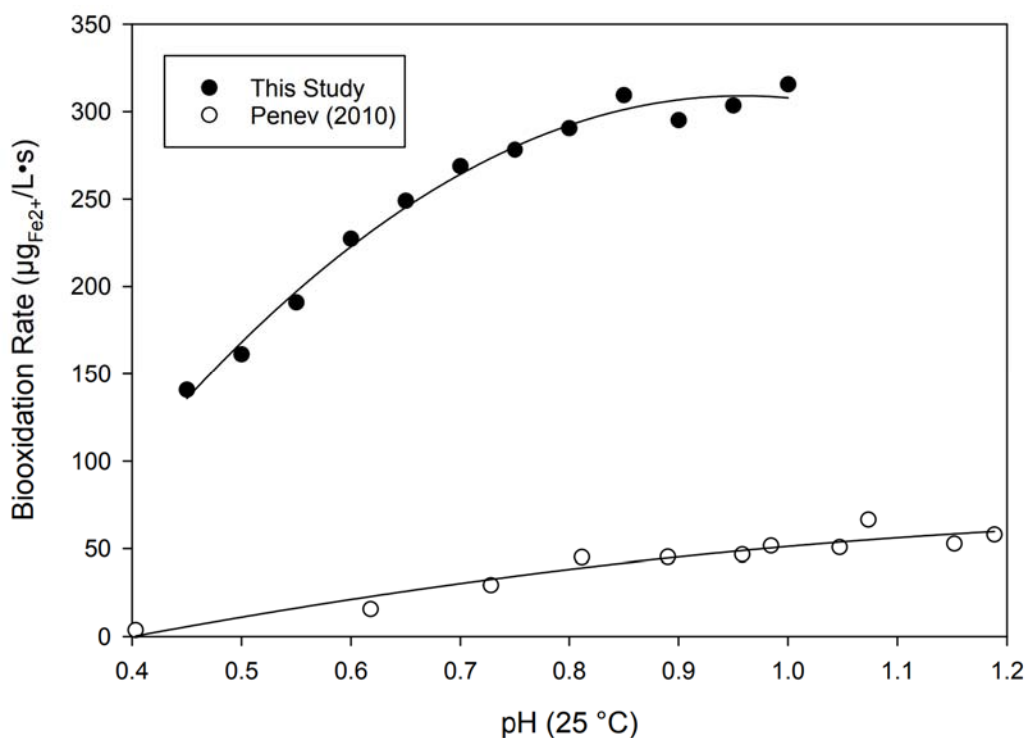
7.1 Biological Aspects

The principal iron oxidizing microbe in the BioGenerator used in this study is *L. ferriphilum* and has been in continuous use in the bioreactor under hyperacidophilic conditions for more than 15 years. Optimizing the BioGenerator of course starts with the determination of the best operating conditions for the microbes which allow the BioGenerator to function. When first isolated by Coram and Rawlings in (2002) it was reported that the microbe had an optimum pH between 1.4 and 1.8 with optimum temperatures from 30 to 37 °C with some isolates demonstrating growth at 45 °C. Other sources place the optimum pH and temperature similarly as given in Table 7.1.

Table 7.1 Optimal temperature and pH of select *L. ferriphilum* strains.

pH	T (°C)	Strain	Source
1.6	40	YSK	Gao et al. 2007
1.7	40	D1	Liu et al. 2007
1.5 - 2.0	39	ATC 49881	Plumb et al. 2008
1.6	40	YTW315	Zhang et al. 2010
1.0 - 2.0	30 - 45	-	Bernardez et al. 2021
1.5	40	CC	Vardanyan et al. 2023

A study of pH and temperature effect on biooxidative activity in the case of the BioGenerator by Penev (2010) gave similar results as well with a plateaued optimum pH from 1.0 to 2.0 and temperature optimum of 42 °C. This study was completed 14 years prior and given the operating conditions of the BioGenerator (pH ~0.8) a potential for microbial strain differentiation exists. Therefore, pH and temperature optimum studies were revisited to establish any changes in the microbial culture since then. An analysis of biooxidation rates with respect to pH was performed in broth extracted from a functioning bioreactor with a ferric ion content of (~40 g/L) and temperature of ~20 °C as seen in Figure 7.1.

**Figure 7.1** Biooxidation rate of *L. ferriphilum* in the BioGenerator with respect to pH.

A noticeable improvement in acid resistance by the current *L. ferriphilum* is observed appearing to be shifted by -0.3 pH units from the original natural culture and demonstrating an optimum pH plateau closer to pH 0.85. This is very desirable as the production of ferrous iron by fuel cells produces an expected drop in pH directly affecting the biooxidation rate. In a laboratory setting where a fuel cell is run continuously at constant current to feed the microbes this can lead to a runaway depletion of ferric ions in the bioreactor resulting in a near total conversion of the broth to ferrous sulfate which takes a long time (~1 week) to be reconverted back to a state of majority ferric ion content. The length of this period comes as a result of both the slow biooxidation rate in general but also a drop in cell concentration as the slow biooxidation results in starvation and increased death rate of the microbes during this period. In a commercialized application the primary issue is in the practical ferric iron concentration that can be used. Increasing the concentration yields better efficiency where the fuel stack voltage will not drop as quickly in accordance with Nernstian principles as the ferrous to ferric ion ratio is increasingly reduced given the same power draw. This, however, comes with a greater rate of pH drop as the catholyte is depleted and therefore the catholyte consumption must be restricted to some lower limit so as not to severely occlude biooxidation rates. In other words, improved biooxidation rates at lower pH values allow for a greater concentration of catholyte and yields improvement in efficiency as well as in the maximum discharge potential.

It should be noted that the biooxidation rates in Figure 7.1 between the two data sets show significant difference though this comparison is completely arbitrary. The difference in perceived overall bioactivity is the result of differences in cell concentrations used in analysis as well as the apparatus and procedures used in the collection of the data. The biooxidation rates recorded from this study are more in line with that seen from a functional airlift bioreactor while the results of Penev (2010) were obtained from averages of batch reaction in shake flasks.

A re-analysis of optimum temperature profile for the current *L. ferriphilum* was also performed, however changes from the original culture were not expected to be observed as the BioGenerator is operated near 40 °C which is near the optimum given in literature

(Table 7.1), and no natural selection pressure exists. In any case the analysis was performed as given in Figure 7.2 and agrees with the presumption that no change would be found. An optimum temperature of roughly 45 °C was found and the Arrhenius behaviour matches what was originally observed by Penev (2010).

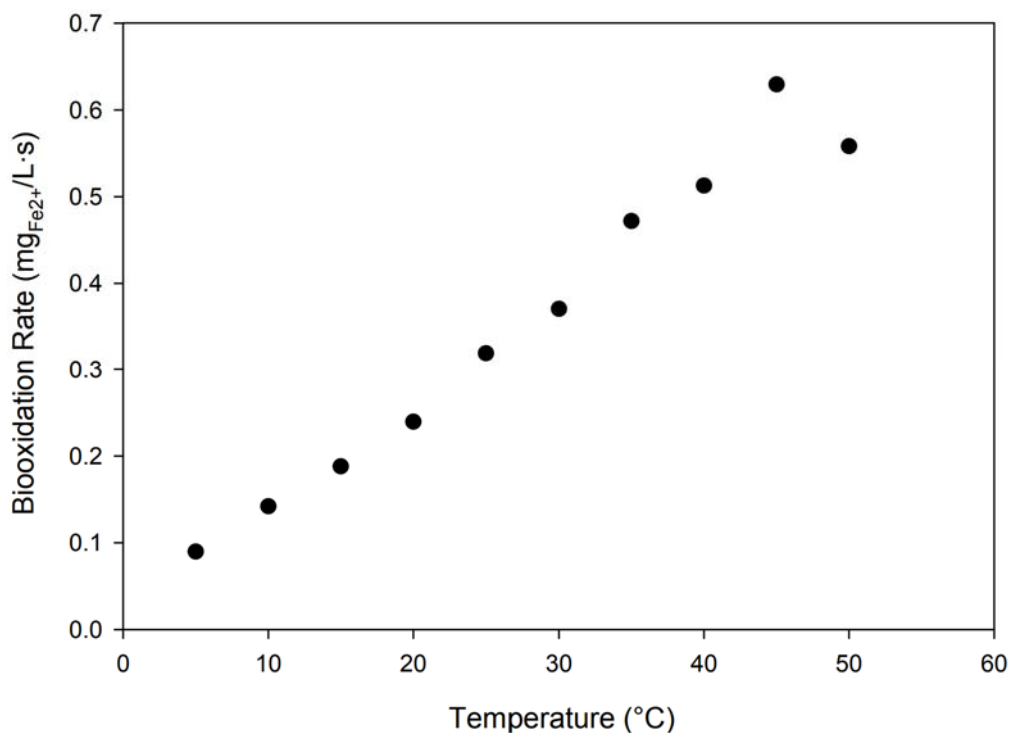


Figure 7.2 Biooxidation rate of *L. ferriphilum* in the BioGenerator with respect to temperature.

7.2 Chemical Aspects

In a strictly chemical sense, the stability of the broth is also a significant constraint in the selection of operating conditions, mostly as a factor of the upper pH limit. The primary issue is in the production of mineral deposits that coat surfaces exposed to the broth and is therefore most concerning to the effects on the fuel cell operation, specifically the coating of the PEM and active sites of the cathode felt which will hinder ion transport and diminish electrochemical activity. These mineral deposits are termed “jarosite” which is used in the more technical sense as ferric ion containing crystalline formations as part of the alunite supergroup of minerals with the general chemical formula given by Equation

7.1. where $A = K^+, Na^+, NH_4^+, H_3O^+$; $M = Al^{3+}, Fe^{3+}$; $T = S^{6+}, As^{5+}, P^{5+}$ (Jambor 1999). In some cases, A may be occupied by ions $Ca^{2+}, Ba^{2+}, Pb^{2+}, Bi^{3+}$, and trivalent rare earths.



In the case of the BioGenerator the exact formulation of the “jarosite” is likely a combination of hydronium jarosite $[(H_3O)Fe_3(SO_4)_2(OH)_6]$ and ammoniojarosite $[(NH_4)Fe_3(SO_4)_2(OH)_6]$ with traces of jarosite $[KFe_3(SO_4)_2(OH)_6]$ (Jambor 1999) where the ammonium and potassium ions are provided by the nutrient growth salts. In this work the term jarosite will be used in the technical sense encompassing the various specific mineral species constituting the deposits.

Given the highly entropic composition of jarosite, the appearance of agglomerate growth may appear as a thin rough yellow-orange scale or in cases where the deposits have built up over a longer term appear as a highly textured orange-brown scale with protruding flakes (Figure 7.3). The formation of jarosite is evidenced to occur both through growth on existing deposits as well as particulate nucleation from within the solution which grow in size and eventually settle out in undisturbed solutions contributing to thick deposits on the bottom. Microcrystalline jarosite suspended in solution gives the appearance of turbidity, consisting of spheroid particles with average diameters on the order of 0.5 – 5.0 μm and must therefore be viewed through electron microscopy (Gao et al. 2019, Ryu and Kim 2022, Smith et al. 2006). Elimination of these suspensions was achieved where needed with use of a 0.45 μm pore size mixed cellulose ester filter (Whatman 7141-104) along with the use of a spectrophotometer in scan mode as a before and after affirmation.



Figure 7.3 Severe mineral depositing of jarosite.

The formation of jarosite is highly dependent on the pH of the medium, below pH ~1 jarosite formation does not occur but where the broth is higher than this a linear increase in formation rate is observed up to pH ~2 (Daoud and Karamanev 2006, Dutrizac 1996). For this reason, the BioGenerator is operated at pH ~0.8 to eliminate the issue of jarosite formation entirely, however this acidity is not the most favourable for the biological aspect where it can be seen in Figure 7.1 that biooxidation rate drops off quickly once pH dips below 0.8 which will occur during operation. Determination of the exact point at which jarosite formation stops under the BioGenerator operating conditions was performed to better pinpoint the highest allowable pH of the system. The production rate of jarosite over a six month period with respect to pH levels is given in Figure 7.4.

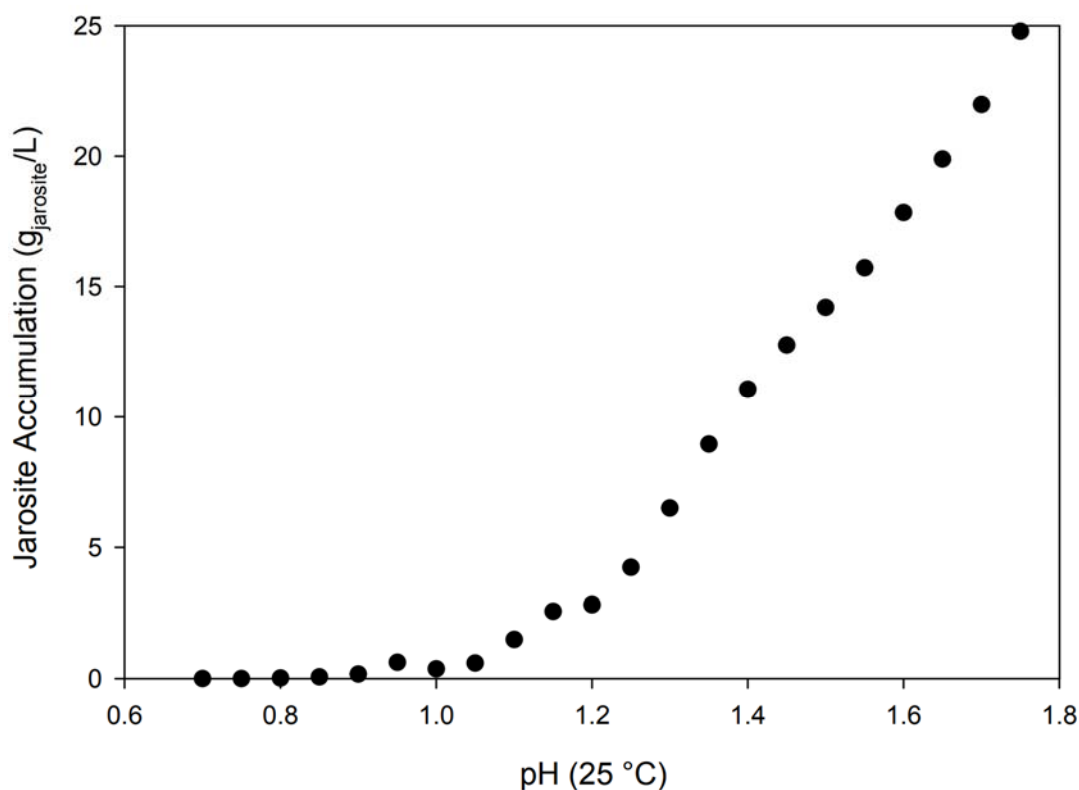


Figure 7.4 Acidity effects on jarosite accumulation in the BioGenerator.

The findings of Figure 7.4 are found to agree with the literature where the production demonstrates a linear relationship down to pH 1.00. The point of interest however is in the observation that jarosite formation does not completely stop at pH 1.00 and still forms in trace amounts down to pH 0.85 which was also confirmed by observing the surface

deposits with the naked eye. Operation of the BioGenerator at pH 1.00 would be much more beneficial from the biological aspect as a pH shift from 1.00 to 0.80 for instance produces a negligible effect on biooxidation rates (Figure 7.1).

Some potential possibilities to eliminate trace jarosite production were explored through dissolution of the deposits. One such method might make use of the addition of sulfate reducing bacteria to consume the sulfate component of the jarosite and release the remaining ions or transform the jarosite to freed goethite or vivianite that can be filtered from the broth (Gao et al. 2019, Gao et al. 2020). These biological processes require anaerobic conditions and are rather slow and not suited to the BioGenerator. In other cases, the addition of chlorine containing acids are presented such as that of concentrated perchloric acid, though these compounds are likely to have toxic effects (Smith et al. 2006).

Solving the issue with broth additives adds an additional dimension to system complexity and none of the explored possibilities present a viable solution that does not significantly interfere with the functioning of the bioreactor microflora. Meeting the objective of operation at pH 1 does not need to be needlessly complicated however and can likely be solved with proper process control. Given that in practice the BioGenerator fuel cells will be expected to be fed with catholyte only for a portion of the day, the fuel cells could be fed with a cleaning/rejuvenating solution of highly acidic water in the interim. This would serve to wash away and dissolve microcrystalline jarosite while also acting to leach ferric ions out of the PEM to maintain high electric current production. The production of jarosite scale would then be limited to the insides of the airlift bioreactor which may be beneficial to act as a microbial support for immobilization of bacteria. Though current literature only specifies the use of jarosite as an observed microbial support for *At. ferrooxidans* (Pogliani and Donati 2000, Zhou et al. 2006).

7.3 Restart Dynamics

7.3.1 Dynamics of a Benchtop Scale BioGenerator

Predicting the restart dynamics of the BioGenerator with respect to the substrate (ferrous ion) concentration can be made through the material balance of the bioreactor where the

rate of change in substrate concentration (dS/dt) in the reactor volume (V_r) is equal to the substrate entering the bioreactor by the fuel cell minus the amount leaving to the fuel cell and that consumed through biooxidation as given by Equation 7.2. This was demonstrated at the benchtop scale through the use of a trickling bed bioreactor arrangement operated at 40 °C. Given that the formation of biomass is minimal through the biooxidation reaction, the substrate consumption rate is given as Equation 7.3 made up of the following variables; the maximum specific growth rate (μ_m), the microbial concentration (x), the substrate/biomass yield coefficient (y), the effectiveness factor as mass transfer limitations through biofilm (η), and the Michaelis constant (K_s).

$$V_r \frac{dS}{dt} = \dot{F}S_{in} - \dot{F}S_{out} - V_r r_s \quad 7.2$$

$$r_s = \frac{\mu_m x}{y} \frac{S}{K_s + S} \eta \quad 7.3$$

Since it has been shown that the Michaelis constant for the microbial culture in the BioGenerator is equal to 0.0067 g/L (Penev and Karamanev 2010), the substrate consumption rate equation can be greatly simplified where $S \gg K_s$ during substrate production giving the approximation in Equation 7.4 stating that the biooxidation rate can be considered a constant.

$$r_s \approx \frac{\mu_m x}{y} = \text{constant} \quad 7.4$$

The specific behaviour of substrate concentration can then be mathematically defined during a stop and restart cycle. During substrate stoppage the biooxidation rate is equal to the observed rate of change in substrate concentration over time as given by Equation 7.5. When substrate generation restarts, an initial unsteady-state period will exist according to Equation 7.6 followed by the return to steady-state conditions as Equation 7.7.

$$r_s = -\frac{dS}{dt} \quad 7.5$$

$$r_s = \frac{\dot{F}}{V_r} (S_{in} - S_{out}) - \frac{dS}{dt} \quad 7.6$$

$$r_s = \frac{\dot{F}}{V_r} (S_{in} - S_{out}) = \text{constant} \quad 7.7$$

These three periods represented by mathematical functions can be represented graphically as Figure 7.5. Specific time periods are defined as the substrate stoppage period (t_s), the zero substrate concentration period (t_o), and the time period to reach steady state (t_h). The exact behaviour of the dynamics during the t_h phase require experimental observation and can be predicted to follow one of several possibilities; the steady state substrate concentration (S) shows a long-term increase (1), the substrate concentration may show a short term overshoot (S_h) and return to the previous concentration (2), or the steady state substrate concentration may simply return to the previous level (3).

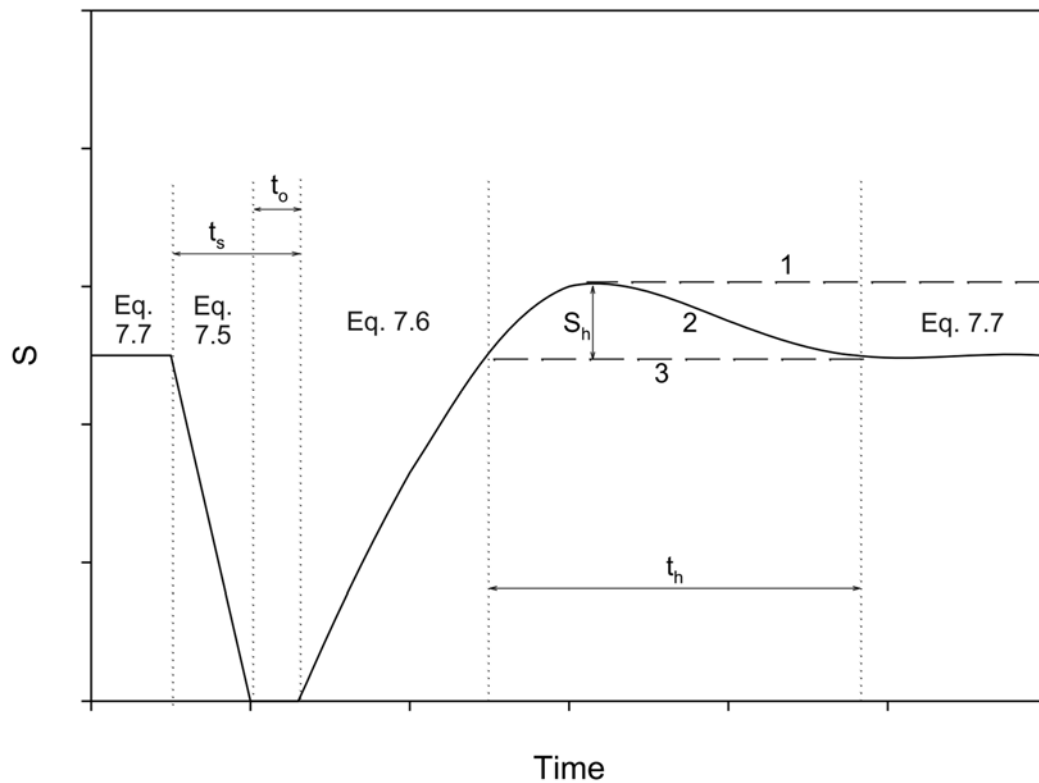


Figure 7.5 Predicted change in substrate concentration as a result of feed flow interruption and restart.

Given that the feed stoppage is expected to happen once per day in accordance with daily grid power supply and demand mismatch, stoppage periods were constrained to a

maximum substrate stoppage period of one day. Stoppage periods of 6, 18, and 24 hours were chosen. A 6 hour run was used as the benchmark for the minimum time period that allowed the substrate to fall to zero while the 24 hour run was set as the maximum. An 18 hour stoppage period represented a better fit to a real world scenario of energy production for 6 hours and then off for the rest of the day. The dynamic response for the three scenarios can be seen in Figures 7.6, 7.7, and 7.8.

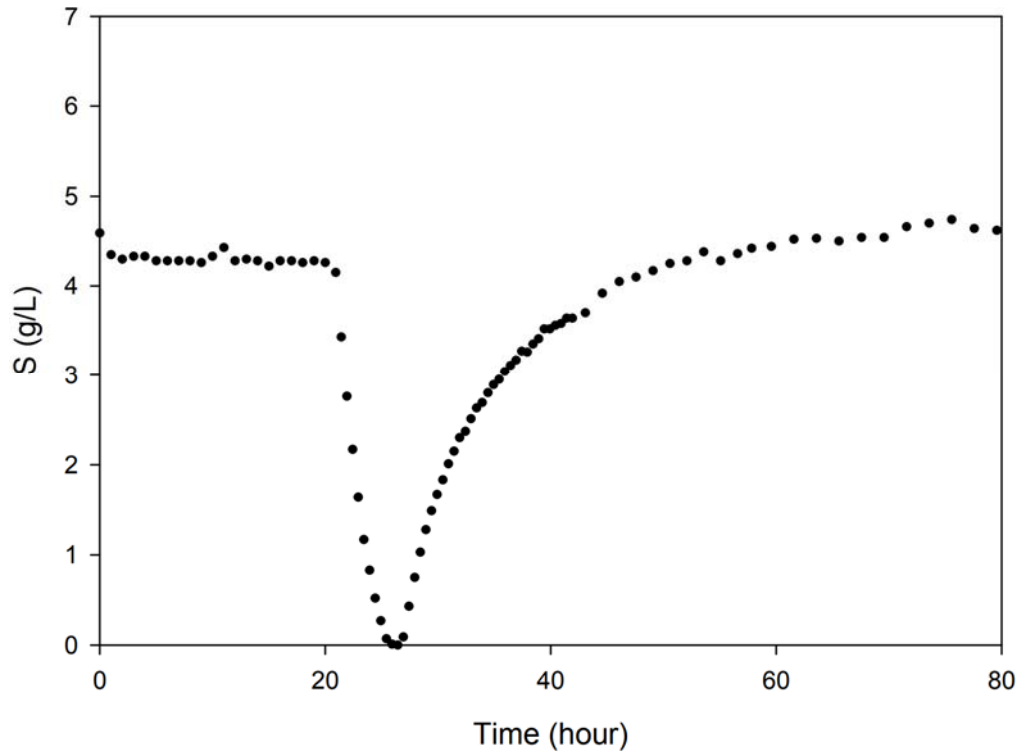


Figure 7.6 Dynamics of a benchtop scale 6 hour feed stoppage.

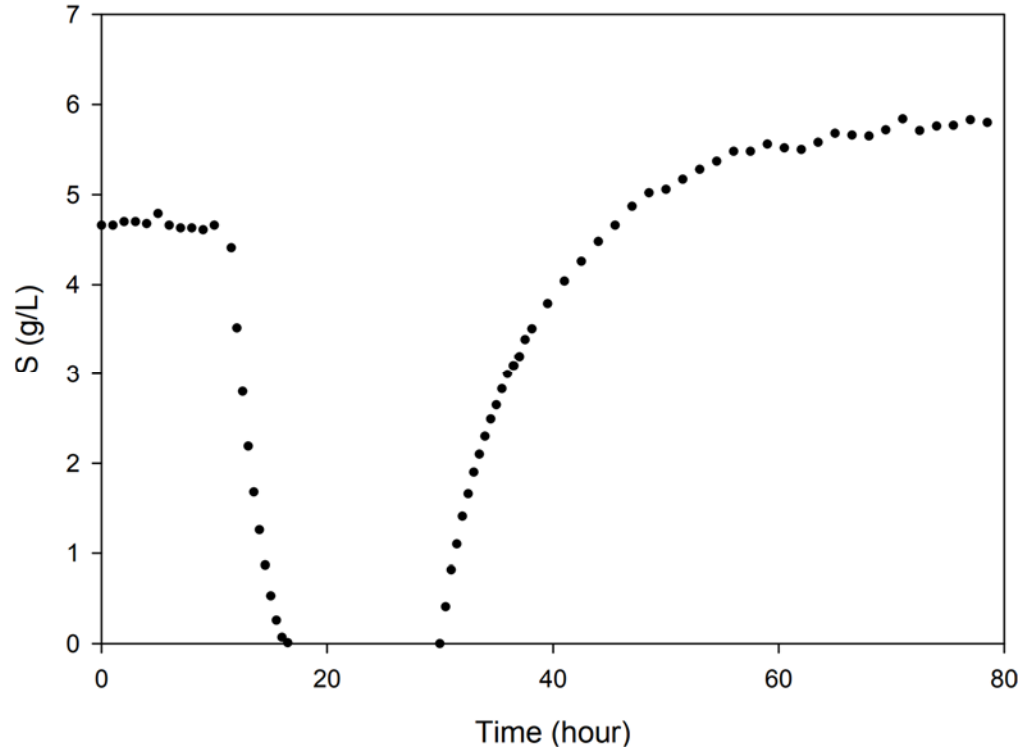


Figure 7.7 Dynamics of a benchtop scale 18 hour feed stoppage.

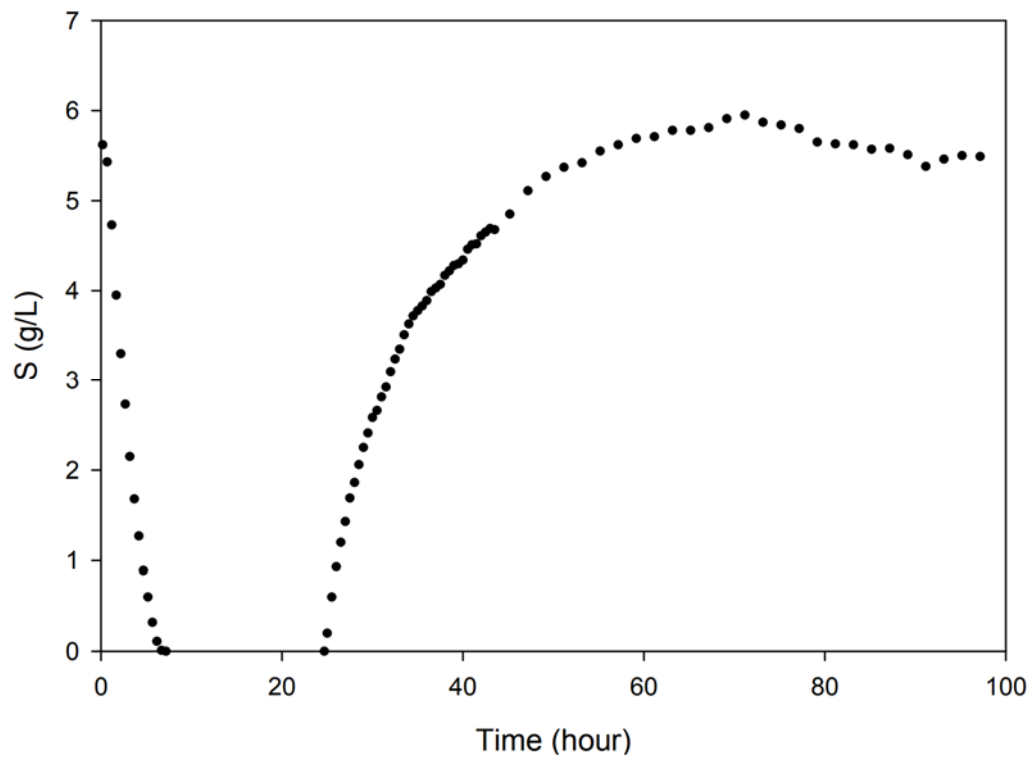


Figure 7.8 Dynamics of a benchtop scale 24 hour feed stoppage.

The dynamics observed between runs were found to give all three types of anticipated pattern, often demonstrating combinations of both overshoot and offset from the starting concentration. A definitive pattern in the dynamic responses corresponding to the t_s period wasn't clearly demonstrated. The only significant correlation between the observed behaviours was in the steady state concentration which always fell between a range of 4 to 6 g/L. Due to this behaviour the steady state substrate concentration at the start of experiments also varied and this was anticipated to play a role in the observed behaviour as well. These results indicate that a hysteresis effect is probable and can be explained mathematically with Equation 7.8 that equates the substrate production to the electrical power generation. Variable W represents the electrochemical production rate as the multiplication of the Faraday constant (F), the molar mass of iron (m), the electric current (i), and the ion valance charge exchange (z) which is 1 in this case. Equation 7.8 may then be combined with Equation 7.7 to yield Equation 7.9 which directly couples the biooxidation rate to the electrochemical production rate.

$$\dot{F}(S_{in} - S_{out}) = \dot{F}(S_{in} - S) = W = z\dot{m}i/F \quad 7.8$$

$$r_s = \frac{\dot{F}}{V_r}(S_{in} - S) = \frac{W}{V_r} = constant \quad 7.9$$

Equation 7.9 demonstrates that if the electrochemical production rate is held constant with an external constant current load and the bioreactor volume is also fixed, then any hysteresis effects must be a result of changes to the biooxidation rate. Specifically, the value of the substrate/biomass yield coefficient is altered by changes to temperature and pH, in this case temperature is held constant however the pH is directly coupled to S through Equation 5.6. Therefore, the biooxidation rate is linked to the value of S and at steady state may stabilize within a range of values. This also means any overshoot is likely to lock the steady state value of S at an offset higher than the starting point where the pH decreases and in turn so does the biooxidation rate. This was further evidenced with a short interruption in substrate feed for 3 hours that did not reduce S to zero and didn't generate any overshoot effects, demonstrating a reset effect seen in Figure 7.9.

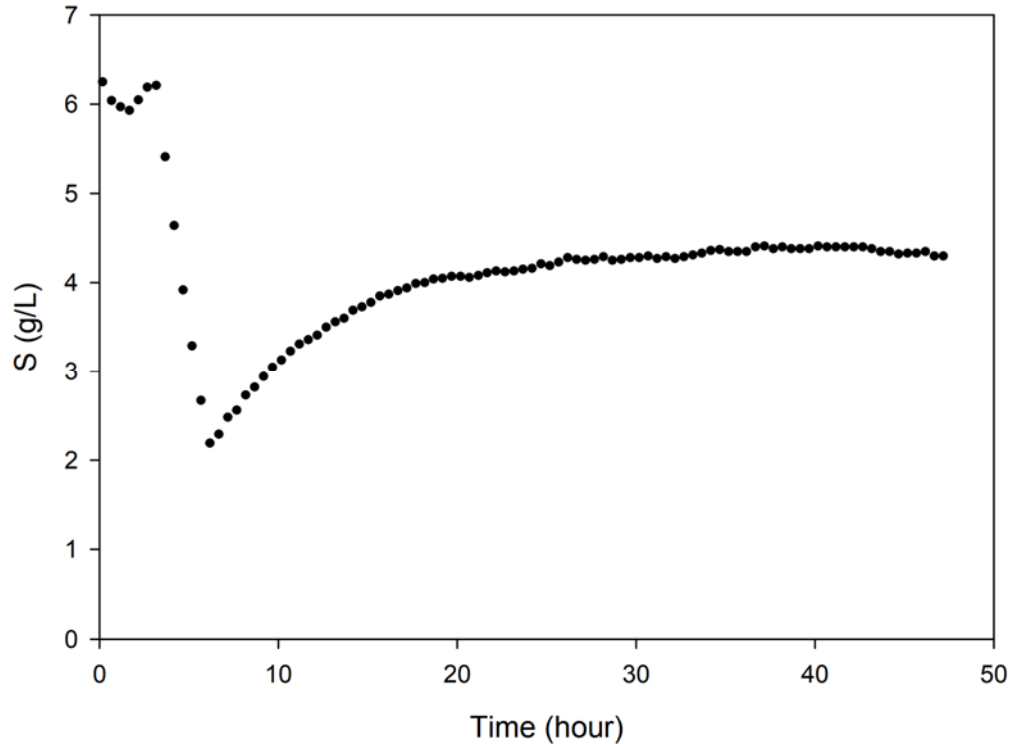


Figure 7.9 Dynamics of a benchtop scale 3 hour feed stoppage.

There is also the question of level of overshoot S_h which appears to be linked to the period of t_o , where the longer an absence of substrate occurs the greater the level of overshoot. The likely explanation is also an effect on the biooxidation rate (Equation 7.9) where starvation will undoubtedly lead to cell death and a reduction in the microbial concentration x . With less microbes available at restart the value of S would be expected to surpass its starting point as ferrous ions build up and at some later time the microbial concentration will build up to its previous steady state level and produce a dip in S back towards the starting value of S . This is observed in Figure 7.8 and would be expected where greater cell deaths would cause this effect to become accentuated. The effect of microbial death rates in the absence of substrate was examined when stored at temperatures of 20 °C and 40 °C respectively in Figure 7.10 and demonstrates a linear reduction in bioactivity over time from the moment substrate in solution is depleted. A lower operating temperature, despite having an overall lower biooxidation rate, can be expected to produce a much more stable operation which is desirable.

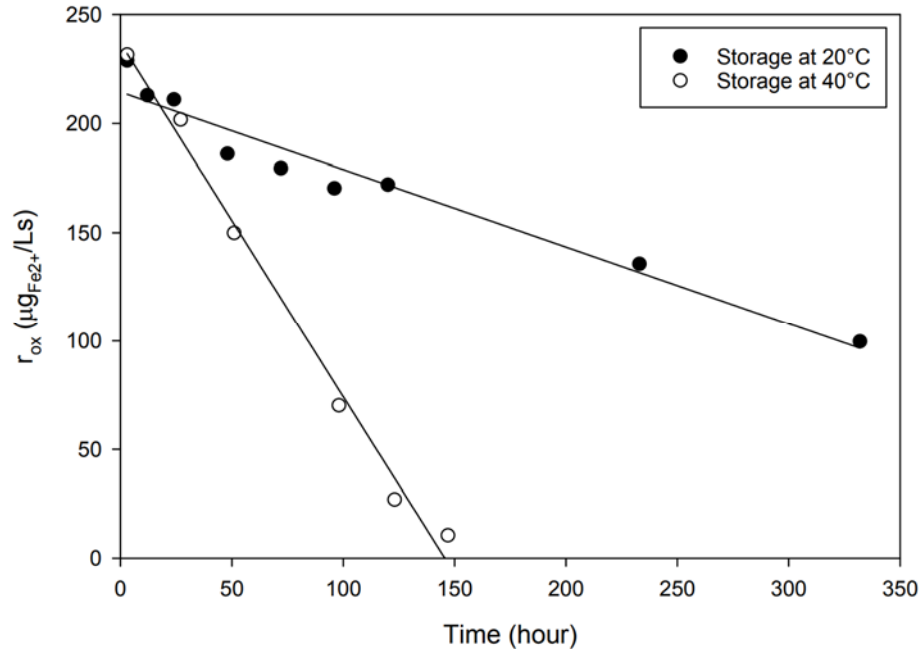


Figure 7.10 Reduction in biooxidation rate as an effect of microbial death in broth stored without substrate.

7.3.2 Dynamics of a Pilot Scale BioGenerator

Given the findings of the benchtop experiments, the operating temperature of 20 °C used in the pilot scale BioGenerator should be expected to demonstrate reduced restart dynamics which is more favourable for operation. A substrate stoppage period of 24 hours was examined at pH levels in fully oxidized broth set at 1.0, 0.9, and 0.8 as shown in Figure 7.11 at the beginning of the stoppage and later at the restart of substrate in Figure 7.12. No dynamics in the form of overshoot or offset were detectable. However, the fuel cells used in the pilot scale were not able to keep a high steady state substrate level in the bioreactor and as a result the redox probe was operating near the limit of its resolution. A better method of detecting dynamic behaviour was found to be through DO measurements and a similar 24 hour stoppage was performed with the beginning of the stoppage in Figure 7.13 and later at the restart of substrate production in Figure 7.14. Similarly, no relevant overshoot or offset phenomenon was detected which is desired for commercialization of the BioGenerator. Some variances over time in the steady state DO level can be seen but is more likely to be a result of other factors affecting the air blower performance such as air temperature and line voltage variance.

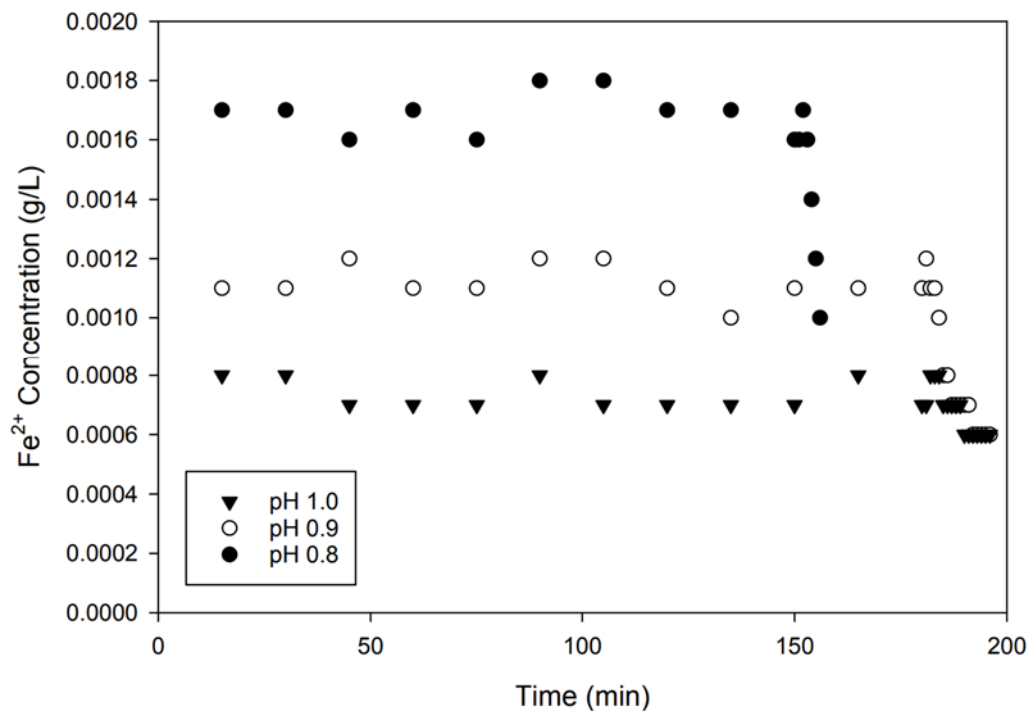


Figure 7.11 Redox probe readings of pilot scale at time of initial substrate stoppage.

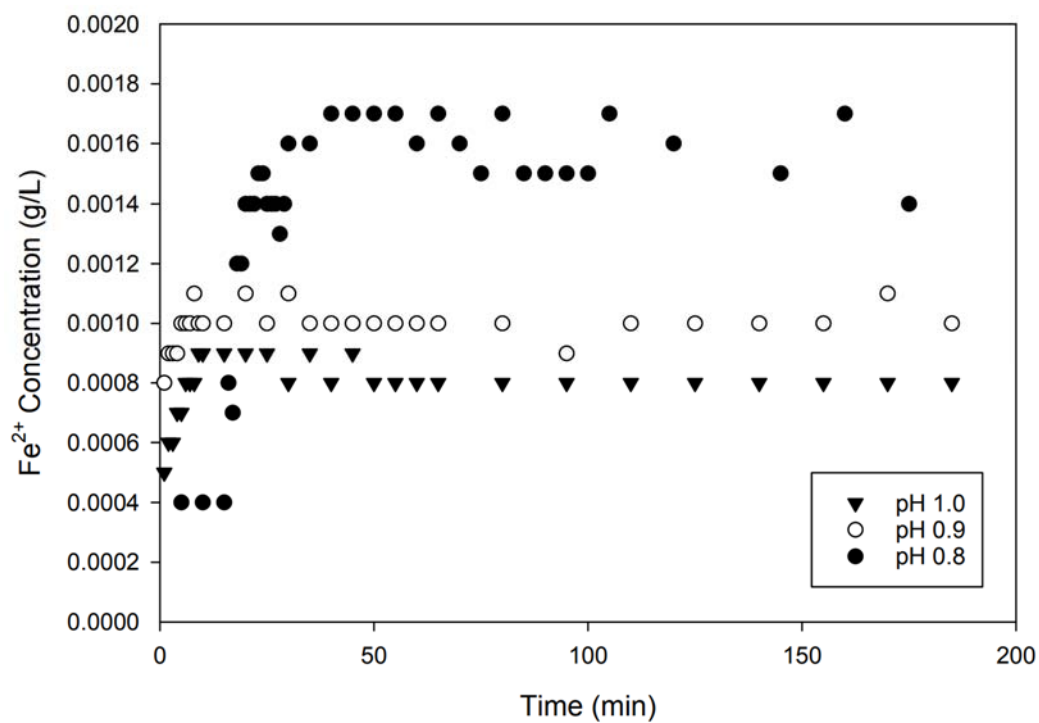


Figure 7.12 Redox probe readings of pilot scale after 24 hour substrate stoppage.

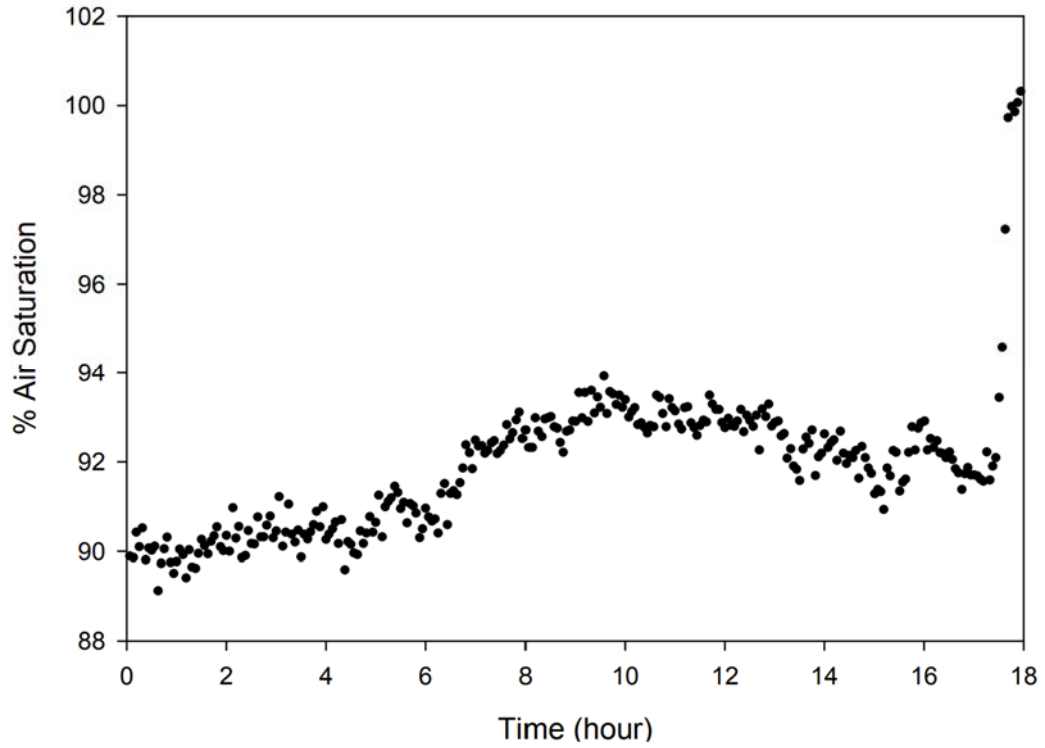


Figure 7.13 DO probe readings of pilot scale at time of initial substrate stoppage.

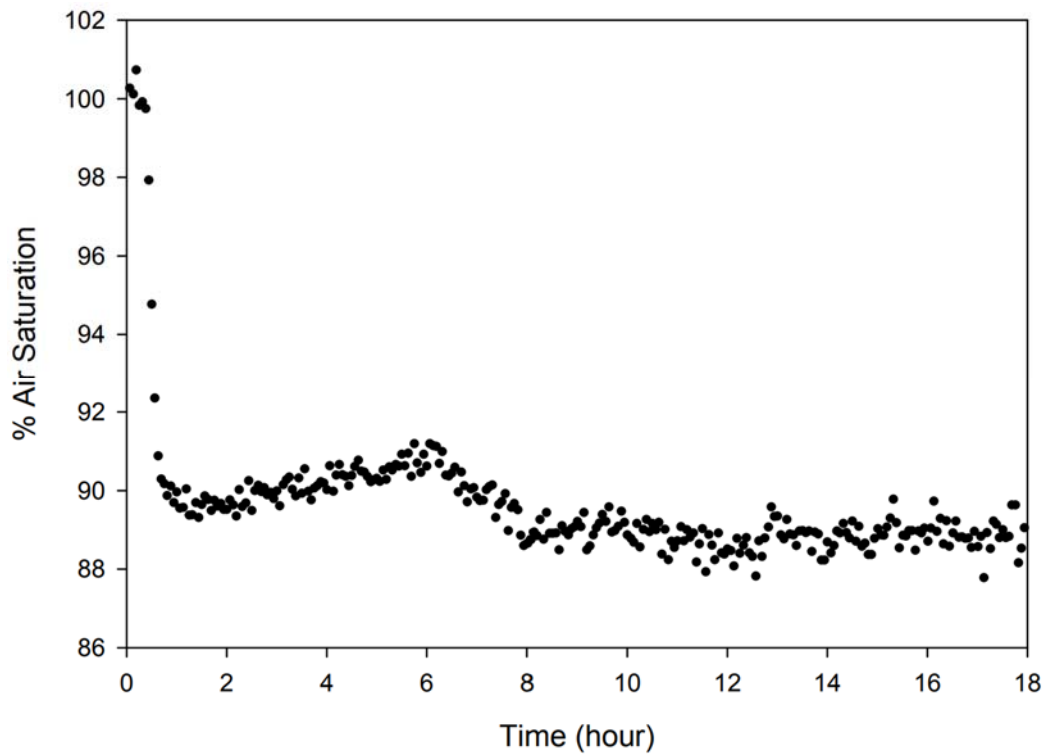


Figure 7.14 DO probe readings of pilot scale after 24 hour substrate stoppage.

7.4 Summary of Chapter 7

The biooxidation rate of the *L. ferriphilum* used in the bioreactor was re-evaluated and demonstrated an apparent improvement in performance over the originally used culture from over 15 years ago. A downward pH shift in the biooxidation rate curve of approximately -0.3 pH units was noted which is favourable in terms of the stability of operation where discharge of the BioGenerator catholyte into ferrous ions produces an associated reduction in the pH but impacts the biooxidation rate less severely. The optimum temperature and overall biooxidation rate with respect to temperature was assessed and found to be unchanged. A study into the production of jarosite was performed over a six month period where the pH limit to eliminate jarosite was found to be pH 0.85 and below but could most likely be pushed to pH 1.00 if the fuel cells are circulated with a cleaning phase when power generation is not required. Strong dynamics are found to occur under high operational temperatures (~40 °C) likely because of the increased rate of microbial breakdown and is generally undesirable for a system designed for frequent stop and start operation. Running the BioGenerator at reduced temperature (20 °C) was found to eliminate dynamics within a 24 hour ferrous iron feed stoppage.

Chapter 8

8 Efficiency Analysis of the BioGenerator

While the stop and start behaviour of substrate generation is integral to BioGenerator function, other operating behaviours such as broth aeration and mixing require attention and comparisons to laboratory observations. Since the bioreactor has been demonstrated to be easily pushed into an anoxic state through addition of ferrous iron in Chapter 6, it is necessary to assess the DO distribution in the system. In the case of fully hypoxic conditions, bioreactivity will be non-existent and dead zone regions can be expected to occur leading to inefficient operation. Of course, the question of electric power output is also at hand but is more difficult to give an answer for as the output power is just in a simple sense dictated by how large a fuel cell is used. Of greater importance is the assessment of the electric power generation efficiency or rather the identification of sources of inefficiency. Ultimately, the greatest source of inefficiency can be expected to occur as a result of thermal losses from the bioreactor itself and requires proof testing.

8.1 Bioreactor Thermal Retention and Stability

Testing of the pilot scale BioGenerator occurred during cold weather to realistically assess the temperature stability of the system in operation. One airlift segment was selected for this task with a volume of approximately 2 m³ and an operating temperature targeting 20 °C was selected to avoid excessive heat loss through the air exhaust. Initial warm up of the bioreactor took several days to complete using an electric heater operating at a continuous output of 1.6 kW followed by small amounts of make-up heat after reaching a steady-state temperature. The bioreactor was able to maintain an approximate 20 °C difference between the interior and exterior temperatures where outdoor temperatures hovered around 0 °C as seen in Figure 8.1. Airflow through the bioreactor at up to 100 kg/h was demonstrated producing temperature fluctuations not more than 2 °C. Temperature stability is of the utmost importance as the biooxidation rate is directly coupled to this parameter.

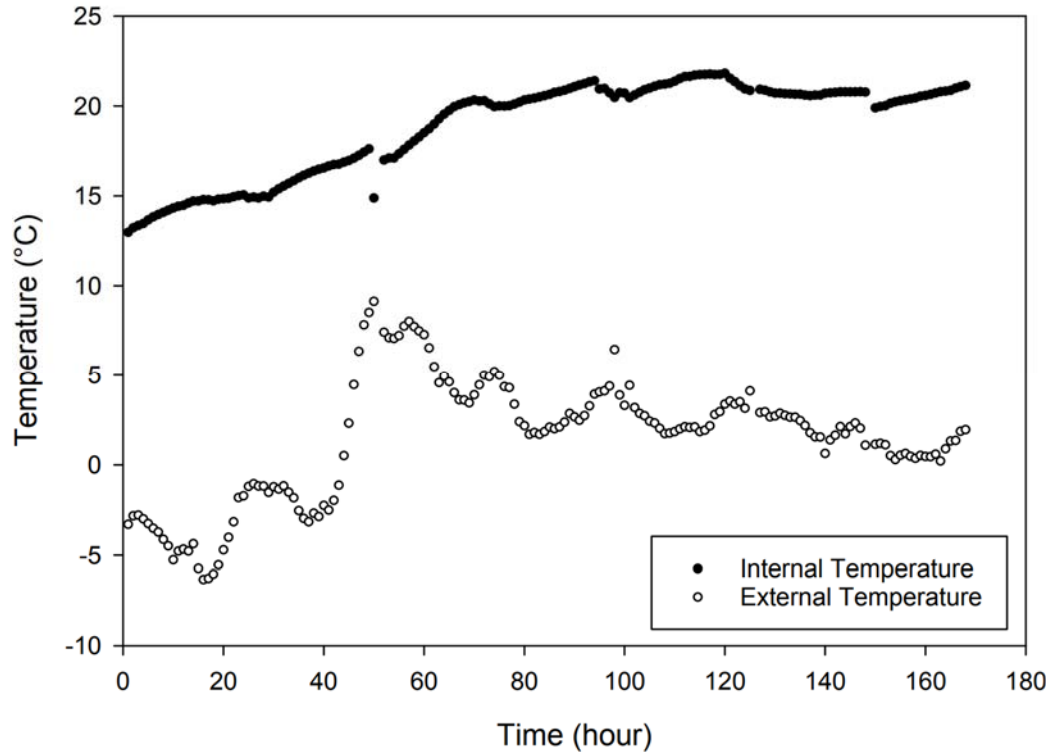


Figure 8.1 Temperature stabilization of a pilot scale BioGenerator.

8.2 Packed Bed Aeration

Due to the construction of an airlift bioreactor, only a portion of the liquid broth is exposed to air bubbles in operation and the broth is therefore responsible for delivering DO into the downcomer packed bed for distribution to microbes. Analyzing the behaviour of DO in the packed bed is necessary in refining the operating conditions and dimensioning of the BioGenerator. A semi-pilot scale BioGenerator was used to initially examine the DO profile by varying the air flow rate (32.2 or 15.6 L/min) and the temperature (38.0 or 16.5 °C). A DO probe was submerged into the bed to record DO measurements in increments of 5 cm across the full height of the bed and the results of which are given in Figure 8.2. Where higher temperatures are used it can be seen that two undesirable effects emerge as a result of the high biooxidation rate. The first effect is the generation of DO gradients across the height of the bed, while it is not necessarily bad in all cases, if the gradient is too large there is a potential that DO may drop to zero and a portion of the bed will become a dead zone. The second effect is the rapid consumption

of available DO to the point that biooxidation only occurs in the riser near the bubbles when air flow rates become too low and an insufficient pumping action results in slow liquid cycling that can't deliver DO to the bed before it is consumed. The results suggest that a lower temperature operation will result in better DO distribution that can better keep up with the liquid turnover rate dictated by the air flow rate. This finding supports the conclusions found of the previous energy conservation and dynamic stability studies in that a lower operating temperature should offer advantages in DO delivery and distribution. DO measurements were taken at the top and bottom of the pilot scale packed bed with respect to the air flow rates at an operating temperature of roughly 20 °C and the results of which are given in Figure 8.3. A DO gradient of about 15% air saturation was measured across the bed and remained essentially constant regardless of air flow, likely a result of slower liquid flow in the downcomer where a larger packed bed introduces more resistance to flow. A minimum air flow is also established by the findings at 55 kg/hour where flow rates lower than this will lead to increasing amounts of dead zone at the bottom of the packed bed.

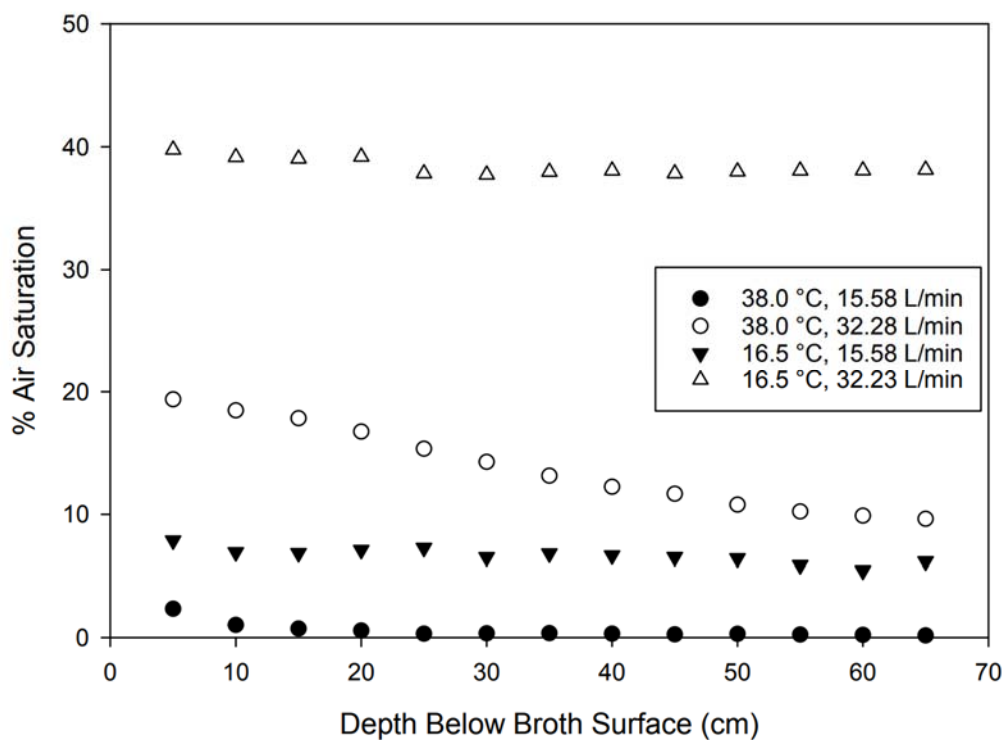


Figure 8.2 Downcomer packed bed DO profile in semi-pilot scale bioreactor.

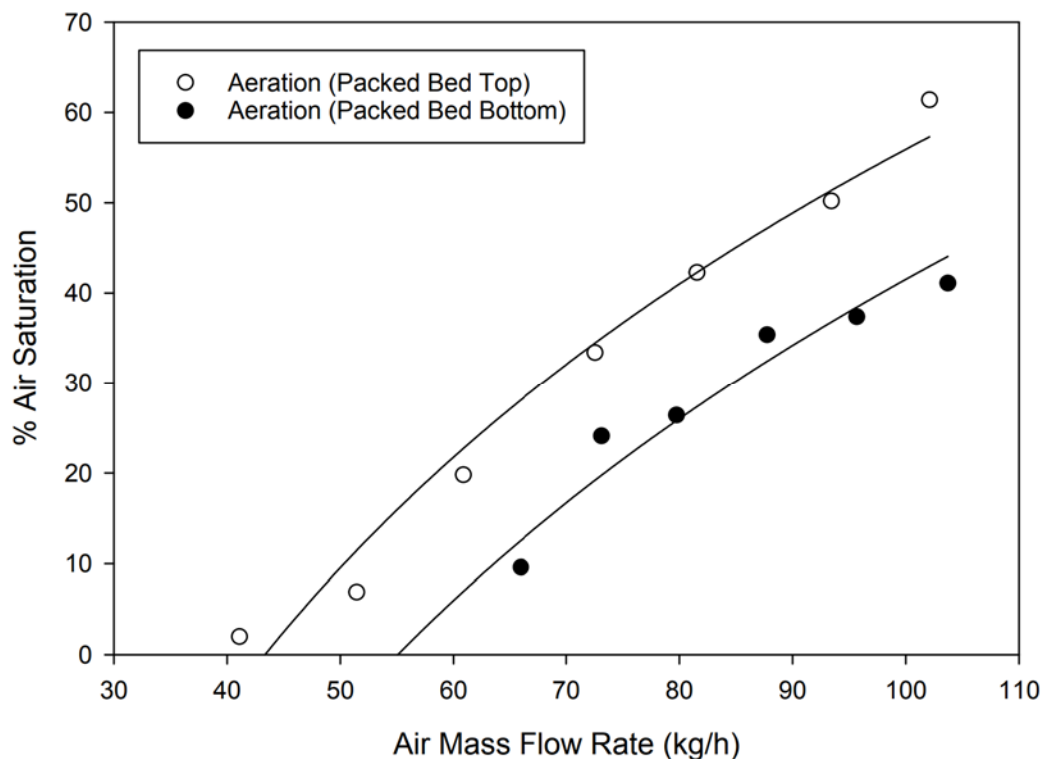


Figure 8.3 Downcomer packed bed DO profile in pilot scale bioreactor.

8.3 Power Output Potential

8.3.1 Polarization Curves

Polarization curves of the fuel cell array of a pilot scale BioGenerator were taken at several levels of ferrous/ferric concentration ratio in the bioreactor simulating operation under real world conditions. In practice, the decrease in the ferric ion content of the reactor must be restricted to some lower limit where excessive depletion leads to decreased cell voltage and decreased power output while the pH of the bioreactor is also decreased in the process which hinders biooxidation rates and results in long catholyte recharge time. A limit of ~30% depletion in this study was selected primarily to prevent excessive acidity where the biooxidation rate of the microbes drops off rapidly after pH 0.7. These curves are presented in Figure 8.4 and demonstrate the characteristic activation loss, ohmic loss, and mass transport loss regions. The overall current density is low in this case compared to hydrogen/oxygen fuel cells though can be significantly increased by a factor of more than 8 times through heat treatment of the cathode felt

(Pupkevich et al. 2007b). Slightly higher than expected ohmic losses are also suspected where the fuel cell array was a cluster of four single cells wired in series instead of a stack design using bipolar graphite conduction plates. The use of only monopolar conduction plates leads to an increased overall thickness in the combined thickness of carbon plates used and adds many more electrical junction points, both of which will add electrical resistance. These shortcomings in performance at this stage are not such a major issue however because known remedies exist, and the problems are easily dealt with.

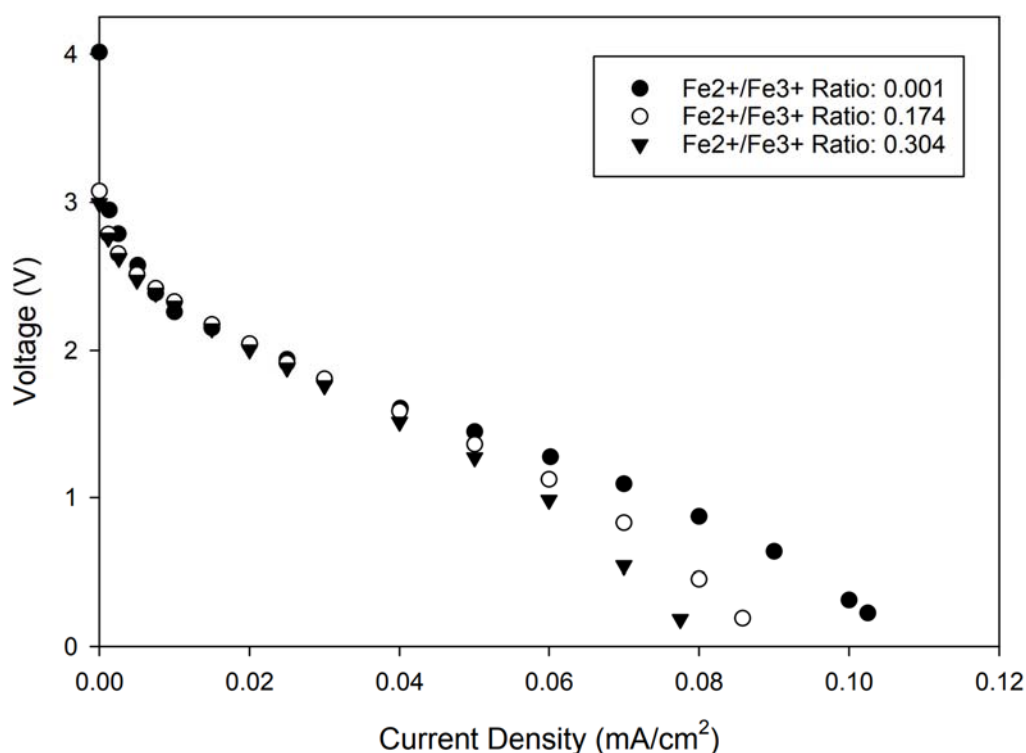


Figure 8.4 Pilot scale BioGenerator fuel cell bank polarization curves.

One noticeable attribute of using the ferric ion catholyte is the elimination of the rapid drop off in voltage at high current density in the mass transfer loss region. In the case of hydrogen/oxygen fuel cells, a sudden drop in voltage to zero with respect to the current density occurs near 400 mV as a result of the slow kinetics of the ORR failing to keep pace with the rest of electrochemical reactions (Giotakos and Neophytides 2023). This is not demonstrated in the case of the BioGenerator and the most significant factor affecting performance at high current density is the mass transport losses associated with increased

levels of ferrous ions that crowd out ferric ions from accessing the cathode. The lack of ORR kinetics in the BioGenerator also appears to offer a benefit in the region of activation losses where a drop of 19.2% from the experimentally observed open circuit voltage is encountered compared to a 28.6% drop demonstrated by hydrogen/oxygen fuel cells (Giotakos and Neophytides 2023). In the case of the hydrogen/oxygen fuel cell, even with platinum catalyst present at the cathode the activation energy of splitting dioxygen still results in a significant overpotential loss.

8.3.2 Parasitic Losses

While polarization curves offer a convenient means of comparing fuel cell performance, they are limited by what they detect through closed loop electric current across a sensing load. It is also possible to have parasitic current paths within the fuel cells that consume reactants and generate resistive heating of the cell without contributing to the output power. It is therefore necessary to perform a material balance around the fuel cell to assess parasitic losses which are not detectable through the electrical output.

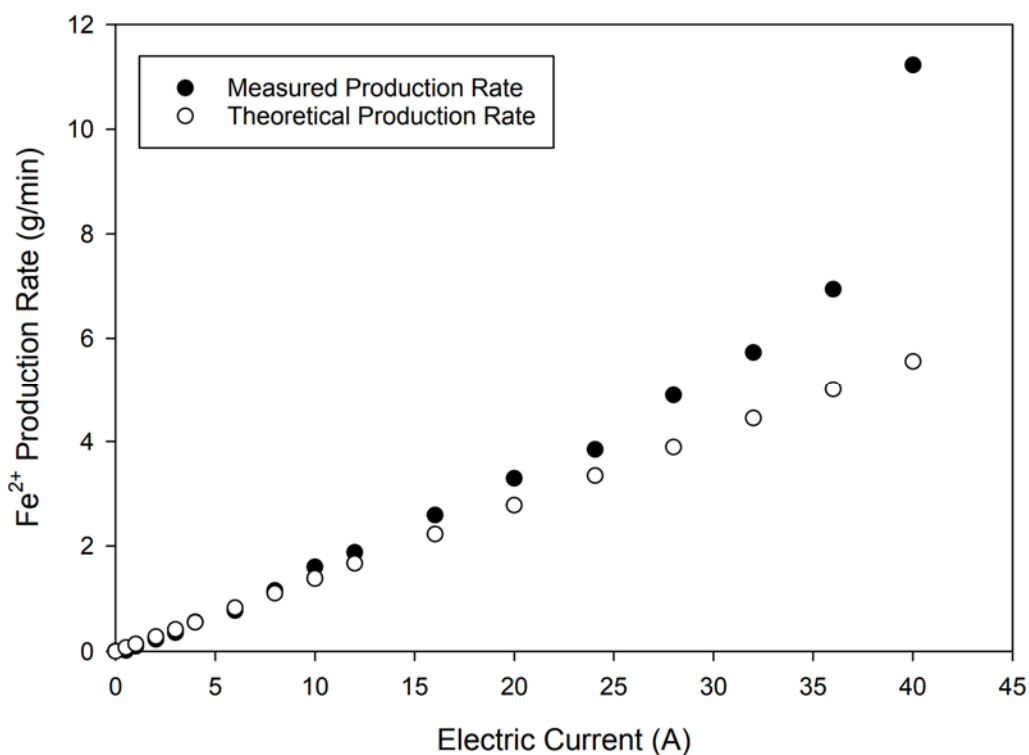


Figure 8.5 Fuel cell parasitic losses as a measure of excess ferrous ion generation.

Figure 8.5 demonstrates the presence of these losses that were encountered in the pilot scale BioGenerator. Numerous potential sources of parasitic loss may exist in the fuel cells and contribute collectively. For instance, at the anode parasitic currents may develop in the carbon felt where overvoltage needed for hydrogen oxidation is smaller than the difference of the ohmic drops of the proton conduction and the electron conduction inside the anodic catalyst layers, resulting in the regeneration of hydrogen gas between the interface of the PEM and anode felt (Schalenbach et al. 2015). Of course, losses as a result of general short circuit by reactants diffusing across the membrane will also occur and is commonly encountered as the fuel passing into the cathode chamber and reacting, sometimes referred to as cross-over loss (Andreadis et al. 2008). In the case of the BioGenerator it is the oxidant that has been demonstrated to pass through the PEM though the overall amount is small and the expected losses are negligible compared to the useful power output.

One major source of parasitic loss was found as a result of the power draw level from the fuel cells resulting from electrolyte concentration gradient development across the cathode. During operation of the fuel cell the catholyte is passed through the channels of the graphite conduction plate containing the cathode carbon felt where ferrous ions are generated as a gradient across the plate from the entrance to the exit noted by Pupkevich (2014). The concentration of ferrous ions is therefore non-uniform and as a result leads to a voltage differential within the graphite plate in accordance with the Nernst principle. Parasitic currents form through the graphite and the broth as a result, generating resistive heating and lowering the efficiency of the cell. The most effective solution to this issue appears to be in proper design of the graphite plate where the channel lengths should be kept as short as possible and the catholyte flow should be maintained at as high a flow rate as possible without compromising the PEM through excessive fluid pressure.

Another potential path of parasitic currents where multiple fuel cells exist may occur through the electrolyte itself, where such problems can occur specific to microbial fuel cells electrically connected in series within a common electrolyte (Zhuang and Zhou 2009). Inspection of the fuel cell arrangement used in the pilot scale BioGenerator (Section 3.3.3) reveals that three of the four individual fuel cells do appear to contain a

short circuit path through the electrolyte, however the contribution must be minimal as ferrous ions would be detected at the catholyte return to the bioreactor at zero current, which as can be seen in Figure 8.5 no ferrous ions are detected. Conductivity testing of the electrolyte was performed and the results given in Figure 8.6 reveal Ohmic behaviour specifically at low voltages where there is no lower limit to conduction as might be expected from water electrolysis (1.23 V minimum). An examination of changing parameters such as the ferric ion concentration and the pH was performed but no changes could be detected between the tested conditions. It was hoped that this phenomenon might explain the excess ferrous ion generation observed in operation however no ferrous ions were detected in solution after running an electrolytic cell for 100 hours using carbon felt electrodes in ferric sulfate with a constant voltage of 1.20 V.

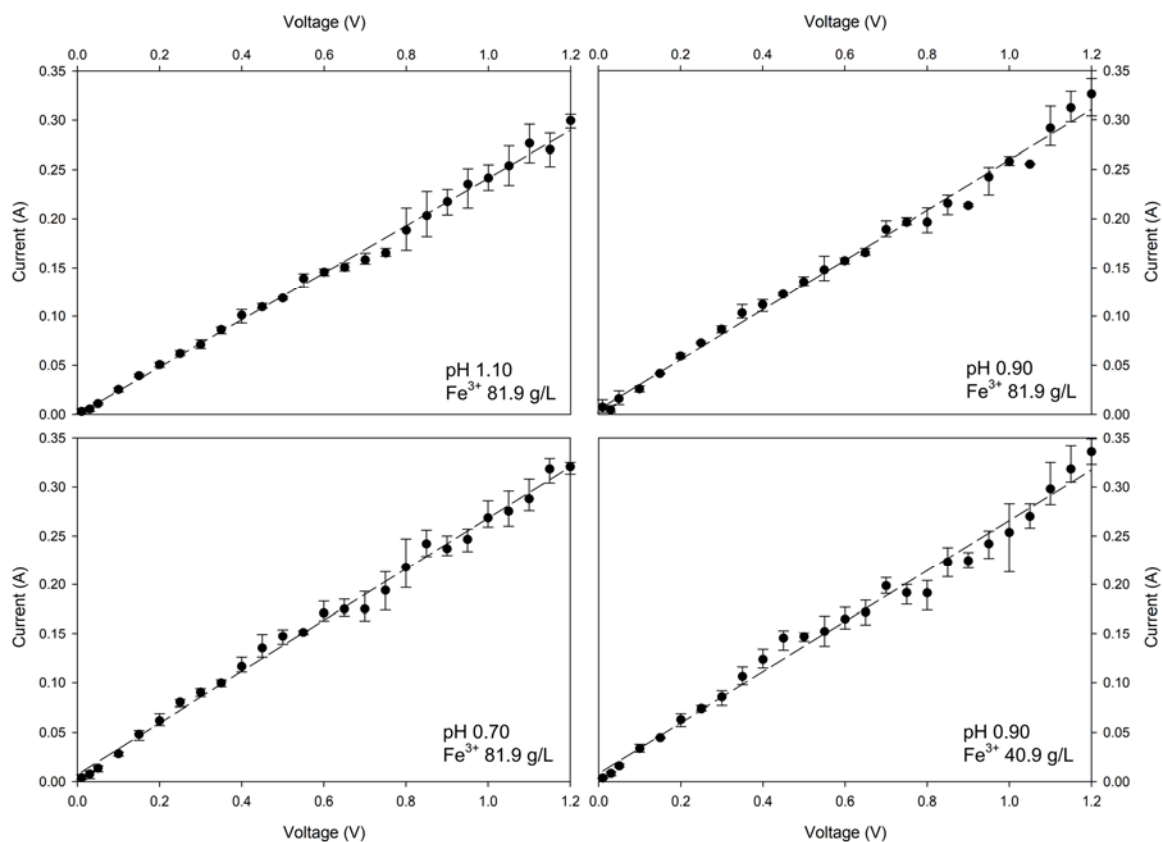
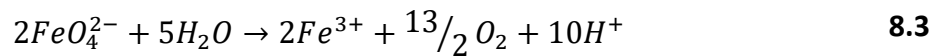
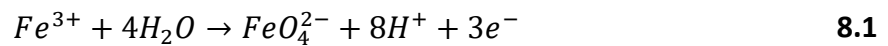


Figure 8.6 Voltage-current relationship of ferric sulfate electrolytic cell with carbon felt electrodes (Sigratherm graphite felt 120 cm²).

Generally parasitic losses recorded in literature are found not to result in the direct consumption of catholyte within the cathode compartment and an explanation for the observation of excess ferrous ion generation wasn't established. It may simply be the case that the flowrate of catholyte returning to the bioreactor was unstable and varied between measurements, but this seems unlikely from the point of view of the apparatus operation. An explanation as a simple offset error also seems unlikely given the observed deviation wasn't a linear relationship. Excess ferrous ion production was also considered as possibly a result of ferrate ion generation as a parasitic pathway given as electrochemical Equations 8.1 and 8.2 where the ferrate ion is unstable and may decay faster than it could oxidize the ferrous ions through Equation 8.3 (Lee et al. 2002). While the production of ferrate ions had been successfully observed through the backward operation of the BioGenerator fuel cell being run as an electrolysis reaction for hydrogen production, this explanation seems unlikely given the voltage needed to drive the electrochemical production of ferrate ions must be above 2.20 V to proceed (Lee et al. 2002). This voltage might be developed as a short circuit through the catholyte as the open circuit voltage of the fuel cell bank was found to reach more than 3.00 V. Unfortunately time constraints on the operation of the pilot scale BioGenerator limited further exploration of this issue and is currently a subject for future study.



8.3.3 Maximum Power Point

Using the polarization curves it is possible to chart the power output curves at varying levels of ferrous/ferric iron concentration levels which can be seen in Figure 8.7. The maximum power potential declines as the ferrous to ferric ion concentration ratio grows where cell voltage declines according to the Nernst equation. The drop in the maximum power output can be considered a reduction in efficiency and so the concentration ratio should be held as high as possible during operation. A limit of ~30% ferrous to ferric iron

was considered for reasons of impact to the biooxidation rate, however factoring in electrochemical efficiency, a smaller limit may be more desirable. The operating curve based on the maximum power points is given in Figure 8.8 and gives a near linear relationship where power output capacity can be expected to drop by 17% at a discharge of ~30%.

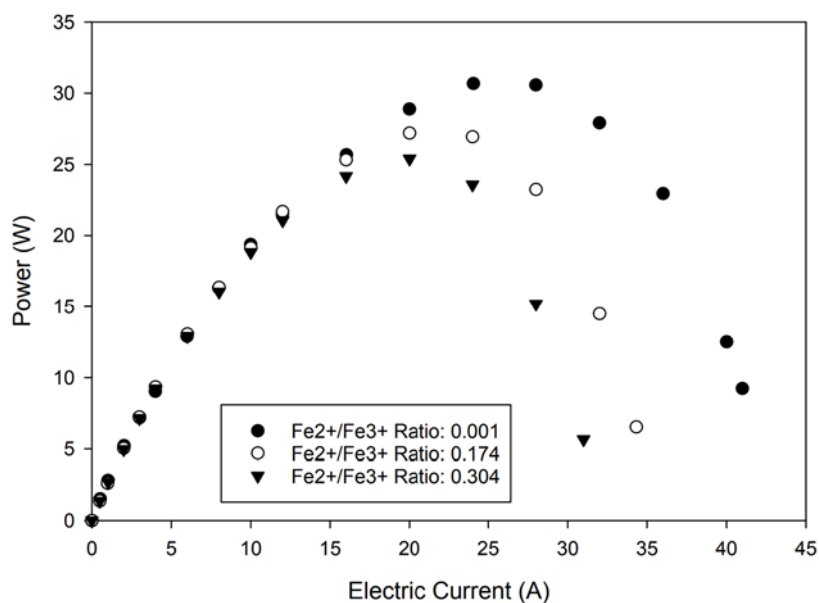


Figure 8.7 Power output maxima of fuel cell bank.

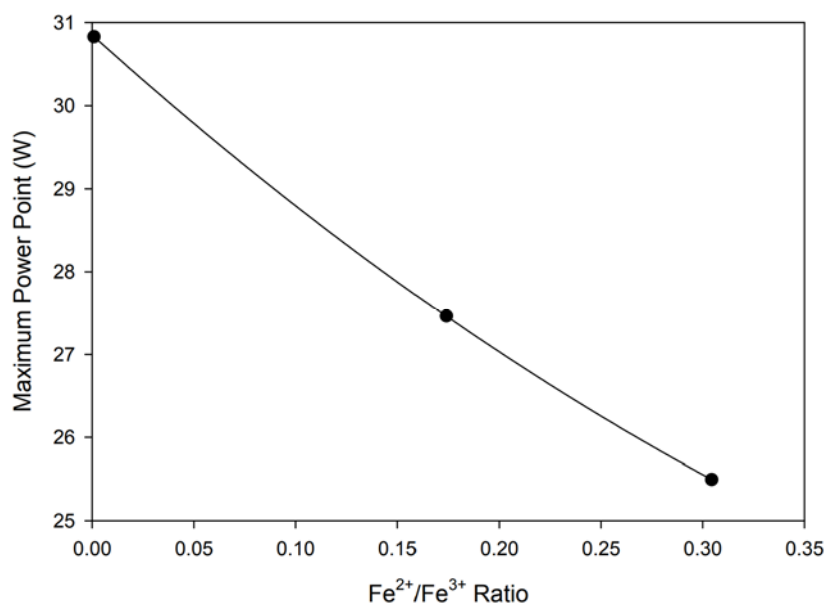


Figure 8.8 Maximum power point operating curve.

8.4 Summary of Chapter 8

Operation of a pilot scale BioGenerator was performed with an emphasis on the packed bed aeration profile and the fuel cell power output performance. Use of a lower temperature was shown to be better in terms of DO distribution in the downcomer packed bed ensuring a more homogenous coverage that avoided the formation of dead zones. The design of the fuel cells with respect to the chemical aspect must be carefully considered in construction to mitigate parasitic losses. These losses were demonstrated to be exasperated by too low of catholyte flow rate through the cell resulting in unwanted electric current generation within the graphite conduction plates as well as excessive ferrous ion generation at currents greater than the maximum power point produced by some unidentified process. The level of catholyte discharge must also be restricted to ensure that the biooxidation rate can be kept high enough to regenerate the catholyte in a reasonable time. If the pH falls too significantly the microbes will be stalled in their ability to consume iron leading to an additional reduction in cell concentration through increased death rates resulting in a long catholyte recovery time. Limiting the catholyte discharge is also important from the standpoint of efficient energy production from the hydrogen fuel, increased levels of ferrous iron present in the catholyte results in voltage drop across the fuel cell.

Chapter 9

9 The Limits of Life - Hyperacidophiles

The study of microbial adaptation to extreme acidic environments picks up on the work of Penev (2010) in the examination of hyperacidophile activity approaching pH 0 and into negative pH. In experimentation by Penev (2010), a stepwise reduction in pH starting at 0.7 in a spouted bed reactor containing porous crushed ceramic particles and iron sulfate broth was performed and biooxidation measured over long term steady state conditions. Significant changes in the microbial culture were documented through PCR-DGGE analysis where at pH 0.32 the initially dominant *L. ferriphilum* was no longer detected. The culture was identified as dominated by a member of the *Ferroplasmaceae* speculated to be *F. acidarmanus* given the origin of the bacterial culture (Pikuta et al. 2007), which represented the only iron oxidizing microorganism detected. Two other microbes in minor presence were detected in addition to the dominant microbe, the red alga *C. caldarium* and a probable γ -proteobacterium. The presence of these microbes at such low pH levels is in accordance with the literature where the minimum recorded pH for growth of both *C. caldarium* and *F. acidarmanus* is pH 0. *F. acidarmanus* is in fact related to the record holder for low pH tolerance, *P. oshimae* and *P. torridus*, that demonstrated growth at a reported pH -0.2 (equivalent to 1.2 M or ~10% w/w H₂SO₄) (Fütterer et al. 2004, Pikuta et al. 2007).

At the beginning of 2020, a miniaturized illuminated airlift bioreactor containing a dividing wall of porous crushed ceramic (Appendix A, Figure F) was constructed and filled with a solution of ferrous sulfate (10 g_{Fe2+}/L) and 9K nutrients (Silverman and Lundgren 1959) acidified with sulfuric acid to pH -0.10, with the expectation that oxidation of the ferrous ions would raise pH slightly bringing it back towards pH 0. The design of the bioreactor was such that a favourable environment might exist for any organism in solution, exterior lighting for algal growth was provided (16 hours on, 8 hours off) along with an inner dividing wall of porous particles in a darkened environment that might facilitate the growth of *F. acidarmanus* or any other microbe. Absorption of light energy kept the bioreactor warmed to approximately 36 °C when the

lights were on. Soon after, the Covid-19 epidemic forced a shutdown of facilities, and the bioreactor was left to operate unattended for a period of six months. On return, it was observed that the liquid contents of the bioreactor had partially oxidized with a portion evaporated and through the distilling effect of the outlet condenser, the internal pH had dropped to roughly pH -0.15 (9.6% w/w H₂SO₄). Small colonies of algal growth were observed growing within the liquid in regions obscured by the light. Given the visually observed growth of algae at such low pH, the focus was shifted from iron oxidizing microbes to the culturing and isolation of the observed algae. This bioreactor was operated for a period of three years, occasionally topping up the liquid level with fresh acid solution, until a pH of -0.35 (12.3% w/w H₂SO₄) was measured. The algae deposits were extracted from the bioreactor and grown under various conditions over the course of a fourth year in an attempt to find an optimum growing environment using enclosed Petri dishes with variable intensity light sources (Appendix A, Figure H). The discarded Petri dish growth was deposited into a larger storage bioreactor (Appendix A, Figure G) operated with no iron sulfate present and a pH of -0.35.

9.1 Growth Rate Optimization

From the first observations of growth of the algae, it was apparent that light levels influenced growth where high light levels had a negative effect on growth and none was observed growing in the direct path of the light sources. This observation is in line with the reported growth habits of *C. caldarium*, in that axenic cultures of the algae display the property of growth only under dim light conditions (Brown and Richardson 1968). This property is likewise displayed by that of the closely related *Cavernulicolaceae* family, able to thrive under the low light conditions of caves but under near neutral pH. This dim light growth property makes sense given the living conditions the algae was extracted from (abandoned acidic flooded mine). In fact, the alga is recorded in literature as being capable of growth without the presence of light through a heterotrophic metabolic pathway able to make use of organic carbon compounds present in solution, though the characteristic green colour of chlorophyll becomes diminished and the cells take on a straw colour (Brock 1978). This dark growth alga is also likely to be responsible for the

biological deposits often found in the fuel cell cathode carbon felt of the BioGenerator where the carbon felt acts as an ideal immobilizing surface (Figure 2.7).

Given that low light is observed to boost growth rates and the formation of algal colonies, an investigation into determining the optimal level of light was performed in efforts to boost growth rates under the highest levels of acidity. In addition to growth under dim light, the *C. caldarium* under investigation also demonstrates a high tolerance to dissolved salts of iron and has been observed growing in tubing carrying ferric sulfate broth with an iron content greater than 40 g/L. An examination into the relevance of iron presence in solution was also briefly explored.

9.1.1 Light Level Optimization

Initial experimentation in light level growth optimization was performed using a range of intensities from 5 to 50 W/m² of illumination on the samples under two temperature regimes, 20±1 °C and 40±1 °C. The upper temperature limit for *C. caldarium* is given as 55-57 °C though initial reports gave upper limits of 70-80 °C, these higher limits appear to be unfounded with demonstrated damage to the photosynthetic apparatus detected (denaturation of phycocyanin and a₂ phosphorylase) and an inability to grow the algae under laboratory conditions at these temperatures (Ascione et al. 1966, Saini et al. 2021). The optimum growth temperature is found to fall within 45-50 °C (Doemel and Brock 1970), however lower temperatures were used in the examination to limit the effects of evaporation which was aided with the inclusion of open flasks of water kept in the incubator to increase overall humidity. The growth profiles of the alga are given in Figure 9.1 having been grown for a period of 220 days. The results follow the expected increase in growth with decreasing light levels demonstrating an exponential trend with growth picking up significantly below 15 W/m². In terms of temperature, growth at 40 °C proved better than 20 °C which would be expected, though growth at room temperature performed much better than expected comparatively as the light intensity decreased.

A second run of experiments (Figure 9.2) in the 0 to 10 W/m² region incrementing by 0.5 W/m² was performed in the search for an optimum based on the previous findings using a temperature of 40±1 °C and grown for a period of 160 days. The level of growth was

demonstrated to be nearly double that of the previous lowest intensity used, though unfortunately a maximum was still not found. Based on the results the optimum appears to lie around 1 W/m² though more resolution is required to give an exact value.

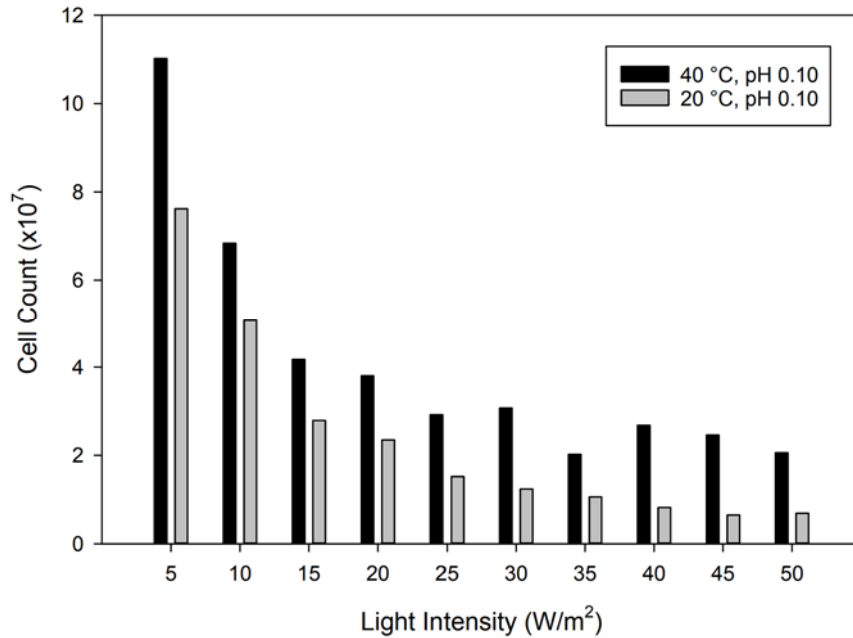


Figure 9.1 Light intensity growth optimization (first series).

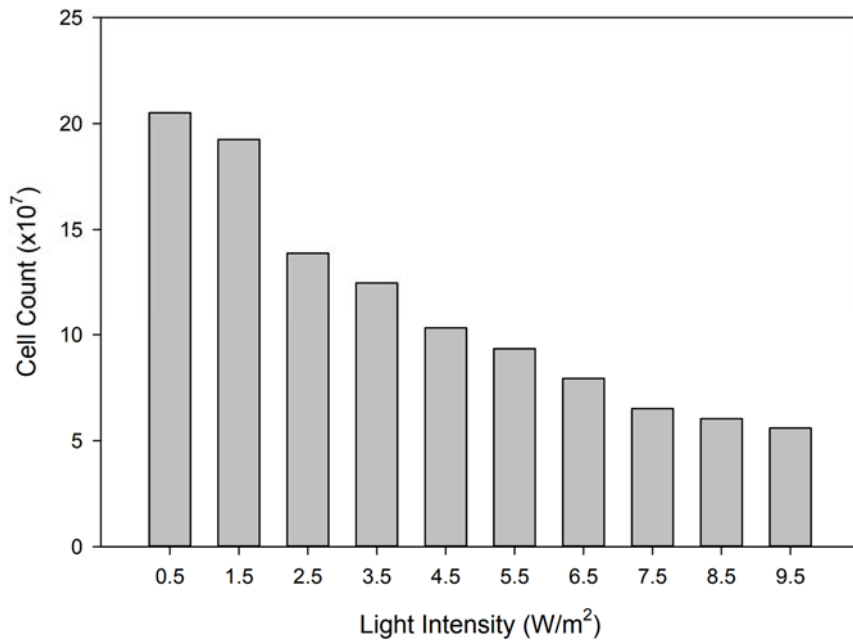


Figure 9.2 Light intensity growth optimization (second series).

9.1.2 Effect of Iron

The effect of iron on growth was examined in the same manner as the results in Figure 9.1, however 10 g/L of ferrous iron was included in solution. The results of the growth are given in Figure 9.3, though the presence of iron ions in solution presents a problem in the use of fluorescence measurements as both ferric and ferrous ions strongly absorb UV-A radiation which attenuates the output signal. As a result, the data is measured in this case as the raw signal from the transimpedance amplifier circuit that is responsible for converting the photoelectric current generated by the photodiode of the sensor and converting to an amplified voltage signal. It can still be seen that a similar trend exists to that found in Figure 9.1 and the overall growth was found to be comparable when inspected manually by microscope cell count and even by viewing with the naked eye. The presence of iron ions amongst the alga appears to have a benign effect on growth showing no significant differences overall and can be eliminated from solution to allow use of the fluorescence sensor. Regarding fluorescence sensing, it should be noted that the readings may not be completely faithful to the cell count in all cases as the signal is in reference to the overall chlorophyll content which may differ in concentration within the cells under different conditions, though is acceptable for use as a rough estimate.

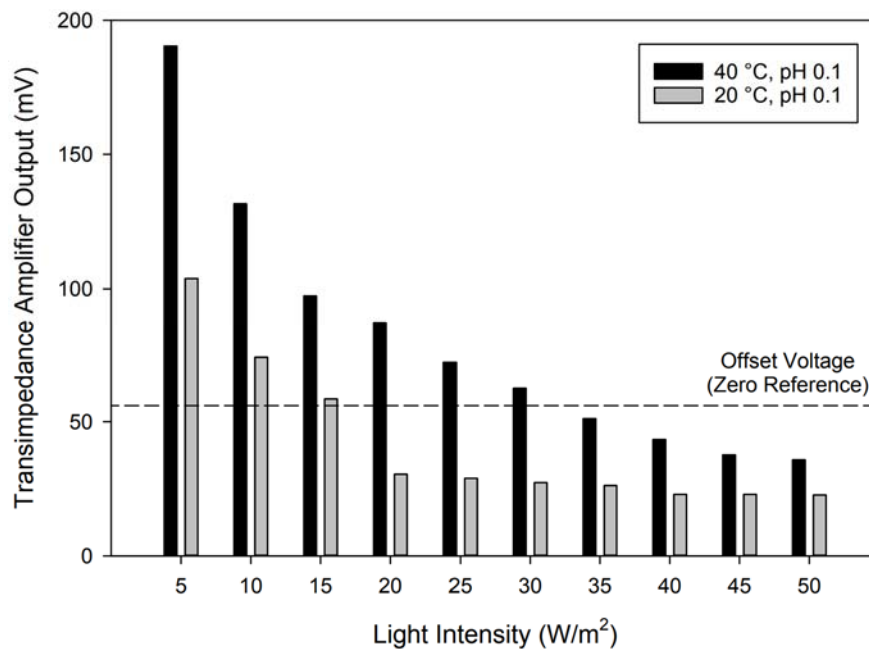


Figure 9.3 Growth optimization (first series) with iron.

9.2 Acid Tolerance Examination

Acidity levels of the extracellular environment of microbes has detrimental effects on the ability to survive, and especially so at extremely low pH levels. While it can be imagined that the threat of being chemically dissolved might be of greatest significance there are in fact numerous other complications to consider which include excessive H^+ diffusion into the cytoplasm disrupting the internal functioning of the cell, interference with the efficiency of external proteins of chemolithotrophs, and the general desiccation effects of sulfuric acid. This can be demonstrated for example with *L. ferriphilum* in Figure 9.4 where the microbes can be demonstrated to remain functional to pH 0.1 where increasingly low pH appears to negatively impact the efficiency of the external cytochrome c₂ protein to oxidize ferrous iron and the primary threat to life becomes starvation.

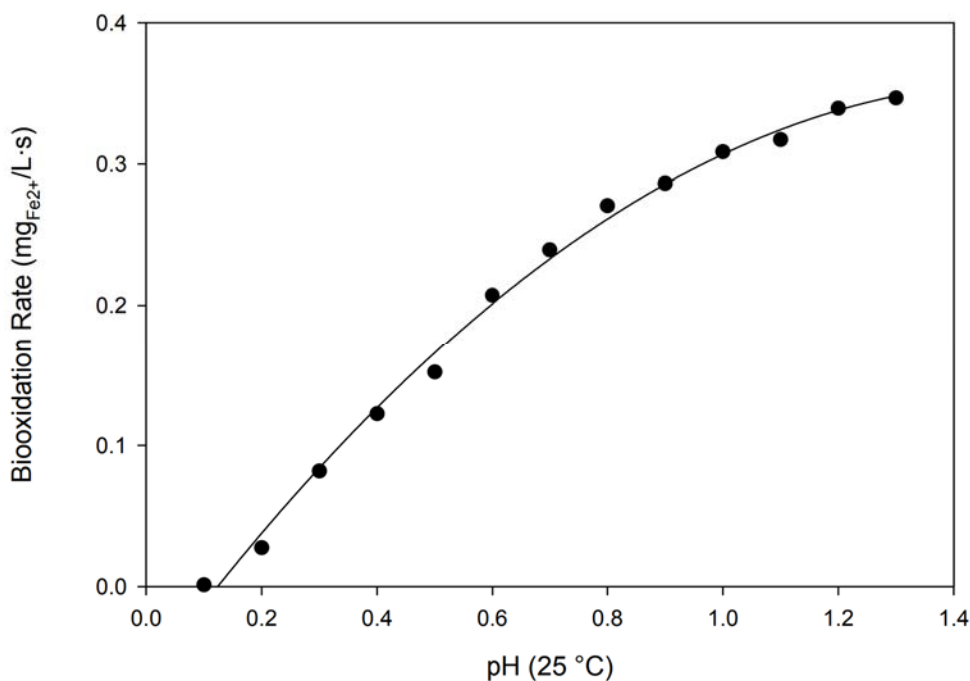


Figure 9.4 Acid tolerance of *L. ferriphilum* with respect to biooxidation capability.

In terms of handling extremely low pH, chemolithotrophic microbes in general do not fare so well due to the suppressing effects of the high H^+ activity on externally exposed proteins of their electron transport pathway. The most acid resistant microbes given in

literature (Table 9.1) appear to be heterotrophic which is more logical as metabolic processes may take place internally, shielded from the chemically intense extracellular fluid.

Table 9.1 Commonly cited extreme acidophiles.

Name	Attribute		Source
<i>Picrophilus oshimae</i> / <i>Picrophilus torridus</i>	Optimum pH	1.10	Baker-Austin and Dopsin 2007
	Lower Limit pH	-0.20	Pikuta et al. 2007
<i>Ferroplasma acidarmanus</i>	Optimum pH	1.20	Baker-Austin and Dopsin 2007
	Lower Limit pH	0.00	Pikuta et al. 2007
<i>Cyanidium caldarium</i>	Optimum pH	1.00	Doemel and Brock 1971
	Lower Limit pH	0.05	Doemel and Brock 1971
<i>Dunaliella acidophila</i>	Optimum pH	1.00	Pollio et al. 1988
	Lower Limit pH	0.20	Pollio et al. 1988

Given that the specimen of *C. caldarium* in this study already demonstrated acid tolerance on par with *P. oshimae* and *P. torridus*, it was necessary to determine the absolute lower limit of pH. Growth dishes were prepared from pH 0.00 to -0.95, inoculated with algae, and left to grow under a light intensity of 5 W/m² for a duration of 160 days. The results of the growth gave a lower limit of pH -0.85 (19.5% w/w H₂SO₄) as seen in Figure 9.5, far exceeding the commonly cited *P. oshimae* and *P. torridus* as the record holder. Additionally, the growth dish demonstrating the lowest pH at which growth was detected was very fortunate to also include a single algal colony (Figure 9.6) allowing for additional confirmation with the naked eye of the prominent green of chlorophyll that could only have come from cellular reproduction.

The unusually low pH tolerance may not be so surprising and some reasons for it can be speculated. Firstly, in the work of Doemel and Brock (1971) the recorded lower limit appears to have been set based on a difficulty in measurement below pH 0 rather than as the observed absolute limit, which has been passed down through the literature. Secondly, the sample was collected from Iron Mountain which demonstrates one of the most acidic environments known, down to pH -3.6 (Nordstrom et al. 2000). Thirdly, the nutrients used for growth were lacking in carbon sources which may have accentuated autotrophic metabolism, limiting the need for absorption of external carbon sources and

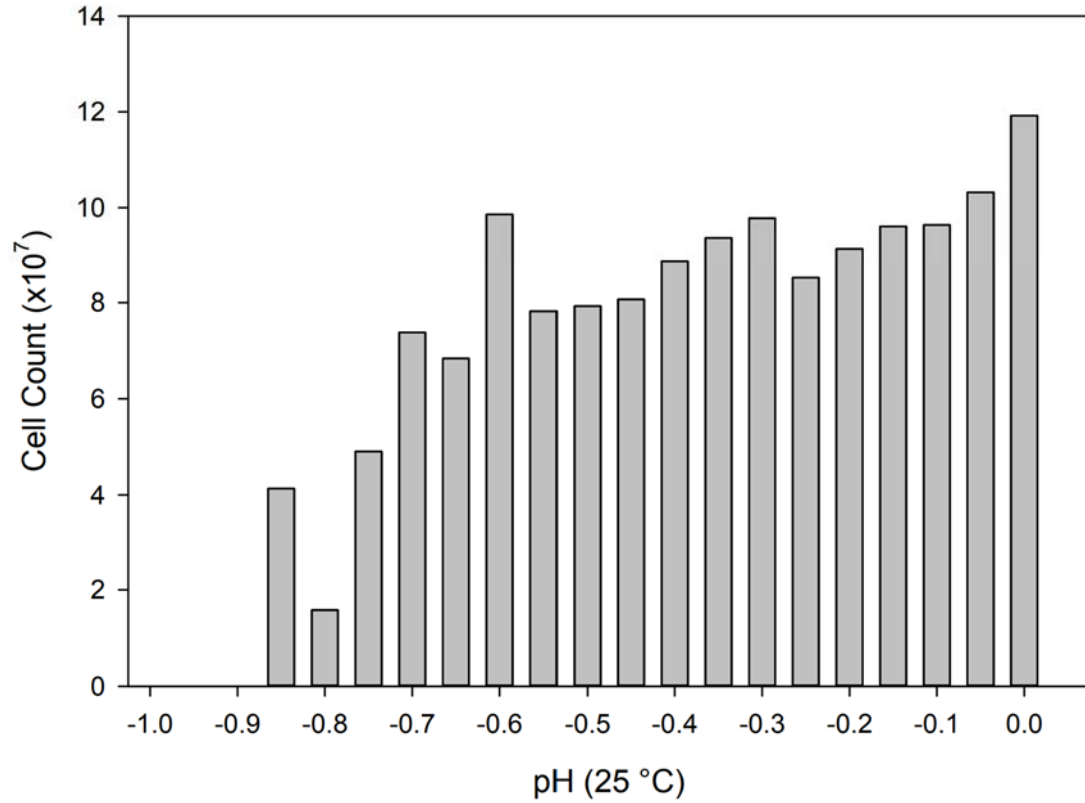


Figure 9.5 Lower limit pH study of *C. caldarium* from Iron Mountain.

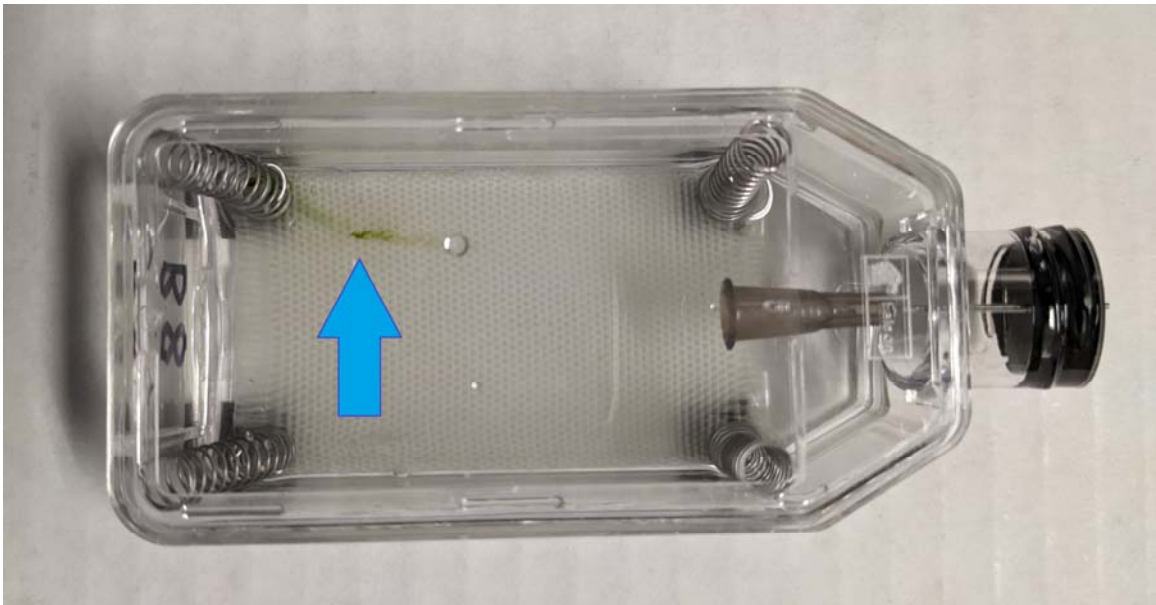


Figure 9.6 Submerged algal colony growth at pH -0.85 visible to the naked eye.

potentially allowing for growth of a thicker cell wall able to better resist permeation of H^+ into the cell. It is also possible that the acid tolerance may be the result of strain development given the conditions and duration over which the algae was initially grown.

9.3 Morphology and Identification

Morphologically, *C. caldarium* is difficult to differentiate through physical characteristics from other related red algae species under visible light microscopy (Figure 9.7) (Kuroiwa et al. 1994, Park et al. 2023, Seckbach 1994). Nevertheless, the physical appearance matches the descriptions given in literature as spherical unicellular bodies having a diameter of 2 – 6 μm with a blue-green hue (Kuroiwa et al. 1994). One potential method of identification may be made in the reproduction phase of the algae where it has been noted that *C. caldarium* undergoes a division to four endospores while other species in this class divide into other numbers (Seckbach 1994). This was difficult to definitively capture since the alga was vortexed prior to addition to the microscope slide, though a probable case is seen in the top-center of Figure 9.7.

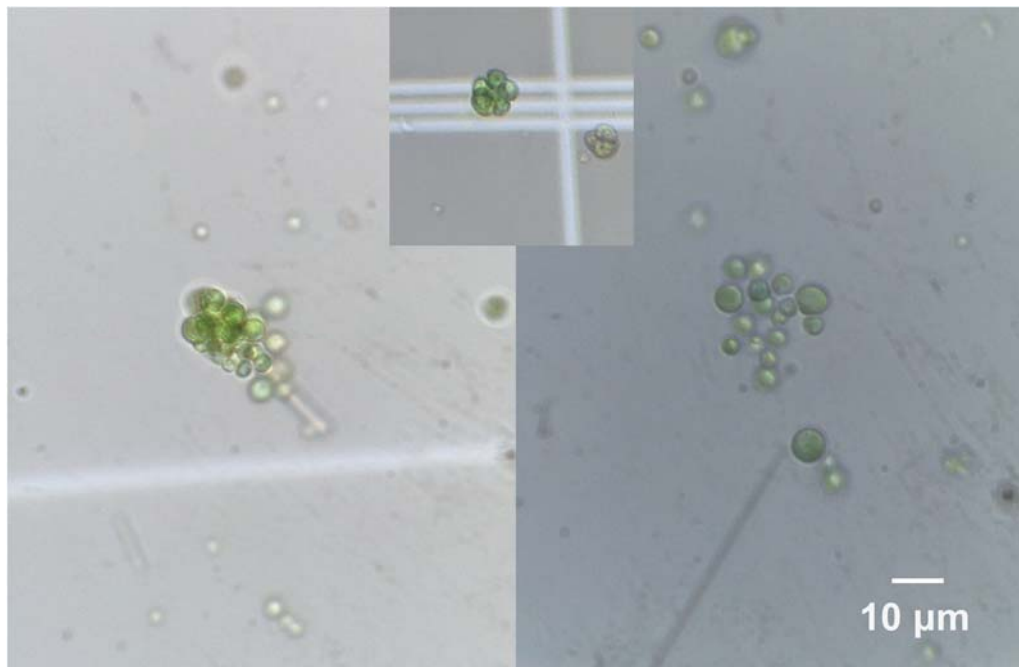


Figure 9.7 Microscope view of *C. caldarium* (100x mag.). Left: Algal cluster immobilized on glass fiber. Center: Probable reproduction through endospores. Right: Alga cell dispersion on slide surface.

9.4 Summary of Chapter 9

Growth of a strain of *C. caldarium* was observed and isolated from an unattended airlift bioreactor that demonstrated growth below pH 0 and was cultivated for a period of four years. The alga preferentially grows under dim light conditions and a study into the optimization of lighting was performed yielding an approximate optimum illumination intensity of 1 W/m². The alga was found to be able to grow in the presence or absence of both ferric and ferrous sulfate and the growth rate was not significantly affected by the presence or absence of the iron ions. An investigation into the absolute lower pH limit tolerable by the alga demonstrated growth to pH -0.85 that was confirmed through fluorescence sensing as well as confirmation by the naked eye. The findings of the lower pH limit exceed that of the currently established record holder for acid tolerance by *P. torridus* and *P. oshimae* given as pH -0.20. The extremely high acid tolerance demonstrated by *C. caldarium* may carry significance in the realm of space exploration and the seeding of life on other celestial bodies that exhibit similar environmental properties (Limaye et al. 2018, Merino et al. 2019). Additionally, it is documented that *C. caldarium* can grow in an atmosphere of pure CO₂ which gives rise to increased growth rates which may be useful in continued work (Seckbach et al. 1970, Seckbach and Libby 1970).

Chapter 10

10 Summary of the Results

Presented here are the final results and conclusions that have been made through this multifaceted research project delving into the scale-up of the BioGenerator system:

1. The BioGenerator requires a large input of low pressure air for sparging operations and accounts for a significant level of energy consumption. For a theoretical 1 MW system the amount of air needed was found to be within the supply range of a large trompe, making the system plausible through the use of a simple and predictable source of green energy.
2. The pH and iron ion concentrations in the broth may be monitored in-situ through predictable absorption characteristics demonstrated by the ferric ion in response to pH, temperature, and ferric ion concentration which can be used in place of expensive and short lived electrochemical pH and redox probes.
3. The ferric ion absorption characteristics are quite convoluted and the foundation for a potential fully functional model and custom spectrophotometer system have been explored.
4. A method of determining the saturated dissolved oxygen content of the broth has been successfully developed in place of models presented in the literature which appear to make an erroneous use of dissolved oxygen meters. The saturated dissolved oxygen content in a broth having an iron content of ~ 33 g/L was found to be 5.50 mgO₂/L.
5. A method of determining the volumetric oxygen mass transfer coefficient for niche application with iron sulfate containing airlift bioreactors has been successfully developed that allows much greater precision in measurements over other commonly used techniques. This is particularly important for use in optimizing bioreactor construction and mitigating energy losses.
6. The k_La measurements between a semi-pilot scale system and a full pilot scale system were found to not be comparable, with the pilot scale underperforming in comparison. This may be partially attributed to the greater liquid depth of the pilot

scale bioreactor which may lead to reduced interfacial area of the bubbles near the bottom when under compression as well as the orientation the sparger was placed in. In any case, greater attention should be given to the sparger design to reduce bubble agglomeration at the gas outlets and promote better break-up of bubbles.

7. Analysis of the biooxidation rate of the *L. ferriphilum* culture used in the BioGenerator appears to demonstrate an improvement with regard to the broth acidity where a shift of -0.3 pH units in the biooxidation rate curve has been noted in the ~15 years the microbes have been in service. This is a very fortunate and desirable attribute for operation with the BioGenerator.
8. The BioGenerator can likely be operated at pH 1.00 as opposed to the typically operated pH 0.80 where minimal microcrystalline jarosite growth was observed which could be washed from the fuel cells during catholyte recharge periods before having a chance to adhere to the internals. Operation at pH 1.00 is demonstrated to be more advantageous in maintaining biooxidation rate stability and helps avoid the possibility of quenching the bioreactions where pH falling too low leads to severe degradation of the microbial culture.
9. Strong substrate dynamics were noted for operation of the BioGenerator at 40 °C in the laboratory which are undesirable as the system must be stopped and started routinely. Reducing the system temperature of the pilot scale system to 20 °C was found to eliminate the dynamics completely within the necessary time span of expected on-off operation. The reduced temperature was also found to be favourable from an energy management perspective where the bioreactor was able to maintain this temperature at an external ambient temperature near 0 °C.
10. Reduced operating temperature was found to be favourable in the dissolved oxygen distribution within the packed bed which ensured a more homogenous mixture. Higher temperatures were found to produce too aggressive of a bioreaction rate to the point that much of the bioreactor packed bed acted as dead space.
11. Study of the fuel cell operation at the pilot scale revealed the importance of eliminating parasitic losses within the fuel cells, especially as a result of the build-up of ferrous ion concentration gradients. A higher than expected production of

ferrous ions at the fuel cell bank outlet was noted as the electric current draw was increased, becoming excessively high when operating past the maximum power point of the fuel cells.

12. Study into the acid tolerance of the iron oxidizing microbes within the BioGenerator lead to the accidental discovery of significantly higher acid tolerance displayed by a red alga, most probably *C. caldarium*, than was recorded in the literature. A lower limit of growth was found to occur at pH -0.85 which far surpasses the previous record holder of acid tolerance held by the microbes *P. oshimae* and *P. torridus* at pH -0.20.

Bibliography

- Abou Jarboua T, Davison M, Karamanev D. 2019. Cost analysis of a 1MW BioGenerator, a bioelectrochemical technology for energy storage. *Journal of Energy Storage*, 21: 328-336.
- Acar C, Dincer I, Zamfirescu C. 2014. A review on selected heterogeneous photocatalysts for hydrogen production. *International Journal of Energy Research*, 38(15): 1903-1920.
- Acsente T. 2007. Laser diode intensity noise induced by mode hopping. *Romanian Reports in Physics*, 59(1): 87-92.
- Ahmadi L, Fowler M, Young SB, Fraser RA, Gaffney B, Walker SB. 2014. Energy efficiency of Li-ion battery packs re-used in stationary power applications. *Sustainable Energy Technologies and Assessments*, 8: 9-17.
- Ajanovic A, Sayer M, Haas R. 2022. The economics and the environmental benignity of different colors of hydrogen. *International Journal of Hydrogen Energy*, 47(57): 24136-24154.
- Andreadis GM, Podias AKM, Tsiakaras PE. 2008. The effect of the parasitic current on the direct ethanol PEM fuel cell operation. *Journal of Power Sources*, 181(2): 214-227.
- Andreev M, De Pablo JJ, Chremos A, Douglas JF. 2018. Influence of ion solvation on the properties of electrolyte solutions. *Journal of Physical Chemistry B*, 122(14): 4029-4034.
- Angelov A, Liebl W. 2006. Insights into extreme thermoacidophily based on genome analysis of *Picrophilus torridus* and other thermoacidophilic archaea. *Journal of Biotechnology*, 126(1): 3-10.
- Ascione R, Southwick W, Fresco JR. 1966. Laboratory culturing of a thermophilic alga at high temperature. *Science*, 153(3737): 752-755.
- Avdeev YaG, Andreeva TE, Anfilov KL, Kuznetsov YuI. 2022. About the observance of the Nernst equation in acid corrosive media containing oxidative cations. *International Journal of Corrosion and Scale Inhibition*, 11(2): 752-761.
- Ayodele DT, Ogunbiyi OD, Akamo DO, Otun KO, Akinpelu DA, Adegoke JA, Fajoluwo DP, Oladoye PO. 2023. Factors affecting biohydrogen production: Overview and perspectives. *International Journal of Hydrogen Energy*, 48(71): 27513-27539.
- Aysla Cista De Oliveira M, D'Epifanio A, Ohnuki H, Mecheri B. 2020. Platinum group metal-free catalysts for oxygen reduction reaction: Applications in microbial fuel cells. *Catalysts*, 10(5): 475.
- Badami M, Mura M. 2012. Leakage effects on the performance characteristics of a regenerative blower for the hydrogen recirculation of a PEM fuel cell. *Energy Conversion and Management*, 55: 20-25.

- Bagotsky VS. 2006. Fundamentals of Electrochemistry, 2nd Edition. Wiley.
- Baker-Austin C, Dopsin M. 2007. Life in acid: pH homeostasis in acidophiles. Trends in Microbiology, 15(4): 165-171.
- Bakhtiari L, Karamanev D. 2022. A theoretical overview of compressed air energy storage technologies and developments. Ecological Engineering and Environmental Protection, 2(2022): 30-44.
- Bandyopadhyay B, Humphrey AE, Taguchi H. 1967. Dynamic measurement of the volumetric oxygen transfer coefficient in fermentation systems. Biotechnology and Bioengineering, 9(4): 533-544.
- Barbier G, Oesterhelt C, Larson MD, Halgren RG, Wilkerson C, Garavito MR, Benning C, Weber APM. 2005. Comparative genomics of two closely related unicellular thermo-acidophilic red algae, *Galdieria sulphuraria* and *Cyanidioschyzon merolae*, reveals the molecular basis of the metabolic flexibility of *Galdieria sulphuraria* and significant differences in carbohydrate metabolism of both algae. Plant Physiology, 137(2): 460-474.
- Benson BB, Krause Jr. D. 1984. The concentration and isotopic fractionation of oxygen dissolved in freshwater and seawater in equilibrium with the atmosphere. Limnology and Oceanography, 29(3): 620-632.
- Bernardez LA, de Oliveira LEL, de Andrade Lima LRP. 2021. Acid mine drainage at the Bahia Belt (Brazil): microbial isolation and characterization. Environmental Monitoring and Assessment, 193(2): 60.
- Blake II RC, Shute EA, Greenwood MM, Spencer GH, Ingledew WJ. 1993. Enzymes of aerobic respiration on iron. FEMS Microbiology Reviews, 11(1-3): 9-18.
- Blay-Roger R, Bach W, Bobadilla LF, Reina TR, Odriozola JA, Amils R, Blay V. 2024. Natural hydrogen in the energy transition: Fundamentals, promise, and enigmas. Renewable and Sustainable Energy Reviews, 189: 113888.
- Bockris JO'M. 1972. A hydrogen economy. Science, 176(4041): 1323.
- Boodhun BSF, Mudhoo A, Kumar G, Kim SH, Lin CY. 2017. Research perspectives on constraints, prospects and opportunities in biohydrogen production. International Journal of Hydrogen Energy, 42(45): 27471-27481.
- Boretti A. 2023. High-efficiency internal combustion engine for hybrid hydrogen-electric locomotives. International Journal of Hydrogen Energy, 48(4): 1596-1601.
- Bovo A, Poli N, Trovò A, Marini G, Guarnieri M. 2023. Hydrogen energy storage system in a multi-technology microgrid: Technical features and performance. International Journal of Hydrogen Energy, 48(32): 12072-12088.
- BP. 2023. Statistical Review of World Energy 2022. 71st Edition.
- Brock TD. 1978. Thermophilic Microorganisms and Life at High Temperatures. Springer-Verlag.
- Brown TE, Richardson FL. 1968. The effect of growth environment on the physiology of algae: Light intensity. Journal of Phycology, 4(1): 38-54.

- Bryan JR, Riley JP, Williams PJ. 1976. A Winkler procedure for making precise measurements of oxygen concentration for productivity and related studies. *Journal of Experimental Marine Biology and Ecology* 21(3): 191-197.
- Bryant BD, McGroarty KM, Costerton JW, Laishley EJ. 1983. Isolation and characterization of a new acidophilic *Thiobacillus* species (*T. albertis*). *Canadian Journal of Microbiology*, 29:1159-1170.
- Buchmann I. 2017. Batteries in a Portable World: A Handbook on Rechargeable Batteries for Non-Engineers, 4th Edition. Cadex.
- Bui M, Adjiman CS, Bardow A, Anthony EJ, Boston A, Brown S, Fennell PS, Fuss S, Galindo A, Hackett LA, Hallett JP, Herzog HJ, Jackson G, Kemper J, Krevor S, Maitland GC, Matuszewski M, Metcalfe IS, Perit C, Puxty G, Reimer J, Reiner DM, Rubin ES, Scott SA, Shah N, Smit B, Trusler JPM, Webley P, Wilcox J, Mac Dowell N. 2018. Carbon capture and storage (CCS): The way forward. *Energy and Environment Science*, 11(5): 1062-1176.
- CEC – China Electricity Council. 2023. Analysis and Forecast of China's Power Supply and Demand Situation in the Third Quarter of 2023.
- Chang P, Yamagata T, Schopf P, Behera SK, Carton J, Kessler WS, Meyers G, Qu T, Schott F, Shetye S, Xie SP. 2006. Climate fluctuations of tropical coupled systems – The role of ocean dynamics. *Journal of Climate*, 19(20): 5122-5174.
- Chao RE. 1974. Thermochemical water decomposition processes. *Industrial and Engineering Chemistry Product Research and Development*, 13(2): 94-101.
- Chen LT, Bice W. 1982. Some psychrometric aspects of a hydraulic air compressor (HAC). *Journal of Energy Resources Technology, Transactions of the ASME*, 104(3): 274-276.
- Chen PJ, Wang HT, Lin LY, Hsu BD, Liu DR, Hwang CH, Wu WH. 2017. A practical portable photometer using LEDs as inspection light source. I2MTC 2017 - 2017 IEEE International Instrumentation and Measurement Technology Conference, Proceedings, 7969714.
- Choi CH, Kwon HC, Yook S, Shin H, Kim H, Choi M. 2014. Hydrogen peroxide synthesis via enhanced two-electron oxygen reduction pathway on carbon-coated Pt surface. *Journal of Physical Chemistry C*, 118(51): 30063-30070.
- Ciniglia C, Cennamo P, De Natale A, De Stefano M, Sirakov M, Iovinella M, Yoon HS, Pollio A. 2019. *Cyanidium chilense* (Cyanidiophyceae, Rhodophyta) from tuff rocks of the archeological site of Cuma, Italy. *Phycological Research*, 67(4): 311-319.
- CNESA – China Energy Storage Alliance. 2023. Energy Storage Industry White Paper.
- Coram NJ, Rawlings DE. 2002. Molecular relationship between two groups of the genus *Leptospirillum* and the finding that *Leptospirillum ferriphilum* sp. nov. dominates south African commercial biooxidation tanks that operate at 40°C. *Applied and Environmental Microbiology*, 68(2): 838-845.

- CREA – Canada Renewable Energy Association. 2023. Canada's current installed wind, solar, and energy storage capacity. <<https://renewablesassociation.ca/by-the-numbers>> (Retrieved February 19, 2024)
- Crowl DA, Louvar JF. 2002. Chemical Process Safety – Fundamentals with Applications, 2nd Edition. Prentice Hall.
- Dai F, Zhang S, Luo Y, Wang K, Liu Y, Ji X. 2023. Recent progress on hydrogen-rich syngas production from coal gasification. *Processes*, 11(6): 1765.
- Daoud J, Karamanev D. 2006. Formation of jarosite during Fe²⁺ oxidation by *Acidithiobacillus ferrooxidans*. *Minerals Engineering*, 19(9): 960-967.
- Darmawan A, Atmirabekti P, Nasruddin N, Dewi EL, Budiman AH, Aziz M. 2023. Efficient utilization of industrial waste heat for hydrogen production via Cu-Cl thermochemical water splitting cycle. *Chemical Engineering Transactions*, 103: 565-570.
- Debarshi S, Khan MM. 2019. Portable and low-cost LED based spectrophotometer for the detection of nitrite in simulated-urine. *Proceedings - 2019 International Conference on Electrical, Electronics and Computer Engineering, UPCON 2019*, 8980097.
- De Luca P, Taddei R, Varano L. 1978. *Cyanidioschyzon merolae*: A new alga of thermal acidic environments: *Cyanidioschyzon merolae*: Una nuova alga di ambienti termali acidi. *Webbia*, 33(1): 37-44.
- Degen F, Schütte M. 2022. Life cycle assessment of the energy consumption and GHG emissions of state-of-the-art automotive battery cell production. *Journal of Cleaner Production* 330(2022): 129798.
- Dewoolkar KD, Vaidya PD. 2017. Tailored Ce- and Zr-doped Ni/hydrotalcite materials for superior sorption-enhanced steam methane reforming. *International Journal of Hydrogen Energy*, 42(34): 21762-21774.
- Di W, Lei Y, Junjie K. 2022. Key drivers of China's 2021 power shortages, their implications, and lessons learned for the country's 2023-2060 goals. *Oxford Energy Forum*, 131: 17-20.
- DoE – U.S. Department of Energy. 2023a. Vehicle Registration Counts by State. Alternative Fuels Data Center.
- DoE – U.S. Department of Energy. 2023b. U.S. liquified natural gas exports by destination country (Jan 2021 – Jun 2023). LNG Reports.
- Doemel WN, Brock TD. 1970. The upper temperature limit of *Cyanidium caldarium*. *Archiv für Mikrobiologie*, 72(4): 326-332.
- DoT – U.S. Department of Transportation. 2024. New and Used Passenger Car and Light Truck Sales and Leases. <<https://www.bts.gov/content/new-and-used-passenger-car-sales-and-leases-thousands-vehicles>> (Retrieved February 24, 2024)

- Dopson M. 2016. Physiological and phylogenetic diversity of acidophilic bacteria. *Acidophiles: Life in Extremely Acidic Environments*. Quatrini R and Johnson DB, Poole: Caister Academic Press, 79-92.
- Dopson M, Baker-Austin C, Hind A, Bowman JP, Bond PL. 2004. Characterization of *Ferroplasma* Isolates and *Ferroplasma acidarmanus* sp. nov., Extreme Acidophiles from Acid Mine Drainage and Industrial Bioleaching Environments. *Applied and Environmental Microbiology*, 70(4): 2079-2088.
- Drandev S, Penev KI, Karamanev D. 2016. Study of the hydrodynamics and mass transfer in a rectangular air-lift bioreactor. *Chemical Engineering Science*, 146: 180-188.
- Dutrizac JE. 1996. The effect of seeding on the rate of precipitation of ammonium jarosite and sodium jarosite. *Hydrometallurgy*, 42(3): 293-312.
- EERE – U.S. Office of Energy Efficiency & Renewable Energy. Hydrogen Storage. <<https://www.energy.gov/eere/fuelcells/hydrogen-storage>> (Retrieved February 15, 2024)
- EG&G Technical Services, Inc. 2004. Fuel Cell Handbook, 7th Edition. U.S. Department of Energy.
- EIA – U.S. Energy Information Administration. 2021. International – Primary Energy Source 2021. <<https://www.eia.gov/international/overview/world>> (Retrieved February 21, 2024)
- EIA – U.S. Energy Information Administration. 2022. U.S. battery storage capacity in 2010 through 2022. <<https://www.eia.gov/energyexplained/electricity/energy-storage-for-electricity-generation.php>> (Retrieved February 16, 2024)
- EIA – U.S. Energy Information Administration. 2023a. Energy use per person, 2022. <<https://ourworldindata.org/grapher/per-capita-energy-use>> (Retrieved February 20, 2024)
- EIA – U.S. Energy Information Administration. 2023b. Preliminary Monthly Electric Generator Inventory. <<https://www.eia.gov/todayinenergy/detail.php?id=55719>> (Retrieved February 17, 2024)
- EIA – U.S. Energy Information Administration. 2024a. Monthly Energy Review January 2024. <<https://www.eia.gov/mer>> (Retrieved February 9, 2024)
- EIA – U.S. Energy Information Administration. 2024b. Short-Term Energy Outlook – Regular Gasoline Retail Prices. <<https://www.eia.gov/outlooks/steo/realprices/>> (Retrieved February 24, 2024)
- Eitches E, Crain V. 2016. Using gasoline data to explain inelasticity. *U.S. Bureau of Labor Statistics*, 5(5).
- Elmanakhly F, DaCosta A, Berry B, Stasko R, Fowler M, Wu XY. 2021. Hydrogen energy transition plan: A case study on Ontario. *AIMS Energy*, 9(4): 775-811.

- Energy Institute. 2023. Global primary energy consumption. <<https://ourworldindata.org/grapher/global-primary-energy>> (Retrieved February 14, 2024)
- EU Council. 2023. Amending Directive (EU) 2018/2001, Regulation (EU) 2018/1999 and Directive 98/70/EC as regards the promotion of energy from renewable sources, and repealing Council Directive (EU) 2015/652. Official Journal of the European Union 2023/2413.
- Ewan BCR, Allen RWK. 2005. A figure of merit assessment of the routes to hydrogen. *International Journal of Hydrogen Energy*, 30(8): 809-819.
- Falagán C, Johnson DB. 2016. *Acidithiobacillus ferriphilus* sp. nov., a facultatively anaerobic iron- and sulfur-metabolizing extreme acidophile. *International Journal of Systematic and Evolutionary Microbiology*, 66(1): 206-211.
- Falagán C, Moya-Beltrán A, Castro M, Quatrini R, Johnson DB. 2019. *Acidithiobacillus sulfuriphilus* sp. nov.: An extremely acidophilic sulfur-oxidizing chemolithotroph isolated from a neutral pH environment. *International Journal of Systematic and Evolutionary Microbiology*, 69(9): 2907-2913.
- Franke AC, Kotzé E. 2022. High-density grazing in southern Africa: Inspiration by nature leads to conservation? *Outlook on Agriculture*, 51(1): 67-74.
- Friedlingstein P, O'Sullivan M, Jones MW, Andrew RM, Bakker DCE, Hauck J, Landschützer P, Le Quéré C, Luijkx IT, Peters GP, Peters W, Pongratz J, Schwingshackl C, Sitch S, Canadell JG, Ciais P, Jackson RB, Alin SR, Anthoni P, Barbero L, Bates NR, Becker M, Bellouin N, Decharme B, Bopp L, Brasika IBM, Cadule P, Chamberlain MA, Chandra N, Chau TTT, Chevallier F, Chini LP, Cronin M, Don X, Enyo K, Evans W, Falk S, Feely RA, Feng L, Ford DJ, Gasser T, Ghattas J, Gkritzalis T, Grassi G, Gregor L, Gruber N, Gürses Ö, Harris I, Hefner M, Heinke J, Houghton RA, Hurtt GC, Iida Y, Ilyina T, Jacobson AR, Jain A, Jarníková T, Jersild A, Jiang F, Jin Z, Joos F, Kato E, Keeling RF, Kennedy D, Goldewijk KK, Knauer J, Korsbakken JI, Körtzinger A, Lan X, Lefèvre N, Li H, Liu J, Liu Z, Ma L, Marland G, Mayot N, McGuire PC, McKinley GA, Meyer G, Morgan EJ, Munro DR, Nakaoka SI, Niwa Y, O'Brien KM, Olsen A, Omar AM, Ono T, Paulsen M, Pierrot D, Pocock K, Poulter B, Powis CM, Rehder G, Resplandy L, Robertson E, Rödenbeck C, Rosan TM, Schwinger J, Séférian R, Smallman TL, Smith SM, Sospedra-Alfonso R, Sun Q, Sutton AJ, Sweeney C, Takao S, Tans PP, Tian H, Tilbrook B, Tsujino H, Tubiello F, van der Werf GR, van Ooijen E, Wanninkhof R, Watanabe M, Wimart-Rousseau C, Yang D, Yang X, Yuan W, Yue X, Zachle S, Zeng J, Zheng B. 2023. Global Carbon Budget 2023. *Earth System Science Data*, 15: 5301-5369.
- Fujishima A, Honda K. 1972. Electrochemical photolysis of water at a semiconductor electrode. *Nature*, 238(5358): 37-38.
- Fukada S, Ono S. 2007. Partial oxidation of methane in permeable Ni tube for effective hydrogen production. *Separation Science and Technology*, 42(1): 73-87.
- Fütterer O, Angelov A, Liesegang H, Gottschalk G, Schleper C, Schlepers B, Dock C, Antranikian G, Liebl W, Söll D. 2004. Genome sequence of *Picrophilus torridus*

- and its implications for life around pH 0. Proceedings of the National Academy of Sciences of the United States of America, 101(24): 9091-9096.
- Ganopolski A, Winkelmann R, Schellhuber HJ. 2016. Critical insolation-CO₂ relation for diagnosing past and future glacial inception. *Nature*, 529(7585): 200-203.
- Gao J, Zhang CG, Wu XL, Wang HH, Qiu GZ. 2007. Isolation and identification of a strain of *Leptospirillum ferriphilum* from an extreme acid mine drainage site. *Annals of Microbiology*, 57(2): 171-176.
- Gao K, Hu Y, Guo C, Ke C, He C, Hao X, Lu G, Dang Z. 2020. Effects of adsorbed phosphate on jarosite reduction by a sulfate reducing bacterium and associated mineralogical transformation. *Ecotoxicology and Environmental Safety*, 202: 110921.
- Gao K, Jiang M, Guo C, Zeng Y, Fan C, Zhang J, Reinfelder JR, Huang W, Lu G, Dang Z. 2019. Reductive dissolution of jarosite by a sulfate reducing bacterial community: Secondary mineralization and microflora development. *Science of the Total Environment*, 690: 1100-1109.
- Ge Q, Huang YM, Qiu FY, Zhang CW. 1999. New bifunctional catalyst for direct synthesis of dimethyl ether. *Journal of Natural Gas Chemistry*, 8(4): 280-285.
- Geitler L. 1933. Diagnosen neuer Blaualgen von den Sunda-Inseln. *Archiv für Hydrobiologie – Supplements*, 12: 622-634.
- Georgiou S, Shah N, Markides CN. 2018. A thermo-economic analysis and comparison of pumped-thermal and liquid-air electricity storage systems. *Applied Energy*, 226: 1119-1133.
- Giotakos PI, Neophytides SG. 2023. Unraveling the elusive oxygen reduction reaction electrokinetics and energetics in PEM fuel cells. *Electrochimica Acta*, 439: 141591.
- Glas J. 2022. Alternative approach to small scale photovoltaic solar power and energy storage. *Ecological Engineering and Environment Protection*, 1(2022): 22-34.
- Glasel JA. 1995. Validity of nucleic acid purities monitored by 260nm/280nm absorbance ratios. *BioTechniques*, 18(1): 62-63.
- Gokon N, Sagawa S, Kodama T. 2013. Comparative study of activity of cerium oxide at thermal reduction temperatures of 1300-1550 °C for solar thermochemical two-step water-splitting cycle. *International Journal of Hydrogen Energy*, 38(34): 14402-14414.
- Golyshina OV, Pivovarova TA, Karavaiko GI, Kondratéva TH, Moore ER, Abraham WR, Lünsdorf H, Timmis KN, Yakimov MM, Golyshin PN. 2000. *Ferroplasma acidiphilum* gen. nov., sp. nov., an acidophilic, autotrophic, ferrous-iron-oxidizing, cell-wall-lacking, mesophilic member of the Ferroplasmaceae fam. nov., comprising a distinct lineage of the Archaea. *International Journal of Systematic and Evolutionary Microbiology*, 50(3): 997-1006.
- Gosnell H, Grimm K, Golstein BE. 2020. A half century of Holistic Management: what does the evidence reveal? *Agriculture and Human Values*, 37(3): 849-867.

- Guo JJ, Liu JZ, Zhang T, Hu F, Li PF, Liu ZH, Zheng CG. 2024. Science China Technological Sciences.
- Habib N, Rao MPN, Jan SA, Banerjee A, Thamchaipenet A, Li WJ. 2023. Genome-based reclassification of *Picrophilus torridus* Zillig et al. 1996 as a later heterotypic synonym of *Picrophilus oshimae* Schleper et al. 1996. International Journal of Systematic and Evolutionary Microbiology, 73(4): 005851.
- Hallberg KB, Lindstrom EB. 1994. Characterization of *Thiobacillus caldus* sp. Nov., A moderately thermophilic acidophile. Microbiology, 140(12): 3451-3456.
- Hallberg KB, González-Toril E, Johnson DB. 2010. *Acidithiobacillus ferrivorans*, sp. Nov.; facultatively anaerobic, psychrotolerant iron-, and sulfur-oxidizing acidophiles isolated from metal mine-impacted environments. Extremophiles, 14(1): 9-19.
- Harrison S, Smith DE, Glasser NF. 2019. Late quaternary meltwater pulses and sea level change. Journal of Quaternary Science, 34(1): 1-15.
- Hedrich S, Johnson DB. 2013a. *Acidithiobacillus ferridurans* sp. nov., An acidophilic iron-, sulfur- and hydrogen-metabolizing chemolithotrophic gammaproteobacterium. International Journal of Systematic and Evolutionary Microbiology, 63 (Part 11): 4018-4025.
- Hedrich S, Johnson DB. 2013b. Aerobic and anaerobic oxidation of hydrogen by acidophilic bacteria. FEMS Microbiology Letters, 349(1): 40-45.
- Hedrich S, Schlömann M, Johnson DB. 2011. The iron-oxidizing proteobacteria. Microbiology, 157(6): 1551-1564.
- Hernández A, Martin-Puertas C, Moffa-Sánchez P, Moreno-Chamarro E, Ortega P, Blockley S, Cobb KM, Comas-Bru L, Giralto S, Goosse H, Luterbacher J, Martrat B, Muscheler R, Parnell A, Pla-Rabes S, Sjolte J, Scaife AA, Swingedouw D, Wise E, Xu G. 2020. Modes of climate variability: Synthesis and review of proxy-based reconstructions through the Holocene. Earth-Science Reviews, 209: 103286.
- Hippe H. 2000. *Leptospirillum* gen. nov. (ex Markosyan 1972), nom. rev., including *Leptospirillum ferrooxidans* sp. nov. (ex Markosyan 1972), nom. rev. and *Leptospirillum thermoferrooxidans* sp. nov. (Golovacheva et al. 1992). International Journal of Systematic and Evolutionary Microbiology, 50(2): 501-503.
- Hirt RC, King FT, Schmitt RG. 1954. Graphical absorbance-ratio method for rapid two-component spectrophotometric analysis. Analytical Chemistry, 26(8): 1270-1273.
- Hodges A, Hoang AL, Tsekouras G, Wagner K, Lee CY, Sweigers GF, Wallace GG. 2022. A high-performance capillary-fed electrolysis cell promises more cost-competitive renewable hydrogen. Nature Communications, 13(1): 1304.
- Hsu WY, Gierke TD. 1982. Ion clustering and transport in 'nafion' perfluorinated membranes. Proceedings – The Electrochemical Society, 82(10): 158-177.

- Huang MQ, Zhang M, Zhan SL, Chen L, Xue ZL. 2022. Saturated dissolved oxygen concentration in in-situ fragmentation bioleaching of copper sulfide ores. *Frontiers in Microbiology*, 13: 821635.
- Ibrahim H, Ilinca A, Perron J. 2008. Energy storage systems – Characteristics and comparisons. *Renewable and Sustainable Energy Reviews*, 12(5): 1221-1250.
- IEA – International Energy Agency. 2022a. EV, sales, cars, China, 2010-2022. <<https://www.iea.org/data-and-statistics/data-tools/global-ev-data-explorer>> (Retrieved February 22, 2024)
- IEA – International Energy Agency. 2022b. Global Hydrogen Review 2022.
- IEA – International Energy Agency. 2023. Catching up with climate ambitions. Global EV Outlook 2023.
- Ilbert M, Bonnefoy V. 2013. Insight into the evolution of the iron oxidation pathways. *Biochimica et Biophysica Acta – Bioenergetics*, 1827(2): 161-175.
- Jain MK, Das A. 2017. Impact of mine waste leachates on aquatic environment: A review. *Current Pollution Reports*, 3(1): 31-37.
- Jambor JL. 1999. Nomenclature of the alunite supergroup. *Canadian Minerologist*, 37(6): 1323-1341.
- Jarboe J. 2008. Taking the pressure off blower selection. *Pollution Engineering*, 40(10): 41-44.
- Jensen AB, Webb C. 1995. Ferrous sulphate oxidation using *Thiobacillus ferrooxidans*: A review. *Process Biochemistry*, 30(3): 225-236.
- Jin J, Wei X, Liu M, Yu Y, Li W, Kong H, Hao Y. 2018. A solar methane reforming reactor design with enhanced efficiency. *Applied Energy*, 226: 797-807.
- Johnson DB. 1998. Biodiversity and ecology of acidophilic microorganisms. *FEMS Microbiology Ecology*, 27(4): 307-317.
- Johnson DB, Aguilera A. 2019. Extremophiles and acidic environments. *Encyclopedia of Microbiology*, 4th Edition, 206-227.
- Karamanev DG, Nagamune T, Endo I. 1992. Hydrodynamic and mass transfer study of a gas-liquid-solid draft tube spouted bed bioreactor. *Chemical Engineering Science*, 47(13-14): 3581-3588.
- Karamanev DG, Nikolov LN, Mamatarkove V. 2002. Rapid simultaneous quantitative determination of ferric and ferrous ion in drainage waters and similar solutions. *Minerals Engineering*, 15(5): 341-346.
- Karamanev D. 2009. Biofuel cell (US Patent No. 7572546 B2). U.S. Patent and Trademark Office.
- Kayano H, Matsunaga T, Karube I, Suzuki S. 1981. Hydrogen evolution by co-immobilized *Chlorella vulgaris* and *Clostridium butyricum* cells. *BBA – Bioenergetics*, 638(1): 80-85.

- Kim M, Oh HS, Park SC, Chun J. 2014. Towards a taxonomic coherence between average nucleotide identity and 16S rRNA gene sequence similarity for species demarcation of prokaryotes. *International Journal of Systematic and Evolutionary Microbiology*, 64(Part 2): 346-351.
- Knibbe R, Harding D, Burton J, Cooper E, Zadeh ZA, Sagulenko M, Meehan PA, Buckley R. 2023. Optimal battery and hydrogen fuel cell sizing in heavy-haul locomotives. *Journal of Energy Storage*, 71: 108090.
- Kucera J, Pakostova E, Lochman J, Janiczek O, Mandi M. 2016. Are there multiple mechanisms of anaerobic sulfur oxidation with ferric iron in *Acidithiobacillus ferrooxidans*? *Research in Microbiology*, 167(5): 357-366.
- Kumar G, Mudhoo A, Sivagurunathan P, Nagarajan D, Ghimire A, Lay CH, Lin CY, Lee DJ, Chang JS. 2016. Recent insights into the cell immobilization technology applied for dark fermentative hydrogen production. *Bioresource Technology* 219: 725-737.
- Kuroiwa T, Kawazu T, Takahashi H, Suzuki K, Ohta N, Kuroiwa H. 1994. Comparison of ultrastructures between the ultra-small eukaryote *Cyanidioschyzon merolae* and *Cyanidium caldarium*. *Cytologia*, 59(2): 149-158.
- Lang W, Wolf HU, Zander R. 1979. A sensitive continuous and discontinuous photometric determination of oxygen, carbon dioxide, and carbon monoxide in gases and fluids. *Analytical Biochemistry* 92(2): 255-264.
- Lee DY, Elgowainy A, Dai Q. 2018. Life cycle greenhouse gas emissions of hydrogen fuel production from chlor-alkali processes in the United States. *Applied Energy*, 217: 467-479.
- Lee J, Tryk DA, Fujishima A, Park SM. 2002. Electrochemical generation of ferrate in acidic media at boron-doped diamond electrodes. *Chemical Communications*, 5: 486-487.
- Lee JD, Dewitt BA, Lee SS, Bhang KJ, Sim JB. 2012. Analysis of concrete reflectance characteristics using spectrometer and VNIR hyperspectral camera. *International Archives of the Photogrammetry, Remote Sensing and Spatial Information Sciences – ISPRS Archives*, 39: 127-130.
- Lee JE, Shafiq I, Hussain M, Lam SS, Rhee GH, Park YK. 2022. A review on integrated thermochemical hydrogen production from water. *International Journal of Hydrogen Energy*, 47(7): 4346-4356.
- Li C, Li Y, Xu M, Gong Y, Gong S, Wang P, Li P, Dong B, Men Z. 2021. Studies on pathways to carbon neutrality for indirect coal liquefaction in China. *Clean Energy*, 5(4): 644-654.
- Li H, Niu R, Li W, Lu H, Cairney J, Chen YS. 2022. Hydrogen in pipeline steels: Recent advances in characterization and embrittlement mitigation. *Journal of Natural Gas Science and Engineering*, 105: 104709.

- Li Y, Li Q, Wang H, Zhang L, Wilkinson DP, Zhang J. 2019. Recent progresses in oxygen reduction reaction electrocatalysis for electrochemical energy applications. *Electrochemical Energy Reviews*, 2(4): 518-538.
- Limaye SS, Mogul R, Smith DJ, Ansari AH, Słowik GP, Vaishampayan P. 2018. Venus' spectral signatures and the potential for life in the clouds. *Astrobiology*, 18(9): 1181-1198.
- Liu H, Lu H, Hu H. 2024. CO₂ capture and mineral storage: State of the art and future challenges. *Renewable and Sustainable Energy Reviews*, 189: 113908.
- Liu JS, Xie XH, Xiao SM, Wang XM, Zhao WJ, Tian ZL. 2007. Isolation of *Leptospirillum ferriphilum* by single-layered solid medium. *Journal of Central South University of Technology (English Edition)*, 14(4): 467-473.
- Liu SL, Chiang YR, Yoon HS, Fu HY. 2020. Comparative Genome Analysis Reveals *Cyanidiococcus* gen. nov., A New Extremophilic Red Algal Genus Sister to *Cyanidioschyzon* (Cyanidioschyzonaceae, Rhodophyta). *Journal of Phycology*, 56(6): 1428-1442.
- Liu SX, Hermanowicz SW. 2008. Empirical correlation of volumetric mass transfer coefficient for a rectangular internal-loop airlift bioreactor. *Journal of Environmental Engineering and Science*, 7(4): 411-415.
- Luo J, Tian W, Jin H, Yang J, Li J, Wang Y, Shen W, Ren Y, Zhou M. 2023. Recent advances in microbial fuel cells: A review on the identification technology, molecular tool and improvement strategy of electricigens. *Current Opinion in Electrochemistry*, 37: 101187.
- Lyu A, Lee J, Nam JH, Kim M, Lee YK. 2023. Hydrogen absorption and embrittlement of martensitic medium-Mn steels. *Corrosion Science*, 221: 111304.
- Ma Y, Lin L, Takata T, Hisatomi T, Domen K. 2023. A perspective on two pathways of photocatalytic water splitting and their practical application systems. *Physical Chemistry Chemical Physics*, 25(9): 6586-6601.
- Maloney JO. 2008. Perry's Chemical Engineers' Handbook, 8th Edition. McGraw-Hill.
- Malik L, Hedrich S. 2022. Ferric iron reduction in extreme acidophiles. *Frontiers in Microbiology*, 12: 818414.
- Marchese D, Giosuè C, Staffolani A, Conti M, Orcioni S, Soavi F, Cavalletti M, Stipa P. 2024. An overview of the sustainable recycling processes used for lithium-ion batteries. *Batteries*, 10(1): 27.
- Marino N, Aronson HS, Bojanova DP, Feyhl-Buska J, Wong ML, Zhang S, Giovannelli D. 2019. Living at the extremes: Extremophiles and the limits of life in a planetary context. *Frontiers in Microbiology*, 10(MAR): 780.
- Martínez-Bussenius C, Navarro CA, Jerez CA. 2017. Microbial copper resistance: Importance in biohydrometallurgy. *Microbial Biotechnology*, 10(2): 279-295.

- Marisa Dispensa J, Brulle RJ. 2003. Media's social construction of environmental issues: Focus on global warming – a comparative study. *International Journal of Sociology and Social Policy*, 23(10): 74-105.
- Matos CR, Cameiro JF, Silva PP. 2019. Overview of large-scale underground energy storage technologies for integration of renewable energies and criteria for reservoir identification. *Journal of Energy Storage*, 21: 241-258.
- Mazuelos A, Garcia-Tinajero CJ, Romero R, Iglesias N, Carranza F. 2017. Oxygen solubility in copper bioleaching solutions. *Hydrometallurgy*, 167: 1-7.
- Mekonnen ZA, Riley WJ. 2023. Climate change will increase biomass proportion of global forest carbon stocks under an SSP5–8.5 climate trajectory. *Geophysical Research Letters*, 50(23): e2023GL104612.
- Millar DL. 2014. A review of the case for modern-day adoption of hydraulic air compressors. *Applied Thermal Engineering*, 69(1-2): 55-77.
- Mokheimer EMA, Shakeel MR, Harale A, Paglieri S, Mansour RB. 2024. Fuel reforming processes for hydrogen. *Fuel* 359: 130427.
- Möller S, Friedmann S, Walter M, Dam JT. 2007. SOLREF – Development of an advanced solar high-temperature reformer. *International Solar Energy Conference*, 269-276.
- Morrissey P. 2023. An overview of the polysulfide/bromine flow battery. *Flow Batteries: From Fundamentals to Applications: Volume 1, 2 and 3*, 2: 765-790.
- Mortimer CH. 1956. The oxygen content of air-saturated fresh waters, and aids in calculating percentage saturation. *International Association for Theoretical and Applied Limnology*, 6.
- Moya-Beltrán A, Beard S, Rojas-Villalobos C, Issotta F, Gallardo Y, Ulloa R, Giaveno A, Esposti MD, Johnson DB, Quatrini R. 2021. Genomic evolution of the class Acidithiobacillia: deep-branching Proteobacteria living in extreme acidic conditions. *ISME Journal*, 15(11): 3221-3238.
- M. P. 1908. Production de l'air comprimé à la mine Victoria au moyen de trompes Taylor. *La Houille Blanche*, 7:1, 19-20.
- Mullen D, Herraiz L, Gibbins J, Lucquiaud M. 2023. On the cost of zero carbon hydrogen: A techno-economic analysis of steam methane reforming with carbon capture and storage. *International Journal of Greenhouse Gas Control*, 126: 103904.
- Muthudineshkumar R, Anand R. 2019. Anaerobic digestion of various feedstocks for second-generation biofuel production. *Woodhead Publishing Series in Energy*, 157-185.
- Nagarajan D, Lee DJ, Chang JS. 2019. Recent insights into consolidated bioprocessing for lignocellulosic biohydrogen production. *International Journal of Hydrogen Energy*, 44(28): 14362-14379.

- Nandiyanto ABD, Zaen R, Oktiani R, Abdullah AG, Riza LS. 2018. A simple, rapid analysis, portable, low-cost, and Arduino-based spectrophotometer with white LED as a light source for analyzing solution concentration. *Telkomnika (Telecommunication Computing Electronics and Control)*, 16(2): 580-585.
- Nemati M, Harrison STL, Handford GS, Webb C. 1998. Biological oxidation of ferrous sulphate by *Thiobacillus ferrooxidans*: A review on the kinetic aspects. *Biochemical Engineering Journal*, 1(3): 171-190.
- Neukom R, Barboza LA, Erb MP, Shi F, Emile-Geay J, Evans MN, Franke J, Kaufman DS, Lücke L, Rehfeld K, Schurer A, Zhu F, Brönnimann S, Hakim GJ, Henley BJ, Jungqvist FC, McKay N, Valler V, von Gunten L. 2019. Consistent multidecadal variability in global temperature reconstructions and simulations over the common era. *Nature Geoscience*, 12(8): 643-649.
- Ni M. 2006. An overview of hydrogen storage technologies. *Energy Exploration and Exploitation*, 24(3): 197-209.
- Nikolaos PC, Marios F, Dimitris K. 2023. A review of pumped hydro storage systems. *Energies*, 16(11): 4516.
- Nikolov L, Karamanev D. 1987. Experimental study of the inverse fluidized bed biofilm reactor. *The Canadian Journal of Chemical Engineering*, 65(2): 214-217.
- Nordstrom DK, Alpers CN, Ptacek CJ, Blowes DW. 2000. Negative pH and extremely acidic mine waters from Iron Mountain, California. *Environmental Science and Technology* 34(2): 254-258.
- Norris PR, Falagán C, Moya-Beltrán A, Castro M, Quatrini R, Johnson DB. 2020. *Acidithiobacillus ferrianus* sp. nov.: An ancestral extremely acidophilic and facultatively anaerobic chemolithoautotroph. *Extremophiles*, 24(2): 329-337.
- Núñez RRA, Nova PCI, Gutierrez LCJ, Velasco CDA, Ceron Cifuentes JM, Amaya DA, Combariza MY, Tirado CB. 2022. Portable low-cost spectrophotometer for trace detection of cadmium ions in cocoa crops. 2022 IEEE International Conference on Engineering Veracruz, ICEV 2022.
- OECD - Organization for Economic Cooperation and Development. 2024. Crop Production (Indicator). <<https://data.oecd.org/agrooutput/crop-production.htm#indicator-chart>> (Retrieved February 26, 2024)
- Osman AI. 2020. Catalytic hydrogen production from methane partial oxidation: Mechanisms and kinetic study. *Chemical Engineering and Technology*, 43(4): 641-648.
- Osorio H, Mangold S, Denis Y, Ñancucheo I, Esparza M, Johnson DB, Bonnefoy V, Dopson M, Holmes DS. 2013. Anaerobic sulfur metabolism coupled to dissimilatory iron reduction in the extremophile *Acidithiobacillus ferrooxidans*. *Applied and Environmental Microbiology* 79(7): 2172-2181.
- Panda PK, Sahoo B, Ramakrishna S. 2023. Hydrogen production, purification, storage, transportation, and their applications: A review. *Energy Technology*, 11(7): 2201434.

- Panzone C, Phillippe R, Chappaz A, Fongarland P, Bengaouer A. 2020. Power-to-liquid catalytic CO₂ valorization into fuels and chemicals: Focus on the Fischer-Tropsch route. *Journal of CO₂ Utilization*, 38: 314-347.
- Park SI, Cho CH, Ciniglia C, Huang TY, Liu SL, Bustamante DE, Calderon MS, Mansilla A, McDermott T, Andersen RA, Yoon HS. 2023. Revised classification of the *Cyanidiophyceae* based on plastid genome data with descriptions of the *Cavernicolales* ord. nov. and *Galdieriales* ord. nov. (Rhodophyta). *Journal of Phycology*, 59(3): 444-466.
- Parker CD. 1945. The isolation of a species of bacterium associated with the corrosion of concrete exposed to atmospheres containing hydrogen sulfide. *Australian Journal of Experimental Biology and Medical Science*, 23(2): 81-90.
- Passerini S, Scrosati B. 2016. Lithium and lithium-ion batteries: Challenges and prospects. *Electrochemical Society Interface*, 25(3): 85-87.
- Paulu A, Matušítk J, Trecáková T, Kočí V. 2024. Overlooked source of hydrogen: The environmental potential of chlor-alkali by-product. *International Journal of Hydrogen*, 49:1437-1443.
- Pavese V, Millar D, Verda V. 2016. Mechanical efficiency of hydraulic air compressors. *Journal of Energy Resources Technology, Transactions of the ASME*, 138(6): 062005.
- Penev K. 2010. Kinetics of the ferrous iron oxidation by *Leptospirillum ferriphilum* at high iron concentration and low pH. Ph.D. Thesis, University of Western Ontario, London, Ontario, Canada.
- Penev K, Karamanev D. 2010. Batch kinetics of ferrous iron oxidation by *Leptospirillum ferriphilum* at moderate to high total iron concentration. *Biochemical Engineering Journal*, 50(1-2): 54-62.
- Perret R. 2011. Solar Thermochemical Hydrogen Production Research (SCTH) - Thermochemical Cycle Selection and Investment Priority. Sandia National Laboratories, SAND2011-3622.
- Peters JF, Weil M. 2018. Providing a common base for life cycle assessments of Li-ion batteries. *Journal of Cleaner Production*, 171: 704-713.
- Piatkowski N, Wieckert C, Weimer AW, Steinfeld A. 2011. Solar-driven gasification of carbonaceous feedstock – A review. *Energy and Environmental Science* 4(1): 73-82.
- Pikuta EV, Hoover RB, Tang J. 2007. Microbial extremophiles at the limits of life. *Critical Reviews in Microbiology*, 33(3): 183-209.
- Pinto G, Ciniglia C, Cascone C, Pollio A. 2007. Species Composition of Cyanidiales Assemblages in Pisciarelli (Campi Flegrei, Italy) and Description of *Galdieria Phlegrea* sp. nov. *Journal of Algae and Cyanobacteria in Extreme Environments*, 11: 489-502.
- Plumb JJ, Muddle R, Franzmann PD. 2008. Effects of pH on rates of iron and sulfur oxidation by bioleaching organisms. *Minerals Engineering*, 21(1): 76-82.

- Pogliani C, Donati E. 2000. Immobilisation of *Thiobacillus ferrooxidans*: Importance of jarosite precipitation. *Process Biochemistry*, 35(9): 997-1004.
- Pollio A, Greca MD, Monaco P, Pinto G, Previtiera L. 1988. Lipid composition of the acidophilic alga *Dunaliella acidophila* (*Volvocales*, *Chlorophyta*) I. Non-polar lipids. *Biochimica et Biophysica Acta (BBA)/Lipids and Lipid Metabolism*, 963(1): 53-60.
- Prairie MW, Frisbie SH, Rao KK, Saksri SH, Parbat S, Mitchell EJ. 2020. An accurate, precise, and affordable light emitting diode spectrophotometer for drinking water and other testing with limited resources. *PLoS ONE*, 15(1): e0226761.
- Prashanthi R. 2023. A review on microbial fuel cell and green energy. *Ionics*, 29(5): 1667-1697.
- Pupkevich V. 2014. Scale-up and study of the BioGenerator. Ph.D. Thesis, University of Western Ontario, London, Ontario, Canada.
- Pupkevich V, Glibin V, Karamanev D. 2007a. The effect of ferric ions on the conductivity of various types of polymer cation exchange membranes. *Journal of Solid State Electrochemistry*, 11(10): 1429-1434.
- Pupkevich V, Glibin V, Karamanev D. 2007b. The effect of activation on the electrochemical behaviour of graphite felt towards the $\text{Fe}^{3+}/\text{Fe}^{2+}$ redox electrode reaction. *Electrochemistry Communications*, 9(8): 1924-1930.
- Quatrini R, Jedlicki E, Holmes DS. 2005. Genomic insights into the iron uptake mechanisms of the biomining microorganism *Acidithiobacillus ferrooxidans*. *Journal of Industrial Microbiology and Biotechnology*, 32(11-12): 606-614.
- Rajak A, Munir MM, Abidin MS, Khairurrijal. 2015. A simple spectrometer using various LEDs and a photodiode sensor for photocatalytic performance evaluation. *Applied Mechanics and Materials*, 771: 17-20.
- Rawlings DE. 2008. High level arsenic resistance in bacteria present in biooxidation tanks used to treat gold-bearing arsenopyrite concentrates: A review. *Transactions of Nonferrous Metals Society of China (English Edition)*, 18(6): 1311-1318.
- Rismani-Yazdi H, Carver SM, Christy AD, Tuovinen OH. 2008. Cathodic limitations in microbial fuel cells: An overview. *Journal of Power Sources*, 180(2): 683-694.
- Roh HS, Jun KW, Baek SC, Park SE. 2002. A highly active and stable catalyst for carbon dioxide reforming of methane: Ni/Ce-ZrO₂/θ-Al₂O₃. *Catalysis Letters*, 81(3-4): 147-151.
- Rojas C, Vargas IT, Bruns MA, Regen JM. 2017. Electrochemically active microorganisms from an acid mine drainage-affected site promote cathode oxidation in microbial fuel cells. *Bioelectrochemistry*, 118:139-146.
- Rozendal RA, Hamelers HVM, Rabaey K, Keller J, Buisman CJN. 2008. Towards practical implementation of biochemical wastewater treatment. *Trends in Biotechnology*, 26(8): 450-459.

- Ryu JG, Kim Y. 2022. Mineral transformation and dissolution of jarosite coprecipitated with hazardous oxyanions and their mobility changes. *Journal of Hazardous Materials*, 427: 128283.
- Saini N, Pal K, Sujata, Deepak B, Mona S. 2021. Thermophilic algae: A new prospect towards environmental sustainability. *Journal of Cleaner Production*, 324: 129277.
- Schalenbach M, Zillgitt M, Maier W, Stolten D. 2015. Parasitic currents caused by different ionic and electronic conductivities in fuel cell anodes. *ACS Applied Materials and Interfaces*, 7(29): 15746-15751.
- Schleper C, Pühler G, Klenk HP, Zillig W. 1996. *Picrophilus oshimae* and *Picrophilus torridus* fam. nov., gen. nov., sp. nov., two species of hyperacidophilic, thermophilic, heterotrophic, aerobic archaea. *International Journal of Systematic Bacteriology*, 46(3): 814-816.
- Seckbach J. 1994. *Evolutionary Pathways and Enigmatic Algae - Cyanidium caldarium (Rhodophyta) and Related Cells*. Springer Science and Business Media.
- Seckbach J, Baker FA, Shugarman PM. 1970. Algae thrive under pure CO₂. *Nature*, 227(5259): 744-745.
- Seckbach J, Libby WF. 1970. Vegetative life on Venus? Or investigations with algae which grow under pure CO₂ in hot acid media at elevated pressures. *Space Life Sciences*, 2(2): 121-143.
- Seyam S, Dincer I, Agelin-Chaab M. 2022. Analysis of a newly developed locomotive engine employing sustainable fuel blends with hydrogen. *Fuel*, 319: 123748.
- Shiva Kumar S, Himabindu V. 2019. Hydrogen production by PEM water electrolysis – A review. *Materials Science for Energy Technologies*, 2(3), 442-454.
- Shuler ML, Kargi F. 2002. *Bioprocess engineering – Basic Concepts 2nd Edition*. Upper Saddle River, New Jersey: Prentice Hall.
- Silverman MP, Lundgren DG. 1959. Studies on the chemoautotrophic iron bacterium *Ferrobacillus ferrooxidans*. I. An improved medium and a harvesting procedure for securing high cell yields. *Journal of Bacteriology*, 77(5): 642-647.
- Singh G, Kumar D, Sharma D, Singh M, Kaur S. 2012. Q-Absorbance ratio spectrophotometric method for the simultaneous estimation of prednisolone and 5-amino salicylic acid in tablet dosage form. *Journal of Applied Pharmaceutical Science*, 2(7): 222-226.
- Smdani G, Islam MR, Ahmad Yahaya AN, Bin Safie SI. 2023. Performance evaluation of advanced energy storage systems: A review. *Energy and Environment*, 34(4): 1094-1141.
- Smith AML, Hudson-Edwards KA, Dubbin WE, Wright K. 2006. Dissolution of jarosite [KFe₃(SO₄)₂(OH)₆] at pH 2 and 8: Insights from batch experiments and computational modelling. *Geochimica Cosmochimica Acta*, 70(3): 608-621.

- Song J, Franzmann PD, Lin J, Lin J, Kaksonen AH. 2011. Respirometry studies of bioleaching of low-grade chalcopyrite ore using six acidophilic strains. *Minerals Engineering*, 24(11): 1139-1145.
- Stantec. 2023. Technical and Economic Potential Assessment of Pumped Storage Hydropower on Canada.
- Stom DI, Zhdanova GO, Kalashnikova OB, Bulaev AG, Kashevskii AB, Kupchinsky AB, Vardanyan NS, Ponamoreva ON, Alferov SV, Saksonov MN, Chesnokova AN, Tolstoy MY. 2021. Acidophilic microorganisms *Leptospirillum* sp., *Acidithiobacillus* sp., *Ferroplasma* sp. As a cathodic bioagents in a MFC. *Geomicrobiology Journal*, 38(4): 340-346.
- Sui S, Wang X, Zhou X, Su Y, Riffat S, Liu CJ. 2017. A comprehensive review of Pt electrocatalysts for the oxygen reduction reaction: Nanostructure, activity, mechanism and carbon support in PEM fuel cells. *Journal of Materials Chemistry A*, 5(5): 1808-1825.
- Sun Y, Wang L, Amer WA, Yu H, Ji J, Huang L, Shan J, Tong R. 2013. Hydrogen storage in metal-organic frameworks. *Journal of Inorganic and Organometallic Polymers and Materials*, 23(2): 270-285.
- Surase R, Varpe A, Solankar M. 2018. Development of Non-imaging Spectral Library via Field Spec4. National Conference on Convergence of Technology 2018: 133-136.
- Sze SM, Lee MK. 2012. *Semiconductor Devices – Physics and Technology*, 3rd Edition. New York, New York: John Wiley and Sons, Inc.
- Ter Heijan A, Hamelers HVM, Buisman CJN. 2007. Microbial fuel cell operation with continuous biological ferrous iron oxidation of the catholyte. *Environmental Science and Technology*, 41(11): 4130-4134.
- Theriault EJ, Buswell AM, Hatfield, WD, Rudolfs W, Hinman JJ, Mohlman FW. 1932. The determination of dissolved oxygen by the Winkler method: Preliminary report of the committee on methods of sewage analysis of the federation of sewage works associations, *Sewage Works Journal*, 4(3): 413-427.
- Tomàs E. 1999. The Catalan process for the direct production of malleable iron and its spread to Europe and the Americas. *Contributions to Science*, 1(2): 225-232.
- Tonkovich AY, Zilka JL, LaMont MJ, Wang Y, Wegeng RS. 1999. Microchannel reactors for fuel processing applications. I. Water gas shift reactor. *Chemical Engineering Science* 54(13-14): 2947-2951.
- Toplin JA, Norris TB, Lehr CR, McDermott TR, Castenholz RW. 2008. Biogeographic and phylogenetic diversity of thermoacidophilic *Cyanidiales* in Yellowstone National Park, Japan, and New Zealand. *Applied and Environmental Microbiology*, 74(9): 2822-2833.
- Trenberth KE, Fasullo JT. 2012. Tracking Earth's energy: From El Niño to global warming. *Surveys in Geophysics*, 33(3-4): 413-426.
- Tribe LA, Briens CL, Margaritis A. 1995. Determination of the volumetric mass transfer coefficient (k_La) using the dynamic "gas out-gas in" method: Analysis of errors

- caused by dissolved oxygen probes. *Biotechnology and Bioengineering*, 46(4): 388-392.
- Tyson GW, Lo I, Baker BJ, Allen EE, Hugenholtz P, Banfield JF. 2005. Genome-directed isolation of the key nitrogen fixer *Leptospirillum ferrodiazotrophum* sp. nov. from an acidophilic microbial community. *Applied and Environmental Microbiology*, 71(10): 6319-6324.
- Tzedakis PC, Wolff EW, Skinner LC, McManus JF, Raynaud D. 2012. Can we predict the duration of an interglacial? *Climate of the Past*, 8(5): 1473-1485.
- Valavarasu G, Sairam B. 2013. Light naphtha isomerization process: A review. *Petroleum Science and Technology*, 31(6): 580-595.
- Vardanyan A, Khachatryan A, Castro L, Willscher S, Gaydardzhiev S, Zhang R, Vardanyan N. 2023. Bioleaching of sulfide minerals by *Leptospirillum ferriphilum* CC from polymetallic mine (Armenia). *Minerals*, 13(2): 243.
- Veras G, Silva EC, Silva Lyra W, Soares SFC, Guerreiro TB, Santos SRB. 2009. A portable, inexpensive and microcontrolled spectrophotometer based on white LED as light source and CD media as diffraction grid. *Talanta*, 77(3): 1155-1159.
- Vergara E, Neira G, González C, Cortez D, Dopson M, Holmes DS. 2020. Evolution of predicted acid resistance mechanisms in the extremely acidophilic *Leptospirillum* genus. *Genes*, 11(4): 389.
- Vogelaar JCT, Klapwijk A, Van Lier JB, Rulkens WH. 2000. Temperature effects on the oxygen transfer rate between 20 and 55°C. *Water Research*, 34(3): 1037-1041.
- Wang DIC, Cooney CL, Demain AL, Dunnill P, Humphrey AE, Lilly MD. 1979. *Fermentation and enzyme technology*, 1st Edition. New York: John Wiley & Sons.
- Wang L, Zhang Y, Zou R, Zou R, Huang L, Liu Y, Meng Z, Wang Z, Lei H. 2023. A systematic review of CO₂ injection for enhanced oil recovery and carbon storage in shale reservoirs. *International Journal of Hydrogen Energy*, 48(95): 37134-37165.
- Wang H, Zhong J, Feng D, Meng J, Xie N. 2013. Nanoparticles-modified polymer-based solar-reflective coating as a cooling overlay for asphalt pavement. *International Journal of Smart and Nano Materials*, 4(2): 102-111.
- Wang X, Miao C, Wang C, Yin D, Chen S, Chen L. 2022. Coal production capacity allocation based on efficiency perspective – taking production mines in Shandong Province as an example. *Energy Policy*, 171: 113270.
- Wernau WC, Wilke CR. 1973. New method for evaluation of dissolved oxygen probe response for k_{La} determination. *Biotechnology and Bioengineering*, 15(3): 571-578.
- Wipke K, Sprik S, Kurtz J, Ramsden T, Ainscough C, Saur G. 2012. All Composite Data Products: National FCEV Learning Demonstration (Technical Report: NREL/TP-5600-54021). National Renewable Energy Laboratory.

- Wongthanate J, Chinnacotpong K, Khumpong M. 2014. Impacts of pH, temperature and pretreatment method on biohydrogen production from organic wastes by sewage microflora. *International Journal of Energy and Environmental Engineering*, 5(1): 1-6,76.
- Woolf D, Amonette JE, Street-Perrott FA, Lehmann J, Joseph S. 2010. Sustainable biochar to mitigate global climate change. *Nature Communications* 1(5): 56.
- Xia A, Cheng J, Song W, Su H, Ding L, Lin R, Lu H, Liu J, Zhou J, Cen K. 2015. Fermentative hydrogen production using algal biomass as feedstock. *Renewable and Sustainable Energy Reviews*, 51: 209-230.
- Yang H, Ciais P, Frappart F, Li X, Brandt M, Fensholt R, Fan L, Saatchi S, Besnard S, Deng Z, Bowring S, Wigneron JP. 2023. Global increase in biomass carbon stock dominated by growth of northern young forests over past decade. *Nature Geoscience*, 16(10): 886-892.
- Ye M, Sharp P, Brandon N, Kucernak A. 2022. System-level comparison of ammonia, compressed and liquid hydrogen as fuels for polymer electrolyte fuel cell powered shipping. *International Journal of Hydrogen Energy*, 47(13): 8565-8584.
- Yoshida F, Akita K. 1965. Performance of gas bubble columns: volumetric liquid-phase mass transfer coefficient and gas holdup. *AIChE Journal*, 11(1): 9-13.
- YSI. 2009. *The dissolved oxygen handbook: A practical guide to dissolved oxygen measurements*. YSI Incorporated, Yellow Springs, OH.
- Zapata Y, Kristensen MR, Huerta N, Brown C, Kabir CS, Reza Z. 2020. CO₂ geological storage: critical insights on plume dynamics and storage efficiency during long-term injection and post-injection periods. *Journal of Natural Gas Science and Engineering*, 83: 103542.
- Zgonnik V. 2020. The occurrence and geoscience of natural hydrogen: A comprehensive review. *Earth-Sciences Reviews*, 203: 103140.
- Zhan Y, Yang M, Zhang S, Zhao D, Duan J, Wang W, Yan L. 2019. Iron and sulfur oxidation pathways of *Acidithiobacillus ferrooxidans*. *World Journal of Microbiology and Biotechnology*, 35(4): 60.
- Zhang G, Wang X, Jiao Y, Chen Q, Lee DJ. 2021. Enhanced performance of microbial fuel cells with enriched ferrous iron oxidation microflora at room temperatures. *Bioresource Technology*, 331: 125025.
- Zhang RY, Xia JL, Peng JH, Zhang Q, Zhang CG, Nie ZY, Qiu GZ. 2010. A new strain *Leptospirillum ferriphilum* YTW315 for bioleaching of metal sulfide ores. *Transactions of Nonferrous Metals Society of China (English Edition)*, 20(1): 135-141.
- Zhao C, Wang L, Huang L, Musyoka NM, Xue T, Rabeah J, Wang Q. 2024. Recent advances in intermediate-temperature CO₂ capture: Materials, technologies and applications. *Journal of Energy Chemistry*, 90: 435-452.

- Zhao Q, Wang Y, Li G, Hu C. 2020. CeZrO_x promoted water-gas shift reaction under steam-methane reforming conditions on Ni-HTASO₅. *Catalysts* 10(10): 1-13, 1110.
- Zhong W, Haigh JD. 2013. The greenhouse effect and carbon dioxide. *Weather*, 68(4): 100-105.
- Zhou H, Zhang R, Hu P, Zeng W, Xie Y, Wu C, Qiu G. 2008. Isolation and characterization of *Ferroplasma thermophilum* sp. nov., a novel extremely acidophilic, moderately thermophilic archaeon and its role in bioleaching of chalcopyrite. *Journal of Applied Microbiology*, 105(2): 591-601.
- Zhou HB, Liu X, Qiu GZ, Liu JS, Chen XH. 2006. Immobilization of *Acidithiobacillus ferrooxidans* and ferric iron production. *Transactions of Nonferrous Metals Society of China (English Edition)*, 16(4): 931-936.
- Zhu M, Puls BW, Frandsen C, Kubicki JD, Zhang H, Waychunas GA. 2013. In-situ structural characterization of ferric iron dimers in aqueous solutions: Identification of μ -oxo species. *Inorganic Chemistry*, 52(12): 6788-6797.
- Zhuang L, Zhou S. 2009. Substrate cross-conduction effect on the performance of serially connected microbial fuel cell stack. *Electrochemistry Communications*, 11(5): 937-940.

Appendices

Appendix A: Apparatus Photographs



Figure A Benchtop scale BioGenerator apparatus.

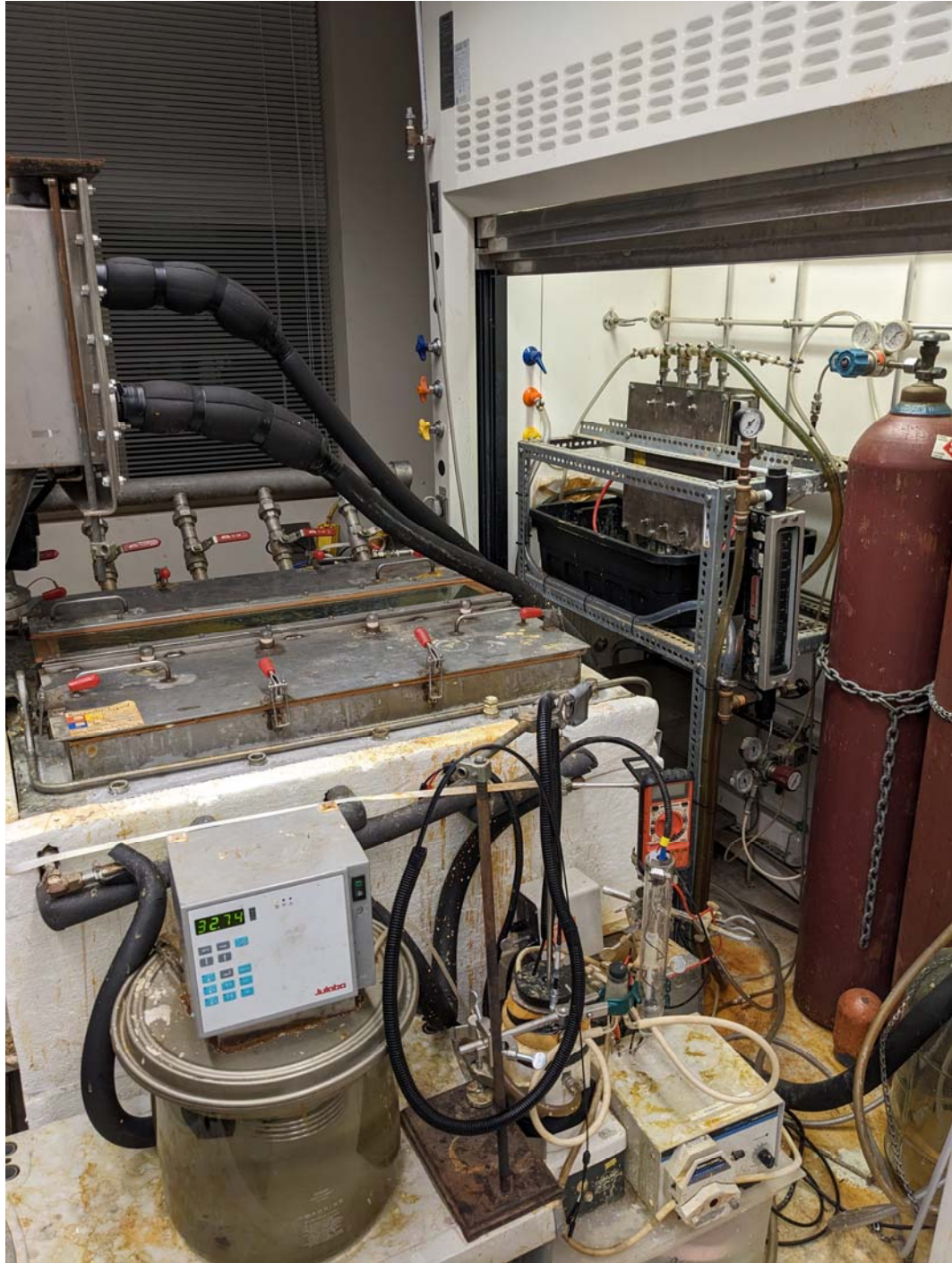


Figure B Semi-pilot scale BioGenerator apparatus.



Figure C Pilot scale BioGenerator bioreactor (exterior).



Figure D Pilot scale BioGenerator fuel cell bank (exterior).



Figure E Pilot scale BioGenerator support equipment (interior).



Figure F BioGenerator broth oxygen solubility measurement apparatus.



Figure F Benchtop algae seed bioreactor.



Figure G Benchtop algae recirculation bioreactor.



Figure H Algae growth dishes and illuminating caddy (exterior and interior view).

Appendix B: Electrochemical Stack Design

(All Dimensions in Inches)

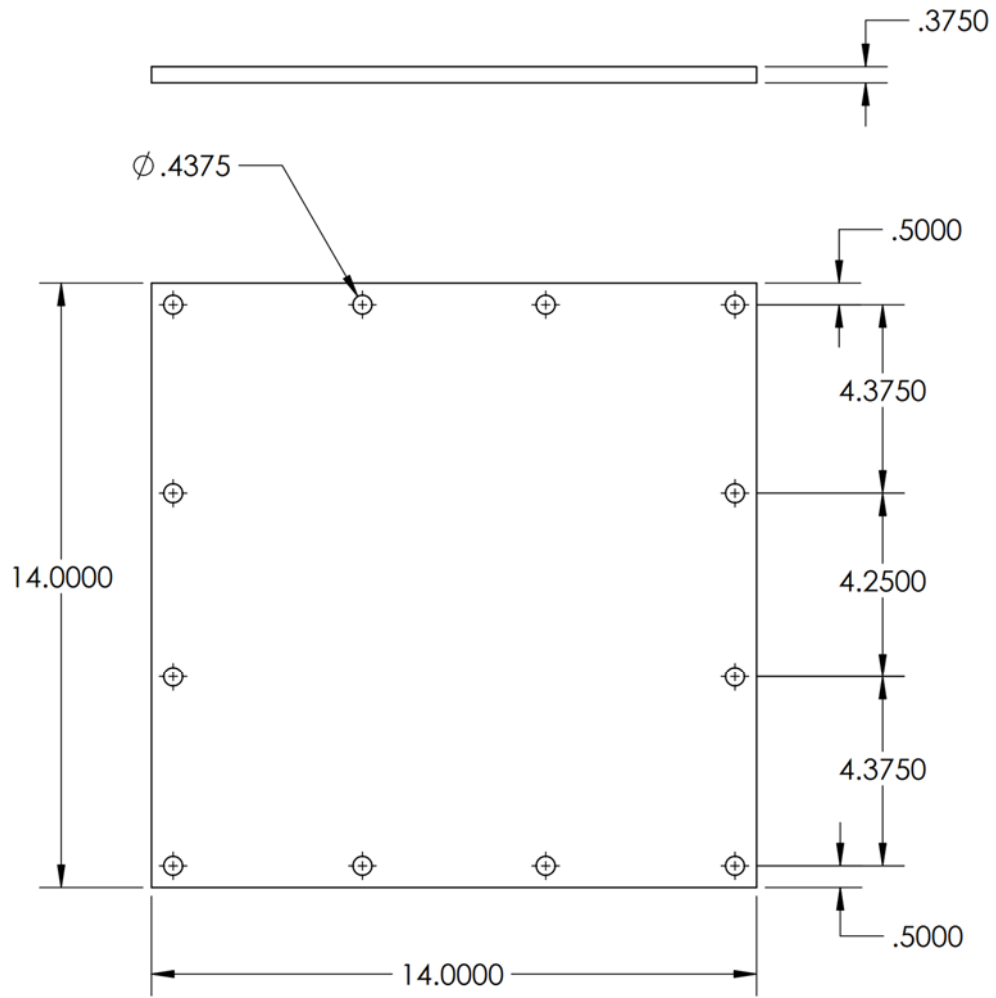


Figure I Carbon steel compression plate.

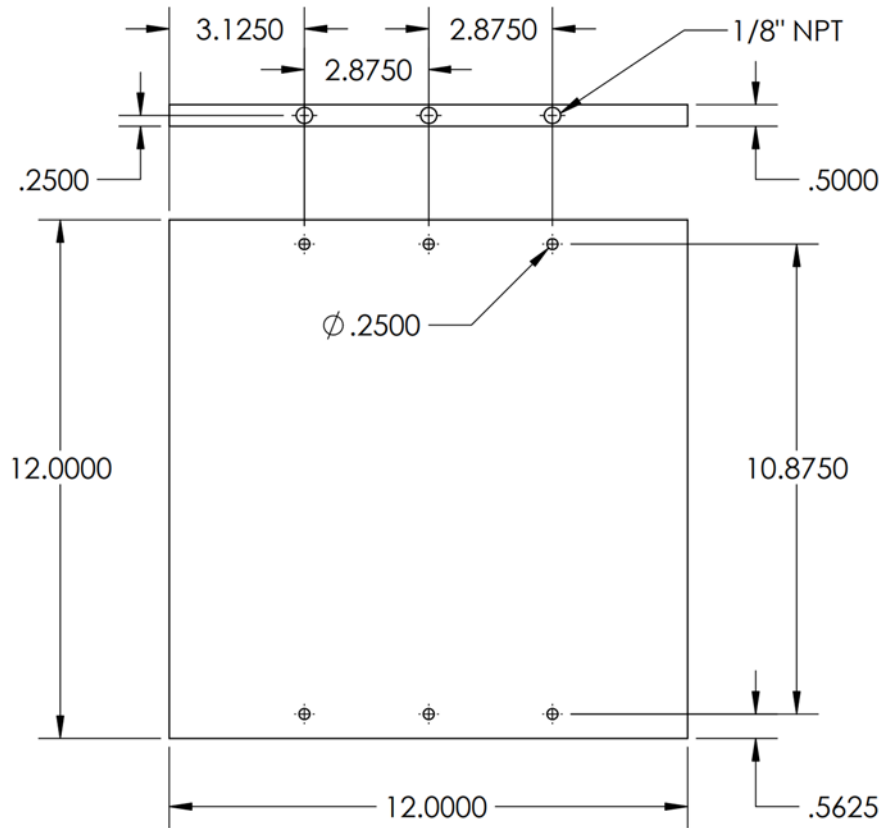


Figure J PVC plastic flow distribution plate.

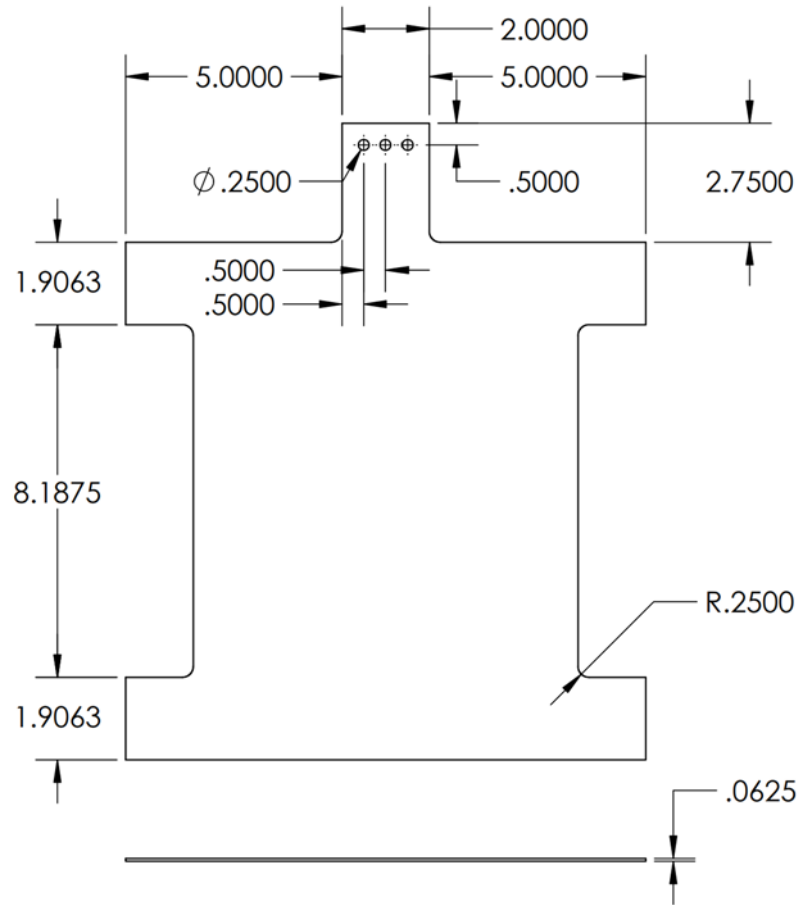


Figure K Copper electrical collector plate.

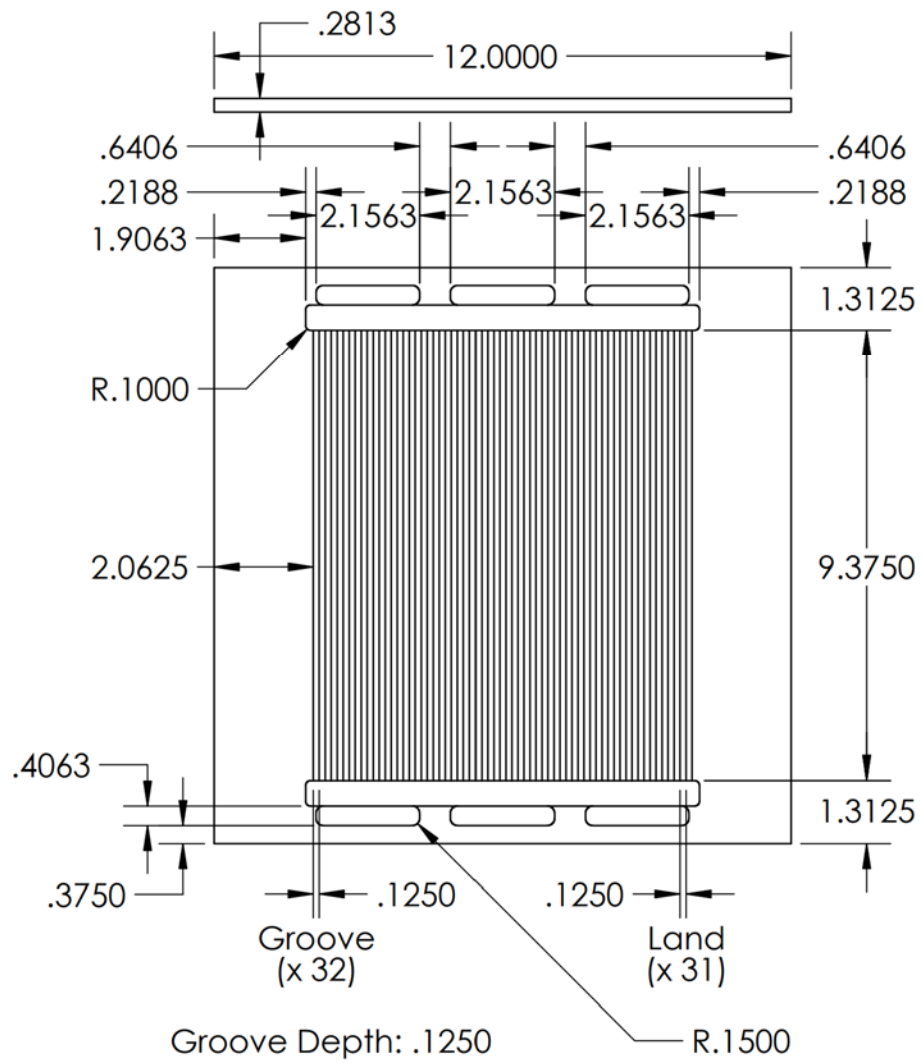


Figure L Graphite monopolar conduction plate.

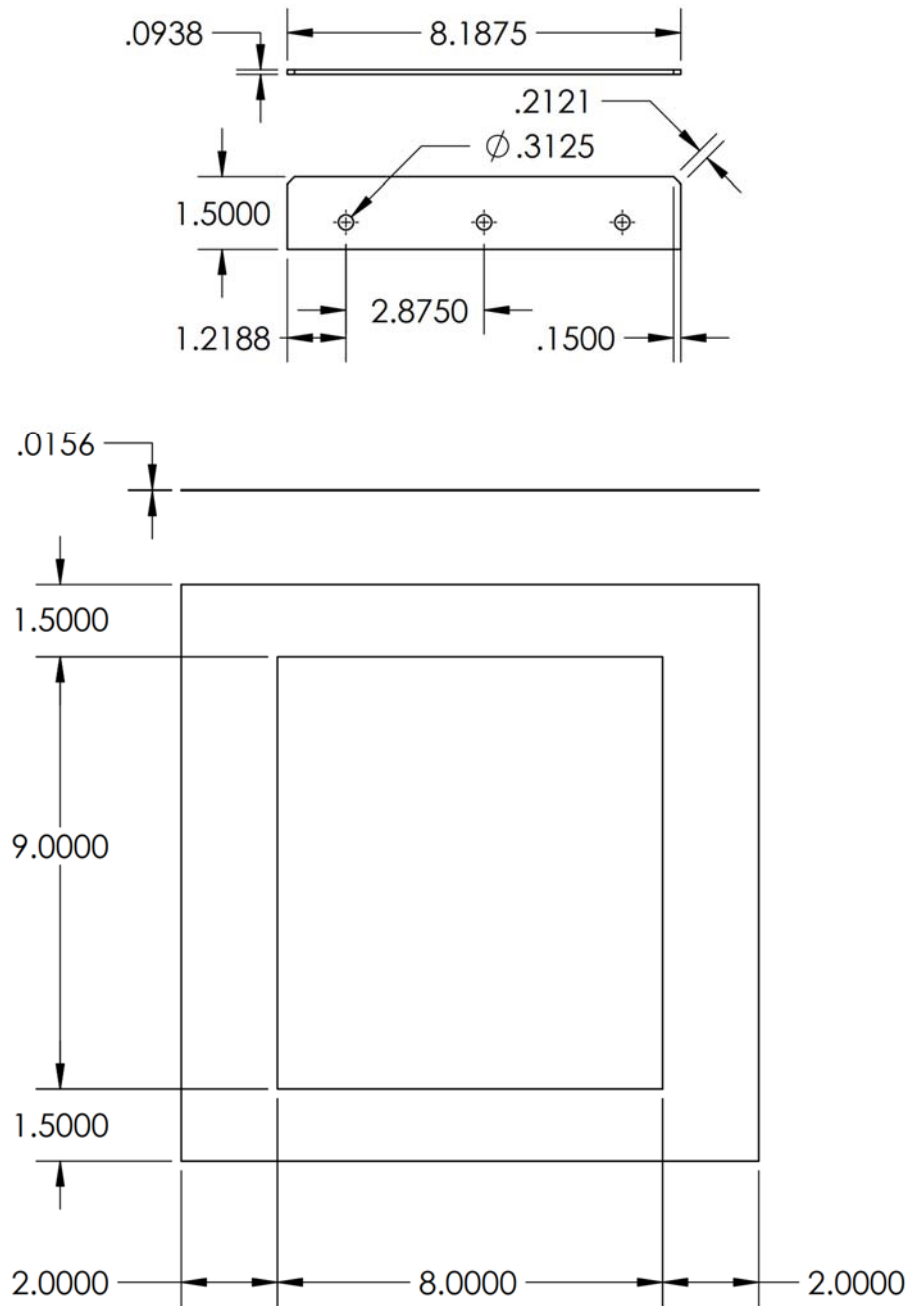
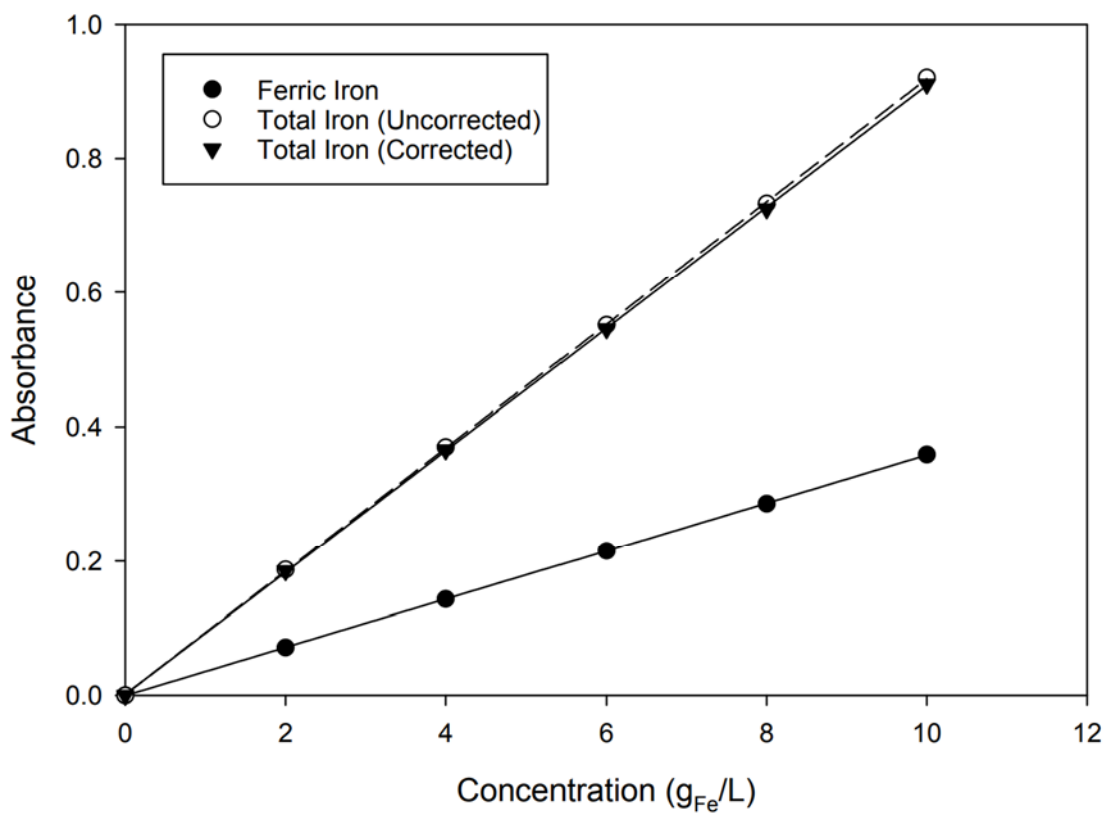


Figure M Silicone rubber sealing gaskets.

Appendix C: Calibrations

Spectrophotometer Calibration

Abs ₅₀₀	Abs ₄₂₅	Correction	Abs _{425'}	g/L
0.000	0.000	0.000	0.000	0.0
0.071	0.187	-0.002	0.185	2.0
0.143	0.370	-0.004	0.366	4.0
0.215	0.551	-0.006	0.545	6.0
0.286	0.733	-0.008	0.725	8.0
0.359	0.921	-0.010	0.911	10.0

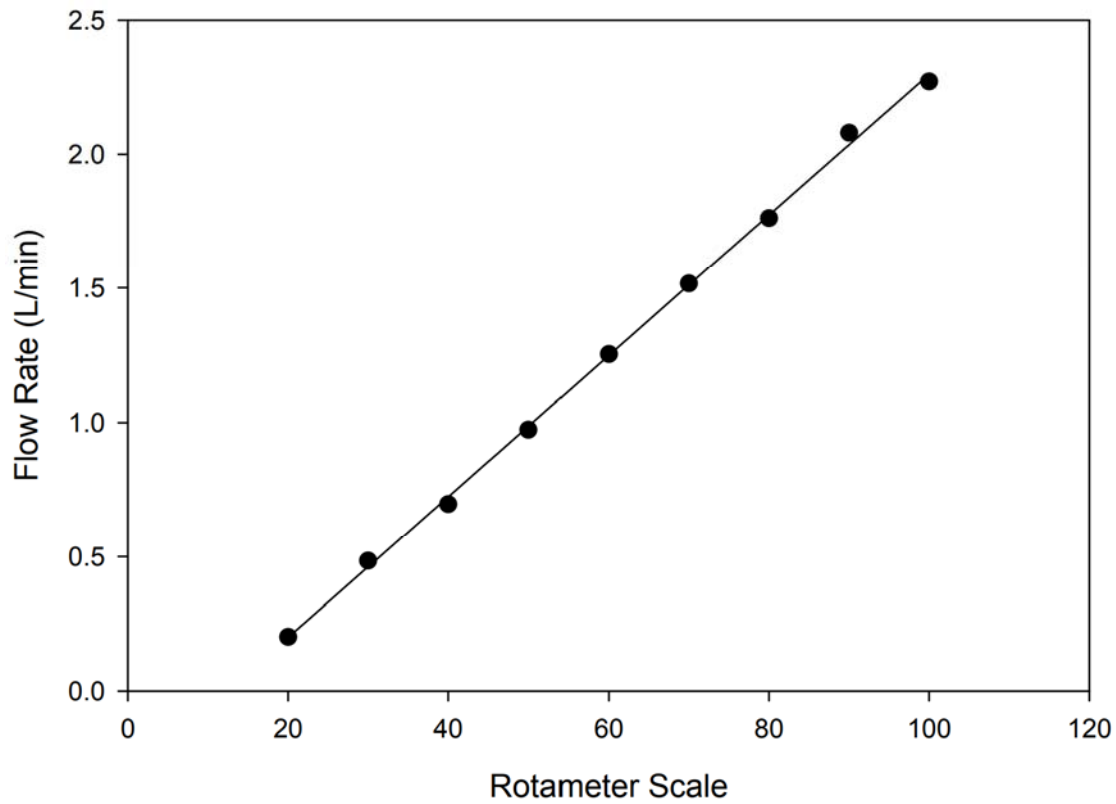


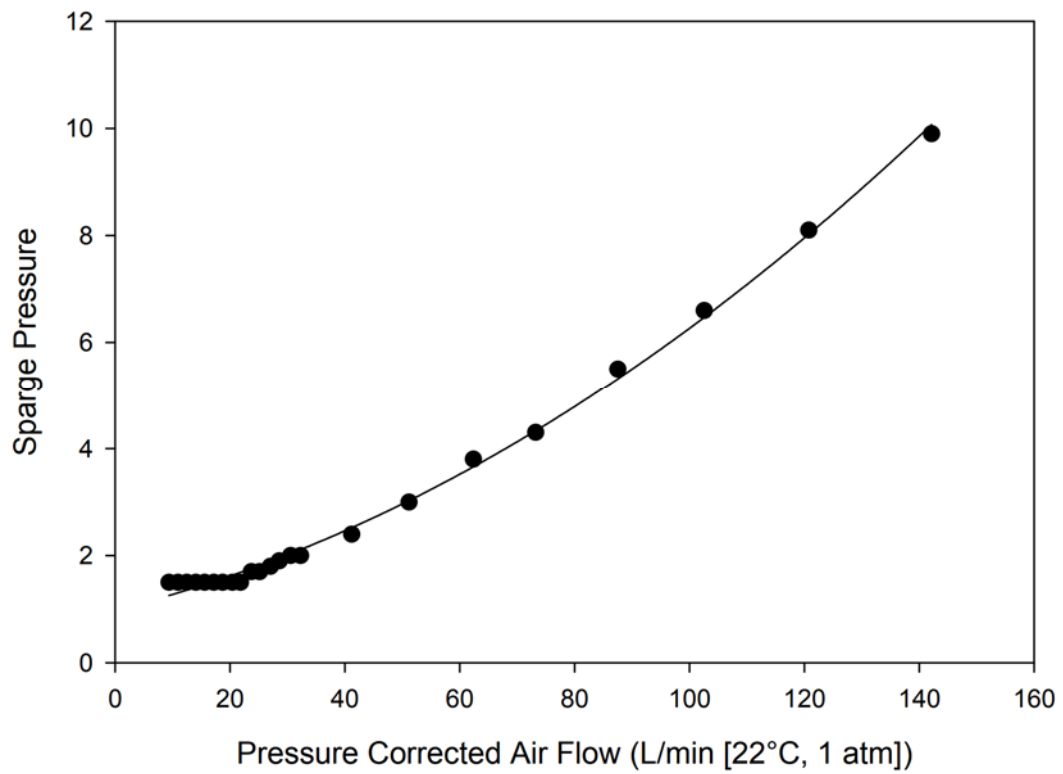
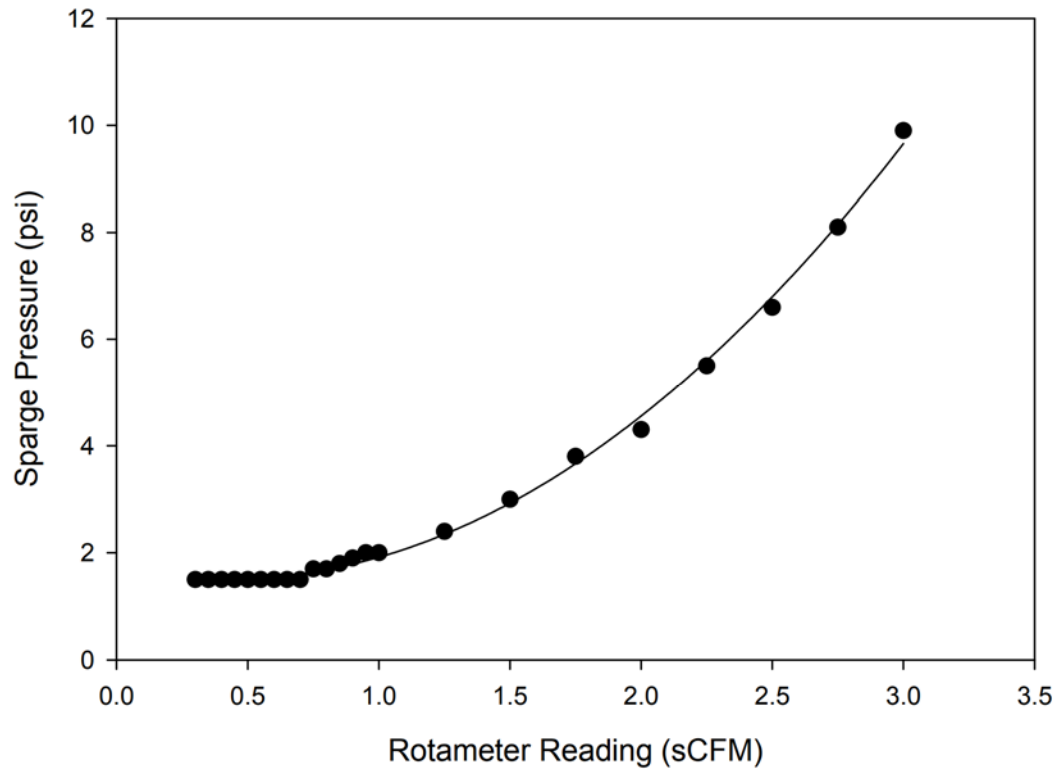
$$Abs = 0.09097Fe_{Total}$$

$$Abs = 0.03583Fe_{Fe^{3+}}$$

Benchtop Scale Sparger Calibration (Gilmont B9500)

Scale	L/min
100	2.272
90	2.080
80	1.762
70	1.516
60	1.253
50	0.973
40	0.697
30	0.484
20	0.201



Semi-Pilot Scale Sparger Calibration (Brooks 1110-08H2G1F)

Redox Probe Temperature Calibration

Fe ³⁺ Starting Volume (mL)	500.00
Vessel Temperature (°C)	11.11
Probe Thermistor (kΩ)	18.64
Dissolved Oxygen (% Sat.)	0.00
Fe ²⁺ Concentration (g/L)	56.85
Fe ³⁺ Concentration (g/L)	47.54

Fe ³⁺ Starting Volume (mL)	500.00
Vessel Temperature (°C)	20.05
Probe Thermistor (kΩ)	12.40
Dissolved Oxygen (% Sat.)	0.00
Fe ²⁺ Concentration (g/L)	56.85
Fe ³⁺ Concentration (g/L)	47.54

mL Fe ²⁺	mV	mL Total	Ratio
0.0	486.4	500.00	0.00000
0.5	436.5	500.50	0.00120
1.0	425.0	501.00	0.00239
1.5	418.2	501.50	0.00359
2.0	413.2	502.00	0.00478
3.0	406.3	503.00	0.00718
4.0	401.4	504.00	0.00957
6.0	394.3	506.00	0.01435
8.0	389.2	508.00	0.01913
10.0	385.4	510.00	0.02392

mL Fe ²⁺	mV	mL Total	Ratio
0.0	501.8	500.00	0.00000
0.5	443.8	500.50	0.00120
1.0	432.2	501.00	0.00239
1.5	425.0	501.50	0.00359
2.0	419.9	502.00	0.00478
3.0	412.8	503.00	0.00718
4.0	407.8	504.00	0.00957
6.0	400.5	506.00	0.01435
8.0	395.3	508.00	0.01913
10.0	391.2	510.00	0.02392

Fe ³⁺ Starting Volume (mL)	500.00
Vessel Temperature (°C)	30.28
Probe Thermistor (kΩ)	8.01
Dissolved Oxygen (% Sat.)	0.00
Fe ²⁺ Concentration (g/L)	56.85
Fe ³⁺ Concentration (g/L)	47.54

Fe ³⁺ Starting Volume (mL)	500.00
Vessel Temperature (°C)	40.29
Probe Thermistor (kΩ)	5.37
Dissolved Oxygen (% Sat.)	0.00
Fe ²⁺ Concentration (g/L)	56.85
Fe ³⁺ Concentration (g/L)	47.54

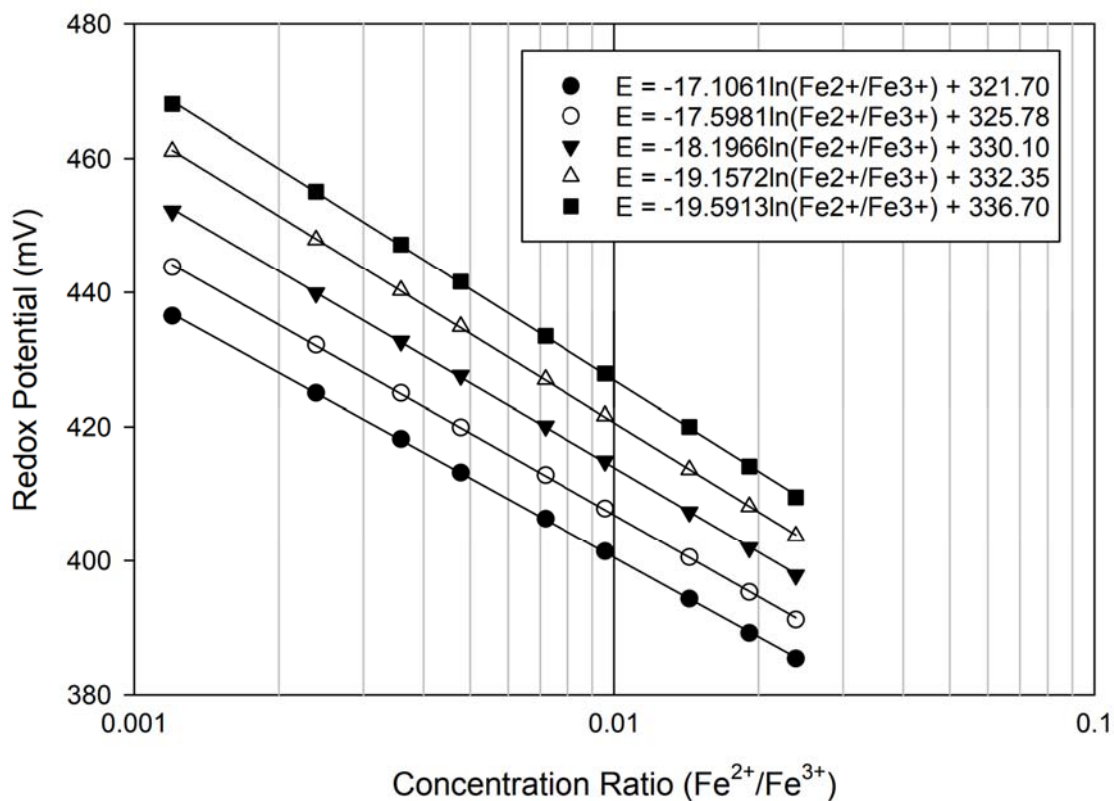
mL Fe ²⁺	mV	mL Total	Ratio
0.0	513.2	500.00	0.00000
0.5	452.2	500.50	0.00120
1.0	439.9	501.00	0.00239
1.5	432.7	501.50	0.00359
2.0	427.6	502.00	0.00478
3.0	420.1	503.00	0.00718
4.0	414.9	504.00	0.00957
6.0	407.3	506.00	0.01435
8.0	401.9	508.00	0.01913
10.0	397.8	510.00	0.02392

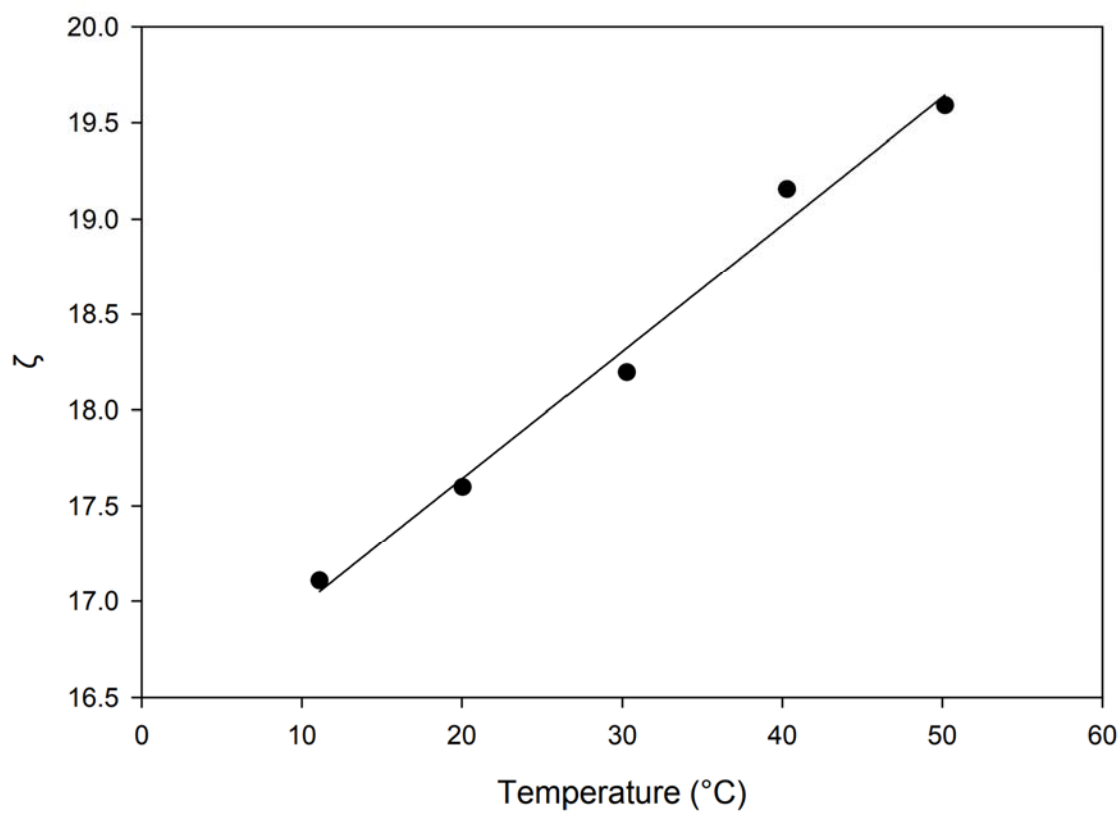
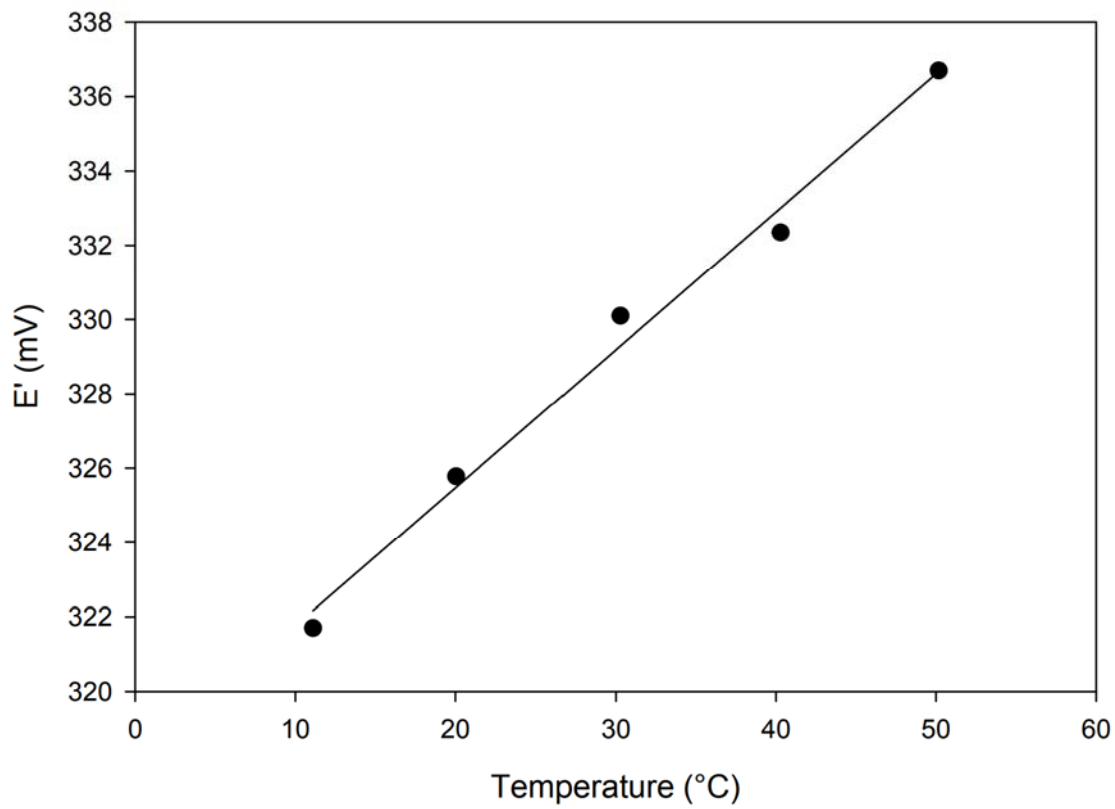
mL Fe ²⁺	mV	mL Total	Ratio
0.0	523.9	500.00	0.00000
0.5	461.1	500.50	0.00120
1.0	447.9	501.00	0.00239
1.5	440.3	501.50	0.00359
2.0	434.9	502.00	0.00478
3.0	427.0	503.00	0.00718
4.0	421.6	504.00	0.00957
6.0	413.6	506.00	0.01435
8.0	408.1	508.00	0.01913
10.0	403.7	510.00	0.02392

Fe ³⁺ Starting Volume (mL)	500.00
Vessel Temperature (°C)	50.16
Probe Thermistor (kΩ)	3.71
Dissolved Oxygen (% Sat.)	0.00
Fe ²⁺ Concentration (g/L)	56.85
Fe ³⁺ Concentration (g/L)	47.54

mL Fe ²⁺	mV	mL Total	Ratio
0.0	531.4	500.00	0.00000
0.5	468.1	500.50	0.00120
1.0	455.1	501.00	0.00239
1.5	447.2	501.50	0.00359
2.0	441.6	502.00	0.00478
3.0	433.5	503.00	0.00718
4.0	427.9	504.00	0.00957
6.0	420.0	506.00	0.01435
8.0	414.1	508.00	0.01913
10.0	409.5	510.00	0.02392

T	E'	ζ
11.11	321.70	17.1061
20.05	325.78	17.5981
30.28	330.10	18.1966
40.29	332.35	19.1572
50.16	336.70	19.5913





UV Fluorescence Cell Count Calibration

Hemocytometer grid region height: 0.1 mm

Average hemocytometer cell count: 44.2 cells per grid region ($1/16 \text{ mm}^2$)

Cell concentration: $(44.2 * 4 * 4) \text{ cells/mm}^2 / 0.1 \text{ mm} = 7070 \text{ cells/mm}^3$

Height of liquid in Petri dish: $18000 \text{ mm}^3 / \pi * (97.0 \text{ mm} / 2)^2 = 2.44 \text{ mm}$

Liquid volume in fluorescence detector FoV: $\pi * 491 \text{ mm}^2 * 2.44 \text{ mm} = 3760 \text{ mm}^3$

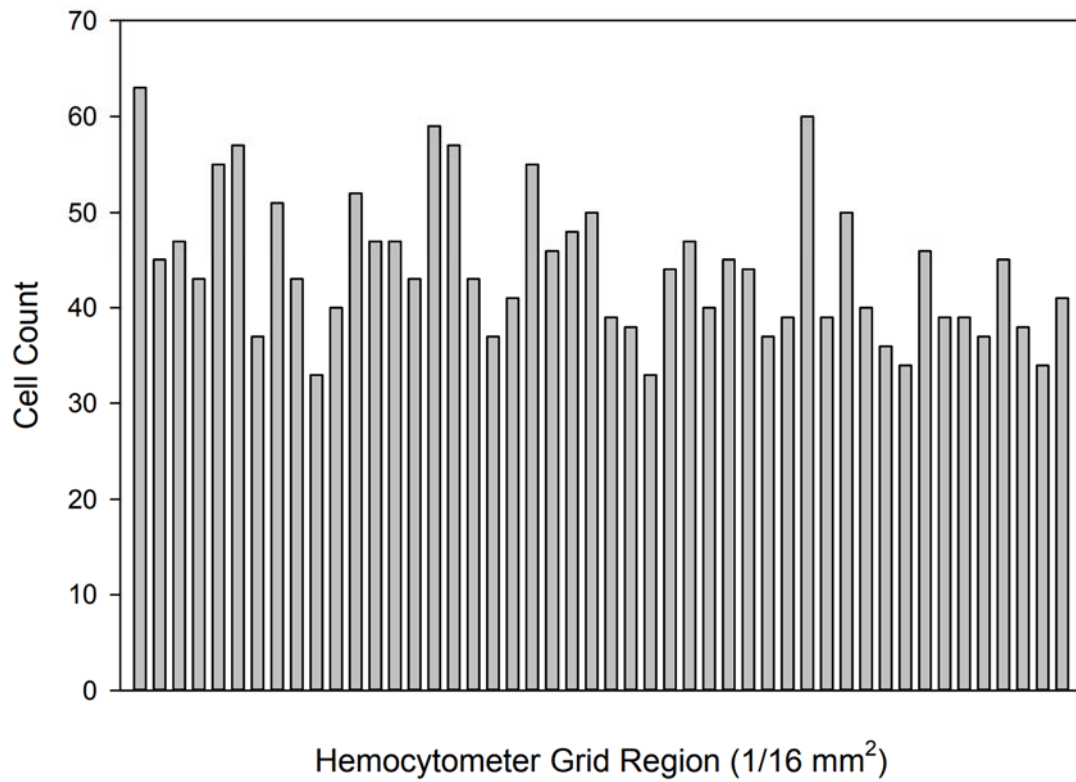
TIA output voltage during UV-A stimulation of calibration sample: 0.334 V

TIA dark current plus blank sample offset voltage: $0.009 \text{ V} + 0.047 \text{ V} = 0.056 \text{ V}$

Conversion Factor: $7070 \text{ cells/mm}^3 * 3760 \text{ mm}^3 / (0.334 \text{ V} - 0.056 \text{ V}) = 9.56 \times 10^7 \text{ cells/V}$

FoV – Field of View

TIA – Transimpedance Amplifier





Appendix D: Chapter 4 Data

Extinction Index Model Data

pH	Temperature (°C)				
	5	10	15	20	25
1.56	0.1921	0.1998	0.2118	0.2264	0.2417
1.50	0.1986	0.1998	0.2070	0.2178	0.2305
1.45	0.1810	0.1706	0.1727	0.1854	0.2045
1.40	0.1458	0.1538	0.1683	0.1864	0.2056
1.35	0.1439	0.1489	0.1605	0.1766	0.1951
1.29	0.1180	0.1246	0.1379	0.1552	0.1742
1.24	0.0956	0.1063	0.1236	0.1445	0.1668
1.19	0.0777	0.0879	0.1058	0.1280	0.1517
1.14	0.0767	0.0842	0.0981	0.1165	0.1375
1.08	0.0308	0.0468	0.0698	0.0966	0.1243
1.03	-0.0179	0.0035	0.0366	0.0749	0.1132
0.98	-0.0628	-0.0317	0.0106	0.0564	0.1006
0.93	-0.0819	-0.0539	-0.0134	0.0324	0.0783
0.87	-0.0673	-0.0503	-0.0184	0.0221	0.0655
0.82	-0.1261	-0.0993	-0.0577	-0.0088	0.0411
0.77	-0.1446	-0.1181	-0.0770	-0.0280	0.0234
0.71	-0.1535	-0.1356	-0.0996	-0.0521	0.0006
0.66	-0.1821	-0.1609	-0.1226	-0.0734	-0.0194
0.61	-0.1968	-0.1777	-0.1403	-0.0907	-0.0353
0.50	-0.2140	-0.1988	-0.1671	-0.1232	-0.0718
0.39	-	-	-0.1789	-0.1445	-0.0967
0.28	-	-	-0.2011	-0.1687	-0.1227
0.17	-	-	-0.2086	-0.1733	-0.1266
0.06	-	-	-	-0.1889	-0.1484
-0.05	-	-	-	-0.2245	-0.1783

Temp.	Polynomial Coefficient			
	x ³	x ²	x	1
25	-1.1583E-01	2.8640E-01	9.0954E-02	-1.6423E-01
20	-1.4163E-01	3.8068E-01	2.6280E-02	-2.0553E-01
15	-2.7600E-01	7.9147E-01	-3.2071E-01	-1.6998E-01
10	-4.3866E-01	1.3184E+00	-8.2129E-01	-6.4671E-02
5	-5.6120E-01	1.7401E+00	-1.2559E+00	5.0690E-02

pH	Temperature (°C)				
	30	35	40	45	50
1.56	0.2562	0.2690	0.2798	0.2887	0.2959
1.50	0.2437	0.2567	0.2691	0.2805	0.2911
1.45	0.2258	0.2465	0.2651	0.2812	0.2948
1.40	0.2244	0.2419	0.2578	0.2720	0.2846
1.35	0.2141	0.2322	0.2489	0.2638	0.2769
1.29	0.1936	0.2123	0.2299	0.2460	0.2607
1.24	0.1888	0.2094	0.2282	0.2449	0.2596
1.19	0.1750	0.1968	0.2166	0.2343	0.2498
1.14	0.1595	0.1815	0.2026	0.2225	0.2408
1.08	0.1513	0.1764	0.1993	0.2196	0.2376
1.03	0.1480	0.1780	0.2032	0.2240	0.2410
0.98	0.1403	0.1747	0.2039	0.2284	0.2489
0.93	0.1208	0.1586	0.1913	0.2193	0.2431
0.87	0.1074	0.1456	0.1790	0.2077	0.2320
0.82	0.0878	0.1295	0.1655	0.1962	0.2221
0.77	0.0732	0.1193	0.1608	0.1973	0.2293
0.71	0.0533	0.1029	0.1478	0.1876	0.2222
0.66	0.0348	0.0861	0.1331	0.1751	0.2122
0.61	0.0210	0.0747	0.1241	0.1684	0.2075
0.50	-0.0169	0.0383	0.0917	0.1419	0.1882
0.39	-0.0416	0.0155	0.0704	0.1209	0.1659
0.28	-0.0682	-0.0101	0.0481	0.1036	0.1550
0.17	-0.0731	-0.0170	0.0384	0.0910	0.1392
0.06	-0.0974	-0.0411	0.0164	0.0719	0.1236
-0.05	-0.1223	-0.0616	-0.0004	0.0582	0.1125

Temp.	Polynomial Coefficient			
	x ³	x ²	x	1
50	3.3964E-02	-1.0305E-01	1.9573E-01	1.1423E-01
45	8.1693E-03	-4.5050E-02	1.9497E-01	6.1160E-02
40	-2.0658E-02	2.2959E-02	1.8770E-01	4.2280E-03
35	-5.2041E-02	1.0182E-01	1.7034E-01	-5.4620E-02
30	-8.4637E-02	1.9085E-01	1.3904E-01	-1.1223E-01

Extinction Index Deviation Data

Fe ³⁺ (g/L)	10 °C (pH 1.2)		
	alpha	487 nm	520 nm
5	0.0384	0.0292	0.0281
10	0.1011	0.0790	0.0714
20	0.1964	0.2253	0.1850
40	0.2969	0.8278	0.6138

Fe ³⁺ (g/L)	20 °C (pH 1.2)		
	alpha	487 nm	520 nm
5	0.0732	0.0368	0.0342
10	0.1708	0.1061	0.0894
20	0.2344	0.2993	0.2365
40	0.2951	0.9578	0.7115

Fe ³⁺ (g/L)	30 °C (pH 1.2)		
	alpha	487 nm	520 nm
5	0.1374	0.0529	0.0461
10	0.2046	0.1444	0.1176
20	0.2536	0.3883	0.3009
40	0.3098	1.1388	0.8333

Fe ³⁺ (g/L)	40 °C (pH 1.2)		
	alpha	487 nm	520 nm
5	0.2182	0.0737	0.0592
10	0.2431	0.1956	0.1532
20	0.2853	0.5050	0.3789
40	0.3311	1.3889	0.9944

Fe ³⁺ (g/L)	10 °C (pH 1.0)		
	alpha	487 nm	520 nm
5	-0.0888	0.0226	0.0247
10	0.0080	0.0502	0.0498
20	0.0618	0.1185	0.1114
40	0.1991	0.4076	0.3338

Fe ³⁺ (g/L)	20 °C (pH 1.0)		
	alpha	487 nm	520 nm
5	0.0032	0.0315	0.0314
10	0.0676	0.0703	0.0657
20	0.1352	0.1658	0.1448
40	0.2272	0.5259	0.4186

Fe ³⁺ (g/L)	30 °C (pH 1.0)		
	alpha	487 nm	520 nm
5	0.0685	0.0317	0.0296
10	0.1344	0.0834	0.0729
20	0.2014	0.2263	0.1849
40	0.2609	0.6629	0.5099

Fe ³⁺ (g/L)	40 °C (pH 1.0)		
	alpha	487 nm	520 nm
5	0.1463	0.0528	0.0456
10	0.1967	0.1139	0.0935
20	0.2456	0.3017	0.2357
40	0.2905	0.8397	0.6267

Fe ³⁺ (g/L)	10 °C (pH 0.8)		
	alpha	487 nm	520 nm
5	-0.1514	0.0409	0.0476
10	-0.0499	0.0919	0.0966
20	0.0529	0.1922	0.1823
40	0.1341	0.6134	0.5363

Fe ³⁺ (g/L)	20 °C (pH 0.8)		
	alpha	487 nm	520 nm
5	-0.0692	0.0530	0.0568
10	0.0017	0.1182	0.1180
20	0.0912	0.2693	0.2458
40	0.1910	0.8166	0.6742

Fe ³⁺ (g/L)	30 °C (pH 0.8)		
	alpha	487 nm	520 nm
5	0.0207	0.0635	0.0622
10	0.1136	0.1535	0.1370
20	0.1518	0.3643	0.3129
40	0.2274	1.0556	0.8401

Fe ³⁺ (g/L)	40 °C (pH 0.8)		
	alpha	487 nm	520 nm
5	0.0982	0.0972	0.0881
10	0.1709	0.1944	0.1638
20	0.2226	0.4912	0.3928
40	0.2734	1.3568	1.0305

Fe ³⁺ (g/L)	10 °C (pH 0.6)		
	alpha	487 nm	520 nm
5	-0.3333	0.0355	0.0497
10	-0.1759	0.0586	0.0699
20	-0.1070	0.1292	0.1438
40	0.0366	0.3703	0.3570

Fe ³⁺ (g/L)	20 °C (pH 0.6)		
	alpha	487 nm	520 nm
5	-0.1096	0.0440	0.0491
10	-0.0329	0.0806	0.0833
20	0.0286	0.1847	0.1795
40	0.1189	0.5222	0.4636

Fe ³⁺ (g/L)	30 °C (pH 0.6)		
	alpha	487 nm	520 nm
5	0.0185	0.0547	0.0537
10	0.0500	0.1005	0.0956
20	0.1081	0.2545	0.2284
40	0.1863	0.7019	0.5823

Fe ³⁺ (g/L)	40 °C (pH 0.6)		
	alpha	487 nm	520 nm
5	0.1092	0.0628	0.0563
10	0.1481	0.1392	0.1200
20	0.2023	0.3511	0.2866
40	0.2441	0.9364	0.7327

pH Correction Model Data

Solution Name	pH at Temperature (°C)									
	5.0	10.0	15.0	20.0	25.0	30.0	35.0	40.0	45.0	50.0
1.50	1.51	1.52	1.54	1.56	1.56	1.57	1.57	1.57	1.58	1.57
1.45	1.42	1.44	1.47	1.49	1.50	1.51	1.51	1.51	1.52	1.51
1.40	1.34	1.38	1.40	1.43	1.43	1.46	1.45	1.46	1.47	1.45
1.35	1.29	1.33	1.35	1.39	1.39	1.42	1.42	1.43	1.44	1.42
1.30	1.24	1.28	1.31	1.35	1.35	1.38	1.38	1.39	1.41	1.39
1.25	1.15	1.20	1.23	1.27	1.28	1.32	1.33	1.33	1.35	1.33
1.20	1.07	1.13	1.16	1.21	1.22	1.27	1.27	1.28	1.29	1.27
1.15	1.03	1.08	1.11	1.16	1.18	1.22	1.23	1.23	1.25	1.23
1.10	0.96	1.02	1.06	1.11	1.13	1.17	1.18	1.18	1.20	1.19
1.05	0.91	0.97	1.01	1.06	1.08	1.12	1.13	1.14	1.16	1.14
1.00	0.96	1.00	1.02	1.03	1.02	1.03	1.04	1.02	1.06	1.06
0.95	0.91	0.94	0.96	0.99	0.98	0.99	1.00	0.98	1.02	1.02
0.90	0.85	0.89	0.91	0.93	0.92	0.94	0.95	0.93	0.96	0.97
0.85	0.80	0.83	0.85	0.88	0.87	0.89	0.90	0.88	0.91	0.92
0.80	0.74	0.77	0.79	0.81	0.80	0.83	0.84	0.82	0.84	0.85
0.75	0.71	0.74	0.75	0.77	0.77	0.79	0.80	0.78	0.81	0.81
0.70	0.67	0.69	0.71	0.73	0.72	0.74	0.75	0.73	0.77	0.77
0.65	0.60	0.62	0.63	0.65	0.65	0.67	0.68	0.66	0.69	0.70
0.60	0.55	0.57	0.58	0.60	0.60	0.62	0.64	0.61	0.64	0.64
0.50	0.42	0.45	0.45	0.46	0.46	0.49	0.50	0.48	0.51	0.51
0.40	0.34	0.36	0.36	0.39	0.38	0.39	0.40	0.41	0.42	0.42
0.30	0.25	0.27	0.27	0.29	0.28	0.29	0.30	0.31	0.31	0.32
0.20	0.15	0.16	0.17	0.19	0.17	0.19	0.21	0.22	0.22	0.23
0.10	0.02	0.03	0.03	0.05	0.03	0.05	0.06	0.07	0.07	0.08
0.00	-0.06	-0.06	-0.07	-0.05	-0.06	-0.04	-0.03	-0.01	-0.01	-0.01

Curve Fitting Coefficients			
pH	x ²	x	c
1.50	-5.152E-05	4.227E-03	1.488E+00
1.45	-7.879E-05	6.321E-03	1.390E+00
1.40	-9.394E-05	7.603E-03	1.308E+00
1.35	-9.848E-05	8.398E-03	1.252E+00
1.30	-9.848E-05	8.786E-03	1.201E+00
1.25	-1.182E-04	1.061E-02	1.101E+00
1.20	-1.455E-04	1.255E-02	1.012E+00
1.15	-1.348E-04	1.207E-02	9.698E-01
1.10	-1.470E-04	1.315E-02	8.998E-01
1.05	-1.455E-04	1.321E-02	8.487E-01
1.00	-3.182E-05	3.398E-03	9.612E-01
0.95	-4.394E-05	4.465E-03	8.985E-01
0.90	-4.545E-05	4.621E-03	8.417E-01

Curve Fitting Coefficients			
pH	x ²	x	c
0.85	-4.697E-05	4.850E-03	7.848E-01
0.80	-4.848E-05	4.788E-03	7.240E-01
0.75	-3.939E-05	4.167E-03	6.963E-01
0.70	-2.424E-05	3.321E-03	6.600E-01
0.65	-2.121E-05	3.167E-03	5.883E-01
0.60	-3.485E-05	3.844E-03	5.328E-01
0.50	-1.667E-05	2.771E-03	4.128E-01
0.40	-1.515E-05	2.567E-03	3.310E-01
0.30	-7.576E-06	1.811E-03	2.465E-01
0.20	1.515E-06	1.698E-03	1.428E-01
0.10	7.576E-06	8.803E-04	1.750E-02
0.00	2.424E-05	9.697E-05	-6.600E-02

Molar Extinction Coefficient Model Data

Absorption Values - 487 nm					
pH	Temperature (°C)				
	5	10	15	20	25
1.56	0.7467	0.7459	0.7764	0.8380	0.9308
1.50	0.4789	0.5351	0.6087	0.6997	0.8081
1.45	0.5416	0.5337	0.5599	0.6203	0.7147
1.40	0.4021	0.4435	0.5019	0.5775	0.6701
1.35	0.4473	0.4611	0.4913	0.5380	0.6010
1.29	0.3568	0.3940	0.4434	0.5051	0.5790
1.24	0.3218	0.3446	0.3792	0.4255	0.4837
1.19	0.2720	0.2946	0.3283	0.3730	0.4288
1.14	0.3465	0.3663	0.3949	0.4325	0.4789
1.08	0.2356	0.2550	0.2830	0.3196	0.3646
1.03	0.1835	0.1940	0.2152	0.2473	0.2902
0.98	0.1413	0.1560	0.1790	0.2105	0.2504
0.93	0.1390	0.1516	0.1717	0.1993	0.2345
0.87	0.1525	0.1599	0.1752	0.1984	0.2296
0.82	0.1263	0.1352	0.1511	0.1740	0.2037
0.77	0.1176	0.1272	0.1422	0.1626	0.1884
0.71	0.1138	0.1198	0.1313	0.1482	0.1705
0.66	0.1064	0.1128	0.1240	0.1399	0.1606
0.61	0.1012	0.1065	0.1164	0.1307	0.1496
0.50	0.0992	0.1041	0.1123	0.1238	0.1386
0.39	0.1098	0.1077	0.1102	0.1174	0.1292
0.28	0.1016	0.1011	0.1042	0.1109	0.1213
0.17	0.1031	0.1025	0.1053	0.1116	0.1212
0.06	0.0996	0.0970	0.0979	0.1024	0.1105
-0.05	0.0903	0.0884	0.0898	0.0944	0.1024

Absorption Values - 487 nm					
pH	Temperature (°C)				
	30	35	40	45	50
1.56	1.0548	1.2101	1.3965	1.6141	1.8630
1.50	0.9339	1.0771	1.2378	1.4158	1.6112
1.45	0.8432	1.0059	1.2026	1.4335	1.6985
1.40	0.7799	0.9068	1.0508	1.2119	1.3901
1.35	0.6804	0.7763	0.8885	1.0172	1.1622
1.29	0.6653	0.7638	0.8746	0.9977	1.1331
1.24	0.5538	0.6356	0.7292	0.8346	0.9519
1.19	0.4956	0.5736	0.6625	0.7626	0.8737
1.14	0.5343	0.5986	0.6717	0.7538	0.8448
1.08	0.4182	0.4803	0.5510	0.6301	0.7179
1.03	0.3439	0.4084	0.4836	0.5697	0.6666
0.98	0.2987	0.3555	0.4206	0.4942	0.5762
0.93	0.2771	0.3273	0.3850	0.4501	0.5228
0.87	0.2687	0.3157	0.3706	0.4335	0.5042
0.82	0.2403	0.2839	0.3344	0.3917	0.4560
0.77	0.2197	0.2564	0.2985	0.3461	0.3990
0.71	0.1983	0.2316	0.2703	0.3144	0.3640
0.66	0.1859	0.2160	0.2509	0.2904	0.3347
0.61	0.1730	0.2009	0.2333	0.2703	0.3117
0.50	0.1567	0.1781	0.2028	0.2308	0.2621
0.39	0.1457	0.1669	0.1927	0.2232	0.2583
0.28	0.1353	0.1530	0.1744	0.1994	0.2280
0.17	0.1343	0.1508	0.1707	0.1940	0.2208
0.06	0.1221	0.1373	0.1560	0.1783	0.2041
-0.05	0.1136	0.1280	0.1457	0.1667	0.1910

Epsilon Values - 487 nm						
Fe ³⁺ (mol/L)	pH	Temperature (°C)				
		5	10	15	20	25
0.1883	1.56	0.9914	0.9904	1.0307	1.1125	1.2358
0.1759	1.50	0.6806	0.7605	0.8651	0.9945	1.1485
0.1862	1.45	0.7272	0.7166	0.7518	0.8328	0.9596
0.2140	1.40	0.4698	0.5181	0.5863	0.6746	0.7829
0.1731	1.35	0.6460	0.6659	0.7096	0.7770	0.8680
0.1792	1.29	0.4978	0.5496	0.6185	0.7046	0.8078
0.1718	1.24	0.4683	0.5015	0.5518	0.6193	0.7039
0.1682	1.19	0.4043	0.4379	0.4879	0.5544	0.6373
0.1661	1.14	0.5216	0.5513	0.5944	0.6509	0.7208
0.1776	1.08	0.3316	0.3590	0.3984	0.4498	0.5133
0.1733	1.03	0.2646	0.2797	0.3104	0.3567	0.4186
0.1755	0.98	0.2013	0.2221	0.2550	0.2998	0.3566
0.1740	0.93	0.1997	0.2178	0.2467	0.2864	0.3369
0.1748	0.87	0.2182	0.2287	0.2506	0.2839	0.3284
0.1775	0.82	0.1779	0.1905	0.2129	0.2450	0.2869
0.1759	0.77	0.1672	0.1807	0.2020	0.2310	0.2677
0.1752	0.71	0.1624	0.1710	0.1874	0.2115	0.2434
0.1757	0.66	0.1514	0.1606	0.1765	0.1991	0.2285
0.1742	0.61	0.1452	0.1528	0.1670	0.1876	0.2146
0.1737	0.50	0.1427	0.1498	0.1616	0.1782	0.1995
0.1728	0.39	0.1589	0.1558	0.1595	0.1698	0.1870
0.1721	0.28	0.1476	0.1468	0.1513	0.1611	0.1762
0.1717	0.17	0.1501	0.1493	0.1534	0.1625	0.1765
0.1718	0.06	0.1449	0.1411	0.1425	0.1490	0.1608
0.1700	-0.05	0.1328	0.1300	0.1320	0.1389	0.1505

Epsilon Values - 487 nm						
Fe ³⁺ (mol/L)	pH	Temperature (°C)				
		30	35	40	45	50
0.1883	1.56	1.4005	1.6066	1.8541	2.1431	2.4734
0.1759	1.50	1.3274	1.5309	1.7592	2.0122	2.2899
0.1862	1.45	1.1321	1.3505	1.6147	1.9247	2.2804
0.2140	1.40	0.9111	1.0593	1.2276	1.4157	1.6239
0.1731	1.35	0.9827	1.1212	1.2833	1.4691	1.6785
0.1792	1.29	0.9281	1.0656	1.2202	1.3919	1.5808
0.1718	1.24	0.8058	0.9249	1.0611	1.2146	1.3852
0.1682	1.19	0.7367	0.8525	0.9848	1.1335	1.2986
0.1661	1.14	0.8042	0.9009	1.0111	1.1346	1.2716
0.1776	1.08	0.5887	0.6761	0.7756	0.8870	1.0105
0.1733	1.03	0.4960	0.5890	0.6975	0.8216	0.9613
0.1755	0.98	0.4254	0.5062	0.5991	0.7039	0.8207
0.1740	0.93	0.3982	0.4703	0.5531	0.6468	0.7512
0.1748	0.87	0.3843	0.4516	0.5302	0.6201	0.7213
0.1775	0.82	0.3385	0.3999	0.4710	0.5518	0.6424
0.1759	0.77	0.3122	0.3643	0.4242	0.4918	0.5671
0.1752	0.71	0.2831	0.3305	0.3858	0.4488	0.5196
0.1757	0.66	0.2646	0.3074	0.3570	0.4133	0.4763
0.1742	0.61	0.2482	0.2882	0.3348	0.3878	0.4472
0.1737	0.50	0.2256	0.2564	0.2919	0.3323	0.3773
0.1728	0.39	0.2109	0.2415	0.2788	0.3229	0.3737
0.1721	0.28	0.1966	0.2223	0.2533	0.2896	0.3313
0.1717	0.17	0.1956	0.2196	0.2486	0.2825	0.3215
0.1718	0.06	0.1777	0.1997	0.2270	0.2594	0.2970
0.1700	-0.05	0.1670	0.1883	0.2143	0.2452	0.2809

Appendix E: Chapter 5 Data

Saturated DO Concentration Study

Fe ³⁺ Starting Volume (mL)	500.00
Vessel Temperature (°C)	39.3
Probe Thermistor (kΩ)	5.18
Dissolved Oxygen (% Air Sat.)	0.00
Fe ²⁺ Concentration (g/L)	32.73
Fe ³⁺ Concentration (g/L)	33.31
Fe ²⁺ Volume (mL)	2.000

April 13, 2023			
	mV	mg Fe ²⁺	Ratio
R:	438.5	73.95	0.00445
1:	443.9	53.13	0.00319
2:	443.5	54.30	0.00326
3:	443.3	54.96	0.00330

April 14, 2023			
	mV	mg Fe ²⁺	Ratio
R:	439.4	69.95	0.00420
1:	445.0	49.47	0.00297
2:	444.8	49.97	0.00300
3:	444.5	50.96	0.00306

April 16, 2023			
	mV	mg Fe ²⁺	Ratio
R:	439.0	71.62	0.00430
1:	444.6	50.63	0.00304
2:	443.8	53.30	0.00320

April 17, 2023			
	mV	mg Fe ²⁺	Ratio
R:	438.3	74.95	0.00450
1:	443.2	55.46	0.00333
2:	443.0	56.13	0.00337

Broth Iron Content Data

Ferrous Iron Solution (g/L)							
Diluted (x5)					Undiluted		
500nm	425nm	Fe 3+	Fe Total	Fe 2+	Fe 3+*	Fe Total*	Fe 2+*
0.002	0.569	0.06	6.63	6.57	0.29	33.14	32.85
0.002	0.566	0.06	6.59	6.53	0.29	32.96	32.67
0.002	0.570	0.06	6.64	6.58	0.29	33.19	32.90
0.002	0.564	0.06	6.57	6.51	0.29	32.84	32.55
0.002	0.566	0.06	6.59	6.53	0.29	32.96	32.67
					0.29	33.02	32.73
					Uncertainty		± 0.2

Ferric Iron Solution (g/L)							
Diluted (x5)					Undiluted		
500nm	425nm	Fe 3+	Fe Total	Fe 2+	Fe 3+*	Fe Total*	Fe 2+*
0.227	0.559	6.57	6.51	-0.06	32.85	32.55	-0.30
0.232	0.574	6.71	6.69	-0.03	33.57	33.43	-0.15
0.229	0.566	6.63	6.59	-0.04	33.14	32.96	-0.18
0.231	0.567	6.69	6.60	-0.08	33.43	33.02	-0.41
0.232	0.572	6.71	6.66	-0.05	33.57	33.31	-0.26
					33.31	33.05	-0.26
					Uncertainty		± 0.4

Redox Probe Output Model (39.3 °C) Data

Fe ³⁺ Starting Volume (mL)	500.00
Vessel Temperature (°C)	39.3
Probe Thermistor (kΩ)	5.18
Dissolved Oxygen (% Air Sat.)	0.00
Fe ²⁺ Concentration (g/L)	32.73
Fe ³⁺ Concentration (g/L)	33.31

Sigmoidal Constants	
A	406.2
B	0.6214
C	3.25E-06
D	-2

Redox Probe Calibration							
mL Fe ²⁺	mV	mL Total	Ratio	Ratio*	ln	Deviation	Regen
0.00	480.9	500.00	0.00000	-	-	-	-
0.10	474.1	500.10	0.00020	5089.31	8.53	27.1	473.7
0.20	469.8	500.20	0.00039	2544.65	7.84	18.0	470.2
0.30	466.9	500.30	0.00059	1696.44	7.44	13.1	466.6
0.40	463.7	500.40	0.00079	1272.33	7.15	10.7	463.4
0.50	460.6	500.50	0.00098	1017.86	6.93	9.5	460.8
0.60	458.5	500.60	0.00118	848.22	6.74	8.1	458.4
0.70	456.4	500.70	0.00138	727.04	6.59	7.2	456.4
0.80	454.6	500.80	0.00157	636.16	6.46	6.5	454.5
0.90	452.7	500.90	0.00177	565.48	6.34	6.1	452.8
1.00	451.3	501.00	0.00196	508.93	6.23	5.5	451.3
1.20	448.3	501.20	0.00236	424.11	6.05	4.9	448.6
1.40	446.2	501.40	0.00275	363.52	5.90	4.1	446.2

Redox Probe Calibration (Continued)							
mL Fe ²⁺	mV	mL Total	Ratio	Ratio*	ln	Deviation	Regen
1.60	443.9	501.60	0.00314	318.08	5.76	3.8	444.1
1.80	442.1	501.80	0.00354	282.74	5.64	3.3	442.2
2.00	440.6	502.00	0.00393	254.47	5.54	2.8	440.5
2.20	438.9	502.20	0.00432	231.33	5.44	2.6	438.9
2.40	437.6	502.40	0.00472	212.05	5.36	2.3	437.5
2.60	436.2	502.60	0.00511	195.74	5.28	2.1	436.2
2.80	434.8	502.80	0.00550	181.76	5.20	2.1	434.9
3.00	433.8	503.00	0.00589	169.64	5.13	1.8	433.8
3.50	431.3	503.50	0.00688	145.41	4.98	1.3	431.1
4.00	429.2	504.00	0.00786	127.23	4.85	0.8	428.8
4.50	426.9	504.50	0.00884	113.10	4.73	0.8	426.8
5.00	425.0	505.00	0.00982	101.79	4.62	0.7	424.9
5.50	423.3	505.50	0.01081	92.53	4.53	0.6	423.3
6.00	421.8	506.00	0.01179	84.82	4.44	0.4	421.7
6.50	420.4	506.50	0.01277	78.30	4.36	0.2	420.3
7.00	418.9	507.00	0.01375	72.70	4.29	0.3	419.0
8.00	416.4	508.00	0.01572	63.62	4.15	0.2	416.6
9.00	414.3	509.00	0.01768	56.55	4.04	0.1	414.4
10.00	412.3	510.00	0.01965	50.89	3.93	0.0	412.5
11.00	410.5	511.00	0.02161	46.27	3.83	0.0	410.8
12.00	409.1	512.00	0.02358	42.41	3.75	-0.3	409.2
15.00	404.9	515.00	0.02947	33.93	3.52	-0.4	405.1
18.00	401.4	518.00	0.03537	28.27	3.34	-0.4	401.7
21.00	398.5	521.00	0.04126	24.23	3.19	-0.5	398.9
24.00	396.0	524.00	0.04716	21.21	3.05	-0.6	396.4
27.00	393.4	527.00	0.05305	18.85	2.94	-0.2	394.2
30.00	391.4	530.00	0.05895	16.96	2.83	-0.3	392.2
40.00	386.0	540.00	0.07860	12.72	2.54	-0.4	386.8
50.00	381.7	550.00	0.09825	10.18	2.32	-0.4	382.6
60.00	377.8	560.00	0.11789	8.48	2.14	0.0	379.2
70.00	374.9	570.00	0.13754	7.27	1.98	-0.1	376.3
80.00	371.8	580.00	0.15719	6.36	1.85	0.4	373.7
90.00	369.7	590.00	0.17684	5.65	1.73	0.3	371.5
100.00	367.5	600.00	0.19649	5.09	1.63	0.4	369.5
200.00	354.0	700.00	0.39298	2.54	0.93	0.6	356.3

Redox Probe Output Model (25.3 °C) Data

Fe ³⁺ Starting Volume (mL)	500.00
Vessel Temperature (°C)	25.3
Probe Thermistor (kΩ)	9.69
Dissolved Oxygen (% Sat.)	0.00
Fe ²⁺ Concentration (g/L)	32.73
Fe ³⁺ Concentration (g/L)	33.31

Sigmoidal Constants	
A	65.14
B	0.8523
C	3.13E-04
D	-2

Redox Probe Calibration							
mL Fe ²⁺	mV	mL Total	Ratio	Ratio*	ln	Deviation	Regen
0.00	447.0	500.00	0.00000	-	-	-	-
0.10	445.0	500.10	0.00020	5089.31	8.53	37.1	445.2
0.20	443.3	500.20	0.00039	2544.65	7.84	26.5	442.4
0.30	440.9	500.30	0.00059	1696.44	7.44	21.8	440.7
0.40	439.0	500.40	0.00079	1272.33	7.15	18.6	439.2
0.50	437.5	500.50	0.00098	1017.86	6.93	16.1	437.8
0.60	436.2	500.60	0.00118	848.22	6.74	14.2	436.5
0.70	435.0	500.70	0.00138	727.04	6.59	12.6	435.3
0.80	433.8	500.80	0.00157	636.16	6.46	11.5	434.1
0.90	432.9	500.90	0.00177	565.48	6.34	10.3	433.1
1.00	432.3	501.00	0.00196	508.93	6.23	9.0	432.1
1.20	430.5	501.20	0.00236	424.11	6.05	7.6	430.2
1.40	428.8	501.40	0.00275	363.52	5.90	6.6	428.5
1.60	427.4	501.60	0.00314	318.08	5.76	5.6	427.0
1.80	425.5	501.80	0.00354	282.74	5.64	5.4	425.6
2.00	423.9	502.00	0.00393	254.47	5.54	5.1	424.3
2.20	422.7	502.20	0.00432	231.33	5.44	4.6	423.1
2.40	422.0	502.40	0.00472	212.05	5.36	3.8	421.9
2.60	420.7	502.60	0.00511	195.74	5.28	3.7	420.9
2.80	419.7	502.80	0.00550	181.76	5.20	3.4	419.9
3.00	419.0	503.00	0.00589	169.64	5.13	2.8	418.9
3.50	417.0	503.50	0.00688	145.41	4.98	2.1	416.8
4.00	414.9	504.00	0.00786	127.23	4.85	1.8	414.8
4.50	413.4	504.50	0.00884	113.10	4.73	1.3	413.1
5.00	411.6	505.00	0.00982	101.79	4.62	1.2	411.5
5.50	410.3	505.50	0.01081	92.53	4.53	0.8	410.1
6.00	408.9	506.00	0.01179	84.82	4.44	0.7	408.7
6.50	407.6	506.50	0.01277	78.30	4.36	0.5	407.5
7.00	406.4	507.00	0.01375	72.70	4.29	0.4	406.3
8.00	404.2	508.00	0.01572	63.62	4.15	0.3	404.2

Redox Probe Calibration (Continued)							
mL Fe ²⁺	mV	mL Total	Ratio	Ratio*	In	Deviation	Regen
9.00	402.4	509.00	0.01768	56.55	4.04	0.0	402.3
10.00	400.7	510.00	0.01965	50.89	3.93	-0.2	400.6
11.00	398.8	511.00	0.02161	46.27	3.83	0.0	399.1
12.00	397.6	512.00	0.02358	42.41	3.75	-0.3	397.7
15.00	393.8	515.00	0.02947	33.93	3.52	-0.5	394.0
18.00	390.6	518.00	0.03537	28.27	3.34	-0.5	390.9
21.00	388.0	521.00	0.04126	24.23	3.19	-0.6	388.4
24.00	385.7	524.00	0.04716	21.21	3.05	-0.7	386.1
27.00	383.6	527.00	0.05305	18.85	2.94	-0.7	384.1
30.00	381.5	530.00	0.05895	16.96	2.83	-0.5	382.3
40.00	376.3	540.00	0.07860	12.72	2.54	-0.4	377.4
50.00	372.4	550.00	0.09825	10.18	2.32	-0.4	373.5
60.00	368.7	560.00	0.11789	8.48	2.14	0.0	370.3
70.00	365.9	570.00	0.13754	7.27	1.98	0.1	367.7
80.00	363.5	580.00	0.15719	6.36	1.85	0.1	365.3
90.00	361.2	590.00	0.17684	5.65	1.73	0.4	363.3
100.00	358.9	600.00	0.19649	5.09	1.63	0.8	361.4
200.00	346.7	700.00	0.39298	2.54	0.93	0.7	349.3

DO Calculated Biooxidation Rate Study

39.3 °C			
Time (s)	% Air Sat.	Time (s)	% Air Sat.
76.19	91.04	116.27	42.92
80.19	85.53	120.28	39.01
84.20	80.49	124.30	35.61
88.20	73.66	128.31	32.64
92.22	68.79	132.31	29.64
96.23	64.72	136.33	26.98
100.24	61.81	140.33	24.24
104.25	56.62	144.34	19.70
108.25	51.02	148.36	15.61
112.27	48.16	152.37	12.87

25.3 °C			
Time (s)	% Air Sat.	Time (s)	% Air Sat.
152.41	73.75	256.71	32.09
160.44	70.65	264.72	28.97
168.47	67.33	272.75	26.50
176.49	64.69	280.75	23.24
184.50	60.95	288.77	20.56
192.52	57.29	296.78	17.39
200.53	53.83	304.81	14.92
208.56	51.20	312.84	11.80
216.58	48.16	320.88	9.56
224.60	44.92	328.89	7.44
232.62	41.81	336.91	5.22
240.64	38.28	344.92	3.77
248.67	35.46	352.94	2.49

Redox Probe Output Stability Study

Electrode Stability		
Time	Minute	mV
12:30	0	486.1
12:31	1	474.9
12:32	2	474.4
12:33	3	474.1
12:34	4	473.9
12:35	5	473.4
12:36	6	474.4
12:37	7	474.1
12:38	8	473.9
12:39	9	473.8
12:40	10	473.6
12:41	11	473.5
12:42	12	473.5
12:43	13	473.5
12:44	14	473.4
12:45	15	473.4
12:46	16	474.2
12:47	17	474.1
12:48	18	474.0
12:49	19	473.9
12:50	20	473.8
12:51	21	473.7
12:52	22	473.6

Electrode Stability		
Time	Minute	mV
12:53	23	474.2
12:54	24	473.7
12:55	25	473.5
12:56	26	473.3
12:57	27	473.3
12:58	28	473.2
12:59	29	473.3
13:00	30	473.0
13:01	31	473.1
13:02	32	473.0
13:03	33	473.1
13:04	34	473.3
13:05	35	473.4
13:06	36	473.2
13:07	37	473.9
13:08	38	473.6
13:09	39	474.4
13:10	40	473.8
13:11	41	473.5
13:12	42	474.9
13:13	43	474.4
13:14	44	474.2
13:15	45	473.9
Stability		± 1.0

Appendix F: Chapter 6 Data

Benchtop Scale Dynamic Air Stop-Start k_{La} Study

Biological Media		
U_G (m/s)	VVM	k_{La} (1/s)
0.0395	1.04	0.01953
0.0350	0.91	0.01870
0.0305	0.79	0.01236
0.0260	0.67	0.00954
0.0215	0.56	0.00755
0.0169	0.53	0.00318
0.0124	0.42	0.00259
0.0079	0.31	0.00207
0.0034	0.20	0.00098

Semi-Pilot Scale Dynamic Air Stop-Start k_{La} (25.7 °C) Study

25.7 °C						
Flow* (CFM)	Flow (L/min)	Flow (m ³ /s)	VVM	U (m/s)	1/ k_{La}	k_{La}
0.30	9.35	0.000156	0.0820	0.00315	217.5	0.00460
0.30	9.35	0.000156	0.0820	0.00315	222.0	0.00450
0.30	9.35	0.000156	0.0820	0.00315	238.8	0.00419
0.30	9.35	0.000156	0.0820	0.00315	184.0	0.00543
0.40	12.46	0.000208	0.1093	0.00420	191.2	0.00523
0.40	12.46	0.000208	0.1093	0.00420	151.8	0.00659
0.40	12.46	0.000208	0.1093	0.00420	187.8	0.00532
0.40	12.46	0.000208	0.1093	0.00420	226.5	0.00442
0.50	15.58	0.000260	0.1366	0.00525	208.5	0.00480
0.50	15.58	0.000260	0.1366	0.00525	202.5	0.00494
0.50	15.58	0.000260	0.1366	0.00525	214.7	0.00466
0.50	15.58	0.000260	0.1366	0.00525	218.0	0.00459
0.60	18.69	0.000312	0.1639	0.00629	171.8	0.00582
0.60	18.69	0.000312	0.1639	0.00629	184.9	0.00541
0.60	18.69	0.000312	0.1639	0.00629	184.0	0.00543
0.60	18.69	0.000312	0.1639	0.00629	188.8	0.00530
0.70	21.80	0.000363	0.1912	0.00734	182.7	0.00547
0.70	21.80	0.000363	0.1912	0.00734	217.5	0.00460
0.70	21.80	0.000363	0.1912	0.00734	173.4	0.00577
0.70	21.80	0.000363	0.1912	0.00734	201.3	0.00497
0.80	25.14	0.000419	0.2205	0.00846	173.3	0.00577
0.80	25.14	0.000419	0.2205	0.00846	122.3	0.00818
0.80	25.14	0.000419	0.2205	0.00846	161.7	0.00618
0.80	25.14	0.000419	0.2205	0.00846	131.2	0.00762
0.90	28.55	0.000476	0.2504	0.00961	138.2	0.00724
0.90	28.55	0.000476	0.2504	0.00961	138.7	0.00721
0.90	28.55	0.000476	0.2504	0.00961	114.3	0.00875

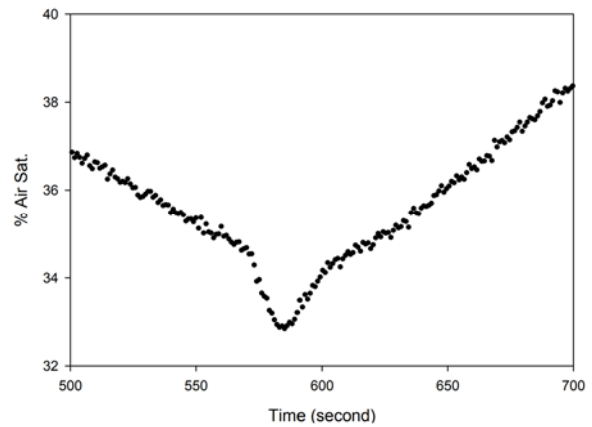
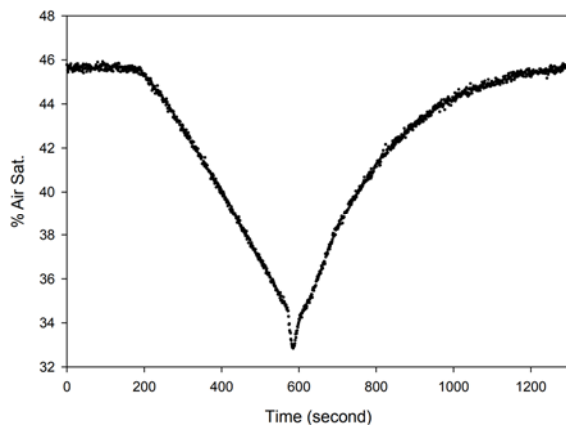
25.7 °C (Continued)						
Flow* (CFM)	Flow (L/min)	Flow (m ³ /s)	VVM	U (m/s)	1/k _{La}	k _{La}
0.90	28.55	0.000476	0.2504	0.00961	157.0	0.00637
1.00	32.28	0.000538	0.2831	0.01087	123.3	0.00811
1.00	32.28	0.000538	0.2831	0.01087	169.3	0.00591
1.00	32.28	0.000538	0.2831	0.01087	120.4	0.00831
1.00	32.28	0.000538	0.2831	0.01087	169.2	0.00591
1.50	51.15	0.000853	0.4486	0.01722	414.1	0.00845
1.50	51.15	0.000853	0.4486	0.01722	391.2	0.00895
1.50	51.15	0.000853	0.4486	0.01722	371.4	0.00942
1.50	51.15	0.000853	0.4486	0.01722	374.9	0.00934
2.00	73.20	0.001220	0.6419	0.02465	424.7	0.01177
2.00	73.20	0.001220	0.6419	0.02465	547.4	0.00913
2.00	73.20	0.001220	0.6419	0.02465	534.1	0.00936
2.00	73.20	0.001220	0.6419	0.02465	664.4	0.00753
2.50	102.57	0.001710	0.8995	0.03454	213.4	0.01406
2.50	102.57	0.001710	0.8995	0.03454	219.7	0.01365
2.50	102.57	0.001710	0.8995	0.03454	358.9	0.00836
2.50	102.57	0.001710	0.8995	0.03454	203.0	0.01478
3.00	142.16	0.002369	1.2467	0.04787	245.0	0.01633
3.00	142.16	0.002369	1.2467	0.04787	367.9	0.01087
3.00	142.16	0.002369	1.2467	0.04787	235.6	0.01698
3.00	142.16	0.002369	1.2467	0.04787	112.4	0.03559

Semi-Pilot Scale Dynamic Air Stop-Start k_{La} (37.5 °C) Study

37.5 °C						
Flow* (CFM)	Flow (L/min)	Flow (m ³ /s)	VVM	U (m/s)	1/k _{La}	k _{La}
0.35	10.92	0.000182	0.0958	0.00368	202.2	0.00495
0.35	10.92	0.000182	0.0958	0.00368	183.2	0.00546
0.35	10.92	0.000182	0.0958	0.00368	176.7	0.00566
0.35	10.92	0.000182	0.0958	0.00368	222.8	0.00449
0.45	14.04	0.000234	0.1231	0.00473	199.4	0.00502
0.45	14.04	0.000234	0.1231	0.00473	206.6	0.00484
0.45	14.04	0.000234	0.1231	0.00473	177.3	0.00564
0.45	14.04	0.000234	0.1231	0.00473	213.9	0.00468
0.55	17.16	0.000286	0.1505	0.00578	205.3	0.00487
0.55	17.16	0.000286	0.1505	0.00578	189.0	0.00529
0.55	17.16	0.000286	0.1505	0.00578	188.6	0.00530
0.55	17.16	0.000286	0.1505	0.00578	219.3	0.00456
0.65	20.41	0.000340	0.1790	0.00687	127.9	0.00782
0.65	20.41	0.000340	0.1790	0.00687	131.4	0.00761
0.65	20.41	0.000340	0.1790	0.00687	175.9	0.00569
0.65	20.41	0.000340	0.1790	0.00687	163.1	0.00613
0.75	23.70	0.000395	0.2078	0.00798	144.9	0.00690
0.75	23.70	0.000395	0.2078	0.00798	148.9	0.00672
0.75	23.70	0.000395	0.2078	0.00798	157.3	0.00636
0.75	23.70	0.000395	0.2078	0.00798	132.9	0.00752

37.5 °C (Continued)						
Flow* (CFM)	Flow (L/min)	Flow (m ³ /s)	VVM	U (m/s)	1/k _{La}	k _{La}
0.85	27.02	0.000450	0.2370	0.00910	132.8	0.00753
0.85	27.02	0.000450	0.2370	0.00910	170.3	0.00587
0.85	27.02	0.000450	0.2370	0.00910	154.6	0.00647
0.85	27.02	0.000450	0.2370	0.00910	133.1	0.00751
0.95	30.56	0.000509	0.2680	0.01029	141.7	0.00706
0.95	30.56	0.000509	0.2680	0.01029	127.3	0.00786
0.95	30.56	0.000509	0.2680	0.01029	140.4	0.00712
0.95	30.56	0.000509	0.2680	0.01029	121.5	0.00823
1.25	41.18	0.000686	0.3611	0.01387	205.2	0.00975
1.25	41.18	0.000686	0.3611	0.01387	226.2	0.00884
1.25	41.18	0.000686	0.3611	0.01387	229.2	0.00873
1.25	41.18	0.000686	0.3611	0.01387	228.6	0.00875
1.75	62.36	0.001039	0.5469	0.02100	203.0	0.00985
1.75	62.36	0.001039	0.5469	0.02100	233.3	0.00857
1.75	62.36	0.001039	0.5469	0.02100	217.2	0.00921
1.75	62.36	0.001039	0.5469	0.02100	217.7	0.00919
2.25	87.55	0.001459	0.7678	0.02948	159.2	0.01256
2.25	87.55	0.001459	0.7678	0.02948	212.1	0.00943
2.25	87.55	0.001459	0.7678	0.02948	164.0	0.01220
2.25	87.55	0.001459	0.7678	0.02948	206.6	0.00968
2.75	120.78	0.002013	1.0592	0.04067	139.5	0.01434
2.75	120.78	0.002013	1.0592	0.04067	114.9	0.01741
2.75	120.78	0.002013	1.0592	0.04067	147.5	0.01356
2.75	120.78	0.002013	1.0592	0.04067	132.0	0.01515

Dynamic Air Stop-Start Method Sample Run Data



Semi-Pilot Scale Static Ferrous Step-Change k_{La} (37.5 °C) Study

Temperature 37.5°C				
Airflow' (CFM)	Pressure (psi)	Airflow (L/min)	VVM	U (m/s)
0.75	1.7	23.68	0.2077	0.00797
1.00	2.0	32.15	0.2820	0.01083
1.25	2.7	41.87	0.3673	0.01410
1.50	3.5	52.56	0.4610	0.01770
1.75	4.4	64.35	0.5645	0.02167
2.00	5.9	79.32	0.6958	0.02671
2.25	7.5	96.16	0.8435	0.03238
2.50	9.6	116.95	1.0259	0.03938
2.75	12.4	143.47	1.2585	0.04831
3.00	16.2	178.46	1.5655	0.06009

Temperature 37.5°C				
% Air Sat.	C (mg _{O2} /L)	QX (mg _{Fe2+} /Ls)	QX (mg _{O2} /Ls)	k_{La} (1/s)
1.21	0.06	0.1618	0.0395	0.00819
2.00	0.10	0.1964	0.0480	0.01002
3.82	0.19	0.2322	0.0567	0.01207
8.06	0.39	0.2527	0.0618	0.01374
13.22	0.65	0.2677	0.0654	0.01542
22.47	1.10	0.2841	0.0694	0.01831
27.94	1.37	0.2934	0.0717	0.02035
74.51	3.64	0.1516	0.0371	0.02972
78.33	3.83	0.1447	0.0354	0.03337
81.25	3.97	0.1502	0.0367	0.04004

Semi-Pilot Scale Static Ferrous Step-Change k_{La} (25.5 °C) Study

Temperature 25.5°C				
Airflow' (CFM)	Pressure (psi)	Airflow (L/min)	VVM	U (m/s)
0.25	1.1	7.60	0.0667	0.00256
0.50	1.4	15.50	0.1359	0.00522
0.75	1.6	23.54	0.2064	0.00792
1.00	1.9	31.96	0.2803	0.01076
1.25	2.5	41.39	0.3631	0.01394
1.50	3.2	51.69	0.4534	0.01740
1.75	4.0	63.00	0.5526	0.02121
2.00	5.1	76.24	0.6687	0.02567
2.25	6.7	92.70	0.8131	0.03121
2.50	9.0	114.07	1.0006	0.03841
2.75	12.3	142.94	1.2539	0.04813
3.00	16.1	177.89	1.5604	0.05989

Temperature 25.5°C				
% Air Sat.	C (mg _{O2} /L)	QX (mg _{Fe2+} /Ls)	QX (mg _{O2} /Ls)	k_{La} (1/s)
37.47	2.24	0.0703	0.0172	0.00460
48.32	2.88	0.0713	0.0174	0.00565
58.80	3.51	0.0725	0.0177	0.00720
60.12	3.59	0.0821	0.0201	0.00843
66.35	3.96	0.0865	0.0211	0.01052
71.13	4.25	0.0902	0.0220	0.01279
76.24	4.55	0.0828	0.0202	0.01427
79.39	4.74	0.0862	0.0211	0.01712
81.61	4.87	0.0881	0.0215	0.01961
84.18	5.03	0.0865	0.0211	0.02238
86.66	5.17	0.0873	0.0213	0.02679
89.23	5.33	0.0846	0.0207	0.03216

Pilot Scale Static Ferrous Step-Change $k_L a$ Study

First Run				
v (m/s)	T (°C)	V (m ³ /s)	Q (kg/s)	Q (kg/h)
4.95	12.0	0.022577	0.027914	100.49
2.00	10.8	0.009122	0.011326	40.77
4.04	9.2	0.018426	0.023008	82.83
3.09	9.5	0.014093	0.017579	63.28
4.47	9.6	0.020388	0.025421	91.51
3.52	10.7	0.016055	0.019941	71.79
2.52	11.2	0.011494	0.014251	51.30

First Run				
% Air Sat.	Fe ²⁺ Rate (g/L·min)	QX (mg _{Fe²⁺} /Ls)	QX (mg _{O₂} /Ls)	C (mg _{O₂} /L)
73.1	0.008457	0.1410	0.0344	4.51
7.7	0.004087	0.0681	0.0166	0.48
47.3	0.009930	0.1655	0.0404	2.92
15.9	0.007482	0.1247	0.0305	0.98
58.6	0.010049	0.1675	0.0409	3.62
21.0	0.008504	0.1417	0.0346	1.30
6.8	0.004977	0.0830	0.0203	0.42

First Run		
$k_L a$ (1/s)	U (m/s)	VVM
0.02076	0.06328	0.726
0.00292	0.02557	0.293
0.01244	0.05164	0.593
0.00587	0.03950	0.453
0.01602	0.05714	0.656
0.00711	0.04500	0.517
0.00353	0.03221	0.370

Second Run				
v (m/s)	T (°C)	V (m ³ /s)	Q (kg/s)	Q (kg/h)
2.47	8.8	0.011266	0.014087	50.71
3.47	9.1	0.015827	0.019769	71.17
4.47	7.7	0.020388	0.025593	92.13
2.00	7.5	0.009122	0.011459	41.25
3.00	7.2	0.013683	0.017207	61.94
3.95	6.6	0.018016	0.022704	81.74
4.95	6.8	0.022577	0.028432	102.36

Second Run				
% Air Sat.	Fe ²⁺ Rate (g/L·min)	QX (mg _{Fe²⁺} /Ls)	QX (mg _{O₂} /Ls)	C (mg _{O₂} /L)
3.6	0.004019	0.0670	0.0164	0.22
21.8	0.009772	0.1629	0.0398	1.35
47.6	0.011738	0.1956	0.0478	2.94
0.2	0.001945	0.0324	0.0079	0.01
11.3	0.007455	0.1243	0.0304	0.70
36.9	0.011602	0.1934	0.0473	2.28
59.3	0.011388	0.1898	0.0464	3.66

Second Run		
k _L α (1/s)	U (m/s)	VVM
0.00275	0.03157	0.362
0.00825	0.04436	0.509
0.01479	0.05714	0.656
0.00129	0.02557	0.293
0.00555	0.03835	0.440
0.01214	0.05049	0.580
0.01847	0.06328	0.726

Third Run				
v (m/s)	T (°C)	V (m ³ /s)	Q (kg/s)	Q (kg/h)
2.52	10.5	0.011494	0.014286	51.43
3.52	7.7	0.016055	0.020154	72.55
4.52	6.9	0.020616	0.025953	93.43
2.00	8.7	0.009122	0.011410	41.08
2.95	7.5	0.013455	0.016902	60.85
3.95	7.2	0.018016	0.022656	81.56
4.95	7.5	0.022577	0.028361	102.10

Third Run				
% Air Sat.	Fe ²⁺ Rate (g/L·min)	QX (mg _{Fe²⁺} /Ls)	QX (mg _{O₂} /Ls)	C (mg _{O₂} /L)
6.9	0.004270	0.0712	0.0174	0.43
26.1	0.009249	0.1542	0.0377	1.61
50.2	0.010562	0.1760	0.0430	3.10
2.0	0.002273	0.0379	0.0093	0.12
19.8	0.007566	0.1261	0.0308	1.22
42.3	0.012303	0.2051	0.0501	2.61
61.4	0.012563	0.2094	0.0512	3.79

Third Run		
k _L α (1/s)	U (m/s)	VVM
0.00303	0.03221	0.370
0.00826	0.04500	0.517
0.01400	0.05778	0.663
0.00153	0.02557	0.293
0.00623	0.03771	0.433
0.01408	0.05049	0.580
0.02149	0.06328	0.726

Appendix G: Chapter 7 Data

Biooxidation (pH) Study

pH	% air sat./s	mg/Ls Fe ²⁺	ug/Ls Fe ²⁺
1.00	0.8032	0.157829	157.83
0.95	0.7723	0.151757	151.76
0.90	0.7511	0.147591	147.59
0.85	0.7873	0.154704	154.70
0.80	0.7394	0.145292	145.29
0.75	0.7079	0.139102	139.10
0.70	0.6840	0.134406	134.41
0.65	0.6337	0.124522	124.52
0.60	0.5785	0.113675	113.68
0.55	0.4860	0.095499	95.50
0.50	0.4104	0.080644	80.64
0.45	0.3581	0.070367	70.37

Jarosite Growth Study

Vial	pH	Start Weight	Finish Weight	Deposit Weight
A	-	5.5793	5.5793	0.0000
B	1.75	5.5515	5.7994	0.2479
C	1.70	5.6028	5.8226	0.2198
D	1.65	5.6025	5.8014	0.1989
E	1.60	5.5889	5.7673	0.1784
F	1.55	5.5669	5.7241	0.1572
G	1.50	5.5813	5.7233	0.1420
H	1.45	5.5632	5.6907	0.1275
I	1.40	5.5610	5.6715	0.1105
J	1.35	5.5484	5.6379	0.0895
K	1.30	5.5620	5.6270	0.0650
L	1.25	5.5919	5.6342	0.0423
M	1.20	5.6260	5.6541	0.0281
N	1.15	5.5689	5.5945	0.0256
O	1.10	5.5839	5.5988	0.0149
P	1.05	5.5553	5.5612	0.0059
Q	1.00	5.6184	5.6221	0.0037
R	0.95	5.5832	5.5894	0.0062
S	0.90	5.5477	5.5494	0.0017
T	0.85	5.6112	5.6118	0.0006
U	0.80	5.5272	5.5274	0.0002
V	0.75	5.5747	5.5747	0.0000
W	0.70	5.5812	5.5812	0.0000

Bioreduction (Temperature) Study

Temp	Rate
5	0.0897
10	0.1419
15	0.1880
20	0.2394
25	0.3195
30	0.3707
35	0.4719
40	0.5127
45	0.6292
50	0.5581

5 °C			
E'	319.90	ζ	16.6433
Time (min)	Voltage	Ratio	[Fe2+]
0	406	0.0057	0.2872
5	406	0.0057	0.2872
10	407	0.0053	0.2705
15	408	0.0050	0.2547
20	409	0.0047	0.2398
25	410	0.0045	0.2259
30	411	0.0042	0.2127
35	412	0.0040	0.2003
40	414	0.0035	0.1776
45	415	0.0033	0.1672
50	416	0.0031	0.1575
55	418	0.0028	0.1397
60	419	0.0026	0.1315
65	421	0.0023	0.1166
70	423	0.0020	0.1034
75	426	0.0017	0.0864
80	428	0.0015	0.0766
85	431	0.0013	0.0640
90	435	0.0010	0.0503
95	439	0.0008	0.0395
100	444	0.0006	0.0293
105	451	0.0004	0.0192

10 °C			
E'	321.75	ζ	16.9758
Time (min)	Voltage	Ratio	[Fe2+]
0	412	0.0049	0.2489
1	412	0.0049	0.2489
2	412	0.0049	0.2489
3	414	0.0044	0.2212
8	415	0.0041	0.2086
13	417	0.0037	0.1854
18	419	0.0033	0.1648
23	422	0.0027	0.1381
25	423	0.0026	0.1302
27	424	0.0024	0.1228
29	425	0.0023	0.1157
31	426	0.0022	0.1091
33	427	0.0020	0.1029
35	429	0.0018	0.0914
37	430	0.0017	0.0862
39	432	0.0015	0.0766
41	434	0.0013	0.0681
43	435	0.0013	0.0642
45	437	0.0011	0.0571
47	440	0.0009	0.0478
49	442	0.0008	0.0425
51	445	0.0007	0.0356
53	448	0.0006	0.0299

15 °C			
E'	323.61	ζ	17.3083
Time (min)	Voltage	Ratio	[Fe2+]
0	417	0.0045	0.2299
5	419	0.0040	0.2048
10	422	0.0034	0.1722
15	425	0.0029	0.1448
20	429	0.0023	0.1150
22	431	0.0020	0.1024
24	433	0.0018	0.0912
26	435	0.0016	0.0813
28	438	0.0013	0.0683
30	440	0.0012	0.0609
32	444	0.0010	0.0483
34	447	0.0008	0.0406
36	452	0.0006	0.0304

20 °C			
E'	325.47	ζ	17.6408
Time (min)	Voltage	Ratio	[Fe2+]
0	434	0.0021	0.1079
1	435	0.0020	0.1020
2	437	0.0018	0.0910
3	438	0.0017	0.0860
4	440	0.0015	0.0768
5	442	0.0014	0.0686
6	443	0.0013	0.0648
7	446	0.0011	0.0547
8	447	0.0010	0.0516
9	450	0.0009	0.0436

25 °C			
E'	327.33	ζ	17.9733
Time (min)	Voltage	Ratio	[Fe2+]
0	424	0.0046	0.2339
1	425	0.0044	0.2213
2	426	0.0041	0.2093
3	427	0.0039	0.1980
4	427	0.0039	0.1980
5	428	0.0037	0.1872
6	429	0.0035	0.1771
7	430	0.0033	0.1675
8	431	0.0031	0.1585
9	433	0.0028	0.1418
10	434	0.0026	0.1341
11	435	0.0025	0.1268
12	437	0.0022	0.1135
13	439	0.0020	0.1015
14	440	0.0019	0.0960
15	442	0.0017	0.0859
16	444	0.0015	0.0769
17	446	0.0014	0.0688
18	448	0.0012	0.0615
19	450	0.0011	0.0551

30 °C			
E'	329.18	ζ	18.3058
Time (min)	Voltage	Ratio	[Fe2+]
0	428	0.0045	0.2293
1	429	0.0043	0.2171
2	430	0.0041	0.2056
3	431	0.0038	0.1947
4	432	0.0036	0.1843
5	433	0.0034	0.1745
6	435	0.0031	0.1565
7	436	0.0029	0.1481
8	437	0.0028	0.1403
9	439	0.0025	0.1257
10	441	0.0022	0.1127
11	442	0.0021	0.1067
12	444	0.0019	0.0957
13	446	0.0017	0.0858
14	449	0.0014	0.0728

35 °C			
E'	331.04	ζ	18.6383
Time (min)	Voltage	Ratio	[Fe2+]
0	427	0.0058	0.2944
1	428	0.0055	0.2790
2	429	0.0052	0.2644
3	430	0.0049	0.2506
4	431	0.0047	0.2375
5	432	0.0044	0.2251
6	434	0.0040	0.2022
7	435	0.0038	0.1917
8	436	0.0036	0.1816
9	438	0.0032	0.1632
10	439	0.0031	0.1546
11	441	0.0027	0.1389
12	443	0.0025	0.1248
13	446	0.0021	0.1062
14	448	0.0019	0.0954
15	451	0.0016	0.0812

40 °C			
E'	332.90	ζ	18.9708
Time (min)	Voltage	Ratio	[Fe2+]
0	423	0.0087	0.4388
1	424	0.0082	0.4163
2	424	0.0082	0.4163
3	425	0.0078	0.3949
4	426	0.0074	0.3746
5	427	0.0070	0.3554
6	428	0.0067	0.3371
7	429	0.0063	0.3198
8	429	0.0063	0.3198
9	430	0.0060	0.3034
10	431	0.0057	0.2878
11	433	0.0051	0.2590
12	434	0.0048	0.2457
13	435	0.0046	0.2331
14	436	0.0044	0.2211
15	438	0.0039	0.1990
16	439	0.0037	0.1888
17	440	0.0035	0.1791
18	442	0.0032	0.1612

45 °C			
E'	334.75	ζ	19.3033
Time (min)	Voltage	Ratio	[Fe2+]
0	427	0.0084	0.4260
1	427	0.0084	0.4260
2	428	0.0080	0.4045
3	429	0.0076	0.3841
4	430	0.0072	0.3647
5	431	0.0068	0.3463
6	432	0.0065	0.3288
7	433	0.0062	0.3122
8	434	0.0058	0.2964
9	436	0.0053	0.2673
10	437	0.0050	0.2538
11	439	0.0045	0.2288
12	440	0.0043	0.2172
13	442	0.0039	0.1959
14	444	0.0035	0.1766
15	446	0.0031	0.1592
16	448	0.0028	0.1435

50 °C			
E'	336.61	ζ	19.6358
Time (min)	Voltage	Ratio	[Fe2+]
0	431	0.0082	0.4142
1	432	0.0078	0.3937
2	433	0.0074	0.3741
3	433	0.0074	0.3741
4	434	0.0070	0.3555
5	435	0.0067	0.3379
6	436	0.0063	0.3211
7	437	0.0060	0.3052
8	439	0.0054	0.2756
9	440	0.0052	0.2619
10	441	0.0049	0.2489
11	442	0.0047	0.2366
12	444	0.0042	0.2137
13	446	0.0038	0.1930
14	447	0.0036	0.1834
15	449	0.0033	0.1656

Benchtop Scale Dynamic Response Study

3 Hour Stoppage		3 Hour Stoppage		3 Hour Stoppage	
Time (h)	Fe ²⁺ (g/L)	Time (h)	Fe ²⁺ (g/L)	Time (h)	Fe ²⁺ (g/L)
0.17	6.25	18.67	4.04	37.17	4.41
0.67	6.04	19.17	4.05	37.67	4.38
1.17	5.97	19.67	4.07	38.17	4.40
1.67	5.93	20.17	4.07	38.67	4.38
2.17	6.05	20.67	4.06	39.17	4.38
2.67	6.19	21.17	4.08	39.67	4.38
3.17	6.21	21.67	4.11	40.17	4.41
3.67	5.41	22.17	4.13	40.67	4.40
4.17	4.64	22.67	4.12	41.17	4.40
4.67	3.92	23.17	4.13	41.67	4.40
5.17	3.29	23.67	4.15	42.17	4.40
5.67	2.67	24.17	4.16	42.67	4.40
6.17	2.19	24.67	4.21	43.17	4.38
6.67	2.29	25.17	4.19	43.67	4.35
7.17	2.48	25.67	4.23	44.17	4.35
7.67	2.56	26.17	4.28	44.67	4.32
8.17	2.73	26.67	4.26	45.17	4.33
8.67	2.82	27.17	4.25	45.67	4.33
9.17	2.94	27.67	4.26	46.17	4.35
9.67	3.05	28.17	4.29	46.67	4.30
10.17	3.13	28.67	4.25	47.17	4.30
10.67	3.23	29.17	4.26		
11.17	3.31	29.67	4.28		
11.67	3.36	30.17	4.28		
12.17	3.41	30.67	4.30		
12.67	3.50	31.17	4.27		
13.17	3.56	31.67	4.29		
13.67	3.60	32.17	4.27		
14.17	3.69	32.67	4.29		
14.67	3.73	33.17	4.31		
15.17	3.78	33.67	4.33		
15.67	3.85	34.17	4.36		
16.17	3.87	34.67	4.37		
16.67	3.91	35.17	4.35		
17.17	3.94	35.67	4.35		
17.67	3.99	36.17	4.35		
18.17	4.00	36.67	4.40		

6 Hour Stoppage		6 Hour Stoppage		6 Hour Stoppage	
Time (h)	Fe ²⁺ (g/L)	Time (h)	Fe ²⁺ (g/L)	Time (h)	Fe ²⁺ (g/L)
0.00	4.59	26.92	0.09	46.08	4.05
1.00	4.35	27.42	0.43	47.58	4.10
2.00	4.30	27.92	0.75	49.08	4.17
3.00	4.33	28.42	1.03	50.58	4.25
4.00	4.33	28.92	1.28	52.08	4.28
5.00	4.28	29.42	1.49	53.58	4.38
6.00	4.28	29.92	1.67	55.08	4.28
7.00	4.28	30.42	1.83	56.58	4.36
8.00	4.28	30.92	2.01	57.83	4.42
9.00	4.26	31.42	2.15	59.58	4.44
10.00	4.33	31.92	2.30	61.58	4.52
11.00	4.43	32.42	2.37	63.58	4.53
12.00	4.28	32.92	2.51	65.58	4.50
13.00	4.30	33.42	2.63	67.58	4.54
14.00	4.28	33.92	2.69	69.58	4.54
15.00	4.22	34.42	2.80	71.58	4.66
16.00	4.28	34.92	2.89	73.58	4.70
17.00	4.28	35.42	2.95	75.58	4.74
18.00	4.26	35.92	3.04	77.58	4.64
19.00	4.28	36.42	3.11	79.58	4.62
20.00	4.26	36.92	3.17		
20.92	4.15	37.42	3.27		
21.42	3.43	37.92	3.26		
21.92	2.76	38.42	3.35		
22.42	2.17	38.92	3.41		
22.92	1.64	39.42	3.52		
23.42	1.17	39.92	3.52		
23.92	0.83	40.42	3.56		
24.42	0.52	40.92	3.58		
24.92	0.27	41.42	3.64		
25.42	0.07	41.92	3.64		
25.92	0.01	43.08	3.70		
26.42	0.00	44.58	3.92		

18 Hour Stoppage		18 Hour Stoppage	
Time (h)	Fe ²⁺ (g/L)	Time (h)	Fe ²⁺ (g/L)
0.00	4.66	36.50	3.10
1.00	4.66	37.00	3.20
2.00	4.70	37.50	3.39
3.00	4.70	38.11	3.51
4.00	4.68	39.50	3.79
5.00	4.79	41.00	4.04
6.00	4.66	42.50	4.26
7.00	4.63	44.00	4.48
8.00	4.63	45.50	4.66
9.00	4.61	47.00	4.87
10.00	4.66	48.50	5.02
11.50	4.41	50.00	5.06
12.00	3.52	51.50	5.17
12.50	2.80	53.00	5.28
13.00	2.19	54.50	5.37
13.50	1.68	56.00	5.48
14.00	1.26	57.50	5.48
14.50	0.87	59.00	5.56
15.00	0.53	60.50	5.52
15.50	0.26	62.00	5.50
16.00	0.07	63.50	5.58
16.50	0.01	65.00	5.68
30.00	0.00	66.50	5.66
30.50	0.41	68.00	5.65
31.00	0.82	69.50	5.72
31.50	1.10	71.00	5.84
32.00	1.41		
32.50	1.66		
33.00	1.90		
33.50	2.10		
34.00	2.30		
34.50	2.49		
35.00	2.65		
35.50	2.83		
36.00	3.00		

24 Hour Stoppage		24 Hour Stoppage	
Time (h)	Fe ²⁺ (g/L)	Time (h)	Fe ²⁺ (g/L)
0.17	5.62	37.50	4.07
0.67	5.43	38.00	4.17
1.17	4.73	38.50	4.22
1.67	3.95	39.00	4.28
2.17	3.30	39.50	4.30
2.67	2.73	40.00	4.34
3.17	2.15	40.50	4.46
3.67	1.68	41.00	4.51
4.17	1.27	41.50	4.52
4.67	0.89	42.00	4.61
5.17	0.60	42.50	4.65
5.67	0.32	43.00	4.69
6.17	0.11	43.50	4.68
6.67	0.01	45.17	4.85
7.17	0.00	47.17	5.11
24.67	0.00	49.17	5.27
25.00	0.20	51.17	5.37
25.50	0.60	53.17	5.42
26.00	0.93	55.17	5.55
26.50	1.20	57.17	5.62
27.00	1.43	59.17	5.69
27.50	1.69	61.17	5.71
28.00	1.86	63.17	5.78
28.50	2.06	65.17	5.78
29.00	2.25	67.17	5.81
29.50	2.41	69.17	5.91
30.00	2.58	71.17	5.95
30.50	2.66	73.17	5.87
31.00	2.81	75.17	5.84
31.50	2.92	77.17	5.80
32.00	3.10	79.17	5.65
32.50	3.24	81.17	5.63
33.00	3.35	83.17	5.62
33.50	3.51	85.17	5.57
34.00	3.63	87.17	5.58
34.50	3.72	89.17	5.51
35.00	3.78	91.17	5.38
35.50	3.83	93.17	5.46
36.00	3.89	95.17	5.50
36.50	3.99	97.17	5.49
37.00	4.03		

Pilot Scale Dynamic Response (Redox Probe) Study

pH 0.8 (Before)							
Time (min)	V (mV)	Th. (k Ω)	T ($^{\circ}$ C)	E'	ζ	Ratio	Fe ²⁺ (g/L)
0	521.4	5.20	40.3	333.02	18.9935	0.00005	0.0017
15	521.7	5.24	40.2	332.95	18.9810	0.00005	0.0017
30	521.8	5.29	39.9	332.87	18.9654	0.00005	0.0017
45	521.2	5.52	38.9	332.48	18.8960	0.00005	0.0016
60	519.7	5.55	38.7	332.43	18.8872	0.00005	0.0017
75	520.7	5.61	38.5	332.33	18.8698	0.00005	0.0016
90	519.5	5.48	39.1	332.54	18.9078	0.00005	0.0018
105	519.1	5.49	39.0	332.53	18.9049	0.00005	0.0018
120	519.5	5.78	37.8	332.06	18.8215	0.00005	0.0017
135	520.1	5.55	38.7	332.43	18.8872	0.00005	0.0017
150	520.6	5.78	37.8	332.06	18.8215	0.00004	0.0016
151	520.1	5.80	37.7	332.03	18.8159	0.00005	0.0016
152	519.5	5.73	38.0	332.14	18.8355	0.00005	0.0017
153	520.8	5.61	38.5	332.33	18.8698	0.00005	0.0016
154	523.2	5.57	38.7	332.40	18.8814	0.00004	0.0014
155	526.9	5.55	38.7	332.43	18.8872	0.00003	0.0012
156	530.0	5.69	38.1	332.20	18.8468	0.00003	0.0010

pH 0.8 (After)							
Time (min)	V (mV)	Th. (kΩ)	T (°C)	E'	ζ	Ratio	Fe ²⁺ (g/L)
0	530.0	10.27	24.4	327.10	17.9338	0.00001	0.0004
5	529.9	10.47	24.0	326.95	17.9054	0.00001	0.0004
10	530.1	10.43	24.1	326.98	17.9110	0.00001	0.0004
15	529.6	10.46	24.0	326.95	17.9068	0.00001	0.0004
16	518.7	10.45	24.0	326.96	17.9082	0.00002	0.0008
17	519.9	10.44	24.0	326.97	17.9096	0.00002	0.0007
18	511.7	10.44	24.0	326.97	17.9096	0.00003	0.0012
19	510.6	10.43	24.1	326.98	17.9110	0.00004	0.0012
20	508.7	10.43	24.1	326.98	17.9110	0.00004	0.0014
21	507.9	10.43	24.1	326.98	17.9110	0.00004	0.0014
22	508.4	10.50	23.9	326.92	17.9012	0.00004	0.0014
23	507.2	10.55	23.8	326.88	17.8942	0.00004	0.0015
24	507.5	10.52	23.9	326.91	17.8984	0.00004	0.0015
25	508.4	10.49	23.9	326.93	17.9026	0.00004	0.0014
26	508.4	10.49	23.9	326.93	17.9026	0.00004	0.0014
27	508.4	10.51	23.9	326.91	17.8998	0.00004	0.0014
28	509.2	10.49	23.9	326.93	17.9026	0.00004	0.0013
29	508.6	10.47	24.0	326.95	17.9054	0.00004	0.0014
30	506.2	10.48	24.0	326.94	17.9040	0.00004	0.0016
35	506.4	10.45	24.0	326.96	17.9082	0.00004	0.0016
40	505.0	10.43	24.1	326.98	17.9110	0.00005	0.0017
45	505.2	10.42	24.1	326.99	17.9124	0.00005	0.0017
50	505.5	10.42	24.1	326.99	17.9124	0.00005	0.0017
55	505.4	10.44	24.0	326.97	17.9096	0.00005	0.0017
60	506.4	10.42	24.1	326.99	17.9124	0.00004	0.0016
65	505.5	10.41	24.1	326.99	17.9139	0.00005	0.0017
70	506.7	10.41	24.1	326.99	17.9139	0.00004	0.0016
75	507.1	10.41	24.1	326.99	17.9139	0.00004	0.0015
80	505.2	10.41	24.1	326.99	17.9139	0.00005	0.0017
85	507.2	10.40	24.1	327.00	17.9153	0.00004	0.0015
90	507.2	10.41	24.1	326.99	17.9139	0.00004	0.0015
95	507.9	10.41	24.1	326.99	17.9139	0.00004	0.0015
100	507.0	10.43	24.1	326.98	17.9110	0.00004	0.0015
105	505.3	10.42	24.1	326.99	17.9124	0.00005	0.0017
120	506.4	10.42	24.1	326.99	17.9124	0.00004	0.0016
145	506.9	10.41	24.1	326.99	17.9139	0.00004	0.0015
160	505.4	10.41	24.1	326.99	17.9139	0.00005	0.0017
175	508.0	10.42	24.1	326.99	17.9124	0.00004	0.0014

pH 0.9 (Before)							
Time (min)	V (mV)	Th. (kΩ)	T (°C)	E'	ζ	Ratio	Fe ²⁺ (g/L)
0	516.8	10.12	24.7	327.23	17.9556	0.00003	0.0011
15	518.6	10.12	24.7	327.23	17.9556	0.00002	0.0010
30	519.0	10.12	24.7	327.23	17.9556	0.00002	0.0010
45	517.4	10.12	24.7	327.23	17.9556	0.00003	0.0011
60	517.9	10.13	24.7	327.22	17.9542	0.00002	0.0011
75	519.0	10.12	24.7	327.23	17.9556	0.00002	0.0010
90	517.1	10.13	24.7	327.22	17.9542	0.00003	0.0011
105	517.2	10.14	24.7	327.21	17.9527	0.00003	0.0011
120	518.3	10.14	24.7	327.21	17.9527	0.00002	0.0010
135	519.7	10.14	24.7	327.21	17.9527	0.00002	0.0010
150	517.5	10.15	24.7	327.20	17.9512	0.00002	0.0011
165	518.8	10.14	24.7	327.21	17.9527	0.00002	0.0010
180	517.6	10.15	24.7	327.20	17.9512	0.00002	0.0011
181	516.6	10.15	24.7	327.20	17.9512	0.00003	0.0011
182	518.9	10.15	24.7	327.20	17.9512	0.00002	0.0010
183	517.6	10.15	24.7	327.20	17.9512	0.00002	0.0011
184	520.8	10.15	24.7	327.20	17.9512	0.00002	0.0009
185	523.2	10.15	24.7	327.20	17.9512	0.00002	0.0008
186	524.8	10.15	24.7	327.20	17.9512	0.00002	0.0008
187	525.5	10.15	24.7	327.20	17.9512	0.00002	0.0008
188	526.3	10.15	24.7	327.20	17.9512	0.00002	0.0007
189	526.8	10.15	24.7	327.20	17.9512	0.00001	0.0007
190	527.1	10.15	24.7	327.20	17.9512	0.00001	0.0007
191	527.6	10.15	24.7	327.20	17.9512	0.00001	0.0007
192	527.9	10.15	24.7	327.20	17.9512	0.00001	0.0007
193	528.0	10.15	24.7	327.20	17.9512	0.00001	0.0007
194	528.2	10.15	24.7	327.20	17.9512	0.00001	0.0007
195	528.4	10.15	24.7	327.20	17.9512	0.00001	0.0007
196	528.4	10.15	24.7	327.20	17.9512	0.00001	0.0007

pH 0.9 (After)							
Time (min)	V (mV)	Th. (k Ω)	T ($^{\circ}$ C)	E'	ζ	Ratio	Fe ²⁺ (g/L)
0	522.5	11.51	21.9	326.17	17.7668	0.00002	0.0008
1	521.0	11.51	21.9	326.17	17.7668	0.00002	0.0008
2	519.3	11.49	21.9	326.19	17.7693	0.00002	0.0009
3	517.9	11.51	21.9	326.17	17.7668	0.00002	0.0009
4	518.3	11.52	21.9	326.16	17.7655	0.00002	0.0009
5	517.0	11.51	21.9	326.17	17.7668	0.00002	0.0010
6	517.7	11.52	21.9	326.16	17.7655	0.00002	0.0009
7	516.3	11.49	21.9	326.19	17.7693	0.00002	0.0010
8	515.9	11.44	22.0	326.22	17.7757	0.00002	0.0010
9	516.4	11.41	22.1	326.24	17.7795	0.00002	0.0010
10	516.7	11.39	22.1	326.26	17.7820	0.00002	0.0010
15	516.5	11.34	22.2	326.29	17.7885	0.00002	0.0010
20	516.3	11.30	22.3	326.32	17.7936	0.00002	0.0010
25	517.6	11.26	22.4	326.35	17.7988	0.00002	0.0010
30	516.2	11.23	22.4	326.37	17.8027	0.00002	0.0010
35	517.2	11.21	22.5	326.39	17.8053	0.00002	0.0010
40	517.2	11.21	22.5	326.39	17.8053	0.00002	0.0010
45	517.0	11.18	22.5	326.41	17.8092	0.00002	0.0010
50	517.6	11.16	22.6	326.42	17.8118	0.00002	0.0010
55	518.3	11.15	22.6	326.43	17.8131	0.00002	0.0009
60	517.2	11.13	22.6	326.44	17.8157	0.00002	0.0010
65	517.6	11.12	22.6	326.45	17.8170	0.00002	0.0010
80	518.3	11.08	22.7	326.48	17.8223	0.00002	0.0009
95	519.3	11.05	22.8	326.50	17.8262	0.00002	0.0009
110	517.5	11.03	22.8	326.52	17.8289	0.00002	0.0010
125	517.5	11.00	22.9	326.54	17.8329	0.00002	0.0010
140	517.6	10.98	22.9	326.56	17.8355	0.00002	0.0010
155	518.1	10.97	22.9	326.56	17.8369	0.00002	0.0010
170	517.0	10.95	23.0	326.58	17.8395	0.00002	0.0010
185	517.4	10.94	23.0	326.59	17.8409	0.00002	0.0010
200	517.8	10.94	23.0	326.59	17.8409	0.00002	0.0010

pH 1.0 (Before)							
Time (min)	V (mV)	Th. (kΩ)	T (°C)	E'	ζ	Ratio	Fe ²⁺ (g/L)
0	519.1	11.03	22.8	326.52	17.8289	0.00002	0.0007
15	517.8	11.00	22.9	326.54	17.8329	0.00002	0.0008
30	518.2	11.00	22.9	326.54	17.8329	0.00002	0.0008
45	519.6	11.03	22.8	326.52	17.8289	0.00002	0.0007
60	519.2	10.98	22.9	326.56	17.8355	0.00002	0.0007
75	519.2	10.97	22.9	326.56	17.8369	0.00002	0.0007
90	518.0	11.00	22.9	326.54	17.8329	0.00002	0.0008
105	519.4	10.95	23.0	326.58	17.8395	0.00002	0.0007
120	519.6	10.94	23.0	326.59	17.8409	0.00002	0.0007
135	519.0	10.94	23.0	326.59	17.8409	0.00002	0.0007
150	519.6	10.92	23.0	326.60	17.8436	0.00002	0.0007
165	518.4	10.92	23.0	326.60	17.8436	0.00002	0.0008
180	519.0	11.23	22.4	326.37	17.8027	0.00002	0.0007
181	518.5	11.27	22.4	326.34	17.7975	0.00002	0.0007
182	517.6	11.26	22.4	326.35	17.7988	0.00002	0.0008
183	516.1	11.28	22.3	326.34	17.7962	0.00002	0.0008
184	517.4	11.29	22.3	326.33	17.7949	0.00002	0.0008
185	518.4	11.30	22.3	326.32	17.7936	0.00002	0.0007
186	519.0	11.33	22.2	326.30	17.7897	0.00002	0.0007
187	519.4	11.32	22.3	326.31	17.7910	0.00002	0.0007
188	519.8	11.32	22.3	326.31	17.7910	0.00002	0.0007
189	520.2	11.33	22.2	326.30	17.7897	0.00002	0.0007
190	520.3	11.35	22.2	326.29	17.7872	0.00002	0.0006
191	520.5	11.37	22.2	326.27	17.7846	0.00002	0.0006
192	520.6	11.38	22.1	326.26	17.7833	0.00002	0.0006
193	520.7	11.35	22.2	326.29	17.7872	0.00002	0.0006
194	520.7	11.30	22.3	326.32	17.7936	0.00002	0.0006
195	520.9	11.26	22.4	326.35	17.7988	0.00002	0.0006
196	521.0	11.24	22.4	326.36	17.8014	0.00002	0.0006
200	521.3	11.22	22.5	326.38	17.8040	0.00002	0.0006

pH 1.0 (After)							
Time (min)	V (mV)	Th. (kΩ)	T (°C)	E'	ζ	Ratio	Fe ²⁺ (g/L)
0	521.0	12.55	20.0	325.47	17.6419	0.00002	0.0005
1	520.8	12.54	20.0	325.48	17.6431	0.00002	0.0005
2	519.7	12.54	20.0	325.48	17.6431	0.00002	0.0006
3	518.3	12.54	20.0	325.48	17.6431	0.00002	0.0006
4	516.3	12.54	20.0	325.48	17.6431	0.00002	0.0007
5	515.6	12.57	20.0	325.46	17.6396	0.00002	0.0007
6	514.0	12.57	20.0	325.46	17.6396	0.00002	0.0008
7	513.9	12.56	20.0	325.47	17.6408	0.00002	0.0008
8	513.2	12.55	20.0	325.47	17.6419	0.00002	0.0008
9	512.8	12.55	20.0	325.47	17.6419	0.00002	0.0009
10	512.5	12.55	20.0	325.47	17.6419	0.00002	0.0009
15	512.9	12.56	20.0	325.47	17.6408	0.00002	0.0009
20	512.9	12.55	20.0	325.47	17.6419	0.00002	0.0009
25	513.0	12.55	20.0	325.47	17.6419	0.00002	0.0009
30	513.3	12.56	20.0	325.47	17.6408	0.00002	0.0008
35	512.1	12.54	20.0	325.48	17.6431	0.00003	0.0009
40	513.6	12.54	20.0	325.48	17.6431	0.00002	0.0008
45	513.0	12.54	20.0	325.48	17.6431	0.00002	0.0009
50	513.8	12.58	20.0	325.46	17.6385	0.00002	0.0008
55	514.2	12.54	20.0	325.48	17.6431	0.00002	0.0008
60	513.2	12.54	20.0	325.48	17.6431	0.00002	0.0008
65	513.8	12.53	20.1	325.49	17.6442	0.00002	0.0008
80	514.6	12.51	20.1	325.50	17.6465	0.00002	0.0008
95	513.2	12.51	20.1	325.50	17.6465	0.00002	0.0008
110	514.6	12.45	20.2	325.54	17.6534	0.00002	0.0008
125	514.7	12.44	20.2	325.54	17.6545	0.00002	0.0008
140	513.8	12.46	20.2	325.53	17.6522	0.00002	0.0008
155	514.0	12.39	20.3	325.58	17.6603	0.00002	0.0008
170	514.3	12.36	20.3	325.60	17.6638	0.00002	0.0008
185	513.9	12.37	20.3	325.59	17.6627	0.00002	0.0008
200	514.5	12.31	20.4	325.63	17.6697	0.00002	0.0008

Pilot Scale Dynamic Response (DO Probe) Study

24 Hour Stoppage (Before)		24 Hour Stoppage (Before)		24 Hour Stoppage (Before)	
Time (h)	% air sat.	Time (h)	% air sat.	Time (h)	% air sat.
0.00	89.97	2.38	89.90	4.75	90.17
0.06	89.89	2.44	90.46	4.81	90.40
0.13	89.86	2.50	90.17	4.88	90.77
0.19	90.42	2.56	90.16	4.94	90.42
0.25	90.10	2.63	90.76	5.00	90.64
0.31	90.52	2.69	90.32	5.06	91.25
0.38	89.81	2.75	90.32	5.13	90.32
0.44	90.07	2.81	90.58	5.19	90.99
0.50	90.02	2.88	90.78	5.25	91.11
0.56	90.11	2.94	90.30	5.31	91.19
0.63	89.12	3.00	90.45	5.38	91.45
0.69	89.73	3.06	91.22	5.44	91.31
0.75	90.05	3.13	90.11	5.50	90.95
0.81	90.31	3.19	90.42	5.56	91.09
0.88	89.75	3.25	91.05	5.63	90.63
0.94	89.51	3.31	90.38	5.69	91.06
1.00	89.77	3.38	90.20	5.75	91.01
1.06	90.04	3.44	90.47	5.81	90.85
1.13	89.92	3.50	89.87	5.88	90.30
1.19	89.41	3.56	90.38	5.94	90.50
1.25	90.03	3.63	90.27	6.00	90.96
1.31	89.65	3.69	90.43	6.06	90.76
1.38	89.62	3.75	90.59	6.13	90.67
1.44	89.95	3.81	90.89	6.19	90.72
1.50	90.26	3.88	90.54	6.25	90.40
1.56	90.12	3.94	90.99	6.31	91.29
1.63	89.94	4.00	90.26	6.38	91.51
1.69	90.22	4.06	90.38	6.44	90.59
1.75	90.34	4.13	90.50	6.50	91.29
1.81	90.54	4.19	90.65	6.56	91.35
1.88	90.10	4.25	90.17	6.63	91.26
1.94	90.01	4.31	90.70	6.69	91.53
2.00	90.35	4.38	89.59	6.75	91.86
2.06	90.00	4.44	90.21	6.81	92.38
2.13	90.97	4.50	90.15	6.88	92.20
2.19	90.29	4.56	89.96	6.94	91.84
2.25	90.55	4.63	89.92	7.00	92.48
2.31	89.86	4.69	90.45	7.06	92.35

24 Hour Stoppage (Before)		24 Hour Stoppage (Before)		24 Hour Stoppage (Before)	
Time (h)	% air sat.	Time (h)	% air sat.	Time (h)	% air sat.
7.13	92.36	9.50	93.22	11.88	93.17
7.19	92.19	9.57	93.92	11.94	92.88
7.25	92.25	9.63	93.08	12.00	92.76
7.32	92.42	9.69	93.57	12.07	92.97
7.38	92.47	9.75	93.52	12.13	92.81
7.44	92.18	9.82	93.28	12.19	92.79
7.50	92.25	9.88	93.49	12.25	92.91
7.57	92.37	9.94	93.22	12.32	93.17
7.63	92.83	10.00	93.39	12.38	92.67
7.69	92.51	10.07	93.00	12.44	93.04
7.75	92.65	10.13	93.12	12.50	92.92
7.82	92.94	10.19	93.21	12.57	92.79
7.88	93.11	10.25	92.83	12.63	93.04
7.94	92.52	10.32	92.87	12.69	92.26
8.00	92.71	10.38	92.77	12.75	93.18
8.07	92.32	10.44	92.64	12.82	93.01
8.13	92.32	10.50	92.81	12.88	93.29
8.19	92.98	10.57	92.78	12.94	92.80
8.25	92.68	10.63	93.49	13.00	92.88
8.32	92.56	10.69	93.44	13.07	92.91
8.38	92.96	10.75	93.08	13.13	92.58
8.44	92.98	10.82	92.78	13.19	92.63
8.50	93.01	10.88	93.41	13.25	92.08
8.57	92.78	10.94	93.21	13.32	92.29
8.63	92.75	11.00	93.14	13.38	91.90
8.69	92.43	11.07	92.84	13.44	91.83
8.75	92.21	11.13	92.73	13.50	91.58
8.82	92.68	11.19	93.21	13.57	92.28
8.88	92.71	11.25	93.23	13.63	92.55
8.94	92.91	11.32	92.87	13.69	92.41
9.00	92.90	11.38	92.76	13.75	92.71
9.07	93.55	11.44	92.59	13.82	91.69
9.13	92.98	11.50	92.81	13.88	92.11
9.19	93.55	11.57	92.93	13.94	92.19
9.25	92.90	11.63	92.89	14.00	92.62
9.32	93.60	11.69	93.49	14.07	92.32
9.38	93.09	11.75	93.29	14.13	92.43
9.44	93.45	11.82	93.17	14.19	92.49

24 Hour Stoppage (Before)	
Time (h)	% air sat.
14.25	92.03
14.32	92.68
14.38	92.19
14.44	91.96
14.50	92.14
14.57	92.09
14.63	92.25
14.69	91.63
14.75	92.34
14.82	92.09
14.88	91.86
14.94	91.74
15.01	91.28
15.07	91.38
15.13	91.33
15.19	90.93
15.26	91.86
15.32	91.68
15.38	92.25
15.44	92.21
15.51	91.34
15.57	91.54
15.63	91.61
15.69	92.21
15.76	92.78
15.82	92.26
15.88	92.75
15.94	92.87
16.01	92.91
16.07	92.26
16.13	92.52
16.19	92.32
16.26	92.47
16.32	92.20
16.38	92.18
16.44	92.09
16.51	92.22
16.57	92.05

24 Hour Stoppage (Before)	
Time (h)	% air sat.
16.63	91.84
16.69	91.75
16.76	91.38
16.82	91.73
16.88	91.87
16.94	91.70
17.01	91.70
17.07	91.68
17.13	91.61
17.19	91.56
17.26	92.22
17.32	91.59
17.38	91.90
17.44	92.09
17.51	93.44
17.57	94.59
17.63	97.23
17.69	99.73
17.76	99.98
17.82	99.86
17.88	100.07
17.94	100.32

24 Hour Stoppage (After)		24 Hour Stoppage (After)		24 Hour Stoppage (After)	
Time (h)	% Air Sat.	Time (h)	% Air Sat.	Time (h)	% Air Sat.
0.00	100.12	2.38	89.68	4.75	90.47
0.06	100.27	2.44	90.25	4.81	90.36
0.13	100.12	2.50	89.49	4.88	90.22
0.19	100.73	2.56	90.00	4.94	90.27
0.25	99.83	2.63	90.13	5.00	90.31
0.31	99.92	2.69	89.97	5.06	90.23
0.38	99.75	2.75	90.07	5.13	90.52
0.44	97.93	2.81	89.89	5.19	90.28
0.50	94.77	2.88	89.95	5.25	90.60
0.56	92.35	2.94	89.79	5.31	90.52
0.63	90.88	3.00	89.99	5.38	90.66
0.69	90.29	3.06	89.61	5.44	90.62
0.75	90.17	3.13	90.15	5.50	90.92
0.81	89.87	3.19	90.27	5.56	90.63
0.88	90.11	3.25	90.34	5.63	90.95
0.94	89.69	3.31	90.03	5.69	90.36
1.00	89.96	3.38	89.86	5.75	91.19
1.06	89.55	3.44	90.32	5.81	90.70
1.13	89.57	3.50	89.93	5.88	90.46
1.19	90.04	3.56	90.55	5.94	90.92
1.25	89.37	3.63	89.98	6.00	90.62
1.31	89.38	3.69	89.76	6.06	91.19
1.38	89.69	3.75	90.06	6.13	91.14
1.44	89.31	3.81	90.12	6.19	91.12
1.50	89.64	3.88	90.22	6.25	90.69
1.56	89.86	3.94	90.19	6.31	90.99
1.63	89.77	4.00	90.02	6.38	90.39
1.69	89.49	4.06	90.63	6.44	90.37
1.75	89.75	4.13	89.98	6.50	90.44
1.81	89.60	4.19	90.39	6.56	90.59
1.88	89.67	4.25	90.66	6.63	89.96
1.94	89.52	4.31	90.40	6.69	90.47
2.00	89.52	4.38	90.36	6.75	90.12
2.06	89.76	4.44	90.12	6.81	89.71
2.13	89.63	4.50	90.38	6.88	90.04
2.19	89.35	4.56	90.61	6.94	90.07
2.25	90.02	4.63	90.77	7.00	89.83
2.31	89.59	4.69	90.49	7.06	89.74

24 Hour Stoppage (After)		24 Hour Stoppage (After)		24 Hour Stoppage (After)	
Time (h)	% Air Sat.	Time (h)	% Air Sat.	Time (h)	% Air Sat.
7.13	89.75	9.50	89.39	11.88	88.41
7.19	90.02	9.57	89.21	11.94	88.38
7.25	90.10	9.63	89.58	12.00	88.51
7.31	90.14	9.69	88.94	12.07	88.47
7.38	89.31	9.75	88.98	12.13	88.08
7.44	89.64	9.82	89.09	12.19	88.78
7.50	89.72	9.88	89.47	12.25	88.40
7.57	89.92	9.94	89.19	12.32	88.61
7.63	88.98	10.00	88.87	12.38	88.80
7.69	89.57	10.07	88.78	12.44	88.41
7.75	89.67	10.13	88.68	12.50	88.32
7.82	89.51	10.19	89.16	12.57	87.82
7.88	88.86	10.25	88.56	12.63	88.72
7.94	88.60	10.32	89.01	12.69	88.32
8.00	88.65	10.38	89.26	12.75	88.79
8.07	88.75	10.44	88.95	12.82	89.07
8.13	88.94	10.50	89.16	12.88	89.58
8.19	88.85	10.57	89.00	12.94	89.34
8.25	89.26	10.63	89.19	13.00	89.35
8.32	88.76	10.69	88.38	13.07	88.87
8.38	89.44	10.75	89.01	13.13	88.77
8.44	88.91	10.82	88.24	13.19	89.26
8.50	88.91	10.88	88.71	13.25	88.89
8.57	88.92	10.94	88.55	13.32	88.87
8.63	88.49	11.00	88.72	13.38	88.60
8.69	89.10	11.07	89.08	13.44	88.97
8.75	88.96	11.13	88.72	13.50	88.98
8.82	88.87	11.19	89.00	13.57	88.93
8.88	89.03	11.25	88.81	13.63	88.97
8.94	89.08	11.32	88.92	13.69	88.45
9.00	89.21	11.38	88.18	13.75	88.94
9.07	89.08	11.44	88.64	13.82	88.89
9.13	89.44	11.50	89.03	13.88	88.23
9.19	88.49	11.57	87.93	13.94	88.23
9.25	88.59	11.63	88.88	14.00	88.69
9.32	88.87	11.69	88.61	14.07	88.41
9.38	89.05	11.75	88.24	14.13	88.60
9.44	89.17	11.82	88.92	14.19	88.97

24 Hour Stoppage (After)		24 Hour Stoppage (After)	
Time (h)	% Air Sat.	Time (h)	% Air Sat.
14.25	88.92	16.63	88.81
14.32	89.16	16.69	88.82
14.38	88.93	16.76	88.78
14.44	88.79	16.82	88.79
14.50	89.22	16.88	88.55
14.57	88.71	16.94	88.96
14.63	89.09	17.01	88.57
14.69	88.58	17.07	88.83
14.75	88.66	17.13	87.78
14.82	88.37	17.19	88.93
14.88	88.37	17.26	88.52
14.94	88.78	17.32	89.22
15.01	89.03	17.38	89.14
15.07	88.87	17.44	88.80
15.13	88.86	17.51	89.00
15.19	89.07	17.57	88.80
15.26	89.30	17.63	88.83
15.32	89.78	17.69	89.63
15.38	89.18	17.76	89.63
15.44	88.54	17.82	88.16
15.51	88.86	17.88	88.53
15.57	88.84	17.94	89.05
15.63	88.98		
15.69	88.98		
15.76	88.48		
15.82	88.97		
15.88	88.92		
15.94	89.04		
16.01	88.71		
16.07	89.04		
16.13	89.73		
16.19	88.96		
16.26	89.29		
16.32	88.64		
16.38	89.23		
16.44	88.58		
16.51	88.92		
16.57	89.22		

Death Rate Study

21 °C Storage		
Time (h)	% air sat./s	µg/Ls
3	1.1648	228.8832
12	1.0837	212.94705
24	1.0741	211.06065
48	0.9475	186.18375
72	0.9136	179.5224
96	0.8672	170.4048
120	0.8755	172.03575
233	0.6908	135.7422
332	0.5073	99.68445

40 °C Storage		
Time (h)	% air sat./s	µg/Ls
3	1.1787	231.61455
27	1.0269	201.78585
51	0.7630	149.9295
98	0.3572	70.1898
123	0.1372	26.9598
147	0.0536	10.5324

Appendix H: Chapter 8 Data

Semi-Pilot Scale Packed Bed Aeration Profile Study

Depth (cm)	38 °C		16.5 °C	
	15.58 L/min	32.28 L/min	15.58 L/min	32.28 L/min
	% air sat.	% air sat.	% air sat.	% air sat.
5	2.34	19.37	7.87	39.77
10	1.02	18.46	6.91	39.16
15	0.72	17.82	6.84	39.03
20	0.56	16.74	7.1	39.19
25	0.31	15.34	7.26	37.84
30	0.33	14.27	6.51	37.74
35	0.35	13.14	6.81	37.96
40	0.31	12.23	6.65	38.06
45	0.25	11.67	6.52	37.83
50	0.29	10.78	6.42	37.99
55	0.23	10.22	5.88	38.06
60	0.21	9.88	5.43	38.08
65	0.17	9.62	6.18	38.13

Pilot Scale Packed Bed Aeration Profile Study

Bottom Measurement					
v (m/s)	T (°C)	V (m ³ /s)	Q (kg/s)	Q (kg/h)	% Air Sat.
5.00	5.9	0.022805	0.028812	103.72	41.1
2.33	5.6	0.010627	0.013441	48.39	0.0
3.52	5.5	0.016055	0.020313	73.13	24.1
4.23	5.9	0.019293	0.024375	87.75	35.4
4.61	5.8	0.021026	0.026574	95.67	37.4
3.85	6.3	0.017560	0.022153	79.75	26.4
3.19	6.8	0.014550	0.018323	65.96	9.6

Top Measurement					
v (m/s)	T (°C)	V (m ³ /s)	Q (kg/s)	Q (kg/h)	% Air Sat.
2.52	10.5	0.011494	0.014286	51.43	6.9
3.52	7.7	0.016055	0.020154	72.55	33.4
4.52	6.9	0.020616	0.025953	93.43	50.2
2.00	8.7	0.009122	0.011410	41.08	2.0
2.95	7.5	0.013455	0.016902	60.85	19.8
3.95	7.2	0.018016	0.022656	81.56	42.3
4.95	7.5	0.022577	0.028361	102.10	61.4

P (kPa)	101.2
R _{air}	287.05
A (m ²)	0.004561

Fuel Cell Polarization Curve Study

Total Electrolyte Flowrate (L/min)	3.913
------------------------------------	-------

Fe ³⁺ (g/L)	37.3700
------------------------	---------

E'	325.47
ζ	17.641

Electronic Load			20°C Redox Probe	
Current	Voltage	Power	Inlet	Outlet
0.0000	4.0125	0.0000	0.711	0.700
0.5175	2.9475	1.5253	0.711	0.679
1.0087	2.7875	2.8118	0.710	0.643
2.0250	2.5750	5.2144	0.710	0.622
3.0037	2.3875	7.1713	0.700	0.611
3.9937	2.2600	9.0258	0.710	0.600
5.9925	2.1525	12.8989	0.705	0.592
7.9912	2.0425	16.3220	0.710	0.582
9.9937	1.9400	19.3878	0.700	0.574
11.9960	1.7925	21.5028	0.695	0.570
16.0270	1.6025	25.6833	0.695	0.562
19.9950	1.4450	28.8928	0.693	0.556
24.0630	1.2750	30.6803	0.670	0.552
27.9970	1.0925	30.5867	0.662	0.546
32.0030	0.8725	27.9226	0.657	0.542
36.0030	0.6375	22.9519	0.637	0.537
40.0080	0.3125	12.5025	0.626	0.525
41.0000	0.2250	9.2250	-	-
Exterior Temperature: 6.5 °C				
Interior Temperature: 27.5 °C				

Electronic Load			20°C Redox Probe	
Current	Voltage	Power	Inlet	Outlet
0.0000	3.0750	0.0000	0.506	0.506
0.4950	2.7850	1.3786	0.506	0.506
0.9862	2.6525	2.6159	0.506	0.506
2.0025	2.5125	5.0313	0.506	0.506
2.9850	2.4200	7.2237	0.506	0.506
4.0050	2.3300	9.3317	0.505	0.505
6.0037	2.1750	13.0580	0.505	0.504
8.0025	2.0450	16.3651	0.505	0.504
10.005	1.9150	19.1596	0.505	0.504
12.003	1.8075	21.6954	0.505	0.503
16.005	1.5825	25.3279	0.505	0.502
20.006	1.3600	27.2082	0.505	0.501
24.007	1.1225	26.9479	0.505	0.501
28.008	0.8300	23.2466	0.505	0.500
32.010	0.4525	14.4845	0.505	0.499
34.320	0.1900	6.5208	-	-
Exterior Temperature: 7.0 °C				
Interior Temperature: 23.0 °C				

Electronic Load			20°C Redox Probe	
Current	Voltage	Power	Inlet	Outlet
0.0000	2.9925	0.0000	0.491	-
0.4950	2.7600	1.3662	0.491	-
1.0200	2.6225	2.6750	0.491	-
2.0025	2.4750	4.9562	0.491	-
2.9887	2.3875	7.1355	0.491	-
4.0050	2.3000	9.2115	0.491	-
6.0075	2.1475	12.9011	0.491	-
8.0062	2.0050	16.0524	0.491	-
10.005	1.8825	18.8344	0.491	-
12.007	1.7550	21.0723	0.491	-
16.008	1.5100	24.1721	0.491	-
20.006	1.2700	25.4076	0.491	-
24.004	0.9825	23.5839	0.491	-
28.008	0.5425	15.1943	0.491	-
31.000	0.1825	5.6575	-	-
Exterior Temperature: 7.0 °C				
Interior Temperature: 24.0 °C				

Fuel Cell Catholyte Consumption Study

Ratio		Fe ²⁺ (g/L)			m (g/min)
Inlet	Outlet	Inlet	Outlet	Produced	
0.0000	0.0001	0.002	0.003	0.001	0.004
0.0000	0.0002	0.002	0.006	0.004	0.017
0.0000	0.0007	0.002	0.026	0.024	0.095
0.0000	0.0016	0.002	0.060	0.059	0.229
0.0001	0.0025	0.003	0.094	0.091	0.356
0.0000	0.0039	0.002	0.145	0.144	0.562
0.0001	0.0054	0.002	0.200	0.198	0.775
0.0000	0.0080	0.002	0.299	0.297	1.162
0.0001	0.0110	0.003	0.411	0.409	1.599
0.0001	0.0129	0.003	0.483	0.480	1.876
0.0001	0.0178	0.003	0.665	0.662	2.589
0.0001	0.0226	0.004	0.845	0.842	3.293
0.0002	0.0265	0.009	0.992	0.983	3.846
0.0003	0.0337	0.012	1.261	1.249	4.886
0.0004	0.0396	0.015	1.480	1.465	5.731
0.0009	0.0484	0.033	1.807	1.774	6.942
0.0014	0.0781	0.051	2.920	2.869	11.226

Theoretical Production Rate			
C/s	C/min	mol/min	g/min
0.0000	0.00	0.000000	0.000
0.5175	31.05	0.001287	0.072
1.0087	60.52	0.002509	0.140
2.0250	121.50	0.005037	0.281
3.0037	180.22	0.007471	0.417
3.9937	239.62	0.009934	0.555
5.9925	359.55	0.014906	0.832
7.9912	479.47	0.019878	1.110
9.9937	599.62	0.024859	1.388
11.9960	719.76	0.029839	1.667
16.0270	961.62	0.039866	2.227
19.9950	1199.70	0.049736	2.778
24.0630	1443.78	0.059855	3.343
27.9970	1679.82	0.069640	3.889
32.0030	1920.18	0.079605	4.446
36.0030	2160.18	0.089555	5.002
40.0080	2400.48	0.099517	5.558

Appendix I: Chapter 9 Data

L. ferriphilum Biooxidation Limit Study

pH	Slope	Rate
1.3	0.010404	0.3468
1.2	0.010184	0.3395
1.1	0.009518	0.3173
1.0	0.009261	0.3087
0.9	0.008594	0.2865
0.8	0.008125	0.2708
0.7	0.007187	0.2396
0.6	0.006221	0.2074
0.5	0.004561	0.1520
0.4	0.003668	0.1223
0.3	0.002455	0.0818
0.2	0.000824	0.0275
0.1	0.000035	0.0012

Light Level Optimization Study

1st - B Series		
W/m ²	mV	Cells (x10 ⁷)
50	271.6	2.06
45	313.5	2.46
40	336.2	2.68
35	267.5	2.02
30	376.8	3.07
25	361.6	2.92
20	454.0	3.80
15	492.0	4.17
10	771.0	6.84
5	1209.0	11.02

1st - D Series		
W/m ²	mV	Cells (x10 ⁷)
50	128.3	0.69
45	123.7	0.65
40	141.8	0.82
35	167.1	1.06
30	185.3	1.24
25	214.5	1.52
20	301.6	2.35
15	347.9	2.79
10	585.0	5.06
5	853.0	7.62

T (°C)	40
Fe ²⁺ (g/L)	0
pH	0.10

T (°C)	20
Fe ²⁺ (g/L)	0
pH	0.10

1st - A Series	
W/m ²	mV
50	35.7
45	37.6
40	43.3
35	51.1
30	62.5
25	72.2
20	87.4
15	97.4
10	131.8
5	190.4

1st - C Series	
W/m ²	mV
50	22.8
45	23.0
40	23.0
35	26.1
30	27.2
25	28.8
20	30.3
15	58.5
10	74.1
5	103.9

T (°C)	40
Fe ²⁺ (g/L)	10
pH	0.10

T (°C)	20
Fe ²⁺ (g/L)	10
pH	0.10

2nd - C Series		
W/m ²	mV	Cells (x10 ⁷)
9.5	642.0	5.60
8.5	687.0	6.03
7.5	737.0	6.51
6.5	886.0	7.93
5.5	1032.0	9.33
4.5	1136.0	10.32
3.5	1363.0	12.49
2.5	1509.0	13.89
1.5	2070.0	19.25
0.5	2201.0	20.51

T (°C)	40
Fe ²⁺ (g/L)	0
pH	0.10

pH Lower Limit Study

2nd - A Series		
pH	mV	Cells ($\times 10^7$)
0.00	1303.0	11.92
-0.05	1136.0	10.32
-0.10	1064.0	9.64
-0.15	1061.0	9.61
-0.20	1012.0	9.14
-0.25	947.0	8.52
-0.30	1079.0	9.78
-0.35	1036.0	9.37
-0.40	985.0	8.88
-0.45	900.0	8.07

T ($^{\circ}$ C)	40
Fe ²⁺ (g/L)	0
W/m ²	5

2nd - B Series		
pH	mV	Cells ($\times 10^7$)
-0.50	886.0	7.93
-0.55	874.0	7.82
-0.60	1087.0	9.86
-0.65	771.0	6.84
-0.70	828.0	7.38
-0.75	569.0	4.90
-0.80	222.0	1.59
-0.85	488.0	4.13
-0.90	57.0	0.01
-0.95	55.0	-0.01

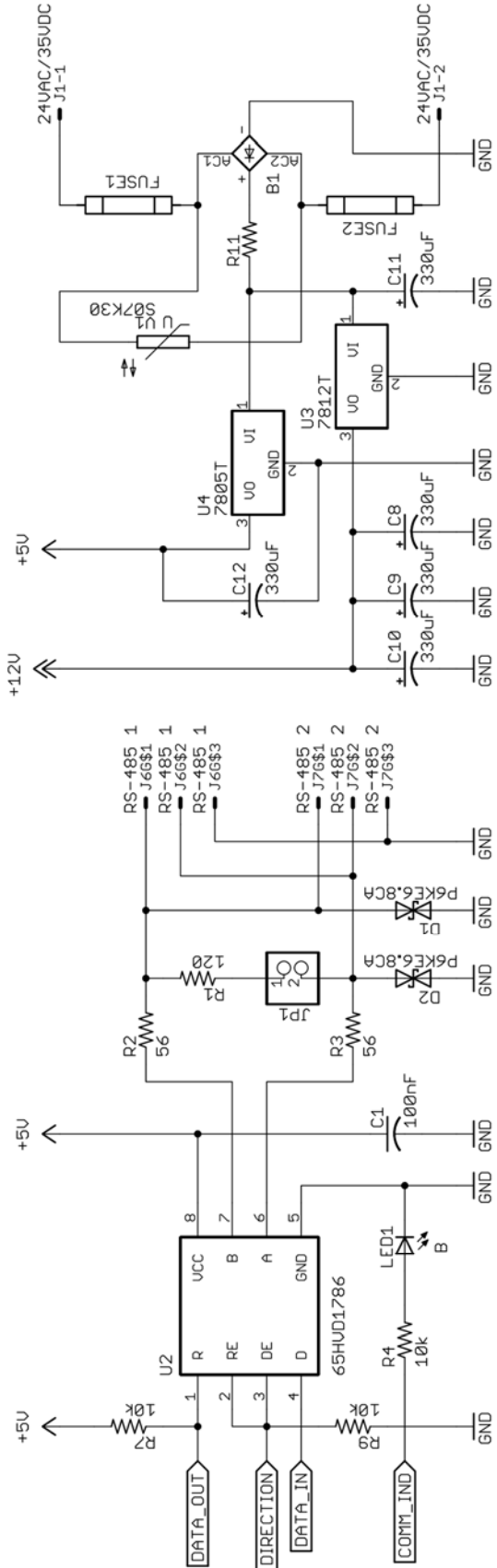
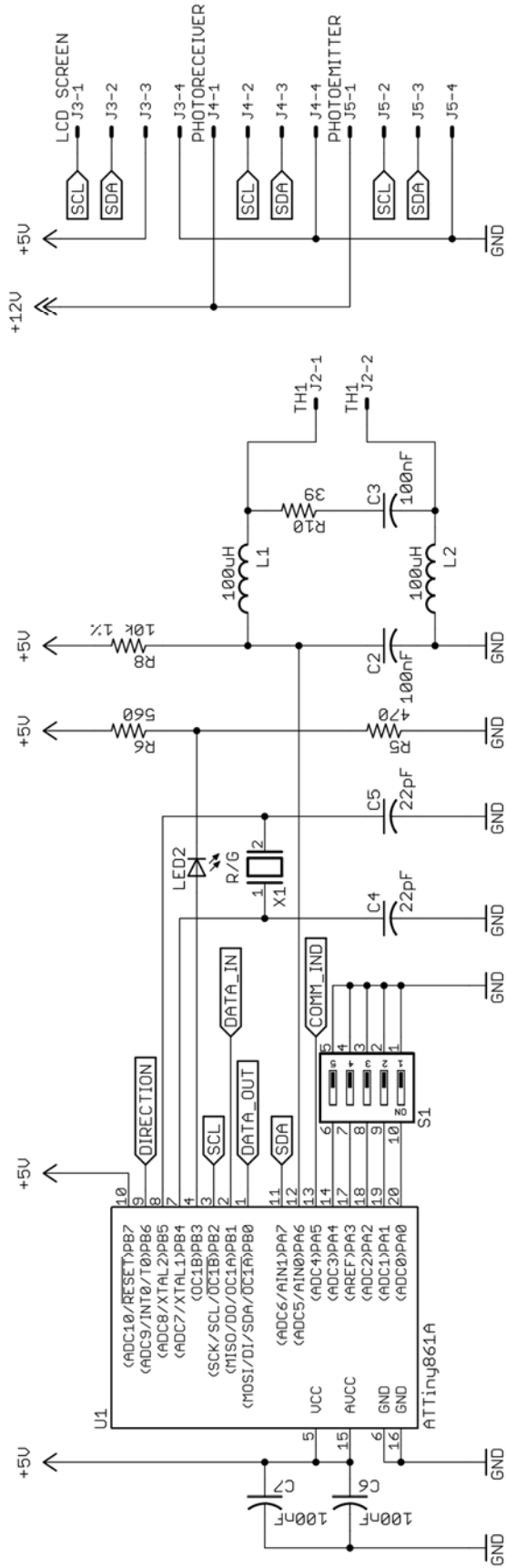
T ($^{\circ}$ C)	40
Fe ²⁺ (g/L)	0
W/m ²	5

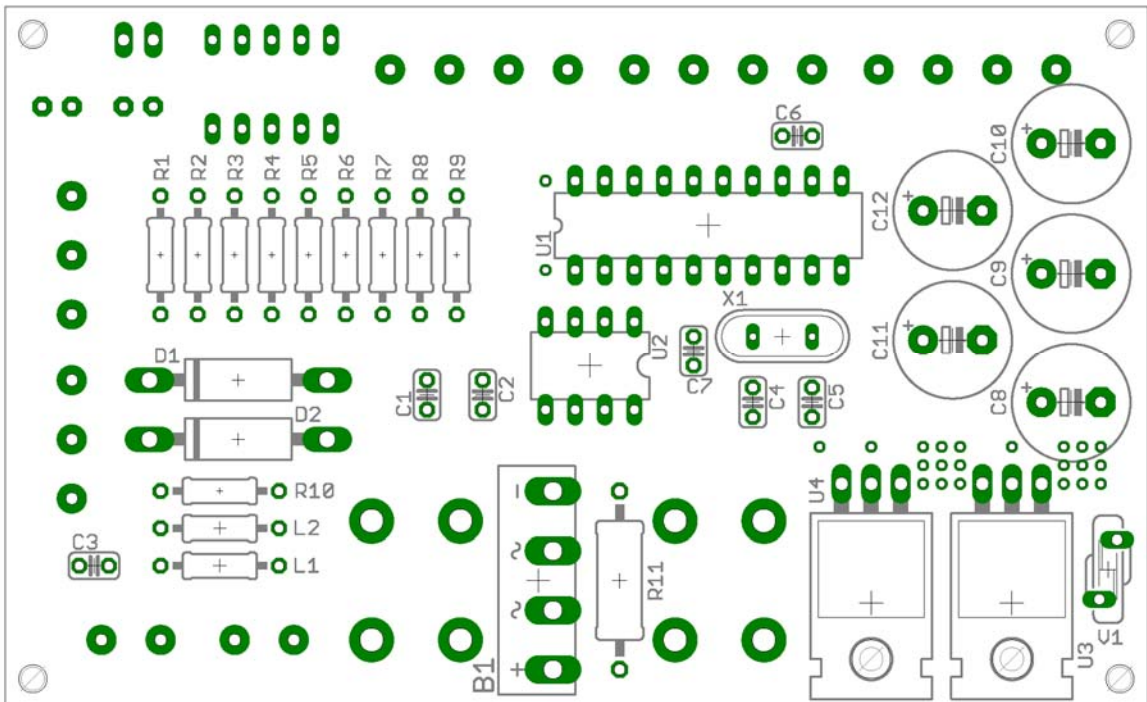
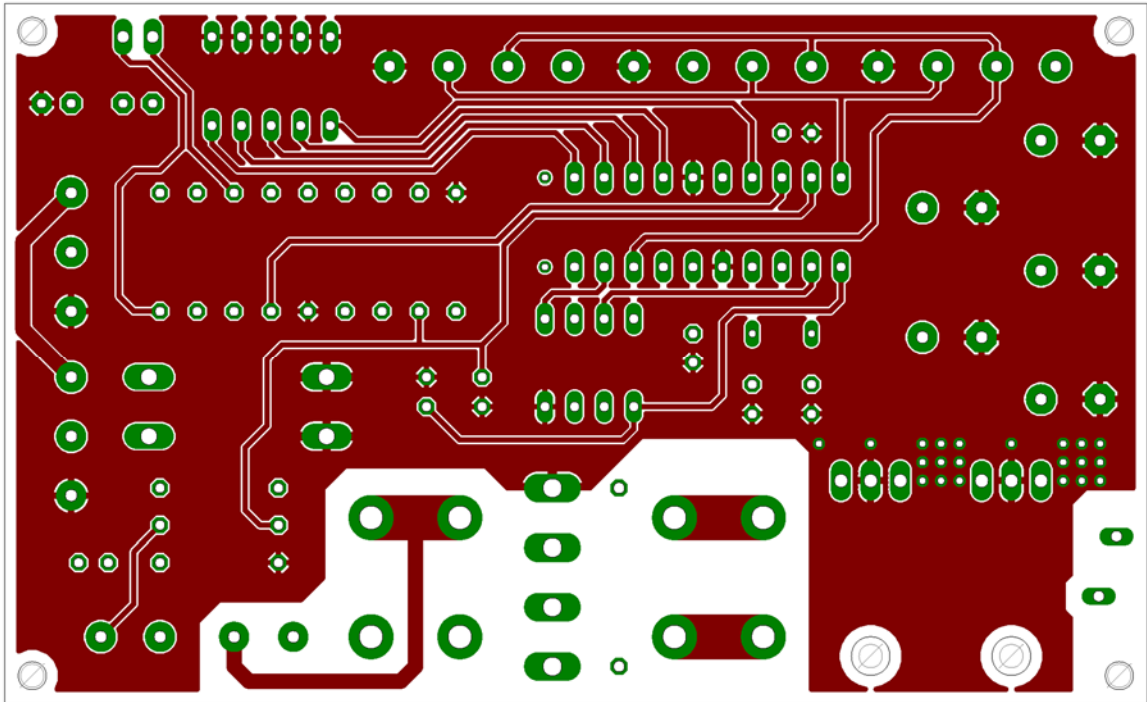
Appendix J: Spectrophotometer Design Notes

Controller Module

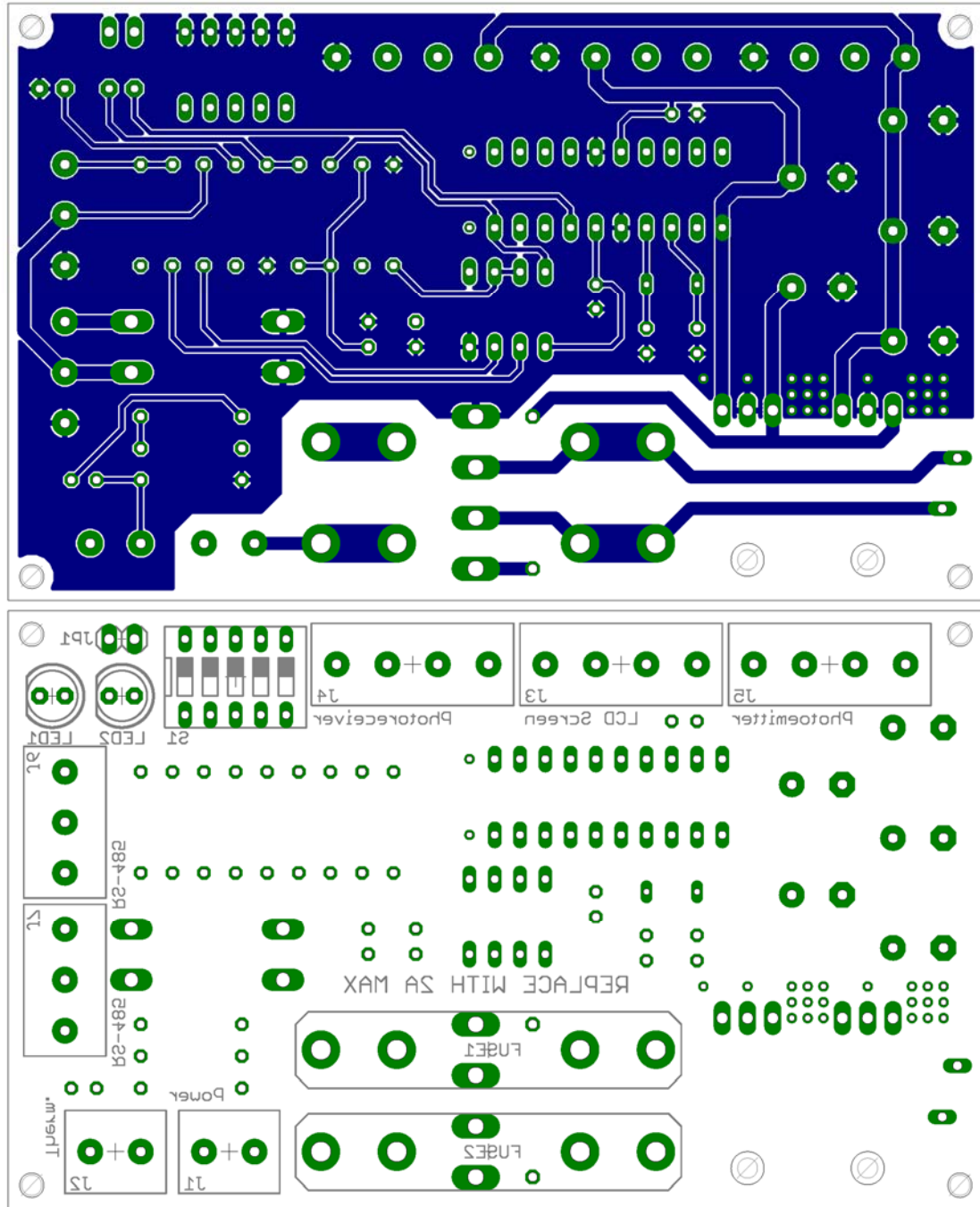


The controller module acts as the master central interface from which the LCD screen, photoreceiver module, and photoemitter module communicate through. The controller module contains three on-board I²C serial communication ports allowing the possibility of expansion and modification along with two dedicated fault-protected RS-485 half duplex serial communication ports to allow for integration to SCADA systems or other external data monitoring hardware. A 5-toggle DIP switch and two indicator LEDs are provided for unit addressing, communication link indication, power status indication, or may be converted for other use. A 2-pin thermistor port with noise filtering is provided for external temperature monitoring using a 10k NTC thermistor (NTCALUG03A103G). The PCB has been designed to accept a microcontroller of type ATtiny261A-PU, ATtiny461A-PU, or ATtiny861A-PU. Power to the controller module may be provided by a 24 volt AC or DC (either polarity) connection and contains fusing on both terminals along with general over-voltage protection provided by a varistor. Electronic schematics and PCB layout design are given in the following diagrams. The outer PCB dimensions are 60 mm by 98 mm which may be used as a measurement reference. These dimensions were selected to match the dimensions of the LCD screen which may be bolted together with the controller module using brass spacers.





Controller Module PCB Upper Side



Controller Module PCB Lower Side

LCD Screen Module



The LCD screen is a commonly found backlit 4 x 20 character matrix based on the HD44780U dot-matrix LCD controller operated in 4-bit mode with an attached PCF8574 I/O expansion module for serial data transmission using I²C interface. The I/O expansion module is a non-standardized design and may potentially be subject to variations in the order of pin connections between the I/O expansion chip and LCD screen connections. Additionally, the I²C address of the I/O expansion chip may vary depending on the specific type used by manufacturer (0x27, 0x3F, others). The I²C address may be altered by the settings of the A0, A1, and A2 jumpers located on the I/O expansion module PCB. The firmware has been developed to operate with the most commonly encountered LCD screen assembly and will function with both the Japanese Standard Font Set (CGROM: A00) or European Standard Font Set (CGROM: A02) present in the HD44780U ROM.

PCF8574 Interfacing to HD44780U:

P0:	Register Select	P4:	Data Bit 4
P1:	Read/Write Select	P5:	Data Bit 5
P2:	Enable Clock	P6:	Data Bit 6
P3:	Enable Back Light	P7:	Data Bit 7

IMPORTANT: Set the LCD screen contrast potentiometer after unit is powered for the first time as incorrect settings can give the appearance of a broken or unresponsive device. Ensure backlight jumper is present on the backside of the device and serial connection cable has been made in the proper orientation. The LCD screen is a third-party manufactured assembly and may be subject to manufacturing variation that requires alteration of the firmware to interface correctly with specific designs.

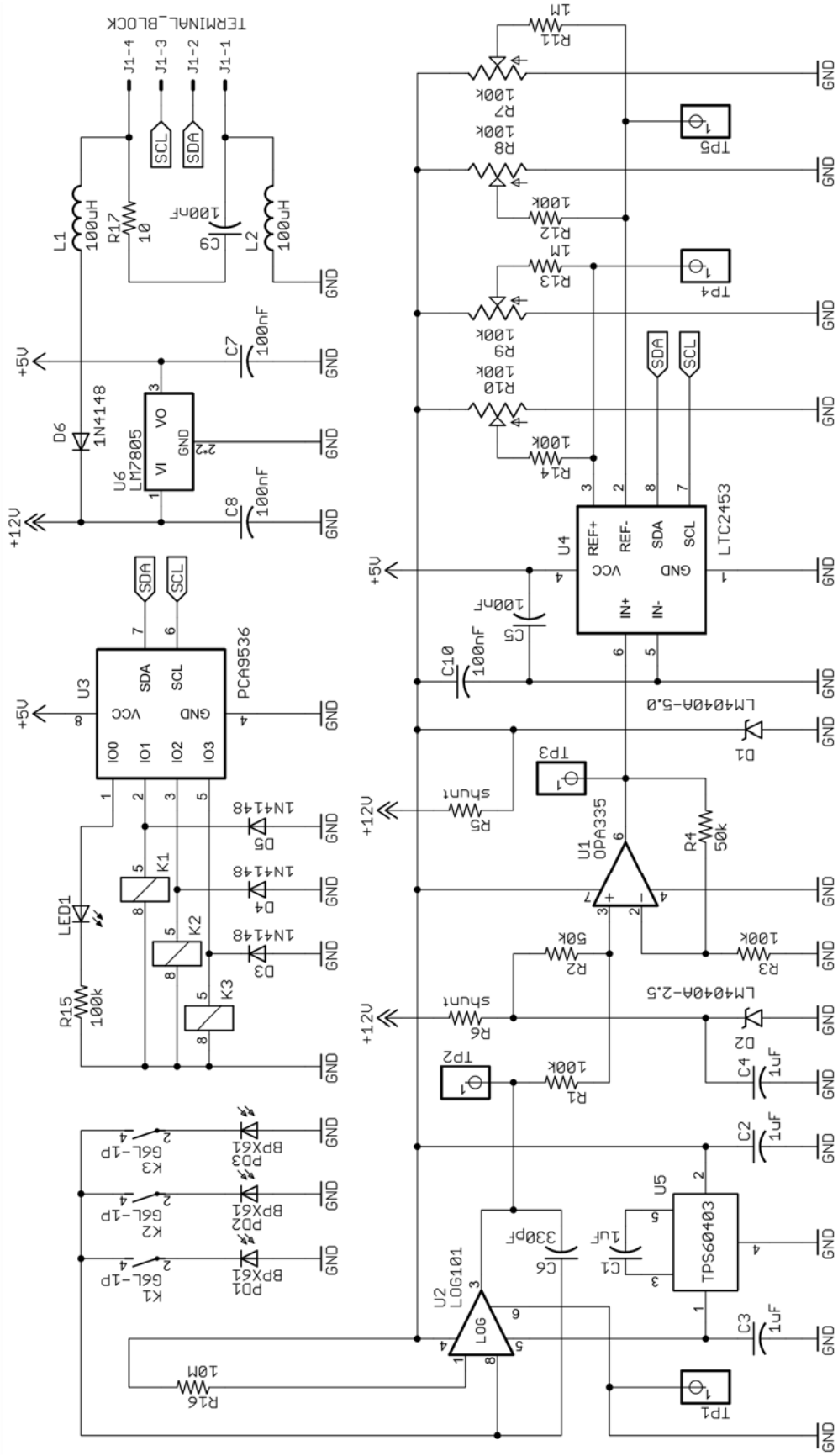
Photoreceiver Module

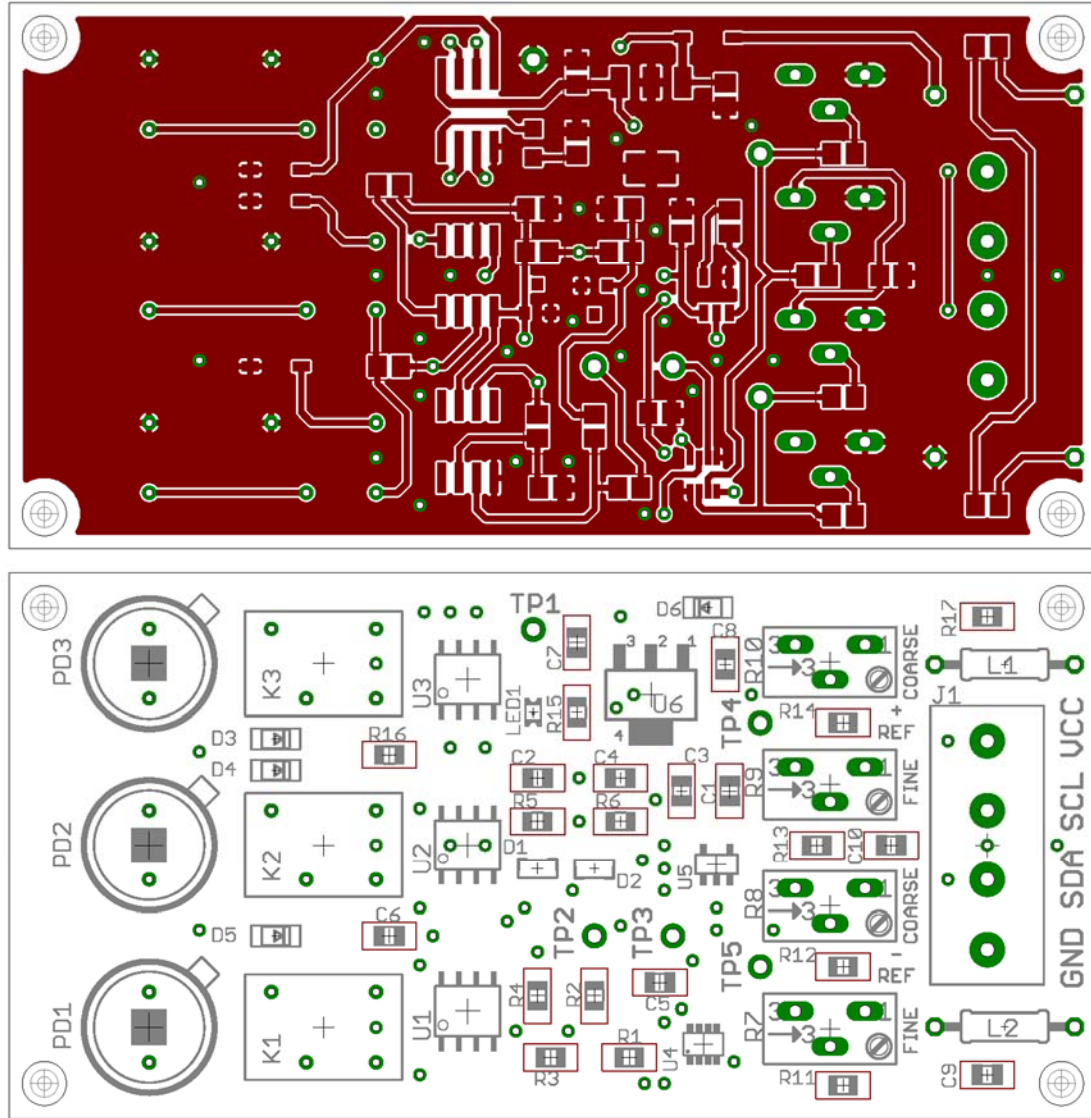


The photoreceiver module makes use of the LOG101 logarithmic amplifier at the core of the design. Inputs from the photodiodes are multiplexed to the amplifier through a series of relays controlled by a PCA9536 I²C 4-bit I/O expansion port and referenced against a common fixed current provided to the logarithmic amplifier by resistor R16. The output from the logarithmic amplifier is passed into a signal conditioning stage using an OPA355 zero-drift op-amp to attenuate and offset the voltage from an input of +5 to -5 V into an output of +5 to 0 V that can be handled by the LTC2453 I²C differential ADC. Negative voltage to the logarithmic amplifier is provided by a TPS60403 charge pump voltage inverter. Coarse and fine potentiometers are used to set the voltage of REF+ through TP4 to 3.960 V and the voltage of REF- through TP5 to 2.500 V. Operation of the ADC under these conditions is outside the specifications and a slight non-linearity appearing as a cubic function was observed, correctable with the equations given below. Eliminating noise from the analog circuitry is an important consideration therefore the high frequency I²C bus lines were routed towards the peripheries of the PCB. The outer PCB dimensions are 1.5625" by 3.1125" which may be used as a measurement reference.

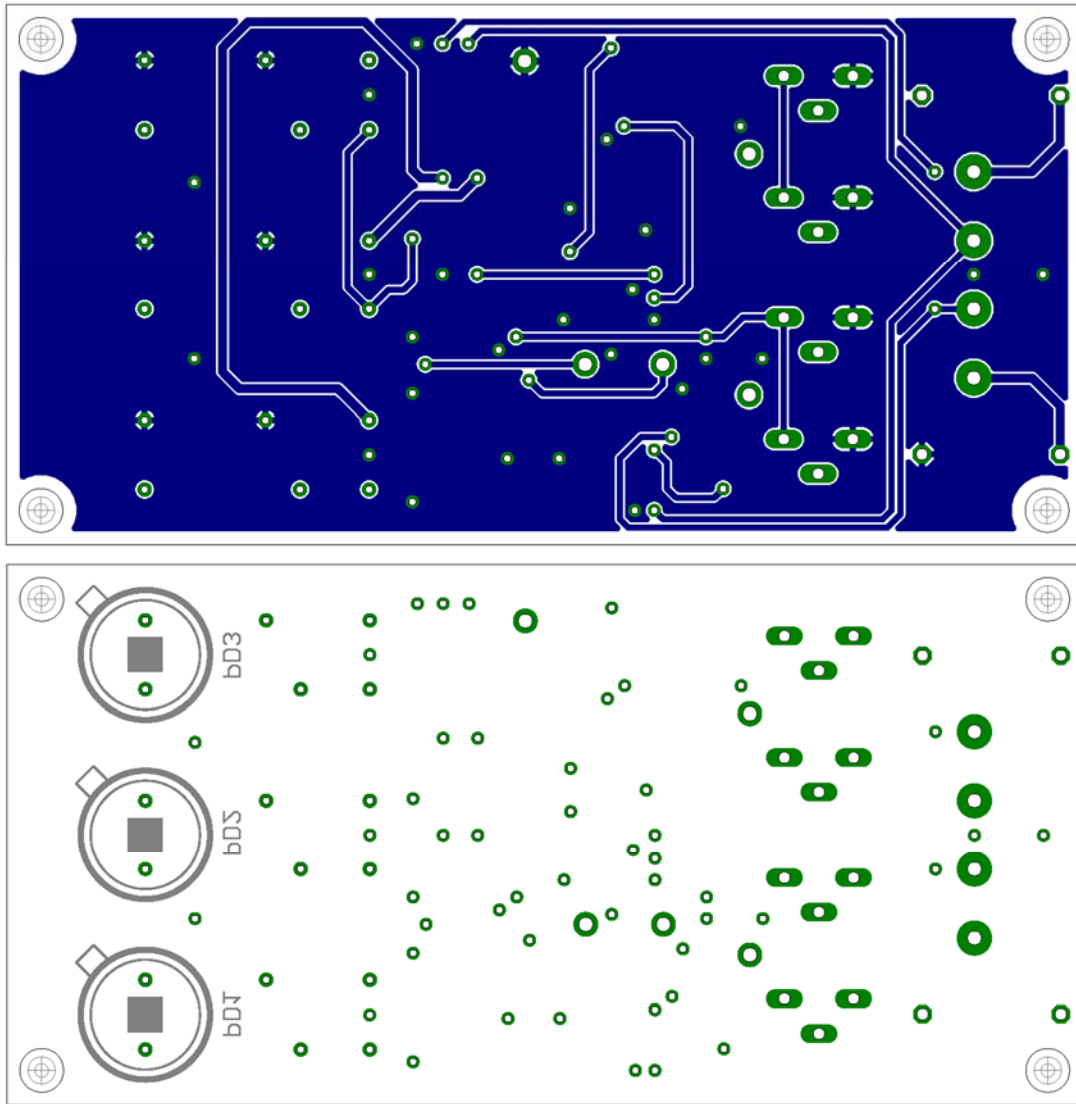
$$[\%_{Abs}] = ADC_{Read} / ((2^{16}/2) - 1)$$

$$e = 0.27273[\%_{Abs}]^3 - 0.38911[\%_{Abs}]^2 + 0.55582[\%_{Abs}] + 0.31633$$



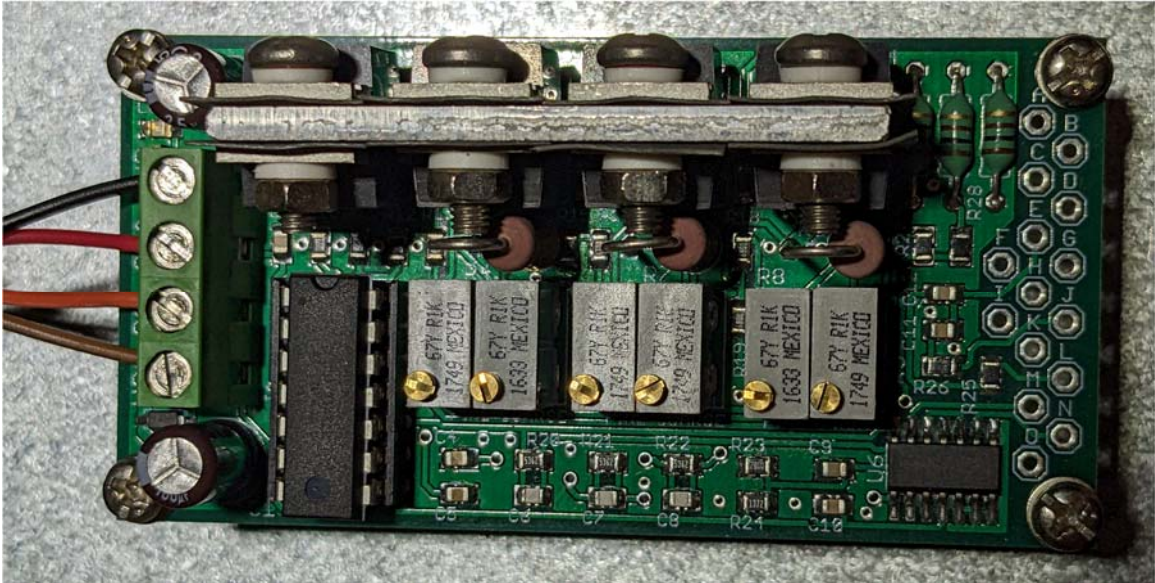


Photoreceiver Module PCB Upper Side



Photoreceiver Module PCB Lower Side

Photoemitter Module



The photoemitter module contains three LM317 constant current drivers with coarse and fine adjustment potentiometers for setting the output power of the laser diodes. An ATtiny84A-PU microcontroller acting as an I²C slave device serves to perform the various functions of the circuit. Laser diode output switching is controlled through three MOSFETs while an internal PID control loop controls a fourth MOSFET through pulse width modulation to regulate resistive heating of the laser diode array module to maintain a stable temperature and avoid mode hopping effects. The resistive heating is turned off temporarily during laser operation to eliminate unwanted noise. The circuit contains additional feedback transimpedance amplifiers for use with laser diodes that contain an output power monitoring photodiode in their construction. The outer PCB dimensions are 1.5625" by 3.1125" which may be used as a measurement reference.

The laser diodes used in the design and their specifications are given in the table below.

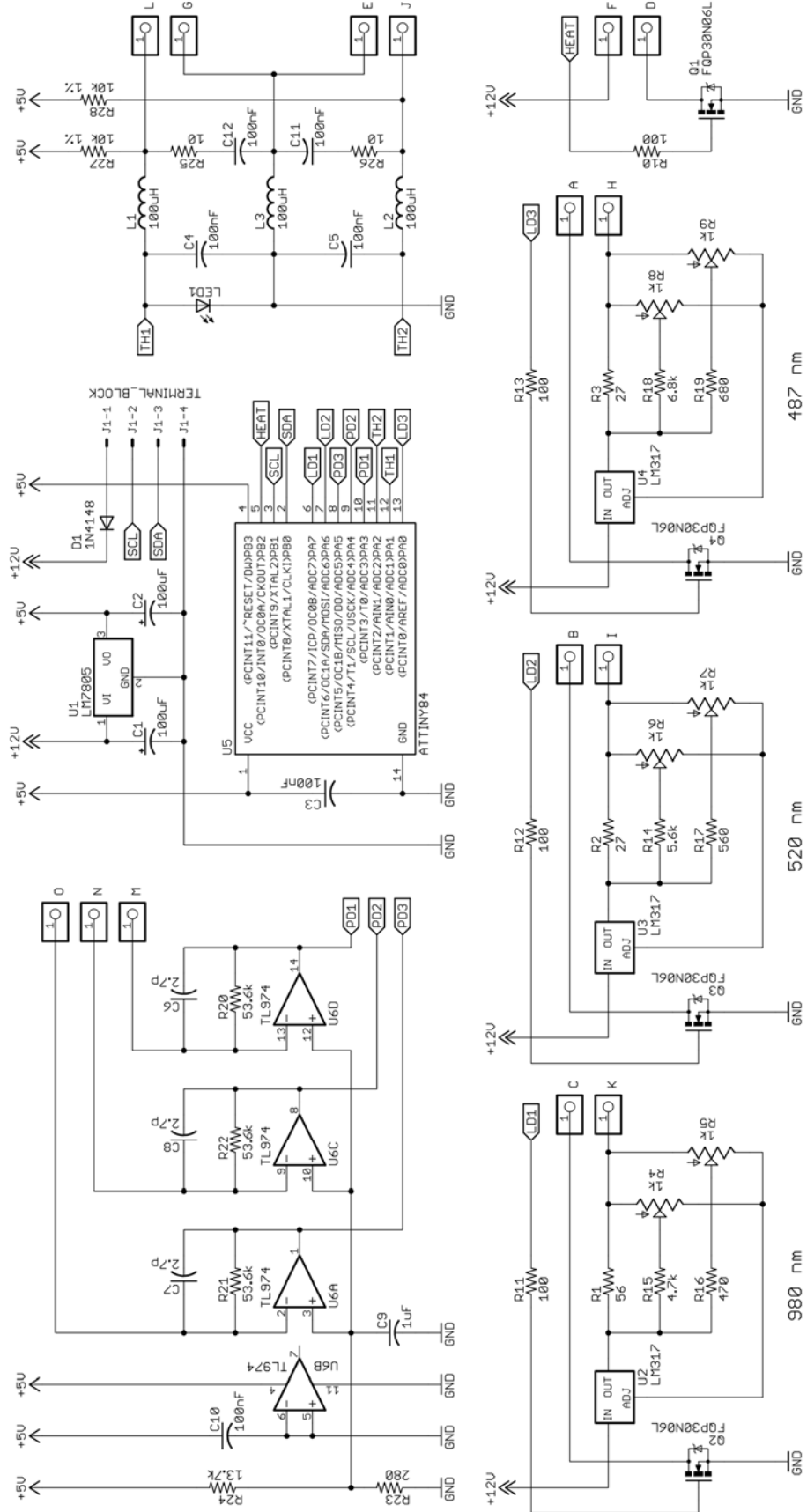
Name	Case	λ	$\Delta\lambda$	P_{optical}	Voltage
GH04850B2G	TO-18	487 nm	± 8 nm	55 mW	6.0 V
PLT5520	TO-18	520 nm	± 2 nm	50 mW	6.9 V
HLD980050N4T	TO-18	980 nm	± 15 nm	50 mW	1.6 V

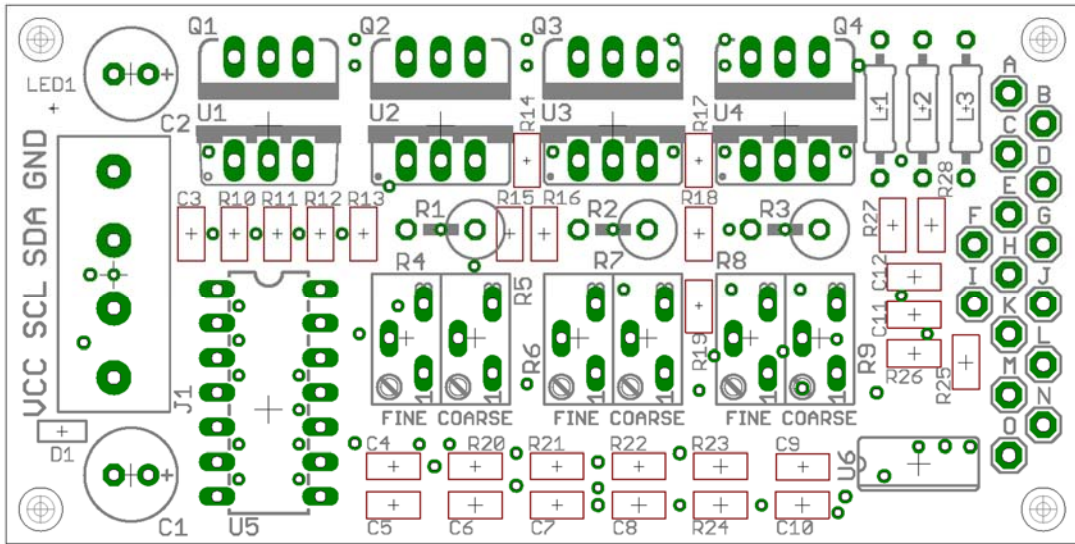
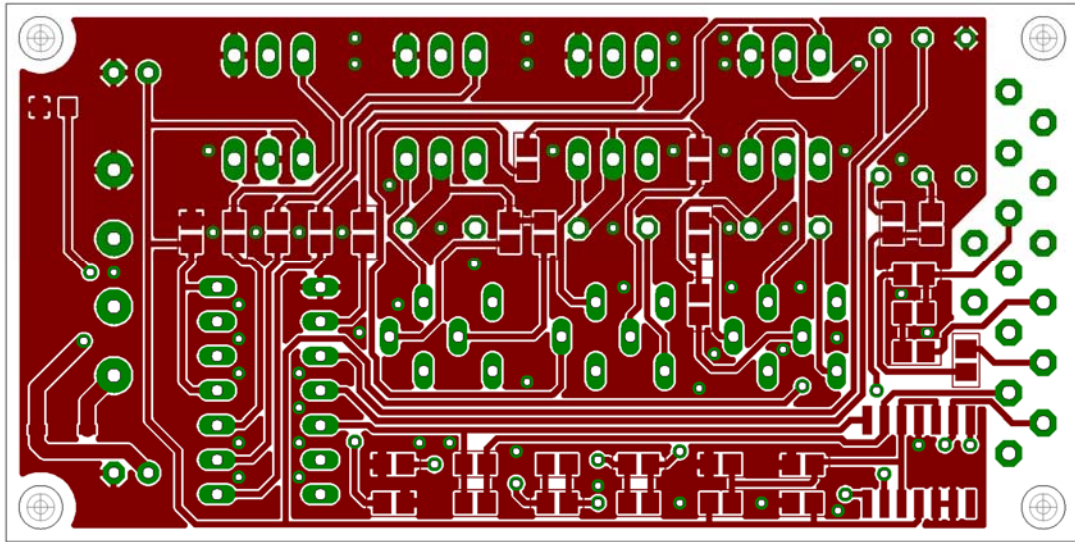
Terminal connections from the circuit board to the laser diode array are given in the table below. Feedback thermistors used in the design were of type NTCALUG03A103G.

Terminal	Function
A	Laser Diode 3 (GH04850B2G) Ground Pin
B	Laser Diode 2 (PLT5520) Ground Pin
C	Laser Diode 1 (HLD980050N4T) Ground Pin
D	Resistive Heater Ground Pin
E	Thermistor 2 Ground Pin
F	Resistive Heater Supply Pin
G	Thermistor 1 Ground Pin
H	Laser Diode 3 (GH04850B2G) Supply Pin
I	Laser Diode 2 (PLT5520) Supply Pin
J	Thermistor 2 Supply Pin
K	Laser Diode 1 (HLD980050N4T) Supply Pin
L	Thermistor 1 Supply Pin
M	Photodiode Input of Laser Diode 1 (Unused)
N	Photodiode Input of Laser Diode 2 (Unused)
O	Photodiode Input of Laser Diode 3 (Unused)

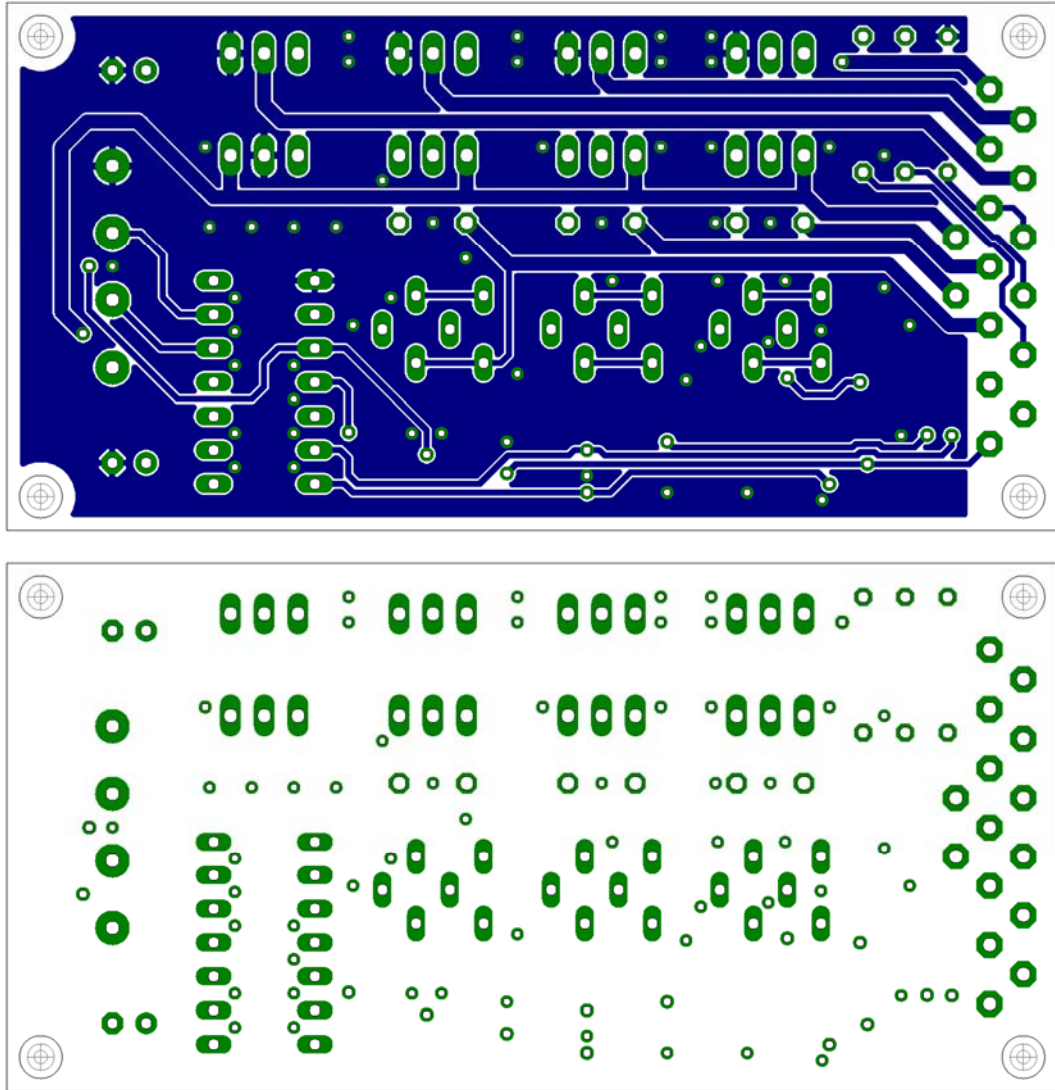
The laser diode array was produced using parts purchased from online retailers consisting of a brass heatsink case modified to fit a laser diode pin plug used to protect the laser diode from thermal damage by avoiding direct soldering of the pins. Collimating lenses were purchased that gave the closest match to the wavelengths in use. An exploded view of the assembly is provided in the picture below.







Photoemitter Module PCB Upper Side



Photoemitter Module PCB Lower Side

Curriculum Vitae

Name: Jason Glas

Post-secondary Education and Degrees: The University of Western Ontario
London, Ontario, Canada
2007-2011 B.E.Sc.

The University of Western Ontario
London, Ontario, Canada
2017-Present Ph.D. Candidate

Related Work Experience Teaching Assistant
The University of Western Ontario
2017-2020

Publications:

Glas J. (2022). Alternative approach to small scale photovoltaic solar power and energy storage. *Ecological Engineering and Environment Protection*, 1(2022): 22-34.

Glas J, Jarboua TA, Nikolov B, Karamanev D. (2021). Process dynamics in a hydrogen-based energy storage system. *Journal of Energy Storage*, 44: 103416.

Glas J, Drandev S, Pupkevich V, Karamanev D. (2019). Energy balance of an airlift bioreactor used for electrical power generation in energy storage. *Chemical Engineering Science*, 210: 115208.